BRNO UNIVERSITY OF TECHNOLOGY
VYSOKÉ UČENÍ TECHNICKÉ V BRNĚ

FACULTY OF ELECTRICAL ENGINEERING AND COMMUNICATION
FAKULTA ELEKTROTECHNIKY A KOMUNIKAČNÍCH TECHNOLOGIÍ

DEPARTMENT OF ELECTRICAL POWER ENGINEERING
ÚSTAV ELEKTROENERGETIKY

MONITORING AND SIMULATION OF ADS EXPERIMENTAL TARGET BEHAVIOUR, HEAT GENERATION, AND NEUTRON LEAKAGE

MONITORING A SIMULACE CHOVÁNÍ EXPERIMENTÁLNÍCH TERČŮ PRO ADS, VÝVINU TEPLA A ÚNIKU NEUTRONŮ

PHD THESIS
DISERTAČNÍ PRÁCE

AUTHOR **Ing. JOSEF SVOBODA**
AUTOR PRÁCE

SUPERVISOR **doc. Ing. KAREL KATOVSKÝ, Ph.D.**
ŠKOLITEL

IN BRNO AND DUBNA 2021

Abstract

Sub-critical Accelerator-Driven Systems (ADS) technology is able to deal with spent nuclear fuel (SNF) of present nuclear reactors, by using the transmutation technique of long-lived radioactive isotopes. As well, the ADS technology is solving the potential problem with the lack of ^{235}U by possible utilisation of ^{238}U or abundant ^{232}Th. This doctoral thesis deals with research on the topic of spallation reaction and heat generation of various experimental targets in the frame of base ADS research. All thermal experiments, in total 13, have been performed at Joint Institute for Nuclear Research (JINR) in Dubna, Russian Federation, during the years 2015-2019. Various targets were irradiated as 512 kg of natural uranium target QUINTA, elongated cylindrical lead target and carbon target, or lead bricks target by 660 MeV protons at the irradiation facility Phasotron at JINR. A special experiment was performed with irradiation of two small $^{\mathrm{nat}}$U cylinders the QUINTA consist of. The author investigates the heat generation by proton reactions (inelastic scattering, and ionisation losses) which are part of spallation reaction including Coulomb scattering (or Rutherford scattering, which represents elastic scattering of charged particles); neutron reaction (mostly contributed by fission); pion$^+$ reaction; and finally gamma heating, the heat generated by photon capturing. The temperature was experimentally measured by highly accurate and specially calibrated thermocouples. The temperature was measured on the surface, and also inside of the target. Additional research was aimed at neutron leakage monitoring by ΔT measurement of tiny volume probes by accurate thermocouples. The first probe contains a small amount of fissile material and the second one of non-fissile material with similar material characteristics. Leaking neutrons (neutron flux outside of the target) were detected due to direct heating by fission reactions. This work deals with accurate temperature measurement by thermocouples. It uses the LabView software for data acquisition, the National Instrument hardware for measuring, and Python 3.7. for data manipulation, analysing and visualisation (with employing several libraries). The particle transportation is simulated by MCNPX 2.7.0. and finally, the heat transfer and surface temperature estimation are simulated by ANSYS Fluent (or ANSYS Transient Thermal for simpler problems).

Keywords

accelerator-driven systems, ADS, ANSYS Fluent, data visualisation, experimental target heat generation, heat transfer, MCNPX, Python, spallation reaction, thermocouples

Abstrakt

Urychlovačem řízené podkritické systémy (ADS) se schopností transmutovat dlouhodobě žijící radionuklidy mohou vyřešit problematiku použitého jaderného paliva z aktuálních jaderných reaktorů. Stejně tak i potenciální problém s nedostatkem dnes používaného paliva, ^{235}U, jelikož jsou schopny energeticky využít ^{238}U nebo i hojný izotop thoria ^{232}Th. Tato disertační práce se v rámci základního ADS výzkumu zabývá spalačními reakcemi a produkcí tepla různých experimentálních terčů. Experimentální měření bylo provedeno ve Spojeném ústavu jaderných výzkumů v Dubně v Ruské federaci. V rámci doktorského studia bylo v průběhu let 2015-2019 provedeno 13 experimentů. Během výzkumu byly na urychlovači Fázotron ozařovány různé terče protony s energií 660 MeV. Nejdříve spalační terč QUINTA složený z 512 kg přírodního uranu, následně pak experimentální terče z olova a uhlíku nebo terč složený z olověných cihel. Byl proveden také speciální experiment zaměřený na detailní výzkum dvou protony ozařovaných $^{\mathrm{nat}}$U válečků, z nichž je složen spalační terč QUINTA. Výzkum byl především zaměřen na monitorování uvolňovaného tepla ze zpomalovaných protonů, spalační reakce a štěpení, způsobeného neutrony produkovanými spalační reakcí. Dále se na uvolňování tepla podílely piony a fotony. Teplota byla experimentálně měřena pomocí přesných termočlánků se speciální kalibrací. Rozdíly teplot byly monitorovány jak na povrchu, tak uvnitř terčů. Další výzkum byl zaměřený na monitorování unikajících neutronů z terče porovnávací metodou mezi dvěma detektory. První obsahoval malé množství štěpného materiálu s teplotním čidlem. Druhý byl složený z neštěpného materiálu (W nebo Ta), avšak s podobnými materiálovými vlastnostmi se stejnými rozměry. Unik neutronů (resp. neutronový tok mimo experimentální terč) byl detekován uvolněnou energií ze štěpné reakce. Tato práce se zabývá přesným měřením změny teploty pomocí termočlánků, s využitím elekroniky od National Instrument a softwaru LabView pro sběr dat. Pro práci s daty, analýzu a vizualizaci dat byl použit skriptovací jazyk Python 3.7. (s využitím několika knihoven). Přenos částic by simulován pomocí MCNPX 2.7.0., a konečně simulace přenosu tepla a určení povrchové teploty simulovaného modelu bylo provedeno v programu ANSYS Fluent (pro jednodušší výpočty ANSYS Transient Thermal).

Klíčová slova

ADS, ANSYS Fluent, MCNPX, přenos tepla, Python, spalační reakce, vývin tepla experimentalních terčů, termočlánky, urychlovačem řízené systémy, vizualizace dat

Reference

SVOBODA, Josef. *Monitoring and simulation of ADS experimental target behaviour, heat generation, and neutron leakage*. Brno, 2021. PhD thesis. Brno University of Technology, Faculty of Electrical Engineering and Communication. Supervisor doc. Ing. Karel Katovský, Ph.D.

Declaration

I hereby declare that this Doctoral thesis was prepared as an original work by the author under the supervision of doc. Ing. Karel Katovský, PhD. The supplementary information was provided by the supervisor specialist prom. fyz. Jindřich Adam, CSc., by colleagues from the Department of Nuclear Spectrometry and Nuclear Chemistry of the Dzelepov Laboratory of Nuclear Problems (DLNP) in Dubna and Department of Electrical Power Engineering (DEPE) under Faculty of Electrical Engineering and Communication (FEEC) at Brno University of Technology (BUT) in Brno. I have listed all the literary sources, publications and other sources, which were used during the preparation of this thesis.

.....
Josef Svoboda
May 11, 2021

Acknowledgements

In the course of this work, I have been lucky to receive the assistance and support of many people, without whose thought, equipment, skills, funding, or friendship none of this work would have been possible.

My supervisor Karel Katovský, who has been motivating and inspiring me as a scientist, as well as a person, for his selflessness, dedication, and unreal kindness. The man who led me to science and aimed my professional career to nuclear topics for the last eight years, as a supervisor of my Bachelor, Diploma, and finally Doctoral theses. Thank you, Karel!

My supervisor specialist Jindřich Adam, that time the head of the ADS group at Dzelepov Laboratory of Nuclear Problems (DLNP) at JINR, who warmly welcomed me in Dubna and led my experimental research topic in Department of Nuclear Spectrometry and Nuclear Chemistry. My thanks belong to all colleagues in Dubna and Brno, whose helped me with experimental research, and also with solving daily problems in a foreign country without Russian language background those time, namely Alexander Alexandrovich Solnyshkin, Jurabek Khushvaktov, Dušan Král, Pavel Tichý, Radek Vespalec, Miroslav Zeman, Lukáš Závorka, Leo Schlattauer, Vratislav Chudoba and Pavel Bláha. I am very grateful to Pavel Zácha, CTU in Prague and TechSoft company, namely Tomáš Prejda for their kind help and consultations in frame of ANSYS Fluent simulations. The daily research life at JINR was very pleasant from the early beginning thanks help of Alojz Kovalík, that time the head of the Czech scientist group in Dubna.

Many experiments in the theme of ADS research in Dubna were performed in the frame of the collaboration of Energy and Transmutation of Radioactive Waste (E&T RAW), namely I would like to thank Sergey Ivanovich Tyutyunikov, the head of the ADS group in Veksler and Baldin Laboratory of High Energies (LHE) for his funding of experiments. Furthermore, to the operating staff of the irradiation facility Phasotron for their hard work during long experiments, usually on Friday nights, namely, to Sergey Alexandrovich Gustov for helping with target preparation and solving our irradiation requirements.

I am grateful for the financial support from the Educational Programme of the Director of the JINR and Plenipotentiary of the Government of the Czech Republic in JINR and for funds allocated in the grants of the Plenipotentiary of the Government of the Czech Republic in JINR and the grants 3+3 in the period between 2016 and 2020. My special gratitude belongs to The Ministry of Education, Youth and Sports of the Czech Republic for the support, and for allowing me to be part of the project between the Czech Republic and JINR in Dubna. To Petr Toman, the head of the DEPE who allows me to work on experimental research abroad during my PhD studies, and to Victor Borisovich Brudanin, head of the Department of Nuclear Spectrometry and Nuclear Chemistry, who passed away in 2020.

Last but not least, my family. I would especially like to thank my mother Hana and father Josef for their upbringing, love, and endless support throughout the study. To my close friends Jiří, Lukáš, Hana and many others, for cheering me up and support and finally, my girlfriend Barbora, for her support, love, and ability to turn dark days into brightened ones, especially during finishing the thesis at long COVID isolation in Dubna.

List of Figures

List of Tables

Contents

Chapter 1

Introduction

Foreword - several subjective words, author's point of view.

Ecology. Economy. Energy.
Three important and well discussed topics, perceptibly connected, which politics across the globe deal with. In the last decade, the world and mostly European Union (EU) have finally begun to genuinely deal with ecology topics. During the developing of Europe, ecology was neglected and overlooked. Its economy was primarily built up on coal, crude oil, and natural gas (Fig. 1.1). By growing the economy, we are still overlooking the nature needs. The planet Earth responds by rising sea levels, more frequent local droughts, increasing numbers of hurricanes, and other more frequent fluctuations. It is scientifically proved, the world is dealing with global warming, chiefly caused by human [1], [2].

We are growing in all ways. Economy, affluence, and so the population. We have lost track of sustainability and the sense of real wealth. What do we expect is the never-ending growth. We are humankind. We think we are uppermost. However, in the end it looks like we are just a spectrum of individuals who live in social bubbles, in the shade of its own comfort zone. We have great tools to communicate, to share knowledge and to get any seeking information. Maybe we were not ready for this information revolution. We are overwhelmed by information, we are enticed by populism. We are searching for a quick and easy solution. As the instant is not real, so the quick is not long lasting. The society polarisation is still growing, year by year, crisis by crisis.

— USA were slowly closing the doors to a democracy principle under the populism leader.
— Independent newspapers are attacked worldwide.
— Humanity is in lethargy (written before the COVID pandemic).

Infinite affluence rising is not sustainable for all of 7.5 billion inhabitants of the planet Earth. Undeveloped countries are longing for their better future economic growth and a piece of affluence they see on Facebook. There are many ideas and several certain ways to aim for the sustainable energy future. All of them start with the fossil fuels limitation, in particular coal. The energy sector is major. Incomplete combustion in household heating is also a health issue (respiration disease). Then the limitation of oil usage in transport and step-by-step reduction of the CO_2 emissions.
Fight against disinformation is the connected topic as well. Critical thinking can suppress hoax spreading as well as source tracking. Unfortunately, people did not master these skills yet. A long-term solution should be found in increased investment in research and education. The science popularisation is required to get people to be involved.
▶ Developed countries must find an ecological solution for the growing undeveloped one.

1.1 Humankind and energy with global warming aspects

Humankind experienced many energy evolutions or even revolutions[1]. If check the history deep enough, the mastering of the fire is a milestone. Humankind scared of the fire earlier. Later, they started to use it very carefully and finally invented the way of its easy control. They reached heat and light. Activity could continue after sunset. Evolution of fire usage comes through the history up to our daily life nowadays. Hundreds of industrial applications are based on it. Later, there are other smaller or bigger victories of evolution. Growth of affluence for a prehistoric man at least 25000 years ago by using hunting weapons like bows and arrows, or fishnets around 12000 years ago. Increased hunting skills ensure enough food, enough energy. Around 6000 B.C.E., cattle were domesticated to lighten the hard work in agriculture and transit weight (energy for transportation), around 4000 B.C.E horses followed. Then the profitability of rotation movement. Domesticated animals were used to power the mills and other rotating facilities. The wind and water power utilisation occurred just several hundreds years C.E. in Persian, followed by China about 1200 C.E. Fireplace centralisation was the move forward to the modern era, as a simple furnace usage at the beginning of the 17th century.

Enormous progress became during the 18th century in Western Europe, generally called the Industrial Revolution, lasting until the middle of the 20th century in North America. The affluence started exponentially growing over those times. Important to notice that France were supplied only by about 20 GJ of primary energy per capita in 1818. It was a little less primary energy than used in the Marcus Aurelius Rome Empire and an equal amount of nowadays consumption in Tanzania or Togo [6]. About 90 % obtained by wood combustion.

Generally, the economy (≈energy) growth is more or less balanced by environmental degradation. It was mostly caused by the fossil fuels usage, see Fig.[2] 1.1 and Appendix A.1. Global warming is not a simple problem we face to. Its complexity, in combination with politics populism, makes the global warming questionable for many people[3].
Global warming is a complex problem and can be observed only on a long-term scale. The long-term average of CO_2 atmospheric concentrations have a similar trend as the temperature anomalies, see Fig. A.1. There are some variants of human-made[4] greenhouse gas (GHG)[5] with various global warming potentials due to different atmospheric lifetimes.

[1] The chapter is inspired by the work of Vaclav Smil, dates are extracted from [3] and [4]. Further inspiration connected with nuclear energy comes from the book written by V. Kumar and K. Katovský [5].

[2] Historical chart data comes from Appendix A, p.155 [7], these data are synthesised by UNO 1956 [8] and 1976 [9], and BP 2009 [10]. A historical area chart shows the relative consumption of primary energy by each source (axis y_1, left), and also contains total primary energy consumption (red line) on the second axis (y_2, right). Nuclear electricity is divided by the average efficiency of thermal plants (38 %) and hydroelectricity is divided by the average efficiency of hydro-power plants (90 %), to receive the primary energy shown in the chart. Unfortunately, this methodology is not consistent with the pie charts for the 2018 year, where data are extracted from BP [11]. The electric energy produced by nuclear, hydro and renewable sources is divided by the efficiency of average thermal power plant (38 %) to derive primary energy.

[3] I have a feel that we live nowadays in post-fact time, where *True* or *False* may reach both values in the same time. This feel is not connected with global warming strictly, it is everywhere around us. Since politicians are not the elite, we are looking up to, since „moral“ is a strange word from a lost dictionary and since the True&False is rather than 1&0, defined as $\mathbf{R} \in (0,1)$. Shades of grey represent black and white.

[4] The most abundant greenhouse gas in the atmosphere is water vapour (H_2O). It is considered that its concentration is changing since the industrialisation time and probably contributes to global clime change as well. Unfortunately, it has been poorly measured and understood yet [12].

[5] Other GHG (CH_4, N_2O, and a group of so-called „*F-gases*“) are more discussed in Appendix A.1.

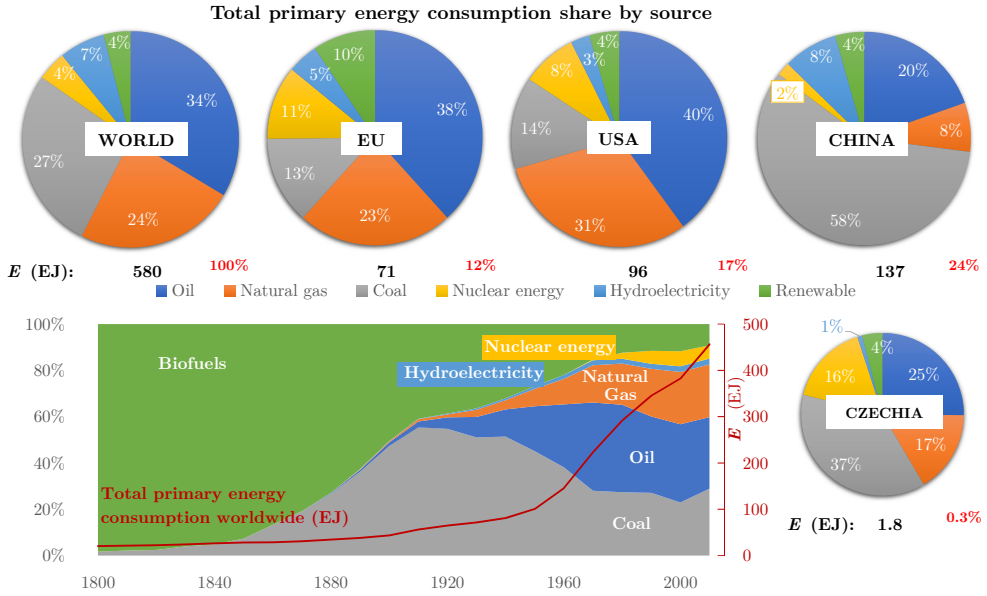

Figure 1.1: One of the most important charts to understand the primary energy consumption worldwide[74]. Pie charts represent primary energy consumption by source per country, data 2018 [11]. Below pie charts is listed the annual energy consumption in [EJ]→[10^9GJ] (black colour) and its relative ratio (red colour). The plane chart lower represents historical relative data of the primary energy share (left y axis by [%]). There is shown also a red curve representing the total primary energy consumption word-wide, which responds to the right $y2$ axis (red), data [7].

China, the most populated country hosting about 1.4 billion of inhabitants with long-term gross domestic product growth more than twice higher than Europe, North America, or the World average [13], has the energy mix based on coal with the share about 60 % (Fig. 1.1). It represents the most significant portion (27 %) of the world annual CO_2 emissions (Fig. A.6). China signed the Paris Agreement[6], however it supports merely „Below 2 °C scenario“. They plan to reduce primary energy consumption by 20 % relatively to 2017 until 2050 and their long-term plan expects to produce about 58 % primary energy from renewable sources[7]. Primary energy share of coal should fall down to 12 % and CO_2 emissions should drop to about 40 % of the present amount. Since China has large and rapidly growing economy, these plans could be more challenging. On the other hand it is fair enough for the kind of country the China represents. Moreover if remind so-called „western“ country - USA[8] with the second biggest annual contribution of CO_2 which withdraw the Paris Agreement[6]. All countries are preparing a long-term energy plan for 2050 based on their renewable energy potential. Nowadays, there are several carbon-neutral energy sources available, including hydro, solar, wind, geothermal, and nuclear energy.

[6]Agreement, signed by 189 parties including EU, dealing with Global warming with the goal to keep the increase of global average temperature below 2 °C relative to pre-industrial times.

[7]Specifically, hydro (6.1 %), wind (25.3 %), solar (15.4 %), biomass (7.4 %), and geothermal (3.9 %) [14].

[8]Impact of populism on energy+ecology topics can be pointed out by USA situation. During 2005 - 2016, the USA were the leaders of CO_2 emission reduction. About 15 % reduction (presidency of Barack Obama, predominantly). It has been achieved mostly by fracking and replacement of some coal power plants by gas [15], but also by investment to renewable sources. The USA finally, together with China, signed the Paris Agreement. After the populist President Donald Trump has taken office, the USA withdrew this agreement. Hopefully, it looks that nowadays President Joe Biden turns the USA back to renewable energy.

Table 1.1: Estimation of the relative CO_2 equivalent emission for various energy sources (synthesised version). Two different data sources merged, 2014 [16] and 2008 [17].

Technology	**Life-cycle emissions** *Min/Median/Max* ($gCO_2e{\cdot}kWh^{-1}$) [16]	**Life-cycle emissions** (gCO_2e/kWh) data [17], 2008
Wind onshore	7 / 11 / 56	9
Wind offshore	8 / 12 / 35	10
Hydroelectric	1 / 24 /2200	10-13
Biomass	130/230/420	14-41
Solar PV utility	18 / 48 /180	32
Nuclear	3.7 / 12 /110	66
Natural gas	410/490/650	443
Coal	740/820/910	960-1050

The perfect and easy solution for decarbonisation has not been found yet. Current electricity energy sources (see shares in Fig. 1.2) brings its pros and cons. The necessity of coal energy reduction is unquestionable, despite its low cost. Natural gas is a fossil fuel which produces about half of the coal emissions, but it has significant benefits for grid operation. Gas turbines can cover the peak of user demand due to a quick start. It is very useful mainly for solar and wind utilisation in real grid (weather changes). It must be taken into account that the gas power station cost of produced MWh is highly dependent on the fuel cost and the carbon emission trading cost. Economical solution for covering these peaks is a challenge for renewable sources. Without covering them, they can not be largely exploited and used in base-load. Electricity storage makes renewable energy rapidly more expensive (discussed in section 1.1) with larger life-cycle emissions. There are large investments in accumulation research, so it is expected the cost will be rapidly reduced soon or later, and so the relative emissions. Solar and wind power has low energy density per area, so these sources need to be installed thoughtfully concerning the impact on nature. Hydro energy, as a mostly utilised renewable energy source, may have its own limitations by natural conditions. Expansion of artificial reservoirs usually causes nature devastation if not designed carefully. However, the pumped hydro plants are the most using storage of energy (Fig. A.11) with quite quick start. Geothermal energy is limited by location and is not widely usable, as shown by its present installed capacity 14.6 GW [11]. The energy production from biomass combustion releases significant direct emissions, but this fact should be seen in context with the amount of CO_2 absorbed by growing plants [16]. Nevertheless, its usage is mostly situated in household heating nowadays. Industrial combustion of biomass has own limitations. Mainly due to low energy density[18] [$J{\cdot}kg^{-1}$] and mass density per area, it is not suitable for larger usage. Renewable electricity generation is rapidly increasing during the last years (Fig. A.9), due to great investment (Fig. A.10). It causes distribution problems, so it is inseparable connected with gas turbines and (or) battery storage. The renewable sources must be compared objectively by taking into account the relative emissions caused by its utilisation in real grid operation.

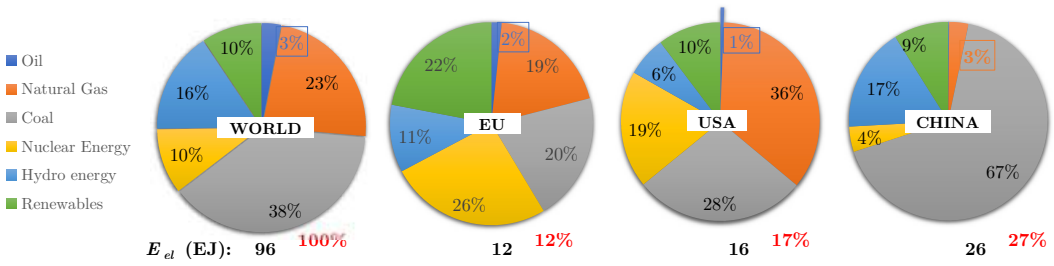

Figure 1.2: Total electricity consumption share by source per chosen entity. Hydro energy is excluded from the renewable sources to be displayed separately. It is important to look deeply to this data and put them into the geopolitical context. It must be pointed, that data were extracted from BP Statistical Review [11], year 2019. It means that displayed EU is already without UK after their withdraw. So the EU represents in this chart 27 countries with total inhabitants about 450 million. The most important fact is that EU and USA slightly decrease year by year its primary energy consumption (10 years average) while China increases about 4 % annually. As well as India which not shown in charts (about 20 % of China's consumption) increases about 6 % annually. It makes bigger picture about challenges discussed in previous pages.

Nuclear energy might be a part of the possible solution for covering the base load with no direct emission of CO_2. Its life-cycle emission is similar to renewable energy sources (shown in Tab. 1.1). Existing nuclear reactors are the most convenient, especially for countries with low potential for expansion of renewable source utilisation or an area with greater population density. Although nuclear energy belongs to the most safety energy sources (the lowest „death per TWh" ratio [18]), the public opinion is very fragile due to several serious nuclear accidents and radiation incidents. Despite public opinion, the problems are mostly high cost and long-term construction with often delays. If humankind expects that some carbon-free technology revolution may arise in further years, it is very hard to make a long-term energy plan for any country. Moreover, it is politically unpopular to take a considerable risk of making a long-term decision with a enormous cost. Existing newest reactors of III^+ generation represent an investment of about 60 years, plus at least a decade of paperwork and construction. The evolution of nuclear energy is expected by small modular reactor (SMR), smaller reactor units with advanced technology, compact size, and lower cost. Other cons are the future decommissioning due to radiation (which already calculated in life-cycle emission) and mostly discussed long-term radioactive spent fuel.

There are conservative plans of long-term storage of SNF, however, there is a possibility of reprocessing, and more challenging ones - the transmutation of a long-lived radioisotopes. This technology of transmutation is able to „convert" long-lived and problematic isotopes (usually very toxic) to a short-lived one, even with releasing some extra energy able to use for potential customers (electricity generation). This dissertation deals with the base research in the frame of ADS, chiefly focused on various experimental target heat generation.

Electricity accumulation and challenges for the future

Electricity - the first sentence about this inspiring form of energy should be similar as its definition from books of physics. Easily converted to many other forms of energy - to heat even without looses. It may be transferred for long distances with tiny losses.
Nevertheless, its economical and „environmental friendly“ storage is a substantial challenge for decades and it is one of the „Achilles heels“ of the renewable decarbonization revolution. Since the installation cost of solar and wind generation rapidly decreased, there is a necessity of finding an economical way for storage which meets the user demand. According to MIT research [19], to cover 100 % of energy consumption in four modelled locations (Arizona, Iowa, Massachusetts, and Texas) by solar and wind energy, the cost of storage must be below 20 $/kWh to renewable could be cost-competitive base-load power. This research is based on weather data gathered for 20 years with hour resolution, so it is a very solid research. Unfortunately, this value is deeply below the present cost, even does not meet with the 2030 outlook [19], [20]. Anyway, if this research calculates a covering of 95 % of 20 years electricity consumption demand, the storage cost must be below 150 $/kWh, which already meets with the outlook goals (see Fig. A.12).

There are many accumulation possibilities with various accumulation principles, which might be divided into two-tier (see [21], Table 3.7.). The first one is suitable for long-term accumulation with the higher cost of power capacity and lower cost of energy capacity. There belongs the pumped hydro storage, which used the most nowadays (about 153 GW in 2017 [22]). Furthermore, there are compressed-air storage[9], or lately proposed flow batteries.
The second pier is more suitable for short-duration storage with higher power due to lower power capacity cost and higher energy capacity cost, such as advanced lithium-ion battery and other kinds of batteries[10], flywheels, and ultra-capacitors. During the years of 2018-2023, the increase of pumped hydro storage in total 26 GW and stationary batteries for 22 GW is expected. Stationary batteries used to have about 5 GW in 2017 [22].

The electricity storage research is under pressure and a type of game changer invention is expected in the following years. Nanomaterial research plays its role in the research as well. Nevertheless, if we look to the previously discussed charts and again put these data in the context of economy, safety, geopolitics situation and think about the energy sector which is very conservative, there is plenty space for nowadays convection electricity production, including mostly the nuclear power of future.

[9] The ration of energy/power for pumped hydro and compressed-air storage is equal 16, in comparison with flywheel or ultra-capacitors with energy/power ratio 0.25 or 0.0125, respectively [21], Table 4.1.

[10] There are many types of batteries with different properties, cost and suitable usage. Currently, the most suitable 4 hours battery energy storage system (BESS), is the Li-ion batteries [21], cost and variants of BESS are shown in [21], Table ES.1 and for non-BESS, Table ES.2. Nowadays, the life-cycle emission of Li-ion battery, in the case of 400 cycles in combination with the wind power plant, is around 300 gCO_2e/kWh [20]

1.2 Aims of Dissertation

The main objectives of this doctoral thesis and the author's PhD research are following:

- to classify the nuclear energy sources sector to world energy consumption, discuss its pros and cons, and challenges to the future
- to describe the ADS technology, spallation reaction, and present research focusing on the latest research at JINR in Dubna where the PhD experimental research is performed
- to design experimental research of thick target heat distribution monitoring
- to design online neutron and proton flux estimation based on samples heating monitoring
- to provide hardware equipment and software support for experimental measurement
- to carry out the experimental irradiation on 660 MeV proton beam for at least two different thick targets
- to simulate experimental setting by suitable solution with detailed description to be possible to repeat the results
- to compare the experimental results with simulation prediction, discuss the achievements, failures, and improvement possibilities

Thesis organisation

This doctoral research deals with the base thermal research in the frame of Sub-critical Accelerator-Driven Systems (ADS). The thesis[11] is divided into six main parts including the introduction and conclusion.

▷ Chapter 1 shortly characterise the energy utilisation from the prehistorical age up to nowadays energy affluence for everybody in developed countries in the form of electricity „plug-and-play“. The author shortly writes about its impact in the form of Global Warming and thinks about future predictions and the impact of undeveloped countries growing economies. This chapter shortly points out GHG emissions, the possibilities of renewable sources, and the limits of present electricity storage.

▷ Chapter 2 describes the history, present, and future challenges of the nuclear energy sector. It specifies the ADS technology, the spallation reaction, and shortly discusses the present research. At the end of the chapter is widely discussed the ADS research at JINR in Dubna where all experiments were carried out.

[11] This thesis was written in TeX Live [23] in the cloud platform OverLeaf [24] with using Writefull plugin [25]. Figures were edited in the online tool PIXLR [26] or software Photoshop CS3 [27], for cropping and resizing PDF was used online tool PDFresizer.com [28]. The 3D models were performed in Sketchup [29] or CAD Inventor [30]. Several of figures were created by MS Excel [31] but the most of figures were created by Python 3.7 [32] with employing *Matplotlib* and *Seaborn* libraries.

▷ Chapter 3 deals with the methodology of this thesis research. The author describes the performed work from the experiment preparation, measurement with invented probes, own fabrication of long thermocouples, pre-experiment testing, experimental measurement, data analysing technique, and widely discussed Python scripts. Several topics are widely discussed, such as MCNPX simulations, the distribution of thermal power density and its approximation, and finally, the heat transfer simulation by ANSYS Fluent. To be pointed out, the entire performed work, including simulation and data analysis, was performed exclusively by the author, unless explicitly otherwise stated[12]. The author learnt the scripting language Python to analyse and manipulate a large amount of measured data. These scripts in Python are described in this thesis and enclosed with open access[13]. All charts were created and used in vector graphics for its better quality and to be ready to use for the following research.

▷ Chapter 4 summarises the thermal experimental research performed on the QUINTA target. Two main parts are characterised - the heat generation monitoring and the estimation of the neutron flux for the target leaking neutrons. Several of the experiments were carried out with the QUINTA target, however, only three majors are listed in this thesis.

▷ Chapter 5 reports about the LEAD and CARBON thick target research. There are described details from the experimental preparation up to the final comparison between fully simulated results with the experimental measurement. Measured data are interpreted and the models are shown with a discussion about their correlation. All data analyses were performed by written Python scripts, some of these scripts are attached in the appendix, and some of them are even described in YouTube video manual, usually linked in a footnote (or summarily listed in p.198). Each of the experimental sections has its own subsection for detail result discussion.

▷ The dissertation thesis is ended by Chapter 6 with conclusion. Due to the results of each experiment were in detail discussed at the last subsection each experimental part, the final conclusion provides the whole research summary with referring to the results.

The author[14] spent several years of experimental research at JINR in Dubna, where all experiments were performed. During the last 2 years, it was expected that two others experiments (focused on the author's experiment accuracy improving) are going to be performed. Unfortunately, this expectation was not met until the dissertation deadline. Therefore, the submitted work was concluded without these experiments.

[12]The MCNPX model of QUINTA (basic geometry) was not created by the author - the version of M.Suchopár was used [33]. The first geometry and basic mesh of the 3D LEAD and CARBON targets model were created by Y.Shu from IMP Lanzhou within the framework of cooperation between BUT and IMP. The setting, adaptation and all calculations were performed by the author. However, the author finally created his own 3D advanced model which used for this thesis research.

[13]Scripts are located in the appendix or uploaded on cloud and listed together with other files on the last three pages of this thesis.

[14]The author of this dissertation is focused on various nuclear sources for the last 8 years of study. The bachelor thesis was aimed at space nuclear energy sources and the diploma thesis was focused on thorium utilisation as a partial fuel of a conventional nuclear reactor. However, the thermal experimental measurement and its simulation were a challenging new topic without any previous experiences.

Chapter 2

Nuclear energy

The nuclear energy fascinates researchers and technical audience especially due to its high energy density. The nuclear fission reaction releases roughly 200 MeV per one fission. Thus, if all ^{235}U atoms in one kg of pure ^{235}U are fission, the energy density is about six orders of magnitude greater than combustion[15] of hydrogen. Moreover, hydrogen combustion has not been commercially usable as a fuel yet. Humankind still burns fossil fuels. Ordinary fossil fuels have about three times lower energy density than hydrogen, and moreover its combustion releases a large amount of dangerous GHG. Its mining and further processes are widely devastating nature. Magnitude of released energy by combustion (see Tab. 2.1) is basically in the same order with the energy released by digestion of food in the organism[16]. Energy density is a simple answer to all questions about so-called „nuclear madness“ during the middle of the last century.

Table 2.1: Energy content of various fuels for combustion [3]

Energy content of fuels	**MJ·kg^{-1}**
Hydrogen	114
Gasoline / Crude oils	44.0–45.0 / 42.0–44.0
Natural gas / Anthracite	33.0–37.0 / 29.0–31.0
Bituminous coal / Lignite	22.0–26.0 / 12.0–20.0
Air-dried wood / Cereal straws	14.0–16.0 / 12.0–15.0

Although nowadays technologies do not allow to fission any fissile mass fully, the nuclear fuel energy density is still enormous[17] in comparison with combustion. As the nuclear fuel is a very concentrated source of energy[18], it is very convenient for fuel transport and low storage capacity requirement, which allows to ensure the energy security of a country for several years[19].

[15] Exothermic redox reaction where the fuel (reductant) reacts with the oxidant (oxygen) in case of high-temperature medium, and release heat due to phenomena that broken chemical bonds of fuel and oxidant release more energy than needs for forming new bonds of reaction products.

[16] For pure lipids, protein and carbohydrates, it is 39, 23 and 17 MJ·kg^{-1} respectively [3].

[17] For example, if some Pressurized Light-Water Moderated and Cooled Reactor (PWR) have burn-up about 50 GWd·t$_{\mathrm{HM}}^{-1}$, it means that energy released from one kg of uranium is roughly 4.3 TJ·kg^{-1}.

[18] It is incorrect to talk about an energy source, since energy can not arise, it might be merely transform. In this thesis is meant by the words *source of energy* only some energy converter, rather the matter which stores energy in any kind of form (mostly chemical energy, nuclear energy, solar energy or kinetic energy, and to a lesser extent other forms) with an ability to release this energy to usable energy (wanted form of energy), mostly in form of heat. To express the usable energy of matter, energy density (content of energy per mass) is used [J·kg^{-1}].

[19] Amount of fuel capacity storage is regulated by law due to treat of nuclear proliferation [34].

2.1 History, present and future of nuclear energy

Since the first human-made (controlled) self-sustaining nuclear chain reaction[20] by E. Fermi in Chicago University at December 2nd, 1942, passed almost 80 years [36]. There are several reasons why nuclear technologies are not as widespread as was expected during the last century. The materials development goes slower than expected, public opinion is fragile due to several severe nuclear accidents and global fears connected with military usage, and finally its complexity. There is another problem with long-lived radioactive waste and its storage. Nuclear energy has its pros and cons as any other energy source, however, the radiation complicates it wider and easier utilisation.

2.1.1 Threats of nuclear energy

At the beginning, the nuclear program was focused on the military usage to prepare the nuclear bomb (the most known are the Little Boy and the Fat Man[21]). It is the dark side of the positively mentioned high density of energy. Long-lasting Cold War where power countries threaten each other with nuclear weapons. Nuclear weapons are regulated nowadays by proliferation law, nevertheless, its history may cause someone nervous of hearing the word „nuclear“, despite its negligible connection with peaceful and safe nuclear energy utilisation.

Another dark side is the risk of nuclear accidents. It actually does not matter if it is caused by human error, the technology problem, or a combination of several errors with weather abnormalities. The point is that during an accident, radiation and toxicity can potentially leak. There are two aspects, the local accident impact and impact on life quality of humankind. There is no room for discussion about risk. In total, there were three serious nuclear accidents in 18,500 reactor years of operation [37]. The Three Mile Islands in 1979, Chernobyl in 1986, and the last decade one - Fukushima in 2011. The risk and impact of nuclear accidents can not be downplayed. It just should be pointed out the real risk to public health from other sources. Nuclear energy is a good servant, but a bad master. Humankind needs a large amount of energy. If compare various energy sources impact on population health, nuclear energy is the clean one [18].

Due to accidents, many improvements have been done all around the world. The design of new nuclear reactors went through many evolution steps. As already discussed, the safety growth (including passive safety) increases the unit cost which complicates, along with its sizeable power density per unit, its wide usage. Nuclear energy is waiting for design revolution and public understanding. Combinations of low design risk, economic cost, and human acceptance are going to be crucial. Maybe these conditions will meet with the IV. generation reactors, maybe with passive small modular reactors, or maybe this combination will never occur.

[20] The earliest nuclear chain reaction was produced by nature itself about 2 billion years ago, as shown by Oklo, Gabon [35]. Due to ^{235}U has about 6-times shorter half-life, that time the ^{nat}U contained about 3.1 % of ^{235}U, almost typical for present nuclear reactors. Location of the natural reactor was flooded by water which moderates the fast neutron to the energetic one, able to fission the nuclei of ^{235}U, and ^{239}Pu produced by capturing fast neutrons on ^{238}U with further decay. Since the water boiled out, the nuclear chain reaction stops.

[21] Nuclear bomb names used in Hiroshima and Nagasaki, Japan, 1945 [36]. Actually, there were many other nuclear bomb testing but these two mentioned were used in WWII and were taking human life.

2.1.2 Summary of NPP commercial utilisation

To meet the expectation of the range of dissertations, this topic is going to be discussed very briefly and mostly referred to the relevant literature. The history of nuclear energy utilisation is sufficiently, but still, kind of shortly discussed in [38]. To reach deeper knowledge about nuclear energy, the author recommends the book of Raymond L. Murray [36]. Finally, for summary knowledge of nuclear reactor utilisation from history up to the future, the author recommends a new book from Alexander Nakhabov [39].

The first commercial nuclear reactor, Calder Hall, started its operation in 1956 [37]. Since that time, in total 624 nuclear reactors were connected to the grid. The number of reactors in operation is 443 nowadays, of which 300 units are PWR, 65 units are BWR, 48 units are PHWR, 13 units are LWGR, 14 units are GCR and finally last 3 units are FBR, based on IAEA database [40] updated in the end of 2019. These reactors produce about 10.4 % of world electricity production (the total net installed power capacity of the nuclear reactors is about 392 GW_e), data for 2019 by [41] (see a comparison in Fig. 1.2).

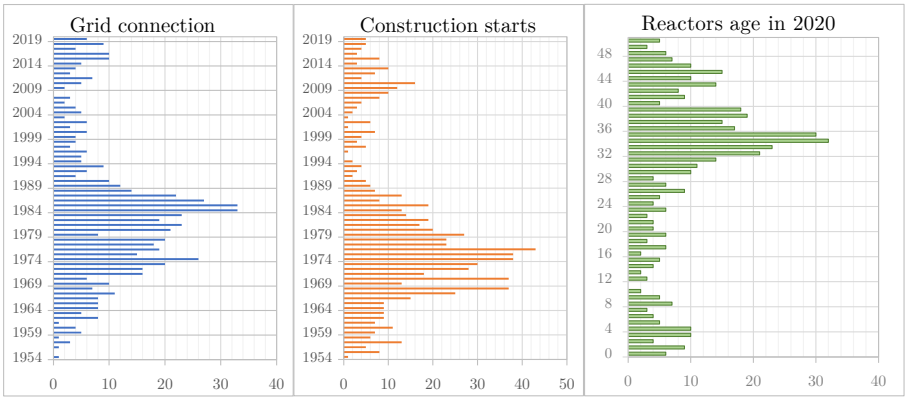

Figure 2.1: Statistical information about commercial nuclear reactors. An x-axis is the number of reactors for each chart. On the left-side chart is shown the number of reactors connected to the grid per year (blue colour). In the middle chart is shown (orange) the number of construction starts per year. Finally, on the right side, there is shown a chart of nuclear reactor age (green), data updated in 01/01/2020 from [40].

In the beginning of 2020, there were 54 units in construction, of which 44 PWR, 4 BWR, 4 PHWR, 1 FBR and 1 HTGR, with a total net power of 57.5 GW_e. Besides the cost of NPP which is increasing rapidly during the last decades, the construction time grows as well. While the median of the nuclear reactor construction time used to be about 100 months (between the late 90's up to 2015), nowadays it is doubled [40]. Nevertheless, this design construction time criterium should be used very carefully, because this rapid increase of the construction time was caused by dealing with the new reactor design. It is expected that the construction time will demean again.
The leader in nuclear power utilisation is the USA with almost 100 GW_e of operation power, followed by France (62 GW_e), China (46 GW_e), Japan (32 GW_e), Russia (28 GW_e) and Republic of Korea (23 GW_e). These countries belong to a group of countries operating with nuclear power above 20 GW_e. There used to be included Germany as well, unfortunately, since they shut down about 18 GW_e due to political decision, they operate nowadays with only 8 GW_e. Similar digress has happened in Japan after the Fukushima accident (shut

down about 17 GW_e). By comparing operation power with country size, the real leader in NPP utilisation is France with about 70 % of electricity produced by nuclear. The most rectors in construction are in China (11 GW_e), the Republic of Korea (5.5 GW_e), India (5 GW_e) and Russia (4.5 GW_e). All data in this paragraph are taken from IAEA database [37]. In construction are mostly so-called Advanced Large Water Cooled Reactors, belonging to GenIII$^+$ design where the passive safety is improved. For more information about Advanced Large Water Cooled Reactors, see [42].

2.1.3 Future expectations of NPP

The future of nuclear power production depends on several factors. The energy mix of each country is one of the most important geo-politic decision. It depends on the country location and the environment. Flat countries can not count on water energy as well as less windy countries do not support wind power turbines. Countries closer to the equator have better conditions for photovoltaic power plants, but if they have an enormous site of gas in their territory, the motivation to build up renewable sources is suppressed. Fortunately, there are political agreements based on climate protection and carbon dioxide emissions reduction. There are several strategies of carbon dioxide reduction, but there is one which all signatories of the Paris Agreement agree with - a coal reduction is mandatory.

In essence, it seems that nuclear energy will never supply more than 12 % of world electricity consumption. Look into the future forecast of the energy mix and consumption analysed by IAEA [41] has two scenarios. The final energy consumption in 2019 was 427 EJ, of which 80.4 EJ was electricity (18.8 %). Based on the expectation, about 592 EJ will be consumed in 2050, of which 161 EJ (27.2 %) will be electricity. The world nuclear electricity production was 2,657 TWh (9.57 EJ) in 2019. Based on the low case scenario, it should be 2,929 TWh (10.54 EJ) in 2050, which represents about 5.7 % of totally produced electricity. Based on the high case scenario, it is 11.2 % of totally produced electricity. Present nuclear power capacity 392 GW_e should decrease to 363 GW_e (low case) or increase up to 715 GW_e (high case). Analysts expect the real scenario somewhere between these two extremes.

The question is what these results mean for the future of nuclear energy. It is expected that the nuclear reactor design will go through a revolution. Smaller mass-produced economical units with high passive safety, so-called SMR presented nowadays, should be a way. The SMR projects in research are listed in [43], Table 1., where all updated information can be found. Moreover, there is a Generation IV of nuclear reactors. It is a group of six reactor designs that were selected by a special commission in 2001. It is a Gas-cooled Fast Reactor (GFR), Lead-cooled fast reactor (LFR), Molten Salt Reactor (MSR), Super Critical Water Reactor (SCWR), Sodium-cooled fast reactor (SFR), and Very-high-temperature reactor (VHTR). The main positive aspects of these chosen are - proliferation resistance, waste minimisation, higher efficiency, and higher safety. Nuclear research worldwide is focused on these reactors. More information may be found in GenIV report [44].

There is a large negative aspect of the current NPP, mostly discussed by ecological activists - the spent fuel and its storage. This topic will be discussed in another section, just to be briefly mentioned, it is one of the most problematic parts (if nuclear energy should be labelled as „green source“). As well, it is a long-term lack of uranium. Both of these problems could be solved by the transmutation process, which is discussed in the following chapter.

2.2 Sub-critical Accelerator-Driven Systems

Accelerator-Driven Systems (ADS) [45] are studied for the last three decades[22], mostly due to seeking a facility producing high energy neutrons able to breed fissile material for peaceful usage. These fast neutrons are simply able to decrease the toxicity and radioactivity of spent nuclear fuel. There were two main groups dealing with ADS technology during 1990'. The first project was led by C. Bowman at Los Alamos National Laboratory [47]. The project Accelerator Transmutation of Waste planned to use about 250 mA proton beam current with an energy of about 1.6 GeV. The second project was carried out at CERN by C. Rubbia [48]. Unlike the previous one, this one was not dealing with nuclear fuel transmutation but rather deals with breeding fissile material by fast neutrons. Its name was The Accelerator Driven Energy Production project, also called Energy Amplifier. The project was expected to use a 1 GeV proton beam with a current of 12.5 mA.
This short history shows that ADS is not a new topic, moreover, many other studies have been already published. Due to the wide range of this PhD topic, ADS principles and spallation and transmutation process details are described only marginally for a basic overview. It is recommended to study the following theses which deeply deal with this topic and allow the audience to completely understand of this interesting topic [46], [49], [50], [51] in English, or [52], [53] in Czech language.

Two main problems of nowadays nuclear energy the ADS tries to deal with:

- Lack of ^{235}U for long-term reactor operation in the future.
- Spend fuel toxicity and radiation of long-living isotopes.

These problems have a common solution - transmutation. Transmutation is a process when the number of neutrons or protons in a nucleus is changed. The physical properties, such as half-life, activity, and radiation energy, are changed. The new nucleus is the same element, but a different isotope. On the other hand, if the number of protons is changed, another nucleus arises with another charge, as well as the atomic number. In this case, the chemical properties are changed.

As listed, there are two main challenges of transmutation in the nuclear energy sector. Ability to breed the fissile fuel, such as fertile ^{232}Th or ^{238}U, and decreasing spent nuclear fuel toxicity and radioactivity of its long-lived radioisotopes. The breeding of fissile isotopes is described by the following equation (decays taken from [54]).

$$^{232}Th + n \rightarrow {}^{233}Th \xrightarrow[22.3m]{\beta^-} {}^{233}Pa \xrightarrow[26.97d]{\beta^-} {}^{233}U$$

$$^{238}U + n \rightarrow {}^{239}U \xrightarrow[23.45m]{\beta^-} {}^{239}Np \xrightarrow[2.35d]{\beta^-} {}^{239}Pu$$

[22] The ADS idea of sub-critical reactor driven by an external source comes from the late 1940'. Due to a lack of uranium, the USA depended on foreign resources. Since the invitation of cyclotron in 1929 by O. Lawrence and his attendance on The Manhattan Project, he came up with an idea to utilise the ADS with a suitable converter as a source of fast neutrons able to breed fissile material. The fertile depleted uranium or natural thorium should be transmuted into fissile ^{239}Pu and ^{233}U. This research project was stopped due to new uranium ore found in Colorado. These early efforts were cancelled due to technical and economic reasons [46].

This process can not be widely achieved in nowadays commercial reactors due to the low probability of neutron capture, in detail discussed in [50] p.5-13, or [49] p.24-28.

The long-term radiotoxicity of the SNF is another topic, however, it may be achieved by similar techniques. The spend fuel composition depends on reactor type, fuel enrichment, and its burn-up[23] [55]. In the case of PWR with a burn-up about 50 GWd·t_{HM}^{-1}, the inventory of the spent fuel is about 93.4 % uranium (where ^{235}U represented by 0.8 %), 5.2 % fission products, 1.2 % plutonium, and 0.2 % minor transuranic elements (neptunium, americium, and curium) [56].

The transmutation of the SNF is widely discussed in book [5] from p.13 or in brilliant theses [49] (English) and [52] (Czech). Since the transmutation reaction study is not the main topic of this thesis, it is outlined just briefly in the following paragraphs.
Radioactive waste is produced by many radiation applications, like electricity production, or sectors such as health, food and agriculture, industry, and the environment. Disposal of radioactive waste is based on the level of radioactivity. It is globally divided into very low-level waste (VLLW), low-level waste (LLW), intermediate-level waste (ILW) and high-level waste (HLW). The SNF belongs to the HLW level and its disposal has very strict conditions [57]. Long-term storage is one of the possible solutions, however, it does not utilise the SNF potential. Due to its long-lasting radioactivity, toxicity, and internal heating, it must be specially encapsulated into an engineered multi-barrier storage system. This kind of SNF repository was already built in Onkalo [58], Finland.
The other more effective solution is the transmutation of long-lived radioisotopes which decrease the storage duration, in detail described in [49], p.9. Moreover, it opens the great potential to use the fuel much more effectively. Generally, the whole idea is called P&T (Partitioning and Transmutation).

Transmutation of problematic isotopes may be achieved by two possible nuclear reactions - neutron fission or neutron capture. For long-lived fission products (FP) is available only the neutron capture and due to its low reaction cross-section, it requires a suitable (rather thermalised) neutron spectrum or (and) high neutron flux. Moreover, the duration of the transmutation process takes a long time. The actinide transmutation requires rather fast neutron spectra with even higher neutron flux. Their fission reaction cross section (CS) are in a similar range for all actinides, and moreover, the neutron capture CS is much lower. It means it does not produce problematic higher actinides, such as Cm or Cf. Since a very high neutron flux is required, the fast reactor is not sufficient (the releasing heat is proportional to the neutron flux production → cooling limit). For this reason, the spallation reaction is much more suitable for high neutron flux production.

[23] Burn-up is the fuel utilisation - it describes the amount of energy extracted from the fuel mass, usually formulated in unit GWd·t_{HM}^{-1}, where *HM* means heavy metal, which corresponds to the mass of the fuel. The energy unit GWd is equal to 86.4 TJ, so the 1 GWd·t_{HM}^{-1} ≈ 86.4 GJ·kg_{HM}^{-1}.

2.2.1 Spallation reaction

Spallation reaction occurs across many scientific disciplines such as astrophysics, radiotherapy, radio-biology, geophysics, and all works dealing with accelerators. Despite this fact, there is no generally accepted definition of this term [59]. In cosmic ray physics, it is referred as „fragmentation“. The verb „to spall“, means to chip with a hammer [60] or more modern - to break into smaller pieces, especially in preparation for sorting [61], anyway the verb dates from the mid 18^{th} century [61]. Spallation refers to nonelastic nuclear reactions that occur when energetic particles, for example, protons, neutrons, or pions interact with an atomic nucleus [59]. The reaction can occur only if one of the reaction partners is a complex nucleus. The received energy increases the interaction energy between nucleons in the nucleus. Therefore, the spallation or spallation reaction is a nucleon–nucleus or pion–nucleus or nucleus-nucleus reaction, in which the energy of the projectile is larger than a tenth of MeV per atomic weight. Actually, it is not certain that the spallation occurs if the described conditions are met, other reactions may occur. The spallation is a complex sequence of nuclear and atomic interactions. Particle production variance of a particle–nucleus interaction if the relativistic projectiles participate is shown in Fig. 2.2.

There is not a clear separation barrier of spallation from the lower energy nuclear reactions. There are several non-exact versions of spallation reaction descriptions, of which the shortest one is: „Spallation is a nonelastic nuclear interaction induced by a high-energy particle $\geq$50 MeV producing numerous secondary particles“ [59]. In essence, it is based on the projectile ability to interact directly with the nucleons of the nucleus. This ability depends on the De Broglie wavelength (see eq. 2.1), which has to be less than the size of the nucleus. For example, 1 GeV proton has λ=9·10^{-14} cm, or 150 MeV has λ=2.3·10^{-13} cm, but on the other hand smaller energies as 10 MeV has λ=9·10^{-12} cm, which is actually the size of heavier nucleus.

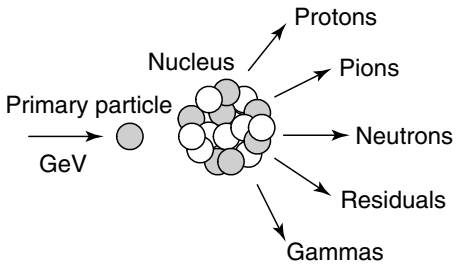

Figure 2.2: Particle production possibilities of the relativistic projectiles particle–nucleus interaction, scheme from [59].

Based on wave-particle duality of quantum mechanics, every particle or quantum entity may be described as a particle or as a wave. De Broglie wavelength describes the probability density of the object being in an exact configuration [59]. It may be described as:

$$\begin{aligned} \lambda &= \frac{h}{p} = \frac{h}{\gamma \cdot m_0 \cdot v} = \frac{h}{m_0 \cdot v} \cdot \sqrt{1 - \frac{v^2}{c^2}} \ , \\ \text{or} : \lambda &= \frac{h}{\sqrt{2 - m_0 \cdot E_p}} = \frac{h \cdot p}{2 \cdot m_p \cdot c^2 \cdot E_p} \ . \end{aligned} \tag{2.1}$$

Finally, if De Broglie wavelength is short enough to the first part of the spallation reaction, so-called intra-nuclear cascade can occur. It is represented by the projectile direct interaction with the target nucleons. Secondary hadrons are created with energies in the range from 20 MeV up to the projectile energy and some of them escape from the nucleus. Some of the lower energy particles below 20 MeV are also escaping the nucleus in the highly excited state. The escaping direction is usually roughly the same as the incident particle direction, as for low energy, and so for high-energy particles. It is caused by so-called Lorentz boost. The time duration of the intra-nuclear or hadron cascade is in the order of 10^{-22} s.

The rest of the energy, which was not taken away by the secondary particle, is shared with other nucleons in the nucleus. Some of those nucleons may leave the nucleus by so-called pre-equilibrium emission. Duration of this stage is about 10^{-18} s.

The last stage is a nuclear de-excitation, or evaporation. Energy of the excited nucleus is relaxed by emitting low-energy (< 20 MeV) neutrons, protons, alpha particles, light heavy ions, residuals, etc. The neutrons are actually the main emitted particles. Final nuclei may be radioactive and release spare energy by emitting a gamma particle. This last process takes about 10^{-16} s.

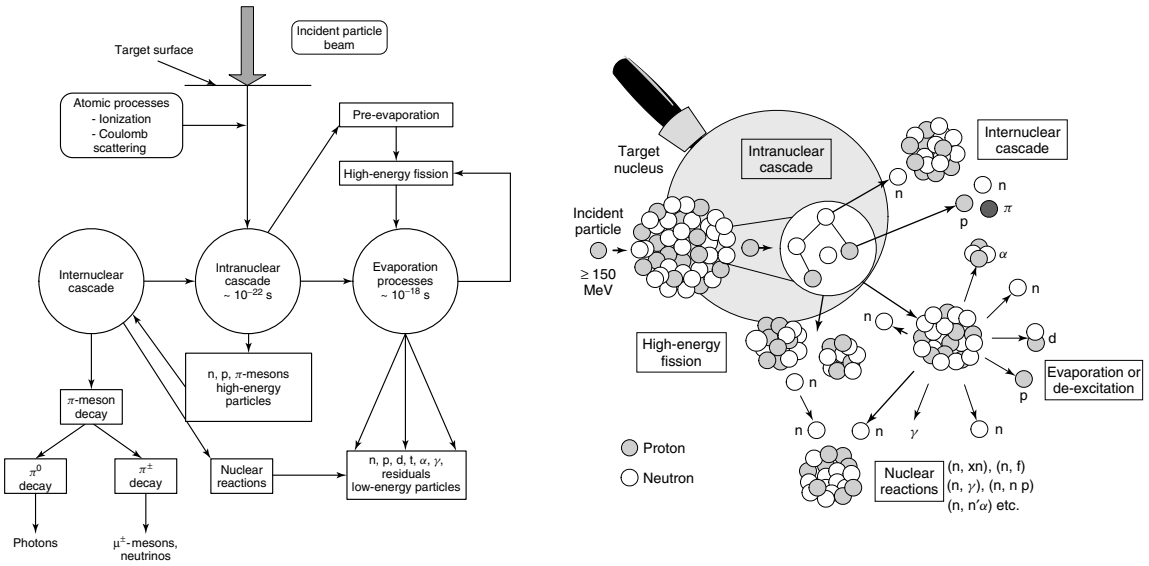

Figure 2.3: Visualisation and logical schema of a spallation reaction, taken from [59].

2.2.2 Components of ADS

One of the biggest advantages of the ADS is its passive safety due to subcriticality. It is a sort of hybrid reactor which requires an external neutron source to sustain fission reactions in the sub-critical fuel assembly. When the external source is switched off, the fission chain reaction can not continue. This source of neutrons may be carried out in various ways. This thesis deals only with a spallation neutron source by employing an accelerator with a high current, typically in the order of mA, and high particle energy, roughly 1 GeV. The target has to be a heavy metal, such as lead, tungsten, wolfram, or others. More suitable seems to be liquid metals such as tungsten, liquid lead, or lead-bismuth eutectic, due to better heat extraction and its operation possibilities at higher temperatures which allows wider utilisation.
The most important parameter of the ADS concept is its energy gain, usually marked as G, and the neutron production number, which is crucial for the design. The number of generated neutrons per incident particle (and final neutron spectrum) defines the capability of fissile material breeding and the capability of nuclear waste transmutation. Due to the high cost of a demo unit, projects are usually designed with multipurpose utilisation, including medicine, material science, geological science, archaeology & heritage conservation, and globally fast neutron applications.

Accelerator of ADS should be in the range of current roughly 10 mA for a demo unit and about 20→100 mA for a commercial power plant if the most effective proton beam energy 1 GeV is used. There are several accelerator variants, however, the most economical is a cyclotron design. Unfortunately, the cyclotron design is limited by energy and either intensity. More variables are linear accelerators which are mostly used for ADS. This accelerator type is more economical if the accelerator facility consists of more than one accelerator. In that case, the required particle energy is achieved by acceleration step by step up in several accelerators.

Target of ADS consists of heavy metal material due to the fact, that a higher mass number of the target increases the neutron yield of the spallation reaction. As mentioned, the heat deposition inside of the target grows with the current of the beam and causes cooling problems. Charged particles (projectiles) lose their kinetic energy passing through matter by excitation of bound electrons and ionisation. The comparison of neutron yield and target heating depends on primary particle energy as shown in Fig. 2.5. The heat is generated chiefly by Coulomb scattering and ionisation loss as the projectile goes through the target. The mean of the heavy charged particles energy loss, the so-called stopping power $\frac{dE}{dx}$, is given by the Bethes' formula [59], see eq. 2.2.

$$-\frac{dE}{dx} = 4\pi \cdot N_A \cdot r_e^2 \cdot m_e \cdot c^2 \cdot z^2 \cdot \frac{Z}{A} \cdot \frac{1}{\beta^2} \times \left[\ln\left(\frac{2m_e \cdot c^2 \cdot \gamma^2 \cdot \beta^2}{I} \right) - \beta^2 - \frac{\delta}{2} \right], \quad (2.2)$$

where N_A - Avogadro number ($6.02{\cdot}10^{23}$ mol^{-1}); r_e - classical electron radius ($2.82 \cdot 10^{-13}$ cm); m_e - electron rest mass (0.511 MeV$\cdot$c^2); z - projectile charge in units of the elementary charge, Z - atomic number, A - atomic weight of the medium (g$\cdot$mole^{-1}); γ - Lorentz factor ($\gamma^2{=}\frac{E}{m_0 \cdot c^{-2}}$); β - relative projectile velocity (ratio of $\frac{v}{c}$); I - average ionisation potential of a medium; γ - density correction. More detailed description may be found in [59], p.33-40.

The average depth of the projectile into the target, based on its material, is shown in Fig. 2.4. It is calculated based on empirical equation [62] (see eq. 2.3).

$$R(E_p) \;=\; \frac{1}{\rho} \cdot 233 \cdot Z^{\,0.23} \cdot (E_p - 0.032)^{1.4}, \tag{2.3}$$

where $Z \geq 10$, $0.1 \leq \mathrm{E} \leq 1$ GeV, ρ = density in [g·cm^3], and E_p = incident proton energy in GeV. R has the dimension [cm] in eq. 2.3 or if multiplied by $\rho \rightarrow$ [g·cm^2].

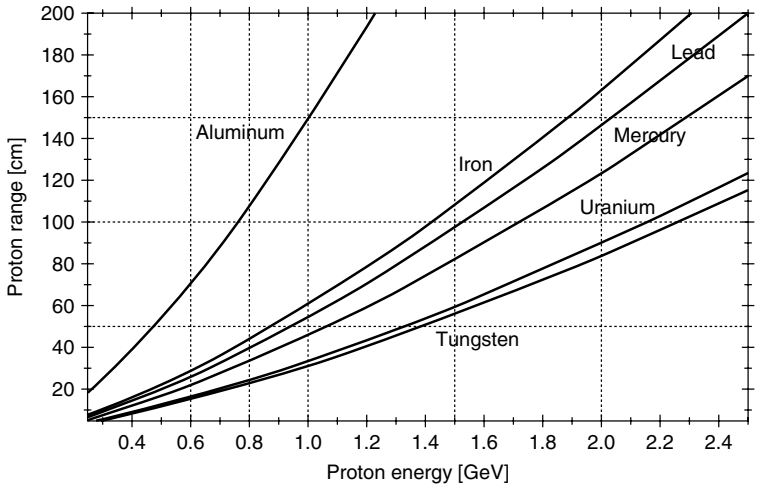

Figure 2.4: Proton penetration depth for various target and energies [59].

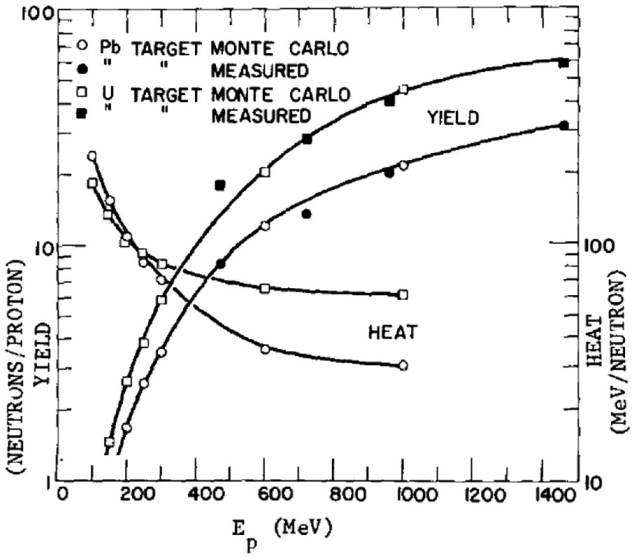

Figure 2.5: Measured and calculated neutron yields and calculated heat production vs. proton energy for 20 cm diameter lead and fully depleted uranium targets [63], edited.

2.3 ADS research and challenges

2.3.1 World research

There are dozens of research focused on ADS technologies. History of this research is very well summarised in the previous colleagues works [52] (Czech) and [49] (English). Ongoing projects and their potentials are well discussed by World Nuclear Association in [64] and by IAEA in a summary publication [65]. The ADS are also discussed in connection with molten salt reactors and thorium energy (for more information see [66] on p.495-521). As the ADS research is not much dynamic, it has been decided to only shortly discuss the most important ongoing projects. Two of them are in Europe, one is in China.

EES (European Spallation Source) [67] in Lund, Sweden, is not actually focused on ADS, but it is an essential project for the future of ADS research. It is already in construction which uses spallation source for many research activities. It is based on a linear accelerator with maximum energy 2 GeV, average current 62.5 mA, frequency 14 Hz, and peak power 125 MW (average 5 MW). The spallation source is made of a 4 t rotating tungsten target (diameter of 2.6 m) which is cooled by liquid helium (-271 °C). Its neutron production rate is about 80 fast neutrons per incident particle. This project does not directly deal with ADS, its neutron research deals with all branches like physics, chemistry, geology, biology, and medicine. However, it is expected that reached knowledge helps in all topics dealing with spallation targets, so the ADS.

MYRRHA project at SKC·CEN [68] in Mol, Belgium, is focused on the transmutation of spent nuclear fuel. There is a synergy with pharmaceutic industry and besides the research of transmutation, it will produce medical radioisotopes.
The financial support of the project, or rather the first phase of the project, has been signed in 2018. It consists of 100 MeV accelerator (0.5 mA) which will be extended to 600 MeV in the second phase by 400 m LINAC. The current of the LINAC should be 4 mA which goes to the reactor. The pool type reactor will be cooled by 7,800 tons of lead-bismuth eutectic [69]. The motivation of MYRRHA project is to revive the idea of the long-lived radioisotope transmutation into much shorter living ones. Present technologies are able to decrease the radioactivity of SNF from 300,000 years to about 10,000 years by reprocessing (so-called MOX fuel). Transmutated SNF reaches similar radioactivity after about 300 years of storage [69]. The last phase of MYRRHA should be finished until 2033.

ADANES complex project [70] at IMP in Lanzhou, China is dealing with ADS Burner (ADB) and a system of Accelerator Driven Recycle Used Fuel (ADRUF). The ADB will achieve transmutation of long-lived radioisotopes, fuel breeding, and energy production. At the same time, ADRUF prepares the recycled fuel. The project is similarly divided into several phases but should be finished already in 2030. The first phase was dealing with breakthroughs of key technologies related to ADB and ADRUF (2011-2016). In the second stage between 2018-2024, the construction starts of the high-power ADB research facility, China Initiative Accelerator Driven System (CiADS) and an ADRUF with a hot cell and a compact neutron source. The CiADS consists of a 2.5 MW superconducting proton LINAC with 500 MeV and 5 mA, a liquid LBE cooled fast reactor with 10 MW_t [70].

The author supposes the rewriting of already written summaries is not appropriate and necessary, however it is usually contained in many theses. There are many research connected with spallation target topics, however, it is mostly used for other purposes than trans-

mutation. Monitoring of current research of ADS may be simply performed by analysing published research papers. The most suitable searching key words seem to be „accelerator-driven system“, it has been analysed by three searching tools - Google Scholar [71], ScienceDirect [72] and Web of Science by employing the Clarivate analytic tool [73]. The methodology of searching and its difference is widely discussed in [74]. GoogleScholar found about 7450 results, ScientDirect 2250 results and finally, Web of Science (WoS) found 790 results (all possible databases chosen).

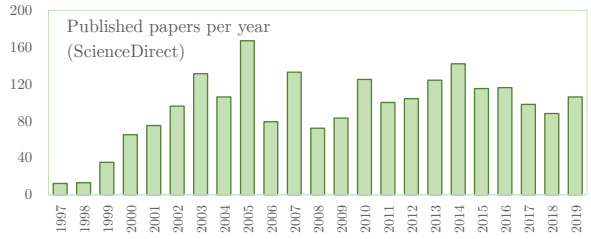

(a) Published papers based on Science Direct searching.

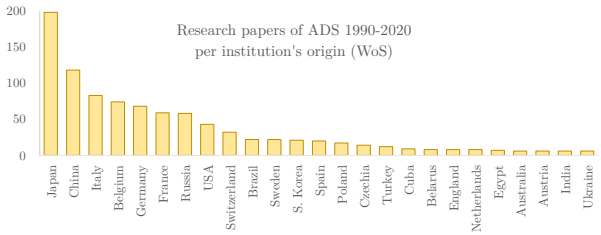

(b) Published papers sorted by institution origin based on WoS.

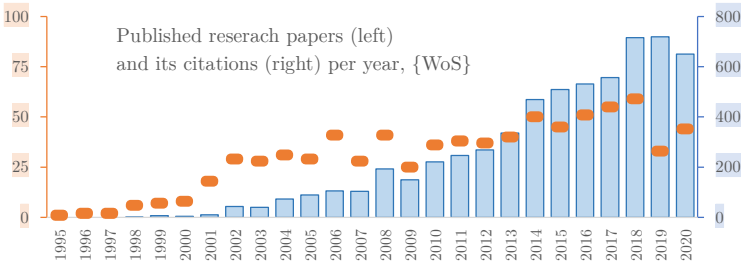

(c) Published research papers (orange) and its citations (blue) per year, based on WoS.

Figure 2.6: Simplified comparison of research activities on ADS topics worldwide, data from [72] and [73]. It shows that ADS topics are cite much more in last years, although the number of published papers is more or less constant during last 20 years. It probably means, the ADS technologies are discussed in papers of other topics. Most of the papers were published by Japan's institutions, followed by China, Italy, and Belgium. Japan is one of the advance nuclear technology leaders, however, the Fukushima accident suppressed the nuclear interest. Its ADS research is called *Japan Proton Accelerator Research Complex* and the most of research papers comes from this research facility. It deals also directly with transmuatation of spent fuel (*Transmutation Experimental Facility*), however, most of the research deals with materials and life science. For more information see [75]. Previous worldwide research projects on ADS topic are summarised in appendix B, p.155.

2.3.2 ADS research at JINR in Dubna

The early first research of spallation reaction or ADS began during the 1970s, however, intense research in DLNP was started in the 1990s. Based on this activity later arose a collaboration Energy and Transmutation of Radioactive Waste (E&T RAW) [76]. Since the 90's there is continuous research dealing with various topics, primarily neutron production studies; neutron transport; transmutation of actinides (in moderated n spectrum or not moderated); energy gain studies; or study of transport code benchmarks.
There was a project The Subcritical Assembly in Dubna (SAD) [77] at the early beginning of this century which dealt with small experimental facility up to 30 kW consisted of lead target cooled by air and sub-critical blanket similar to BN-600 reactor fuel. It should be driven by the Phasotron accelerator proton beam with an energy of 660 MeV. Unfortunately, due to a fire in the experimental hall (March 2005), and finally, lack of finance, the project has been aborted.

Accelerator facilities

This topic is widely described with its historical aspects in [52] p.37-39 (Czech language) or it is discussed in [49] (English). Shortly, the Synchrocyclotron was the early first accelerator at JINR located in DLNP and it was at that time the largest accelerator worldwide (in operation since 1949). It has been reconstructed during 1979-1984 into nowadays Phasotron, both of them accelerate only protons. In the second laboratory, LHE has been built the Synchrophasotron during 1953-1956. It accelerated protons, deuterons, or various light nuclei up to energy 4GeV per nucleon (in operation up to 2000). The last accelerator which was used for ADS research purposes was Nuclotron built during 1987-1992. It is a synchrotron accelerator with a diameter of about 250 m which allows accelerating also heavy nuclei up to 12.8 GeV, it is built below the Sychrophasotron. Due to all experiments were performed at Phasotron, it is not suitable to widely describe previously mentioned[24].

Phasotron

Phasotron accelerator facility contains a proton accelerator with several channels for medical or experimental utilisation. It provides usually 1 μA (3.2 μA maximum) proton beam with an energy of 660 MeV without the ability of energy tuning. However, it allows using a beam with energy 200 MeV for direct irradiation inside of Phasotron - without using any extraction channel. The accelerator diameter is about 5 m, mass about 7 000 t and magnetic field in the range of 1.2-1.6 T. The electricity power consumption of the accelerator is about 1.5 MW and the same for the beam extraction facility (the total power consumption is 3 MW). The experimental channel in the experimental hall (see its extraction in Fig. 3.1) has been used for all performed experiments. Due to this channel setting, the beam parameters are diametrically different to the experimental channel beam extraction values. The irradiation channel beam parameters decrease a lot, the current up to $\approx$ 1-3 % of the accelerator nominal values and the beam geometry (Gaussian FWHM) increase approximately 4 times. These information were extracted from [52] and from discussions with the accelerator staff.

[24] Their technical comparison is shown in Tab. 2.1 of K. Katovský thesis [52].

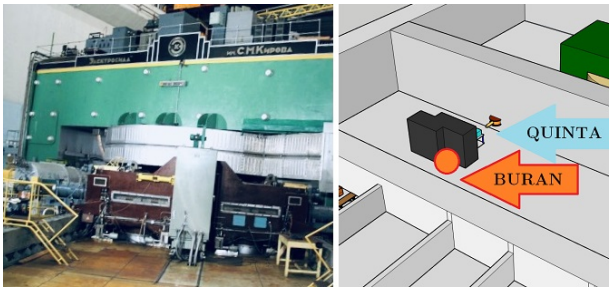

Figure 2.7: Photograph of Phasotron accelerator on the left side and its sketch with irradiation position of experimental target on the right side.

In the following, there is shown the equation to estimate the accelerated protons speed:

$$E = E_0 + E_k; \quad E_0 = m_0 \cdot c^2; \quad E = \gamma \cdot m_0 \cdot c^2; \quad \gamma = \frac{1}{\sqrt{1 - \frac{v^2}{c^2}}}$$

$$E_k = E - E_0 = m_0 \cdot c^2(\gamma - 1) = m_0 \cdot c^2 \left(\frac{1}{\sqrt{1 - \frac{v^2}{c^2}}} - 1 \right)$$

$$\frac{E_k}{m_0 \cdot c^2} + 1 = \frac{1}{\sqrt{1 - \frac{v^2}{c^2}}} \rightarrow \frac{v}{c} = \sqrt{1 - \left(\frac{1}{1 + \frac{E_k}{E_0}} \right)},$$

where E_k=kinetic energy; E_0=rest energy; m_0=rest mass; c=speed of light. The final energy is based on Einstein's theory of Special relativity, $E = m \cdot c^2$, where m=relativistic mass (equal to $\gamma \cdot m_0$); γ=Lorentz factor. The Phasotron accelerates the protons to E_k=660 MeV. As known, the rest mass of proton $m_0 = 1.6726 \cdot 10^{-27}$ kg, and light speed $c = 299,792,458$ m·s^{-1}, so the rest energy is $E_0 = 1.6726 \cdot 10^{-27} \cdot (2.9979 \cdot 10^8)^2 \approx 1.5033 \cdot 10^{-10}$ J $\approx$ 938 MeV. Finally, the accelerated protons velocity relative to the light speed is:

$$\frac{v}{c} = \sqrt{1 - \frac{1}{1 + \frac{660 \text{ MeV}}{938 \text{ MeV}}}} \approx 81 \text{ \%}.$$

Previous experimental targets

The ADS research group studied several experimental setups in previous years. In a short summary, there were studied the following targets: the LEAD block target, GAMMA-2, GAMMA-3, and The Energy plus Transmutation target. Its description is discussed in p.53-55 of L. Závorka thesis [49]. Those targets were irradiated at all previously mentioned accelerators, based on the year of irradiation. The targets of which this thesis deals with are described in following.

TA QUINTA For each of the experimental targets was prepared a 3D CAD model in Autodesk Inventor [30] or SketchUp [29]. The most challenging task was to prepare an accurate model of the QUINTA target due to missing any certain data sheet of the target construction design. It was possible to believe the geometry of the very reliable MCNPX model performed by M. Suchopar [33], but for sure it was better to do double check. Fortunately, it was possible to measure the dimensions during the QUINTA transportation[25]. All cylinders of the QUINTA are locked up and sealed in hexagonal section (see Fig. 2.8, right). The external dimensions and mass of the cylinder were known[26]. Other details were found in the section description located on the top surface of each QUINTA section and partly in [78] (material properties). By knowing the uranium mass, aluminium cladding mass; outer radius; and outer cylinder dimensions, other internal diameters were calculated.

The abbreviation QUINTA is based on its description: quasi-infinite uranium target. It consist of 298 uranium cylinders (^{nat}U) located in five hexagonal sections. While the first section has a beam window (cylindrical air hole) and contains only 54 cylinders, each other section is equivalently fully filled and contains 61 cylinders per section. Details of the target are in summary in following.

Target dimensions (used in following simulations):

- Cylinder ^{nat}U:
  ρ = 19.04 g·cm^{-3}, L = 101.4 mm, D = 33.4 mm, V = 88 160 mm^3, m = 1 679 g, radius of cylinder edge R = 4 mm.
- Al cladding of cylinder:
  ρ = 2.71 g·cm^{-3}, L = 104 mm, D = 36 mm, V = 16 960 mm^3, m = 46 g; specific heat capacity c = 0.12 J·g^{-1}·K^{-1}, thermal conductivity λ = 27.5 W·m^{-1}·K^{-1}; inner dimensions equal to uranium cylinder dimensions. Aluminium cover is welded.
- Aluminium plate covering the front and back side of each section:
  ρ = 2.71 g·cm^{-3}, 350×350×5 mm^3; c and λ is equal to all aluminium material with Al cylinder cladding.
- TA QUINTA:
  - 298 ^{nat}U cylinders; 54 located in the 1st section; each other section has 61 cylinders
  - due to beam window in the first section, the beam interact with 2nd section
  - sections are of hexagonal shape, held by aluminium plate of 3 mm thickness
  - dimensions: 350×350×700 mm^3, or 600×600×900 mm^3 with 10 cm Pb shielding

[25] Due to the radiation safety regulations, the target assembly QUINTA was usually deposited in radioactive material storage at LHE. It is transported and put together just several days before the experiment. The author was allowed to be apart of a construction group where performed the measurement of all QUINTA parts.

[26] There was a special experiment where the single cylinder was irradiated (experiment No.11 short). Before the experiment, the cylinders geometry measurement was performed with the mass weighting.

Figure 2.8: Photos from the TA QUINTA installation in exp. hall, edited in [26].

Detail model of the QUINTA target was made for very detail heat transfer calculation. It is available for download in appendix, p.197, item No. 1. Due to lack of computation power and professional skills in advanced heat transfer simulation, these calculation should be carried out by cooperation with The Institute of Modern Physics (IMP) of the Chinese Academy of Sciences[27]. Unfortunately, it is not included in the frame of this dissertation and it will be published later. Detail model of the QUINTA, including the real dimension of uranium cylinders covered by aluminium cladding, is shown in Fig. 2.9.

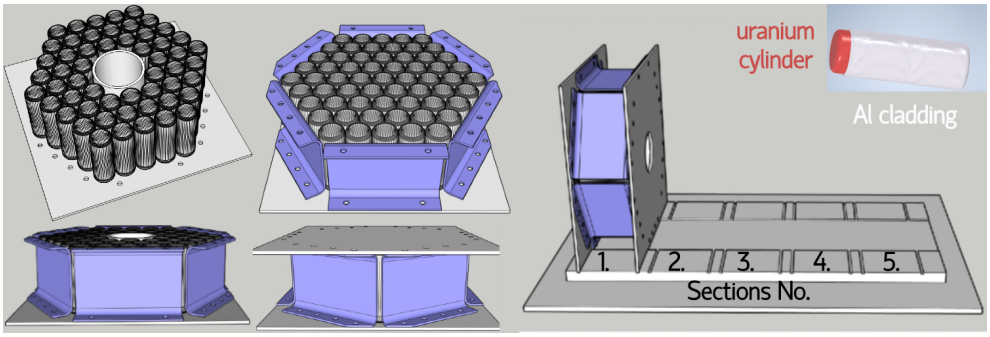

Figure 2.9: Model details of the TA QUINTA construction, edited in [26].

For the first simulation has been prepared a simplified model of QUINTA to ensure easier meshing of the setup and quicker calculation. It is available for download in appendix on p.197, item No. 2. The main differences are:
→ uranium cylinders without radius
→ hexagonal plate without real bend and wholes with screws
→ calculation of perfect welding connection instead imperfect connection
→ model without aluminium holder plates of irradiating foils
Both simulation are shown in following Fig. 2.10. On the left side is shown the real model simulated in SketchUp [29] and on the right side the simplified Inventor [30] version.

[27] This cooperation is under ongoing project *Investigation of Complex Thick Targets Neutronics for Accelerator Driven Nuclear Power Production* between IMP Lanzhou and BUT Brno.

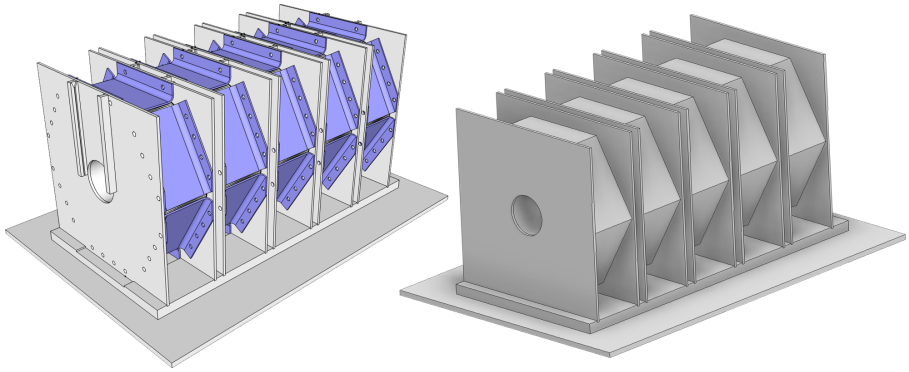

Figure 2.10: TA QUINTA visualisation - left detailed model, right simplified model.

BURAN

The BURAN is a sub-critical cylindrical blanket with length of 1 m and diameter of 1.2 m consisted of 20 t of depleted uranium (0.3 % of ^{235}U), covered by 10 cm of steel cladding. BURAN has 72 measuring channels which may be equipped by activation samples or any other measuring device (such as thermocouples - earlier planned to be apart of this PhD research). In the centre of BURAN, there is a hole of 20 cm in diameter where a cylindrical spallation target with a shape of 19 cm in diameter and length of up to 1 m is supposed to be install. By reason of better neutron flux distribution, it is discussed to use a combination of several target materials in a cylindrical shape with length of 5→10 cm (experimentally studied by *exp12* and *exp13*). Target description, visualisation, and experimental results are shown and widely discussed in chapter 5.1 for the LEAD target and in chapter 5.2 for the CARBON target. The BURAN is supposed to be an „infinite target“ with a small amount (about 15 %) of leaking neutrons (in comparison with 75 % of the QUINTA target, data based on P. Tichý MCNPX simulations [79]). Experiments with BURAN have been planned since 2019. Unfortunately, due to the combination of several complications, the experiments have not been performed yet (written in the end of 2020)[28].

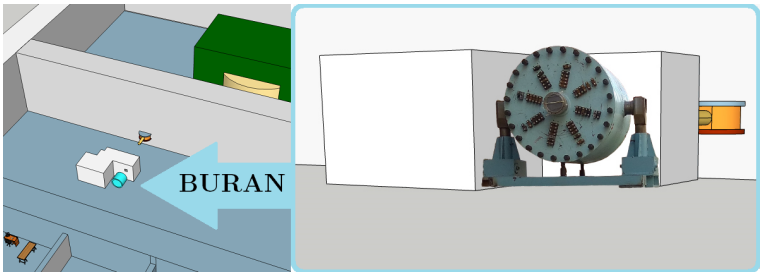

Figure 2.11: Sketch of the experimental hall with BURAN sub-critical blanket, on the right side enlarged view with collage of real photograph. Compare this figure with sketch of already performed experiments disposition shown on Fig. 3.1 where all parts description is given. The 3D Inventor model of the BURAN is available for download in appendix on p.197, item No. 6.

[28]The BURAN experiments were supposed to be part of this PhD study as well. Author prepared a methodology for sample irradiation and, thanks to funds allocated in the grant of 3+3 (see Acknowledgements), purchased the necessary equipment. These experiments are expected to be performed in the middle of 2021, based on the latest information.

Chapter 3

Methodology

The ADS technology topics are researched by many researching groups all around the world. In the research group in Dubna, where all experiments were performed, the researchers usually deal with nuclear data research (reaction cross-section of higher energy), MCNP & Fluka & GEAT4 code benchmark verification, neutron leakage study, and some heat generation research were performed as well. However, the research group in Dubna is primarily focused on research employing the method of gamma-ray spectrometry. Many researchers were formed in this group and performed the experimental part of their postgraduate studies there. Selected dissertations which the author used for getting knowledge in this topic, are listed in following: [52], [49], [33], [46], [50] and [51]. Generally, these dissertations are chiefly focused on nuclear data measuring and MCNPX 2.7.0. simulations. In the topic of heat generation and temperature measurement of thick targets which this dissertation deals with, there were performed some research activities earlier by long-staying researchers in Dubna, such as T. Tumendelger [80], M. Krivopustov [81], A. Voronkov [82], V. Batin [78], and others. A similar topic was studied at CERN by S. Andriamonje [83], J.Calero [84], and others. These pointed researches were performed at the end of 20^{th} century. The reason for continuing spallation target heat generation research activity is based on the utilisation of new targets with different geometries and materials. Moreover, present electronics quality and precision allows measuring very small temperature changes by inexpensive hardware.

This research is unique due to the higher intensity and stability of the proton beam irradiation in comparison with previous researches, which were implemented in Nuclotron irradiation facility. Fortunately, the research has been moved to Phasotron irradiation facility in 2014. The first of the calorimetrical experiments at JINR was performed in June 1998 [80]. The lead cylindrical target had a length of 50 cm and 10 cm in diameter and was irradiated by 1.5 GeV protons for about four hours, including several of the beam outages due to the lower stability of the accelerator. The average proton beam intensity was about 7.4×10^{10}. The maximum of the temperature change caused by this irradiation (measured in the centre of the target at a distance of 4.5 cm) was about 0.3 °C.
Following experiment [81] with lead block target of dimension $50\times50\times80$ cm^3 was irradiated by 5 GeV. The temperature was measured by ten thermocouples at various locations. The irradiation was performed by six irradiation pulses. The total time of experiment was 90 min including 66 min of irradiating and 24 min of beam pause. The total number of incident protons (proton beam integral) was estimated to be about 3.2 x 10^{13}. Calculated released heat inside of the 2300 kg target was determined to about 26 kJ.

Another heat generation experiment [82] used target **Energy plus Transmutation**[29] and was irradiated by 1.5 GeV protons at Synchrophasotron accelerator. The lead cylindrical target was surrounded by several natural uranium cylinders. The experimental irradiation took about 40 minutes[30] and the highest temperature difference (about 1 °C) was reached in the centre of the target. In total, 25 thermocouples were involved in this measurement. The setting and the results of the experiment are most similar to the present experiments performed with the QUINTA target, described by this thesis in Chapter 4.
The last described experiment [78] was observing the secondary particle heating ability of the natural uranium cylinder. Cylinder was located at a radius of 150 mm from the centre of the cylindrical spallation target (lead, D=100 mm, L=500 mm). Uranium cylinder was mostly heated by spallation neutrons, merely by secondary protons, gamma heating, and pions. The lead target was similar to [80], although, in this case irradiated by 1.5 GeV protons. The irradiation took about 260 minutes with the average proton beam current 62 pA. This experiment was similar to the experiment described in Chapter 4.1.

About 3 years earlier, before the first mentioned JINR experiment, there were a type of similar experiments dealing with energy amplifier and heat generation measurements [83] and [84]. Researchers from CERN used for this experiment the irradiation facility CERN-PS with a subcritical assembly from Universidad Politécnica de Madrid. The experiment dealt with the energy amplification determination by temperature measurement of tiny blocks of uranium located at several positions inside of the assembly. The proton beam was set in the range of 600 MeV to 2.75 GeV with about $\approx 10^9$ protons per 14.4 s pulse. The beam was focused in the area ≤ 1 cm^2 with the sharp extracted bunch ≤ 100 ns. The sub-critical assembly with multiplication coefficient $k = 0.92$ (calculated by Monte Carlo) was consisted of 3.62 t of natural uranium in a hexagonal shape lattice and surrounded by light water moderator. The energy amplification (gain) reached up to $G = 30$, based on experimental measurements. The thermometers PT100 were used for measurement. That was a pioneer experiment in the frame of ADS heat generation research.

The main research activities in the frame of the dissertation thesis topic:

- Target heat generation monitoring.
- Relative neutron flux monitoring inside of target by ΔT measurement.
- Neutron leakage monitoring by invented probes (ΔT measurement).

The most crucial task was the target heat generation and neutron leakage monitoring, anyway, several experiments were aimed at inside target neutron flux study. The idea was based on the accurate temperature changing measurement of the fission sample, located inside of the target. It was a very difficult task due to a great amount of heat being generated by the target itself, so accurate measurement of the sample fission contribution was challenging. Special insulation of these samples was invented and tested. The realisation was made difficult by the narrow space of the measurement location. The reason to study this method was based on the requirement of independent verification of the activation foil method technique. Measurement setting and its description are located in chapter 4.

[29] Target Energy plus Transmutation is described at chapter 2.3.2.
[30] Partitioned into 10 min of irradiation followed by a 3 min pause and another 30 min of proton irradiation.

3.1 Heat generation of various experimental targets

This work deals with the heat generation research of several targets. The methodology of temperature measuring and data analysing has been improving task by task. These processes are discussed in the following paragraph. During the author experimental internship in Dubna, altogether 17 experiments were performed in the frame of the ADS research. Some of them were partitioned into short and long irradiation parts (see No.11.). The short one was used for measuring the short-lived radioisotopes by gamma-ray spectrometry (in the range of minutes, due to the lack of automatic sample transportation system). There were 14 of the experiments (if pilot exp. counted) where the thermometric measurement was realised as listed in the following Tab. 3.1. The thermometric experiment was usually only a parallel experiment to the main experiment which focused on offline measurement of various samples by using gamma-ray spectrometry (neutron activation analysis principle). All experiments were irradiated at Phasotron irradiation facility (see Fig. 3.1) by 660 MeV protons.

Table 3.1: List of experiments where thermometric measurement involved.

No.	Exp. date	Start	End	N_p [-]	Target	Note
0.	06.11.2015	16:40	21:18	3.35(22)E+15	QUINTA	pilot exp.
1.	04.12.2015	15:15	21:15	4.40(40)E+15	QUINTA	
2.	04.03.2016	15:15	20:30	2.50(20)E+15	QUINTA	
3.	31.05.2016	17:48	23:24	4.88(31)E+15	QUINTA	pulse irr.
4.	24.06.2016	14:08	19:00	2.44(20)E+15	QUINTA	pulse irr.
5.	02.12.2016	16:50	20:50	4.84(31)E+15	QUINTA	
6.	16.12.2016	18:45	23:45	1.51(14)E+15	QUINTA	
7.	27.01.2017	14:33	20:02	3.28(*)E+15	Pb shielding	
8.	03.02.2017	13:46	19:14	2.43(20)E+15	Pb shielding	
9.	02.03.2017	13:15	18:42	1.03(*)E+15	Pb shielding	
10.	22.06.2017	16:36	21:50	1.52(16)E+15	QUINTA	
11.	29.06.2017	16:33	16:55	3.21(17)E+13	2 cylinders	^{nat}U cyl.
11.	29.06.2017	17:10	17:30	1.02(11)E+14	QUINTA	short irr.
11.	29.06.2017	17:37	22:30	1.43(15)E+15	QUINTA	long irr.
12.	25.05.2018	15:20	20:25	2.42(19)E+15	Carbon	elongated
13.	08.06.2018	15:34	20:34	2.30(18)E+15	Lead	elongated

* These data are reached by approximation of measured data on small activation foil with diameter 21 mm

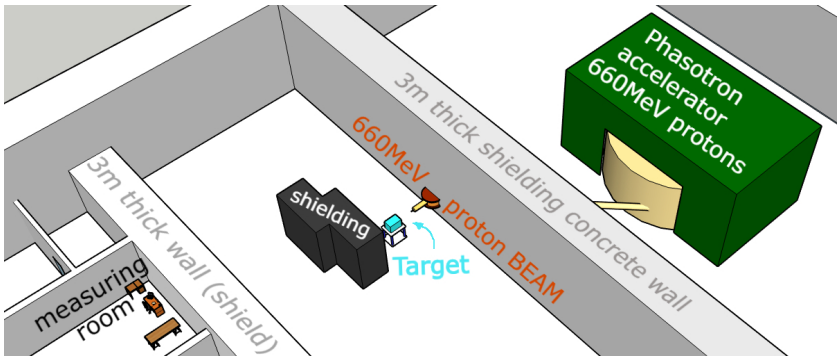

Figure 3.1: Sketch of the experimental hall setup, modelled in [29] and edited in [26].

3.1.1 Temperature measurement and analysing methodology

There are many variants of how to measure the temperature. Unfortunately, many of them were not suitable to use due to a very specific application. The irradiated target was located in a large experimental hall which is not accessible during the irradiation and several hours after the irradiation (except a very short time to pick up samples) by reason of the radiation exposure prevention. The experimental hall is shielded by a 3 m thick concrete wall. There is high radiation exposure close to the target during the irradiation, which is harmful to sensitive electronics. To protect the electronics, it has been decided to locate all electronics in the measuring room (see Fig. 3.1), with a distance from the target of 22 m. Another request to the probe was its geometry to be as tiny as possible, because of the measurement in narrow spots. Moreover, the probes have to have a small volume and can not be shielded by reason of quick reaction to the temperature changes (when the accelerator starts or stops or when an outage occurs), or even to detect tiny changes when the beam current decreases or increases during the irradiation.

After considering all requirements, the exposed thermocouples type T were chosen. It consists of two metals, copper and constantan (an alloy of copper and nickel). The chosen thermocouples fulfil the requirement of the short response time due to the chosen wire with a diameter of 0.51 mm. To ensure as accurate measurements as possible, the thermocouples are connected as a whole, without additional connections. Due to the low finance budget at the beginning, the equipment was acquired partly year by year. There was available only borrowed equipment from the Brno University of Technology for several of the earlier experiments.

Data acquisition was performed by the National Instrument (NI) hardware using the LabView [85] software (also NI). The measuring cards (A/D converter) NI9214 and NI9212 were chosen due to the best ratio of accuracy/number of channels/cost. Converters were inserted to chassis cDAQ9174, also from the NI (more information on the p.35).

Table 3.2: Information about thermocouples extension wire used for experiments [86].

TC length [m]	**Company**	**Type**	**Diameter [mm]**	**Impedance [Ω·m^{-1}]**	**Insulation**
330	NI	T	1.02	0.62	PVC
300	OMEGA	E	0.51	5.84	PFA Neoflon
1500	OMEGA	T	0.51	2.47	PFA Neoflon

Data were analysed by MS Excel [31] at the beginning, by using some advanced function and programming macros. Since analysed a week of measurement with dozens of thermocouples and data sampling of 1 s, excel file size increased to about 250 MB, which was hard to work with. The visual analysing (plotting) was firstly made by MS Excel as well but shortly was replaced by Gnuplot software [87] which allows much more convenient tools for analysing charts. Later, when even larger experiments, data analysing was carried out by scripts in the Python 3.7 [32] with using packages *matplotlib* [88], *pandas* [89], *NumPy* [90], *seaborn* [91], and common *math, os, sys, re*, and *csv* [32]. Finally, during last years were re-analysed all previous data to the uniformed appearance by Python 3.7 (p.34) and plotted in vector graphics.

Thermocouples manufacturing

The most complicated task was to measure all online 88 positions of the QUINTA target. As the thermocouples needed to be used as a whole (for 22 m), about 2000 m of extended thermocouple wire was required, including reserves. To reduce the cost, the thermocouples were self-made by using the thermocouples welder TL-WELD [92]. The low-cost thermocouple extension wire was purchased in the length of 300 m (see Tab. 3.2), cut into 22 m length and welded. The range of the measured temperature will be in range $T_s \rightarrow (T_s+\Delta T)$, where T_s=temperature of surrounded air, ΔT=temperature difference caused by target heating. Based on the pilot experiment, the ΔT was expected to be around 10 °C and surrounded air about 20 °C. The most suitable thermocouples for this application are the thermocouples type T due to the highest accuracy, low impedance, and suitable measuring range with satisfied voltage[31] gain. The thermocouples are based on phenomena of the Seebeck effect, discovered in 1821 [93]. When two different metals are forming a closed loop, it shows magnetic properties (there is a continuous current that flows in the thermoelectric circuit) when one junction is heated.

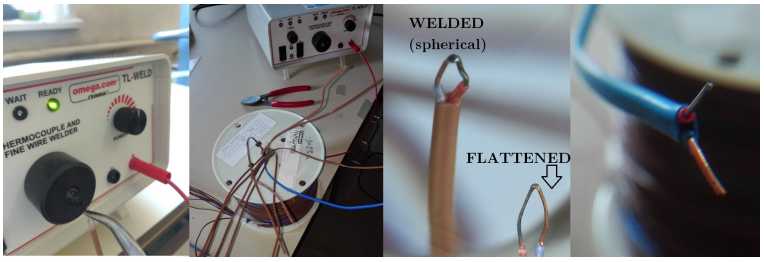

Figure 3.2: Thermocouples manufacturing pictures.

When thermocouples are welded, the joint between the wires is a spherical shape. To increase the junction quality between TC and the measured sample, the spherical weld was forged into a flattened geometry. The weld destruction has been experimentally tested by monitoring the thermocouples voltage gain changes. The *hot junction* was placed into boiling water[32] and *cold junction* (electronics) located in room temperature. The difference between spherical and flattened thermocouples was about 0.3 %. Since the calibration is carried out after the thermocouples are flattened, the dependence of its flattening on the accuracy of the measurement is negligible. The temperature difference between hot and cold junction was $\Delta T \approx 80$ °C, it is equal to about 3350 μV
The thermometers were used as well, primarily for monitoring the temperature inside of the therm insulated box where electronics are located. As far as the thermocouples measure the difference of the temperature, the temperature of the thermocouples cold junction needs to be monitored. Two pieces of the thermometer type RTD CAP-100A-3-A125-060-T-40 [94] and another two pieces of adhesive (adh.) RTD type SA1-RTD-120 [95] were used for controlling the measurement of the temperature inside of the insulated box. These thermometers were also used for calibration purposes. Accuracy of RTDs was for all experiments below ±0.20 °C (calculated by the formula in [94]). Long term stability of RTDs is better than 0.05 °C (0.02 % of resistance).

[31] Word *voltage* is also used for the electromotive force which should be rather abbreviate as *Emf*.
[32] Water temperature measurement was not performed directly by reason to prevent thermocouples oxidation. The thermocouples were covered by plastic cover with negligible thermal insulation.

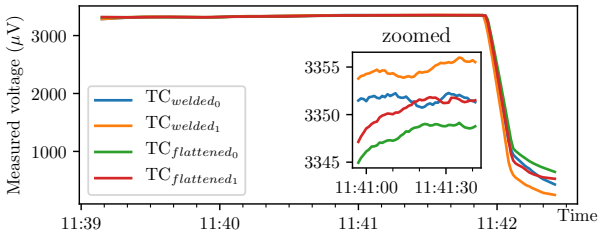

Figure 3.3: Comparison of the spherical and flattened weld (HJ≈100 °C, CJC≈20 °C).

Thermocouples testing

To ensure a high-quality TC junction, the welder was connected with argon gas to provide an inert atmosphere during the welding. When the thermocouple was welded, a strength test was performed to ensure the robustness of the connection for experimental measuring. Many welds were repaired immediately after the test of the weld quality. Finally, only 3 % of welded thermocouples crashed during the experiment measurement preparations. As the length of the thermocouples is 22 m, the risk of accuracy decreasing was discussed and experimentally verified. The check was carried out by calibration measurement. The thermally insulated end of the TC hot junction was located at room temperature and the electronics in the thermally insulated chamber. Several hours later, the temperature difference between the TC hot and cold junction increased to about 9.8±0.15 °C, based on the thermometer measurement (2 located in hot junction therm insulation and 2 located in cold junction area - electronics). This process is described in Fig. 3.5. This insulated box with electronics has a higher temperature than welded thermocouples *hot junction* due to the electronics heating. Measured *Emf* is therefore negative. Based on this measurement, the difference between the long and short thermocouples is negligible in our conditions, where each thermocouple is calibrated itself. This measurement is shown in Fig. 3.4. The difference between the long and short thermocouples (after applying offset calibration) is merely about 0.6 %. As well, the thermocouple degradation by proton and neutron irradiation was studied with results of negligible impact. Therefore, the thermocouples were utilised repeatably.

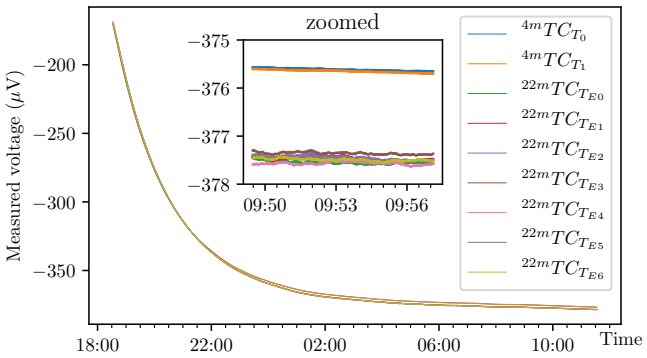

Figure 3.4: Comparison of the short (4m) and long (22m) TC measurement.

All thermocouples are marked after welding. Labels consist of a letter mark, which describes the A/D converter and a number, which represents the exact measuring channel where the thermocouples plugged in. Furthermore, the thermocouples are input into the database of used thermocouples. This database monitors the thermocouples behaviour (changes) → controlling measurement after the experiments.

Controlling measurement of TC quality The TC hot junctions are inserted into the polystyrene insulation one by one, about 3 cm deep of 10 cm thick polystyrene. There are also located 2 thermometers PT100. The electronics (chassis and converter) are inserted into a thermally insulated box with another two RTD. This process is widely described in the previous paragraph. Finally, based on this measurement, the characteristics trend of thermocouples responding is monitored as well as its average gain per degree Celsius in a quite steady state.

Figure 3.5: Photographs of the thermocouples testing.

To observe the TC behaviour at higher temperature ranges, there is a second type of calibration. The thermally insulated box with thermocouples *hot junction* is equipped with a heating source. The heating source consists of PET metal fever film and carbon fibber with thin resistance wire. It is very flattened like a list of hard paper with dimensions about 15 cm×20 cm, powered by 5 V DC. The temperature of the wire reaches about 65 °C based on measuring by thermal imaging camera[33]. This heating source is placed below the insulated box containing the TC *hot junction*. The measuring is realised during heating (where the heat source is switched on) and cooling (heat source switched off).

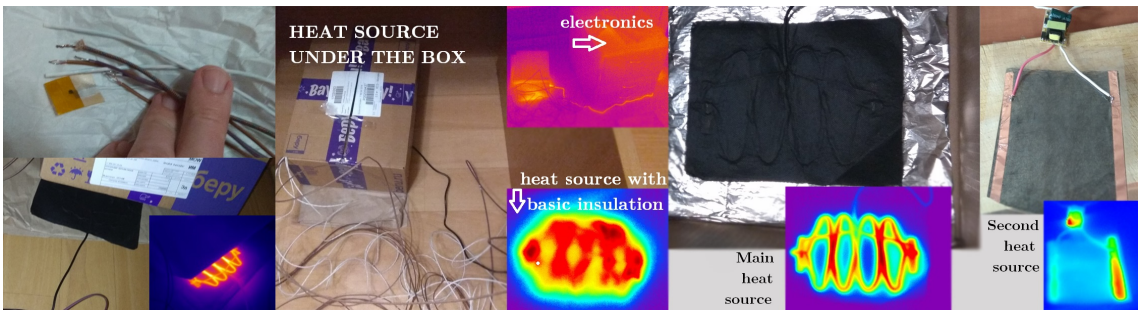

Figure 3.6: Thermocouples calibration gain check with heating source.

[33]The data sheet declares the temperature between 60-70 °C

Measured data are analysed by software written in Python, comparing the results of the measured TC voltage gain per degree Celsius with the expected data based on the data sheet (calibration described in section 3.1.1). Most of the charts were plotted by *matplotlib* library in Python, as well as the following subplots of the measured data. Python code of the chart plotting is enclosed in Appendix C.5.

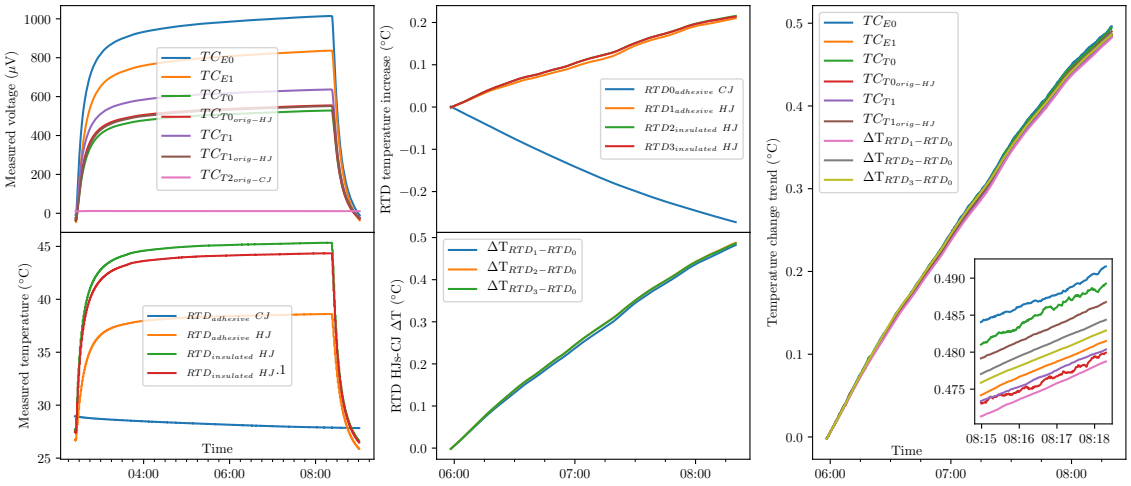

Figure 3.7: Voltage trends of various thermocouples compared with RTD. This figure visualises the comparison of the ΔT measurement for a semi-stable state. Raw data shown on the left side for various temperature measurement positions, relative temperature increase in monitoring interval (6:00-8:30) is shown in the middle, and finally the measured ΔT increase of TC compared with the RTD measurement is shown on the right side.

Python scripting - data analysing

Based on the LabView data collection setting, the collected data are saved to individual files; each contains one hour of temperature measuring (see subsection 3.1.1). Some of the experiments were measured about a week before the experiment started by reason of temperature change monitoring and to ensure the temperature stabilisation at the measuring spot. The measuring usually continues for several hours or days after the experiment finishes for monitoring the instrumental setup cooling. The possibility of long-term temperature measurements depends on the primary experiment requirements. The temperature measurement was usually interrupted by irradiation foils (samples) fixation and its picking. Since the merged output contained about 10^6 lines and 90 columns, it was necessary to use an advanced tool for data manipulation and visualisation. The scripting language Python was chosen due to its spread usage and its variability. It is an interpreted, high-level, general-purpose programming language [32]. Many scripts were written, mostly for working with a group of data, such as merging, sorting, calculation, and finally plotting. Moreover, the Python code has been used for MCNPX output data analysing and for gamma-ray spectrometry data[34]. Written scripts were used mostly for reading data from MCNPX output[35], and MCNPX MESH file to visualise the data, or reading and filtrating cross-section obtained from TALYS[36].

Python scripts were used for working with TC measurement data (Appendix C.1, and following), its analysing and visualisation. Short description of the written script (see p. 156) is summarised in this paragraph. The first part of the written script is loading the used libraries. Next line, the path is set to the user directory and further to merge all files into one. In the following, all data are loaded into DataFrame (*pandas* library) and filtered by Savitzky-Golay filter [97]. Filter was set to using a window of 21 filtered elements. Data are plotted as raw, so the smoothed to being checked. A larger filtration window might be used if the beam outage doesn't appear. In case of a beam outage occurs, it is better to use smart filtration of the data partition to don't lose the sharp edge of the temperature changes. Then the calibration performed as described in the next sub-chapter on p.40. The final part is the most crucial, the visualisation. Based on the temperature measurement, the beginning and the end of the experiment is identify[37] with an accuracy of about$\pm$1 s.

[34]These scripts are attached in Appendix C. Furthermore, the video manual has been recorded to explain how to use the script for MCNPX MESH data visualisation (see the script enclosed C.6, C.7 and the video manual (Czech language): https://youtu.be/kUDWkV0juW8

[35]Used for many tallies calculation→the QUINTA cylinders calculation, where 298 tallies calculated.

[36]TALYS is a nuclear reaction simulation code for analysis and prediction of various types of nuclear reaction cross-section based on the Hauser-Feshbach formalism using different γ-ray strength function [96]

[37]The beam data measured by Phasotron facility staff have a sampling rate about 25 s^{-1}.

Electronics & data collection in LabView

The most crucial part of this experimental research was the right choice of the electronics, chiefly the measuring card equipment[38]. It must be as accurate as possible, since 1 μV is very roughly equal to 0.025 °C. The NI9212 and NI9214 fabricated by the National Instrument company were chosen. For dealing with RTDs measurement, NI9217 card was chosen.

Properties of the NI9212 card:

It is a channel-to-channel isolated thermocouple input module which offers 8 TC channels. The isotherm terminal block has declared the measurement accuracy in the data sheet to 0.29 °C. The reported sensitivity[39] is 0.01 °C. Each channel simultaneously passes through a filtered differential amplifier before being sampled by a 24-bit ADC (Delta-Sigma). It has two internal cold-junction compensation channels and high-resolution timing mode, which optimises accuracy and noise, and it rejects power line frequencies [98].

Properties of the NI9214 card:

Another measuring card type is the NI9114, it has the isotherm terminal block for measurement accuracy up to 0.45 °C. It has lower temperature sensitivity[39] (0.02 °C), and in contrast with NI9212, it has higher input impedance (10 MΩ). The same Delta-Sigma converter is used, and it is equipped with power line noise rejection as well. The last significant difference is that NI9214 has three internal CJCs and extra features, internal-only channel known as the auto-zero channel [99].

The CJC sensors with a typical error 0.25 °C are located in thermal blocks (close to the screw terminal) to minimise any thermal gradient between the TC connection and CJC sensor. The therm block is designed by heavy metal to ensure the good thermal conduction and eliminate hot spots. The NI9212 contains 2 CJC, the first one CJC_0 is designed for $TC_0 \rightarrow TC_3$, the second one CJC_1 for $TC_4 \rightarrow TC_7$ [100]. The NI9214 card have 3 CJC (although offers double number of physical channels), the first one CJC_0 is designed for channels (2, 3, 4, 7, 8 and 9), CJC_1 for channels 10→15 and finally, the CJC_2 for channels (0, 1, 5 and 6) [101].

Properties of the NI9217 card:

This RTD card offers to measure four channels of up to 4-wired RTD PT100 with 24 bits resolution. The range of the measurable resistance is between 0 Ω → 400 Ω. The NI9127 is compatible also with 3-wired RTD and offers the sample rate up to 400 samples per second. It is hot-swappable device (may be plugged in and out when active) and RTD channels share a common ground that is isolated from other modules in the system [102]. The excitation current is 1 mA per channel and as well as previous cards it contains 50 Hz or 60 Hz noise rejection. The noise of high speed resolution (0.01 s per all channels) is 0.02 °C whereas 0.003 °C for high resolution mode (0.8 s per all channels). Typical error is 0.15 °C for 4-wired and 0.20 °C for 3-wired RTD in the conditions applied under this thesis research.

[38] Author is very grateful to **Dr. Jiri Drapela** from BUT in Brno, who helped by his valuable advice with choosing electronics equipment in the early beginning of the experimental research.

[39] The sensitivity is a function of noise and represents the smallest change of temperature certainly detectable by TC with that electronics converter. The values assume the maximum of the full measurement range of the standard thermocouple sensor, according to data sheet [98].

Data acquisition

The data collection was realised by LabView [85] software. The earlier experiments were measured by using its DAQ (Data Acquisition & Analysis) assistant. It is a useful and easy to use tool, moreover, it allows to set some basic parameters. Unfortunately, it does not allow to read raw cold junction compensation (CJC) data. Thermocouples were loaded as a voltage signal, without using internal calibration. Two DAQ assistants were used, the first one to collect the voltage of TC, the second one to collect the temperature of RTD. These signals were in real-time plotted through the collector of 300 samples by wave charts. The collector was used for visual monitoring of the 5 minutes trends, to show what is happening inside of the target. In addition, it helps for spotting the error occurrence. The storage of the signal was performed by the data storage block *Write To Measurement File*. There is an inert setting of this block which round the data to 6 decimals of the measuring units (in this case V). It means the TC data were rounded to an integer of μV and saved. As far as this setting is not possible to change easily, this property was avoided by multiplying the data by a constant (number 1E6) before saving. Finally, the data are stored in units of μV rounded to 6 decimals. A Diagram of the first acquisition software is shown in Fig. 3.8. Data were collected with sample frequency 1 Hz and saving per each 5 s. Output data files were partitioned into multiple files with a 1 hour interval. The simplest setting of the DAQ assistant is shown on the right side of Fig. 3.8. The setting of the RTD data collecting was realised based on manual [95].

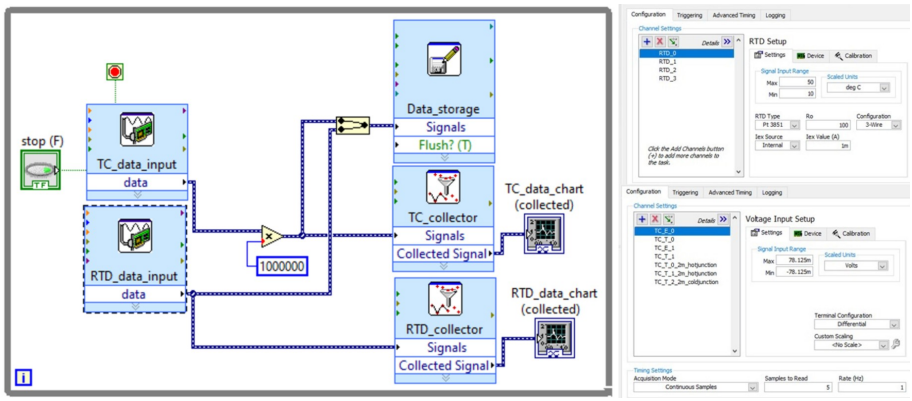

Figure 3.8: Diagram of LabView data acquisition.

This fist acquisition setting had two main problems:

- The saving block is in the same loop with measuring (noise caused by storage process).
- It does not allow to read CJC data.

The storage problem was easy to solve, just to move the storage block into a separated loop. This problem appeared only when measuring with more than 4 cards. The second problem of reading the CJC was not solvable by the DAQ assistant, the acquisition program had to be written by using DAQmx. It means the global change of the code. It has been written in LabView version 2015, but unfortunately, this version contains an error that causes raising a specific error if accessing the internal and physical channel of one card (in the case of NI9214). Over the time of solving this problem, the cards were used only as a simple voltage measuring card without compensation, while the compensation was solved

by external adhesive RTD measurement. It is not reacting as quickly as CJC, but for most of the measurements, it offers sufficient accuracy. By reason to decrease quick temperature changes of the isotherm blocks, the measuring electronics was located inside of the therm insulated box. This method was experimentally tested by reading the internal channels of CJC of NI9212 and NI9214 and simultaneously the temperature measured by adhesive RTD. The RTD was located between cards NI9212 and NI9214. Two experimental measurements were carried out, once for uninsulated electronics (Fig. 3.9), once for thermally insulated electronics (Fig. 3.10).

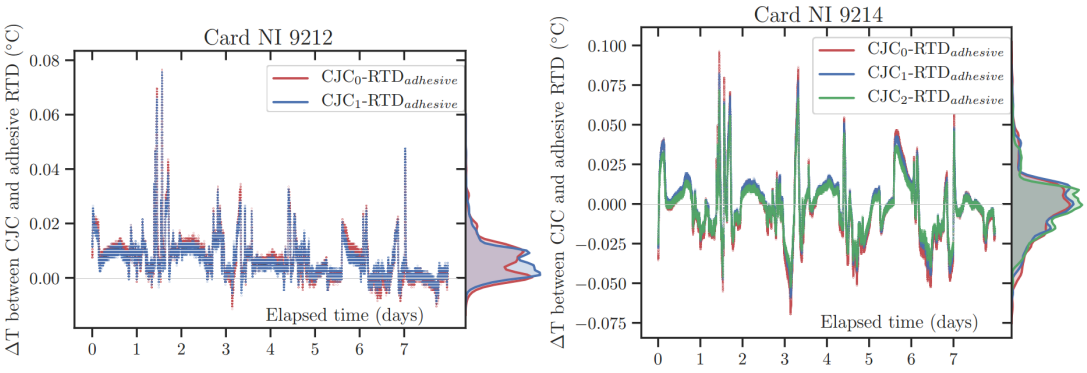

Figure 3.9: This chart is comparing the temperature measurement by CJC and $RTD_{adh.}$ for both cards, without thermally insulated measuring cards. On the right axis of each chart is shown the data distribution (*right y axis*)[40]. Charts were separated for NI9212 (better CJC accuracy, left) and NI9214 (lower accuracy, right). Thermal insulation helps to increase accuracy of this measurement, see the difference on Fig. 3.10.

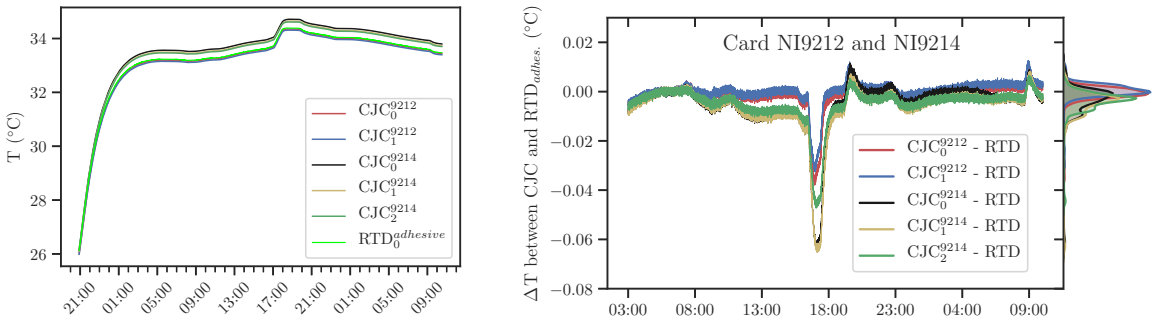

T measured by CJC and RTD

ΔT between CJCs and RTD, offset at 03:00

Figure 3.10: The temperature comparison of CJCs and $RTD_{adh.}$ for standard conditions used for experimental measurement. The electronics is thermally insulated for better accuracy. On the left side is shown the absolute temperature measured by each CJC and by adhesive RTD (*lime* colour). On the right figure is shown the relative temperature between each CJC and $RTD_{adh.}$. The offset was applied by median of interval values 03:00-03:05 of the first measuring day. On the right y axis of the right figure, there is estimated kernel distribution by *KDEplot* function of the *seaborn* library, Python.

The same measurement was performed for standard conditions during summer (higher temperatures), when the electronics were located in the thermal insulation. The measurement started with „cold“ electronics just at the time when the electronics plugged into the electricity. Based on the measuring card data sheet, the electronics heating should take about 15 minutes. Data sheet expects the equal temperature of the electronics and surrounding air. In this case, due to the thermal insulation, the steady temperature of working electronics was much higher. To reach the temperature steady state, it took about 3 hours for thermally insulated electronics.

The LabView program used for data acquisition of this measurement is shown in Fig. 3.11 (already using the DAQmx coding). The thermometers RTDs were read separately (two different types were used). Firstly, the rounding was set to 3 decimals, but as shown in Fig. 3.9, the data scatter plot contains horizontal white line spaces caused by the discussed rounding. This phenomenon is mostly seen on the left side plot due to the about 50 % better CJC accuracy of NI9212 (more precise measurement). For further measurement, the data were rounded on 4 decimals (already applied for Fig. 3.10).

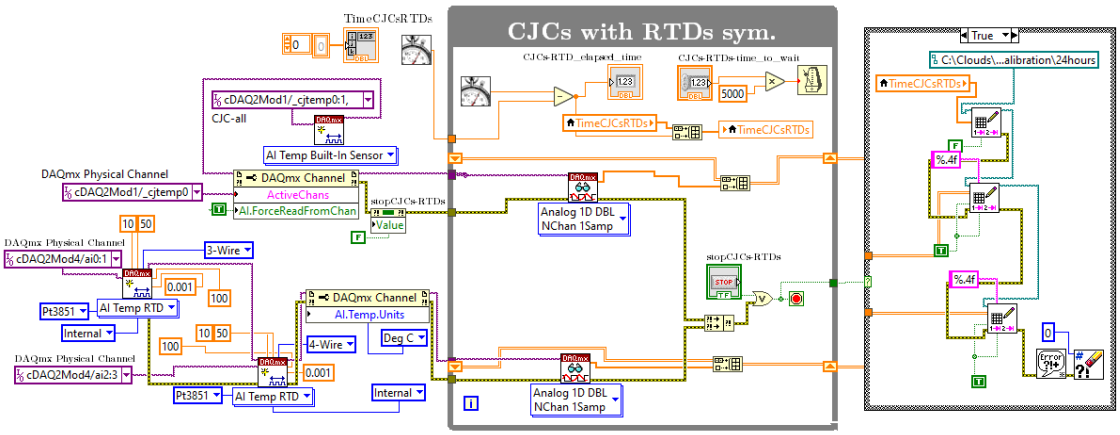

Figure 3.11: LabView code for reading internal CJCs with RTDs measurement.

Finally, a new version of the LabView was installed without the discussed error of simultaneously reading[41]. This problem was not occurring for CompactRIO, only for CompactDAQ. In the new version, there were still occurring similar errors of simultaneously reading, so finally, the reading was realised step by step. Required sampling was set to be about 0.2 samples per second, which fits also to the step-by-step method. Firstly were read the CJCs and in the next step the TC voltage. This program is shown in Fig. 3.12. There is a time delay of about half of the sampling rate for the second step of the measurement (it does not influence the measurement quality).

[41] Based on information from https://www.ni.com/kb, the error should be repaired since ver. 2017.

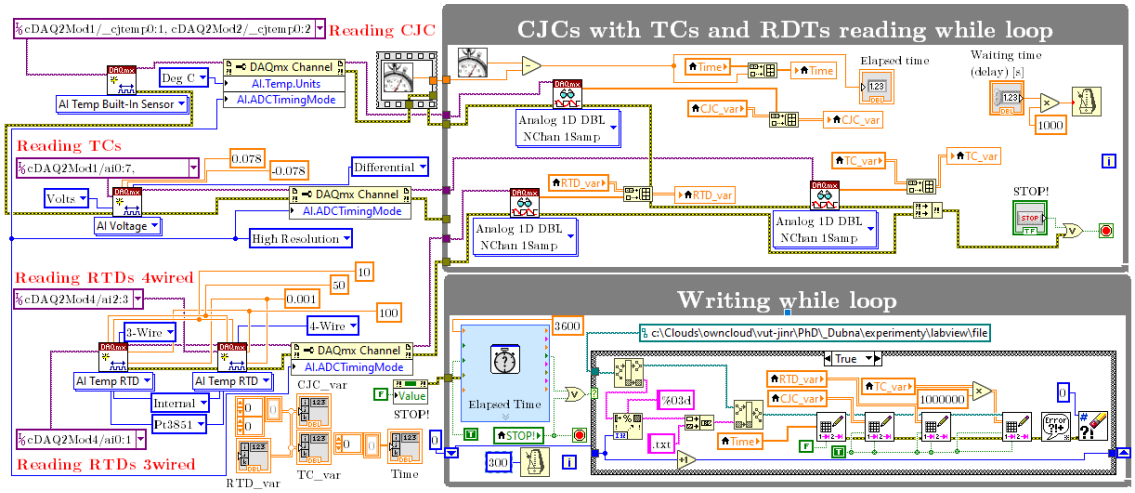

Figure 3.12: LabView code for reading CJC with TC and RTD all together.

To describe the written program[42], it is important to mention the main setting. All cards are set in high resolution mode. The loop executing average time is 5.184 s. If using high speed mode, the loop executing time is in average 514 ms. It may be simply switched by a button (located in the middle of the left part). The upper left part of the code deals with CJC reading setting, above that there is the TC physical channels setting, and the left bottom half deals with RTD reading setting (labelled by red names). As the example before, the RTDs here are read separately for 3-wired and 4-wired cases. Below the RTDs setting (close to the writing loop), there is an initial zero condition for memory (2D array for measuring data and 1D for time). Just above the 1D zero time array, there is setting for the *STOP!* button, to be switched into the False (in the case to switch off the previous measurement and start again). Its „error out“ is connected to the writing loop and the elapsed time „error in“ to ensure the order of the processes.

The writing loop is set to save appended files each one hour, just in case that electricity outage occurs. Partitioning output files is not necessary as the calculated maximal size is about 200 MB which is not causing any problems since executing in a separate loop. The saving case loop is connected to *OR* of *Elapse time* and stop button, to save the data also when the *STOP!* button is switched. Data are appended step by step in order of Time, CJC measurement, RTD measurement, and finally TC measurement, which multiplied by a constant 10^6 to get results in the units of μV.

The most important in the reading „while loop“ is the setting order of processes. Step by step reading of the cards, where the „error out“ of the *DAQmx Read* block of the CJC, is connected to the „error in“ of the *DAQmx Read* block of the TC. Finally, the errors are merged and treated to the loop termination. Reading loop contains also the time delay function, which is set in the controlling panel, it is using in case of the same interval measuring importance, the default set to zero.

[42] Author is very grateful to Dr. Leo Schlattauer (Palacky University Olomouc) for his time, consultation and help with dealing with LabView programming.

Thermocouples calibration and measurement

In essence, the absolute temperature measurement with thermocouple probes is a challenging task. Due to thermocouple properties, it is hard to reach a satisfying result. The TC measurement depends on the type of thermocouple, its accuracy, construction, insulation, state of a measured substance, the diameter of the wire, and finally the signal converter, data analysing and thermocouple calibration. The chosen tiny A class thermocouple type T has an accuracy declared by the manufacturer better than 0.5 °C or 0.4 % [103] (for full measuring range). The most crucial task is to measure the relative temperature (temperature differences during the irradiation) in a specified small temperature range. By using several improvements, much higher accuracy was achieved.

Although the thermocouples are essentially nonlinear temperature probes, their linearity is sufficient in a small specific range. The chart of the voltage gain linear approximation is shown for the range of 15 °C→50 °C on the left side of Fig. 3.13. The linear approximation of the voltage gain derivation[43] (ΔV_{gain}) is shown for the same range on the right side of the same figure. Shown data are based on data sheet calibration [103], where cold junction (CJ) compensated in 0 °C bath. In contrast to data sheet cold bath compensation, this work uses the floating CJ (the CJ temperature is based on the electronics isotherm block temperature). The electronics was located inside of therm insulated box surrounded by room temperature (T) air[44]. The absolute T in the insulated box was equal to the surrounded air temperature at the beginning, but due to electronics heating, the temperature was stabilised around +10 °C above the $T_{surrounded\ air}$. As the measuring room located in an ancient building without required laboratory conditions, the temperature depends a lot on the season and outside weather. The temperature difference (ΔT) between the measuring room and experimentally hall was usually smaller than 3 °C. The temperature differences between the hot and cold junction during the experiment were in the range of -10 °C→15 °C for most of the cases.

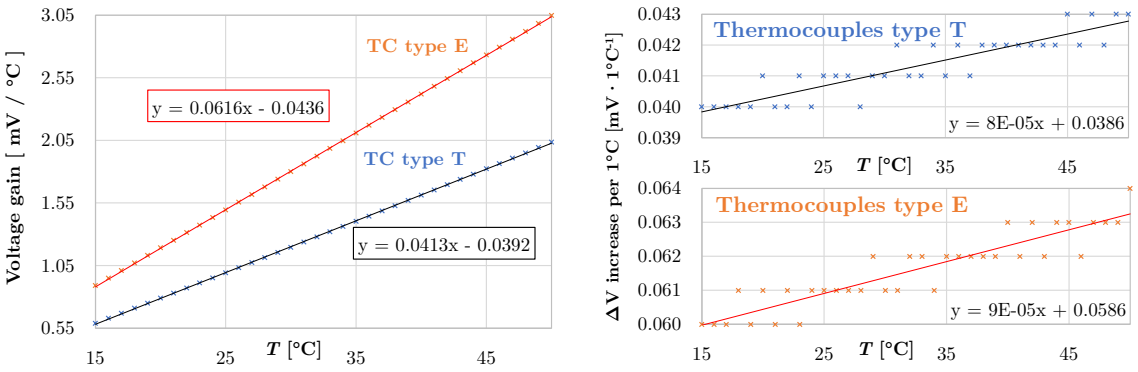

Figure 3.13: TC type T and E voltage gain for selected range on the left side, calibration data [103] and [104]. The figures on the right side show the relative voltage gain ΔV_{gain} - in the axis y described as ΔV increase per 1 °C. Data calculated by the same source as the left figure. It is widely described in the following paragraph.

[43] In the following text, the voltage gain derivation is also titled as relative V gain or just ΔV_{gain}. Basically, it is a function of voltage gain per ΔT = 1 °C. This phenomenon is in detail explained in paragraph 3.1.1, p.43.

[44] The reasons of electronics thermal insulation are explained in subsection **LabView**, p.37.

The standard measurement with a thermocouple is based on automatic calibration by polynomial function based on thermocouple type standard. Polynomial functions of higher order (such as 9^{th}) were earlier used for the whole TC measuring range. It was contained typical fluctuating error of measurement. Much better solution is to partition the calibration curve into several of ranges which may be fitted by lower polynomial functions (usually about 4^{th} or 3^{rd} degree) [105]. Unfortunately, its accuracy is not sufficient for experimental measurement in this work. Unique calibration technique was invented in a way that each thermocouple is calibrated by individual calibration, based on its properties. This methodology is the central pillar of the whole measurement, so it will be in detail described in the following pages.
Globally, the easiest way of the thermocouples calibration is the linear calibration approximation of specific small range. The previous Fig. 3.13 contains the fit and equation of the linear approximation. Although it looks that the linear approximation fits well for this range of $\Delta T = 35$ °C, the right charts are showing that it is not correct. The relative voltage gain (ΔV_{gain}) of the thermocouple type T is very approximated about 41.3 μV, and for the type E, it is about 61.6 μV. The same figure on the right side describes the problem of non-linearity, where the ΔV_{gain} in this range of 35 °C is shown. It increases in this range for about 7.5 % in case of the thermocouple type T, and more than 5 % for the TC type E. The absolute error between the linear, and the polynomial approximation is visually shown in the comparison in Fig. 3.14. The following three temperatures were chosen through the range; 16 °C, 30 °C and 44 °C. The blue marks (for TC type T) and orange marks (TC type E) are the calibration voltage gain from thermocouples data sheet [103] and [104].

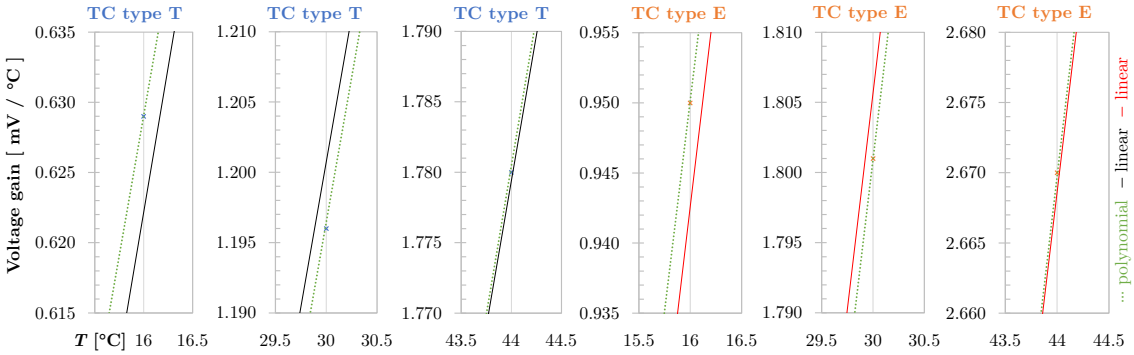

Figure 3.14: Linear vs. polynomial fit of absolute T calibration error, data [103].

The factory polynomial function (or even its linear approximation in a small range) can not be used due to two factors. The TC length is much longer than the calibrated standards, and each thermocouple has a slightly different voltage gain based on its weld quality and flattening destruction. The cold junction is floating. Firstly, it is essential to think about the experimental measurement requirements. Only relative temperature is especially important. Absolute temperature is necessary only for the heat transfer calculation, and its precision determination is not crucial. It may be solved by RTD T measurement at the cold junction (or directly by the internal CJC) by adding the calibrated relative temperature.
Used calibration uses the derivation of the data sheet calibration function[45]. Although the ΔV_{gain} is not linear characteristic, it is approximated by linear function for selected range -10 °C→15 °C with error 0.03 % (based on data sheet data [103], [104]). This simplification does not increase the error while making the calibration much easier.

[45]The calibration data are rounded on 3 decimals of mV (integer of μV).

For each thermocouple must be implemented a correction, according to its characteristics. As the ΔV_{gain} is linear, a two correction points must be measured. The first correction point is measured for negative voltage gain, approximately corresponding to -10 °C (for further explanation labelled as T_1). The temperature -10 °C responds to the steady electronics in thermal insulation (CJ) if the HJ measures the room temperature.The second one for $\approx +15°C$[46] (labelled as T_2). The real temperature is measured by RTDs[47] for both calibration point. The reference temperature of the HJ with maximal error ±0.2°C is substituted by the CJ reference temperature represented by CJC (T_{CJC}) with error about 0.25 °C. Finally, since having the temperature difference and voltage gain measured by calibrated thermocouple, the ΔV_{gain} is calculated. If the voltage gain is divided by the temperature difference, the result is the ΔV_{gain} of the half temperature difference (due to the linear characteristic with unknown slope - rules of the integral under of the linear function). To get calibration of the TC_{cal} which measures voltage gain E_1 and E_2 of equivalent temperature:

$$\begin{aligned}
&\Delta T_1 \;=\; T_1 - T_{CJC}\;, \quad \Delta T_2 \;=\; T_2 - T_{CJC} \\
&\Delta V_{gain}^{\frac{1}{2}\Delta T_1} \;=\; \frac{E_1}{\Delta T_1}\;; \quad \Delta V_{gain}^{\frac{1}{2}\Delta T_2} \;=\; \frac{E_2}{\Delta T_2} \\
&\text{slope of the } \Delta V_{gain} \;=\; \frac{\Delta V_{gain}^{\frac{1}{2}\Delta T_2} - \Delta V_{gain}^{\frac{1}{2}\Delta T_1}}{\frac{1}{2}\cdot|\Delta T_2| + \frac{1}{2}\cdot|\Delta T_1|} \\
&\text{offset} \;=\; \text{slope} \times \frac{1}{2}\cdot|\Delta T_1| + \Delta V_{gain}^{\frac{1}{2}\Delta T_1} \;=\; \Delta V_{gain}^{\frac{1}{2}\Delta T_2} - \text{slope} \times \frac{1}{2}\cdot\Delta T_2
\end{aligned} \tag{3.1}$$

For example if $T_1 = 20$ °C; $T_2 = 45$ °C; $T_{CJC} = 30$ °C; E_1 = -370 μV; $E_2 = 570$ μV:

$$\text{slope} \;=\; \frac{\frac{570}{45-30} - \frac{-370}{20-30}}{\frac{1}{2}\cdot|20-30| + \frac{1}{2}\cdot|45-30|} \;=\; \frac{2}{25}\ \mu\text{V}\cdot^{\circ}\text{C}^{-2}$$

$$\text{offset} \;=\; \frac{2}{25} \times \frac{1}{2}\cdot|20-30| + 37 \;=\; 37.4\ \mu\text{V}\cdot^{\circ}\text{C}^{-1}$$

Therefore, the value is the linear calibration of ΔV_{gain} for time T following:

$$\Delta V_{gain}^{T} = \text{slope} \times T + \text{offset} = \frac{2}{25}T + 37.4\ [\ \mu\text{V}\cdot^{\circ}\text{C}^{-1}]$$

This calibration is calculated for each TC and saved into the database in the form of *slope* and *offset*. Although the calibration was calculated for certain range -10 °C→15 °C, it may be use also for slightly higher values with similar error (values up to ΔT = 20 °C). **This method was evaluated as the most accurate for purpose of this work.**

[46] Temperature about -10 °C is achieved by CJ therm insulated and heated by electronics, while HJ separately therm insulated without any inert heat source. Second reference temperature (about +15 °C) is achieved by the same way in contrast that HJ therm insulation is heated up by under insulation heat source (similar to the heating source in Fig. 3.6).

[47] One RTD measures the temperature of the CJ (simultaneously with CJC) inside of the therm insulated box, mostly for controlling purpose. Another three RTDs measure the HJ with calibrated thermocouples. Measured data from these three RTDs are averaged and used as HJ reference temperature with equivalent error based on used RTDs (maximal ±0.2°C).

The second method (earlier used) was dealing with the data sheet data extraction and its ΔV_{gain} approximation. Difference of each TC calibration was implemented in the end of the calibration process by excepting that gain difference is a constant which changes only the offset. This method was used for the first experiments, but due to lower accuracy was replaced by previously described one (because each TC gain usually has a slightly different slope). This second method was little bit more complicated. The first task was to determine the minimum and maximum measure voltage of calibrated thermocouple, to estimate minimal and maximal ΔV_{gain} (range of thermocouple ΔT measurement). Once the polynomial fit of the relative gain is calculated as:

$$y = -9.180146 \times 10^{-5}x^2 + 9.106027 \times 10^{-2}x + 38.54828, \tag{3.2}$$

the linearity of the expected measuring range must be checked. These data are shown in Fig. 3.14, where linearity range is chosen based on the expected maxim:

$$\Delta T \;=\; T_{HJ} \;-\; T_{CJ} \;=\; (-10°\mathrm{C} \rightarrow 15°\mathrm{C}).$$

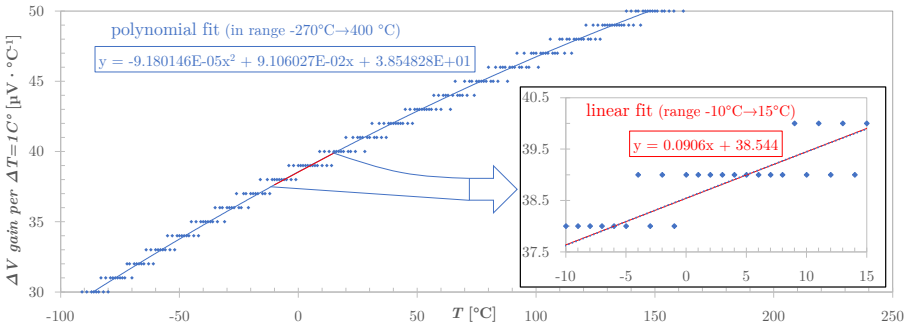

Figure 3.15: TC type T calibration of voltage gain per each increased degree Celsius [103]

Description of the ΔV_{gain} To understand the chart of relative TC gain, lets describe the example. In short, the relative TC gain is the derivative of the absolute voltage gain declared by the data sheet. For the case that *cold junction (CJ)* floated, *hot junction (HJ)* measures seeking temperature ΔT, measured voltage EMF (V_{meas}) is -100 μV and having the formula of polynomial fit of the relative voltage gain (see equation above). The measured voltage is literally the integral of this polynomial function with boundaries at hot & cold junction temperatures, as described by the following equation:

$$\int_{T_{CJ}}^{T_{HJ}} (\text{equation of the relative TC gain})\ dx, \tag{3.3}$$

for describing an example, it is:

$$\begin{aligned} V_{meas} &= \int_{T_0}^{T_{meas}} -9.180146 \times 10^{-5}x^2 + 9.106027 \times 10^{-2}x + 38.5482\ dx \;= \\ &= \left[-3.06005 \times 10^{-5}x^3 + 4.55301 \times 10^{-2}x^2 + 38.5482x\right]_0^{T_{meas}} \;= \\ &= -3.06005 \times 10^{-5} \cdot T_{meas}^3 + 4.55301 \times 10^{-2} \cdot T_{meas}^2 + 38.5482 \cdot T_{meas}, \end{aligned}$$

so finally, the root calculation of equation:

$$-3.06005 \times 10^{-5} \cdot T_{meas}^3 + 4.55301 \times 10^{-2} \cdot T_{meas}^2 + 38.5482 \cdot T_{meas} \;=\; 0 + V_{meas}.$$

There are three roots: $T_{meas}^{(0)}$ = -600.577 °C, $T_{meas}^{(1)}$ = -2.602 °C, $T_{meas}^{(2)}$ = 2091.071 °C, as the measured temperature expecting around -2.5 °C (based on average gain in this range), the measuring temperature is T_{meas} = -2.602 °C.

As the calibration is different for each thermocouple, it is suitable to carry out automatic calibration. The calibration software was written in Python language [32] and is enclose in Appendix Fig. C.2 and C.3 where also the described code and discussed results which shown in Fig. C.4). At the beginning, the minimum and maximum of the measured voltage is located for each thermocouple. Furthermore, the equivalent max and min temperature is calculated as described above (eq. 3.3) and these min and max temperatures are the boundaries of the calibration range. The final range of relative TC gain is approximated by a linear function, unique for each TC.
To describe this method graphically, the T_{CJ}, T_{HJ}^{min} and T_{HJ}^{max} will be marked as RTD, T_1 and T_2, respectively. The marker RTD is used because the coefficients of RTD trends in floated CJ will be used for the last phase of calibration. These temperatures have the relative gain calculated by eq. 3.2, for RTD (which for each cases equal 0,, it is 38.54828 μV·°C^{-1}. For the graphical visualisation of this calibration, see Fig. 3.16.

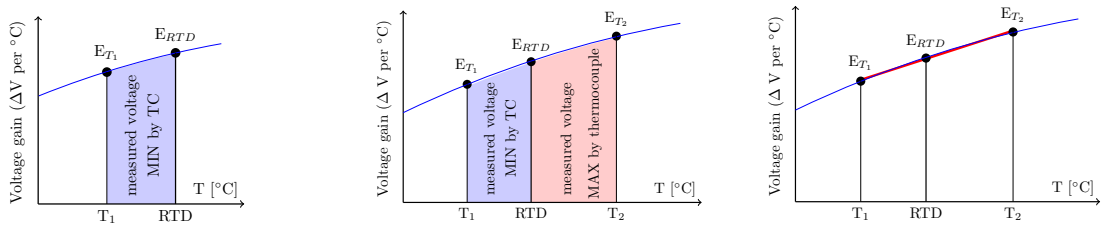

Negative voltage measured | Finding max and min V gain | Linear approximation

Figure 3.16: Calibration of relative voltage gain - widely describe in text.

Displayed charts are based on conditions, where T_1 negative and the minimal measured Emf V_1 is equal to the integral of blue area, respectively T_2 positive and maximal measured Emf V_2 equal to the red area integral. The first limit of the integral is temperature RTD, the second limit is the sought minimal measured (calibrated) temperature (T_1), respectively maximal (T_2). If there is enough of computation power available, each measured voltage could be calibrated to temperature by the described integral calibration method.

To simplify the calibration, the voltage gain data between curve limits (E_{T_1} and E_{T_2}) are approximated by a linear function (Fig. 3.16, right - red line). Each thermocouple has own linear ΔV_{gain} calibration function. It is expected that the slope of calibration is dependent only on chosen range of MIN and MAX of data sheet data. The offset consists of MIN MAX linear approximation offset with adding the difference between calibrated thermocouple and calculated calibration. It was measured chiefly for ΔT = 10°C and expected to be constant across all range. It involves all uncertainties cause by distinction[48] of used thermocouples compared with the standard one, described in the calibration data sheet [103] and [104]. Final result of the calibration is the average voltage gain per dT. Program save this calibration into a new csv file.

[48] Imperfect weld, its flattening and length of thermocouples, as described in subsection 3.1.1.

3.1.2 Monte Carlo N-Particle Transport Code simulation

The experiments were simulated by Monte Carlo radiation transport program, version MCNPX 2.7.0.[49], with employing the data library ENDF [107], Intra Nuclear Cascade modeL INCL4 [108], and the ABLA fission-evaporation event generator [109]. Neutron and proton spectra were calculated for several experiments (only where the samples were measured by gamma-ray spectrometry method). Most of the simulations in this thesis are mostly focused on the heat deposition determination. Each of the MCNPX simulations were fully performed by the author, except the QUINTA target, where the QUINTA geometry model took over and rebuilt from the research work of M. Suchopar [33]. The QUINTA geometry is quite more complicated and Mr. Suchopar's model was already verified and many times used by all other colleagues of the ADS group. There is an example of the most simple simulation of a cylindrical lead target in Fig. C.9. It is shown for the demonstration purpose, to describe the code setting.

The **QUINTA** target is physically rotated along z axis for 2 ° by reason to ensure that each of the protons interacts with any of the uranium cylinders. If QUINTA would not be rotated, some of the protons go through the target without interaction due to the air volume around each cylinder, see [49], p.50. All other experimental targets were set in the axis of the beam without extra rotation. This rotation is performed in the MCNPX input code as the beam rotation. The particle source is defined as following:

$$\text{sdef dir 1 vec } -0.0349\ 0\ 0.9994 \text{ x d1 y d2 z } -12.3,$$

where sdef=source definition; dir=1 is the cosine of the angle between VEC and UUU, VVV, WWW; vec=-0.0349 0 0.9994 is the reference vector for DIR in vector notation; X,Y and Z = coordination of position. The rest of the source definition may be the same as shown in the demonstrated example on page 164.

Other colleagues in the JINR ADS group[50] generally deal with gamma-ray spectrometry utilisation, mostly for the determination of neutron flux and various reaction cross section determination. Study and simulation of heat deposition was not researched by this group before. There are several variants of how to determine the heat deposition in MCNPX. The most easier way is to use the *F6* tally, which determine the energy deposition for selected particles. It may be specified for neutrons *F6:n*, protons *F6:h*, and any other particles included in the mode card, or also for the total heat deposition of all particles (which defined in mode cards) *+F6*, the units are MeV·cm^{-3}·source particle^{-1}. To calculate the energy deposition of neutron fission reaction, there is the *F7* tally. Another possibility is to manually multiply the *F4* tally (track length estimation) [114], see eq. 3.4:

$$\begin{aligned} F6 &= FM4 \quad c \quad m \quad 1 \quad -4\,, \\ F7 &= FM4 \quad c \quad m \quad -6 \quad -8\,, \end{aligned} \tag{3.4}$$

[49] Monte Carlo Neutron Particle Transport code is a very powerful and versatile tool for particle transport calculations, usable for neutrons, protons, photons, electrons, and other particle transport. It has been found in Los Alamos National Laboratory and it has many areas of application, e.g., radiation protection and dosimetry, radiation shielding, nuclear criticality, safety, accelerator target design, fission and fusion reactor design, and many others. The code processes any three-dimensional configuration of materials in geometric cells [106].

[50] Colleagues Jurabek Khushvaktov (Institute of Nuclear Physics ASRU, Tashkent, Uzbekistan) [110] and [111], Pavel Tichy (CTU in Prague) [112] and Miroslav Zeman (BUT in Brno) [113] are using MCNP, FLUKA, or Geant4 codes mostly for calculations of the neutron spectra and flux by purpose of comparing simulations with experimental results measured by activation foil methods. Their dissertation theses are going to be defended during the year 2020.

where $c = 10^{-24}$ × number of atoms per gram, m = material number for the material being heated, *1* = ENDF reaction number for total cross section (barns), *-4* = reaction number for average heating number (MeV/collision), *-6* = reaction number for total fission cross section (barns) and finally *-8* = reaction number for fission Q (MeV/fission).

The principle of the total heat deposition calculation can be described by the following equation:

$$F6 \;=\; \frac{N}{V \cdot \rho} \iiint_{V,t,E} H(E)\phi(x,V,t)\, dV\, dt\, dE \;, \tag{3.5}$$

where N is the atomic density, V is the geometry volume, ρ is the mass density, E is the energy, t represents time, *H(E)* is heat deposition response function and finally the ϕ is the angle integrated scalar flux [115].

To calculate the whole target volume heat deposition, the *F6* tally result must be multiplied by geometry mass (rather mass density and geometry volume), scalar constant (MeV to J conversion) and total number of incident particles → protons N_p in this case. In the case of MESH tally heat deposition (eq. 3.6), where calculated *Relative heat deposition density* (related to cm^{-3}, not mass), only the volume of each cell involved.

For the simulations used in this thesis, only *F6*, *+F6*, and *F7* cards were used for a certain geometry. To describe the specific heat distribution of the experimental target, the heat deposition mesh tally was calculated. Since interested in total heat deposition, mesh number 3 was employed. It is in principle similar with the tally *F6*, where „total“ or a certain particle may be involved[51]. There are several possibilities of how to use the mesh tally. In this thesis, only a rectangular mesh (*RMESH*) was used, where size of the cell is defined by the number and positions of cuts. Size of the cell was usually 2 mm which is a balance between smooth mesh and the size of the working data[52]. In the case of a small target as *Two cylinders experiment*, 1 mm mesh cells size were calculated[53].
The MCNPX input codes are widely discussed in Chapter 4 or Appendix. To describe the basic MESH setting, a simple model of a short lead target with diameter 19 cm and length 35 cm is shown (without any air gap). Due to the cylindrical geometry, it would be more suitable to use cylindrical mesh (CMESH), nevertheless, the RMESH was used for all of this thesis calculations. In general, this target volume for a rectangular mesh will be represented by a block of size 19×19×35 cm^3, where the cylinder is inserted. This block is partitioned by many cuts through all axes (meshed) into individual cells with cube sizes of 2×2×2 mm^3. Therefore, the block is partitioned into 1,579,375 cubes (cells). The heat deposition is calculated for each cube. For visualisation purposes, it is better to add an extra cell out of the boundary of the calculated volume, because if the whole volume is heating, the zero deposition will not be displayed (inappropriate for contrast). In this case, the mesh size is extended by a 2 mm cube in each axis. Volume of mesh is 19.2×19.2×35.2 cm^3, in total 1,622,016 cubes. Again, for the purpose of better visualisation, it is required to align the axis label to the centre of the cell. It is performed by adding a „half of cell“ → 1 mm, for each mesh boundary condition. The MESH definition of this case looks like listed in the following commands, see [114], section *MESH type 3*.

[51] This mesh is in detail described in MCNPX manual [114], section 3.3.5.24.4.

[52] There is a cells number limit for converting binary mesh data by GRIDCONV. Despite the fact that there are some other possibilities of larger number of mesh cells conversion, e.g., MCNP6 utilisation, due to sufficient results, this limit was not necessary to break.

[53] Description of the MCNPX program, the principle of calculation and exact code description will be no more and deeply discussed in this thesis, the knowledge of using this code was reached by [114].

```
tmesh
   rmesh3 total
   cora3  − 9.7 96i  9.7
   corb3  − 9.7 96i  9.7
   corc3  − 0.1 176i 35.3
endmd
```
(3.6)

The MCNPX mesh tally calculation result is a raw binary file with default name *„mdata“*. There are several ways of how to visualise these data. It may be directly plotted in the MCNPX[54] tally plotter (MCPLOT) from MCTAL files or superimposed over the geometry by the geometry plotter (PLOT) from RUNTPEn [114]. Nevertheless, it does not allow export in vector graphics and moreover the visualisation quality is not representative. Other possibility is the binary data conversion to formatted decimal file in *GRIDCONV* software (part of the MCNPX package). It allows to convert a certain mesh plane from the whole meshed volume. Converted data can be plotted by GNUPLOT [87] or any other software (for exampel PAW, IDL or Tecplot, see [114],p.226).
At the beginning of this research, the Gnuplot software was using for plotting. Several mesh cuts were converted by *GRIDCONV*, saved as „.tec“ files and finally plotted. Due to many experiments with different targets, manual plotting was not suitable. The script for multiple visualisation (see appendix C.8) was written in Gnuplot. Gnuplot is a very powerful software which allows vector graphics export and many particular settings. However, it is usable only for visualisation. It does not allow any advanced data manipulation. In the case of this work, it was necessarily to study the heat deposition of each target more deeply. Converting the mesh planes one by one was a very inappropriate solution. Finally, the Python programming was used. For the 3D visualisation of the relative heat deposition density, it is necessarily to visualise the values in several planes. In the following text, the plane is usually described as a volume cross-section or the geometry cut.

The *GRIDCONV* also allows to convert the whole binary mesh mdata file to a decimal text file. Converted data must be sorted and reordered, but finally it allows to work with the whole volume data. The Python script was written to deal with these data and perform manipulation and plotting, see in appendix C.6 and C.7. To simplify the potential utilisation of this code or its parts, a video manual was recorded and it is uploaded on YouTube[34]. Seaborn package is employed to deal with heatmap plotting.
To show the visualisation difference between Gnuplot and Python Seaborn, there are two figures shown in Fig. 3.17. The absolutely identical data were plotted by two different scripts in two different software. Palette colour could be changed. The Pyton Seaborn seems to be more suitable for this visualisation, the charts are definitely more elegant. On the other hand, to handle with Gnuplot is much easier.

[54] Clearly described in [114], section 5.6.23.6, p.225 and appendix B.3.1, p.324.

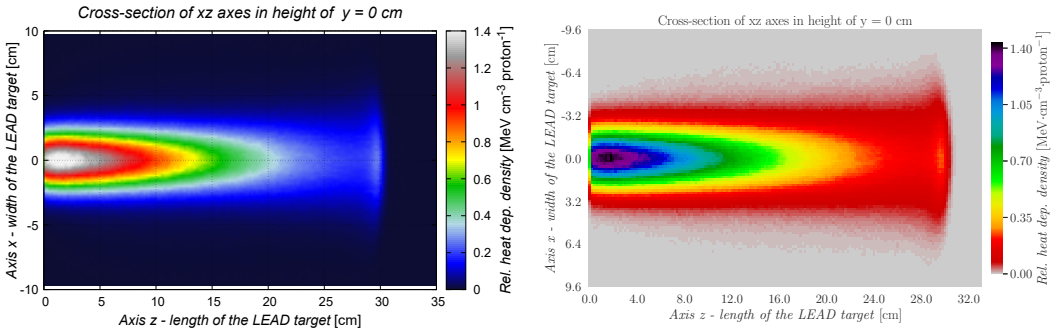

Figure 3.17: Visualisation of the simplified cylindrical Pb target relative heat deposition mesh by Gnuplot (left side) and by Python Seaborn (right side). The mesh cell edge size is 2 mm. The script for Gnuplot auto plotting is in appendix C.8 (uses defined plane, already extracted by GRIDCONV). In contrast the Python script work with whole volume data, so it allows to print each plane of the volume which chosen in the beginning of the script. It is basically based on similar script as listed in appendix C.6

To describe the heat deposition deeply, it is suitable to calculate the heat deposition for each particle which is contributing. Visual example of this calculation is shown in the results, Fig. 5.6 or with comparable scales in Fig. E.1. The largest contributors are usually non-elastic proton reactions (or rather the whole spallation reaction) neutron reactions (mostly fission), gamma heating and pion reactions. Each particle contribution ratio is variable based on the target material and geometry, however, the neutron and proton reactions are usually the major contributors. Other particles such as photons or pions contribute usually negligibly, it is widely discussed in the simulation and the results of each experiment.

3.1.3 Heat transfer simulation by ANSYS

There are several methods of heat transfer calculation by ANSYS software [116]. ANSYS consist of many products which can be easily controlled by the Workbench. It allows to connect various tools for calculation, import data, create geometry, mesh, to include libraries, perform calculations, and finally analyse the results. In this thesis were used calculations in Transient Thermal program and Fluent, partly by using the Workbench environment. In the following pages will be described problems the author dealt with, and finally, the used methods to calculate the required results. There are many variables to estimate and many choices need to be done for each simulation. For better clarity, the possibilities of each model choices will be shown here in Methodology chapter, and in the results part, there will be only listed which exact conditions were used for each calculation.

It must be noted that the author is not an educated heat transfer specialist for CFD simulations. This part of the research should be originally delivered by another institution, based on cooperation on this research topic. Due to their withdraw of this cooperation time range agreement, there was no other choice than perform this simulation by own power. It took several extra months of work, self-education, and many consultations with heat transfer simulation experts, namely, Pavel Zácha from CTU in Prague, Xuezhi Zhang and Yafeng Shu from IMP in Lanzhou, and Eric Olivas from LANL in Los Alamos.

Geometry

- 2D
- 3D

All simulated targets were cylindrical geometries, in the case that the proton beam geometry is approximated to be symmetrical, the heat transfer simulation may be performed in 2 dimensions. It has many positives and several negatives. The most important fact is that due to the symmetrical volume calculation, the required computation power is much lower and finally, it allows to rapidly increase the number of nodes (quality of mesh) and study its dependency on the quality of simulation (by residuals monitoring). The 2D simulation of LEAD target[55] can be typically calculated on an average personal computer in the range of a small number of hours (based on fine mesh quality). On the other hand, it does not calculate with real convection and the fluid does not flow through the whole target volume. It works as a mirror calculation - it calculates only the simulated piece of the target and it expects that the rest of the volume behaves equivalently. When there is an air gap between the cylinders of the target, it expects the cooling air flow only from the centre to radially more distant locations (see Fig. 3.18). .

[55]The video of the LEAD target 2D geometry creation by the author is available at YouTube, see https://youtu.be/npZvOPxPEkY

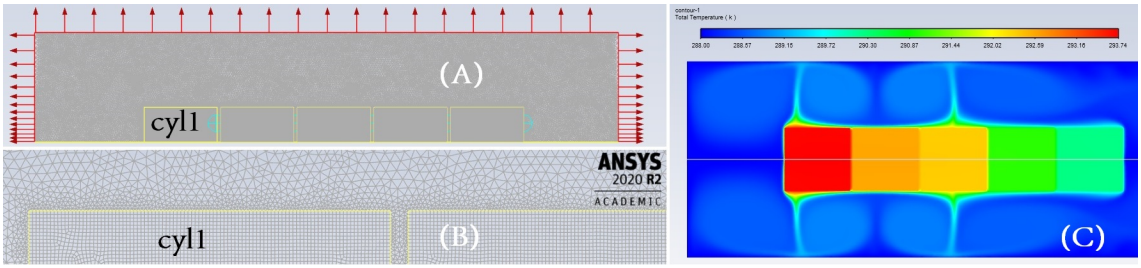

Figure 3.18: These figures describes 2D geometry simulation. The figure (A) shows all simulated cylinders surfaces (yellow) with full mesh (grey), temperature probes locations (cyan) and boundaries conditions (red). To show the mesh quality, there is a zoomed part of this figure below its, on figure (B). Finally, on the right side, see figure (C), the mirroring problem of the Fluent 2D rotating geometry calculation is shown. It includes gravity for calculation, however, only in the calculated piece of the target (calculated volume can be simply imagined as a piece of cake). On this figure is shown the results from CARBON target calculation by laminar viscous model and simplified boundary condition (wall having constant temperature). In the centre of the 2D is shown a line - it is the centre of the target, for 2D it is an axis of mirroring→the same as yellow bottom line in figure (A)→(in the 3D model, it is the rotation axis z).

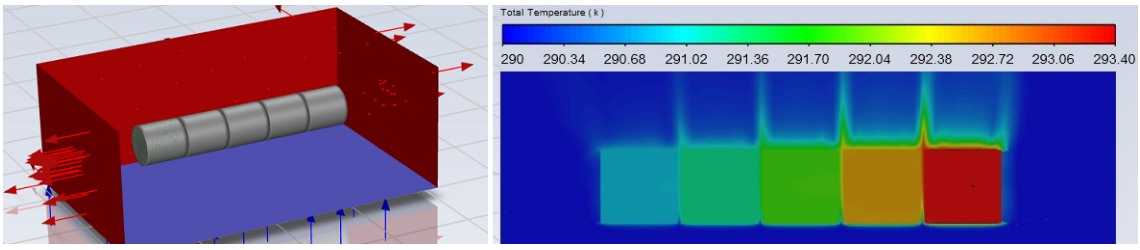

Figure 3.19: The 3 dimensional geometry shown with part of boundaries conditions on the left side. The yz plane in x=0 (centre) of the temperature calculation is shown on the right side. Problems described in previous Fig. 3.18 are not appearing for 3D simulation. The fluid cools the target in real conditions, so the highest temperature fluid goes up from the air gaps between cylinders. However, this simulation is still simplified. In this case, the operation conditions (density primarily) was not correctly set and it was calculated with down plane boundary „velocity inlet“ with value 2 mm·s^{-1}. It created constant movement of the fluid, however, it was only simplification. In latest simulation, only pressure outlet conditions were chosen with correctly estimated constants.

Heat source

- ▶ wall heat flux
  - constant
  - dynamic in time (definition by table)
- ▶ volume heat source
  - homogeneous heat source
    - ▷ constant
    - ▷ dynamic in time (definition by table)
  - inhomogeneous heat source
    - ▷ constant
    - ▷ dynamic in time
      - ○ symmetric
        → approximation curve
      - ○ asymmetric
        → MCNPX mesh mapping

The most easy way of heat source definition is the wall heat flux method. It is used when the wall of the simulated object is connected to some defined heat source which heats the simulated object. However, in the topic of this PhD research, all experimental objects have an internal volume heat source based on a number of heat production reactions and its quantity. The homogeneous heat source definition method was used in *Two cylinders experiment*, see Fig 4.12. Unfortunately, this easy method is not utilisable for other experiments. In the case of a stabilised beam continuously irradiating a target, for example, the CARBON target, the relative heat distribution released inside of the target looks like visualised on Fig. 5.33. It is asymmetrically distributed in the whole target volume. This 3D power heat distribution can be digitised by partitioning the whole volume into small cube cells (in the case of the previously mentioned figure, it is cube with 2 mm edge size), where each cell has a different value. Most usually, the heat source definition is realised by the power density [$W \cdot m^{-3}$]. Since the relative power density of each cube in this mesh is determined by MCNPX simulation (the CARBON target is described by about 4.7 million cubes) and it is finally inserted into ANSYS calculation. There are two ways of how to load these data into ANSYS. The most precise is the mapping of these values in ANSYS, or to approximate these data and describe by rotating equations as described in p.96 for the LEAD target or p.119 for the CARBON target.

Another problem is that the beam is not stabilised. The beam has several outages and moreover, when the beam is present, its current is variable (the beam current is usually shown on the right axis of each experimental data chart). As mentioned, the power is proportionally dependent on the beam current, so besides the 3D location variables (*x;y;z*), the time is the fourth variable for the power definition. It is specified by User Defined Function (UDF) file (programming language C) where the power source is defined. In the following text, the simulation setting and its problems are described.

Viscous model and boundary conditions

The most suitable[56] boundary condition for dealing with natural convection is „pressure outlet“. The fluid motion is generated due to the density difference in the fluid caused by temperature gradients. The pressure outlet boundary condition defines an outflow condition based on the flow pressure (P) at the outlet. The flow is usually described as laminar or turbulent where its transition is characterised by Reynolds number [120]. However, it does not work for natural convection, where the transition is more reliable described by Rayleigh number (Ra) [117].

$$Ra_{_L} = Gr_{_L} Pr = \frac{\beta g L^3 \Delta T}{\nu \alpha}, \tag{3.7}$$

where Prandtl number Pr=$\frac{\nu}{\alpha}$, ν-kinematic viscosity, α-thermal diffusivity (thermal conductivity divided by density and specific heat capacity at constant pressure), and Grashof number Gr_L=$\frac{\beta g L^3 \Delta T}{\nu^2}$, the upper part of the fraction $\beta g L^3 \Delta T$ is Bouyancy force, where β-thermal expansion coefficient, g-gravitational acceleration, L-characteristic length (based on calculated geometry), ΔT-maximum temperature deferential (ΔT=$|T_w - T_\infty|$, where T_w-wall temperature, and T_∞-temperature far from the wall). The index L describes laminar flow. The transition zone is pretty large from $Ra \approx 10^6 \rightarrow 10^{10}$, however, the critical value is expected to be $Ra_c \approx 10^9$, see [117]. Nevertheless, the Grashof is also used as a criterion for the transition to turbulence threshold. The Ra is always used for Nussel number Nu correlation. It means, it must be calculated every time when the heat transfer coefficient based on Nu required to be estimated. This topic is very complicated and too large to be widely discussed in this thesis, for more information see [120], beginning with p.364.

The energy and momentum equations are strongly coupled. The mesh quality can greatly affect the calculation accuracy, primarily on boundary layers, where the heat transfer is maximal. There is a coefficient y^+ (only for turbulent flow calculation) which is recommended to be smaller than 1 to ensure correct resolving of both - the momentum and thermal viscous sublayers. If y^+>1, the mesh should be refined. The author used adaption control directly in Fluent→ $Domain/Adapt/Refine/(method)$. It refines each cell which follows the chosen criteria into 2^3 parts (if cube 8 mm^3, after refine it is 8×1 mm^3, so the number of cells increases greatly in the chosen region. It allows to use the absolute y^+ value as criteria, so it can split marked cells until the $y^+ \leq 1$ if repeating the adaption command. If required to adapt the laminar flow mesh, other *Cell Register* criteria can be chosen such as *Boundary* or *Region*.

Based on the previously discussed laminar-turbulent theory, it is expected that the flow should be laminar for the discussed experiments. However, the result of the performed simulations was double in comparison with experiments. For this reason, the author tried to employ more advanced viscous models which calculate the flow conditions on its own based on an advanced algorithm. It is widely discussed in the subsection about Fluent tips and fails which located in appendix C.6 on p.165. Besides many of the standard errors in UDF, mistakes in geometry or meshing, and other common problems, there are several important tips for dealing with natural convection (even more importantly, for lower temperatures). If calculated with the fluid density defined by a compressible-ideal-gas, the operation density

[56]The author spent many time in finding the right information about natural convection simulation. It is very tricky to set the model right and moreover there are many setting which must be done to the model calculated right. The most important information has been found in lectures performed directly from ANSYS support, see [117] and the online lecture [118] or finally, in book [119].

must be enable (*Physics/Operation conditions/Variable-Density Parameters*). It must be estimated as accurate as possible, as well as the operating pressure (in the same window). Calculation examples and information about how to estimate the constants which dependent on the actual weather are described in mentioned Fluent fails appendix subsection. The last important tip for this kind of calculation is to change model for numerical discretisation for pressure (*Solution/Methods/Spatial Discretization/Pressure*) from *Second Order*, which can give rise to incorrect velocity near the wall, to *PRESTO!* or *Body Force Weighted*. For more information about these tips, see [117].

Simplified calculation - two horizontal cylinders irradiation (exp. No.*11-cyl.*)

This simulation was performed as the first calculation (easier simulation tools were used) with simplified conditions and some manual calculations. The thermal power of the cylinders has been calculated by MCNPX (partitioned tally calculation, see Fig. 4.7) and assign to the 3D CAD model. Between the cylinders, there was a thermal insulation (barrier), so the cylinders were not affecting each other by heat transfer. To simplify the problem, it was expected that the thermal power (proton beam) is consistent. All necessarily material heat constants were assigned based on data sheets or engineering tables. The most crucial task is to determine the heat transfer coefficient. This simulation was calculated in ANSYS Transient Thermal and convection coefficient was manually calculated based on the target geometry and surrounding conditions, and finally assigned to the cylinder partitioned volume.

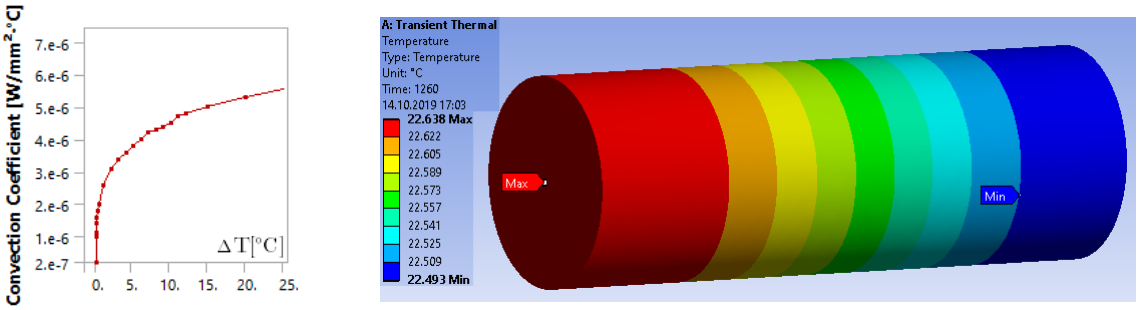

Figure 3.20: On the left side is shown the results of convection coefficient calculation for two uranium cylinders experiment. It was calculated by [121] for exact cylinders geometry. On the right side is shown the transient thermal simplified simulation results. For more information about this experiment and simulation, see p.70.

Dynamic simulation of cylindrical targets

Cylindrical targets (lead or carbon material) were simulated by the same technique. Due to its symmetrical geometry, many simplifications can be made without negative impact on the results accuracy. It is recommended to start with the most simple task with further improving step by step. For this reason, most of the earlier simulations were performed in 2D. The calculation is much quicker and it allows to analyse each change impact on the simulation accuracy. Only the CARBON target simulation will be described here due to the LEAD target being very similar, see differences in section 5. The simulation method of 3D is going to be roughly described in the following text, it is described widely for 2D and 3D in appendix section C.6.

For this thesis purpose, it is used a simplified 3D model without construction parts holding the target, without the wooden plane under the target. The volume of the fluid (surrounding air) is defined as a block with size $60 \times 60 \times 160$ cm^3 where the CARBON target is located directly in the centre, where centre of front carbon face is in position $(x_0; y_0; z_0)$ 0;0;0. Simulation of the LEAD target was simplified even more, because it was found that the heat is generated only in the first 6 cylinders. Based on the experimental measurements, there is no significant temperature change after the 8th cylinder. For these reasons, only 10 cylinders of the LEAD target were simulated in Fluent (fluid block definition is $50 \times 50 \times 850$ cm^3).

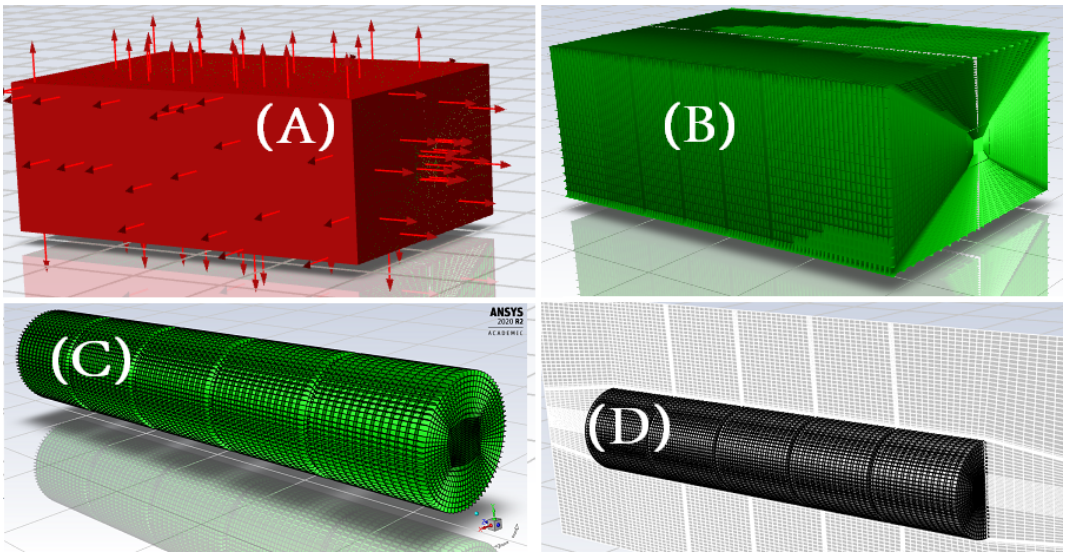

Figure 3.21: Fluent 3D geometry and mesh of the CARBON target. The figure (A) shows the boundaries of the fluid block of air. Figure (B) displays the fluid mesh surface and figure (C) the mesh surface of carbon cylinders (without fluid). Finally, the figure (D) shows the both meshes - carbon surface and the fluid by yz plane. The cells of the fluid closed to solid are fine due to higher accuracy needed close to interfaces.

The wall of the cylinders must be coupled by solid-fluid interface. When the interface is created, each wall is doubled and one side represents the solid, the second (labelled as *:shadow*) represents fluid. The fluid density is set as incompressible ideal gas with specified operation conditions density $\rho_0 = \frac{M \cdot p}{R \cdot T}$, where M-molar mass (kg·mol^{-1}), p-barometric pressure (Pa), R-ideal gas constant (J·mol^{-1}·K^{-1}), T-absolute temperature (K). The heat transfer is highly depended on the surrounding air conditions. It is influenced also by weather, especially its barometric pressure, temperature, humidity, and sun shining conditions, because of the windows in the upper part of the experimental hall. The operating conditions must be set as accurately as possible. The humidity must be included in the operating density and specific heat capacity. Moreover, the temperature of the air is slightly changing during experiment. Due to the experiment being long-lasting (5.5 hours), and situated in afternoon, the outside temperature may decrease about 10 °C, from shining day to dark. It influences the temperature inside of the experimental hall.

The heat source is defined in UDF file by several equations which describe the volume relative power distribution. Due to simplifications, it is expected that the heat source is symmetrical (rotating by axis z). Its calculation and approximation are in detail described in section 5.2.3 for the CARBON and section 5.1.3 for the LEAD target. These approximations were verified by several calculations in Python (including 2D visualisation) and it suited well. However, after implementation into Fluent, it does not fit as well as expected. It is probably caused by the mesh cell size. The advanced mapping option would be more suitable, however, coarse mesh would be more suitable due to the operating data file size.

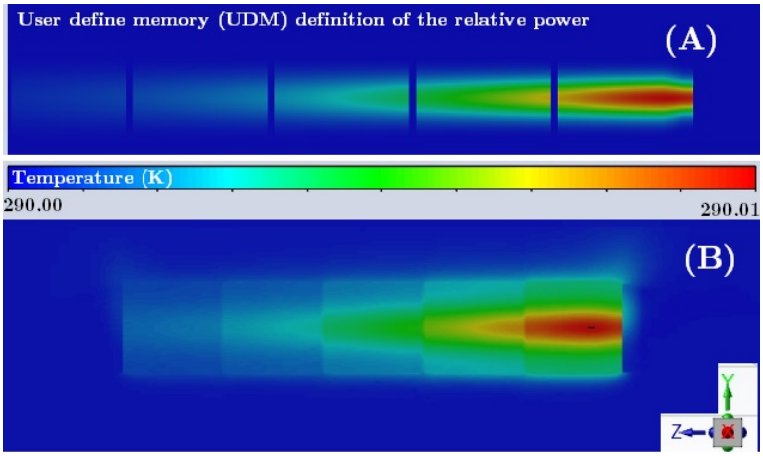

Figure 3.22: Visualisation of the power source in Fluent, figure (A), for the CARBON target simulation. The units are relative, the figure is shown for purpose to describe only relative distribution. The lower figure (B) shows absolute temperature distribution after 33 s of irradiation. The temperature changes are very small so only min and max are displayed.

3.2 Neutron leakage monitoring by ΔT measurement

The second topic of the experimental research is aimed at the neutron flux monitoring by the heating fission sample measurement. This method was invented during the first 2 years of experimental research in Dubna. Various materials in the shape of foils with thickness in range of μm→mm were irradiated with several types of thermal insulation. Invented probes were tested inside of the target, as well as outside. Finally, there were carried out 2 main experiments of neutron leakage monitoring by special temperature probes (see more in chapter 4). The following subsections summary the probe manufacturing, simulations, and finally experimental measurement methodology.

3.2.1 Preparing of the samples and relative temperature measurement

The main idea dealt with the temperature differences measured between the thermally insulated fission sample and its outer insulation. The most optimistic idea was based on the relative neutron flux determination of the leaking neutrons from the target. Thermocouples were flattened to have better contact with the measuring sample. The material of the measured sample was mostly natural uranium, enriched uranium, or thorium. The invented probes consist of the thermocouple inside of the sandwich of two covered thick foils (usually 1.0 - 1.2 mm), surrounded by insulation foam and reflective aluminium tape. The probes are illustrated in the following Fig. 3.23, left-side model visualisation and the real probe on the right side.

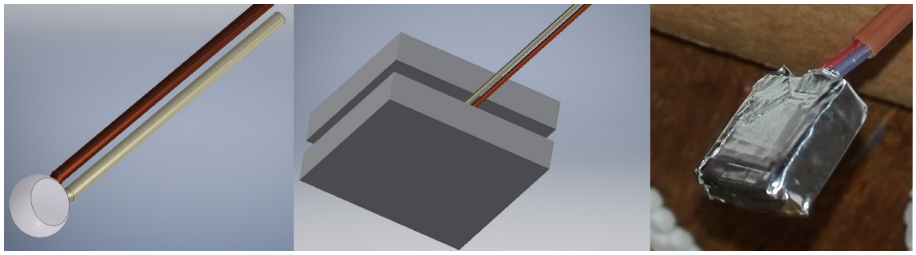

Figure 3.23: Neutron leakage heating probes based on ΔT measurement.

Probes were tested also inside of the target but unfortunately, the heat generation of the target overshadowed the probe heat contribution. Nevertheless, it was mostly used for neutron leakage monitoring outside of the target. Probes were inserted inside of the polystyrene block (about 10×10×10 cm^3) by reason to increase therm insulation. Besides the neutron heating probes, there were placed also blank probes of the same geometry and different material (tungsten or tantalum), for relative comparison. These materials were chosen for the blank sample due to similar material properties as the main probe, but negligible heating by neutron reactions. The fission sample heating (main probe) was expected to be in the order of joule. Temperature inside of the therm insulation was in order of mK. For this reason, the most important task was to increase the measurement sensitivity up to the highest possible range. Thermocouples with the highest gain were chosen, connected to the same CJC of the most accurate NI9212 card. The blank sample was used as a reference, so by comparing the fission probe with the blank one, the offset

error and CJC error were neglected. The only one variable of the measurement is the difference of the *Relative voltage gain*.

There was a special experimental measurement of n leakage (to confirm the expectation and simulation). The cylinder of $^{\text{nat}}$U (the same one which the QUINTA consist of, see Fig. 2.8) was used outside for monitoring the neutron leakage. Two of these cylinders, each with ^{nat}U mass about 1.68 kg, were symmetrically fixed in upper part (1×left-side & 1×right-side) of the third QUINTA section (see Fig. 3.26), located inside of the therm insulated chamber (see Fig. 3.24). Before the experiments, the cylinders are equipped with thermocouples in four locations. The temperature of the insulation and the contact between the chamber and target was measured as well.

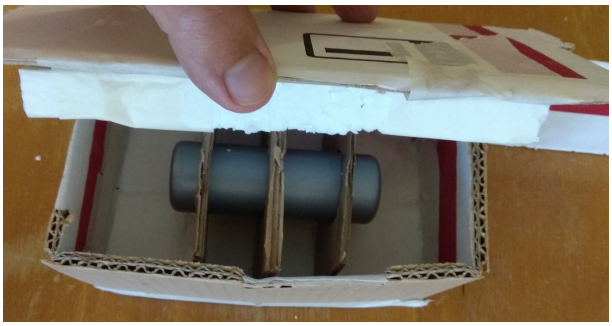

Figure 3.24: Therm insulated side box for uranium cylinder leakage monitoring.

Besides the neutron leakage monitoring, the proton beam has been studied by similar measuring probes as well. The probes with various sample thickness were insulated by a polystyrene block of dimension 3×3×5 cm^3 and fixed in the proton beam axis. It was a very reliable sensor of the proton occurrence, and actually, it relatively reflected the intensity. The timestamp of the start/end/outage was usually monitored only by the Phasotron staff with utilisation of ionisation chambers, where the accuracy is not sufficient (sampling frequency 1/30 Hz). Thermocouple measurement is very accurate, it responds with delay < 1 s. The direct measuring of the beam is in principle the real-time measurement. The experiment setup photograph of this method is shown in Fig. 3.25.

Figure 3.25: Proton beam online monitoring by proton reactions heating probes.

3.2.2 Neutron leakage simulation by MCNPX

The heating of neutron leakage probes were also simulated in MCNPX 2.7.0. to determine the heat generation per each probe. These experiments were carried out predominantly with the QUINTA target. Due to very small probes ($1\times1\times0.2$ cm^3) the single mesh as described in 3.6 was not possible to be calculated. Reasonable size of the fission probe mesh should be at least a cube cell with edge 1 mm. If calculate such a smooth mesh, the binary *mdata* file with size higher than approximately 200 MB cannot be converted by *GRIDCONV* due to memory limitation or some kind of overflow. Another complication is a tiny detector volume which interact with leaking neutrons in radial distance from the target centre about 40 cm. The neutron leakage flux decreases quadratically with radial distance. For this reason it needs to be calculated by much more generation (source histories)[57].
In this case, the mesh must be calculated by a different method. Only certain cuts (cross-sections) are chosen for the calculation, which rapidly decrease the number of cells and so the file size. For example, lets have the following problem - model of experiment No. 11 is displayed on Fig. 3.26 and Fig. 3.27.

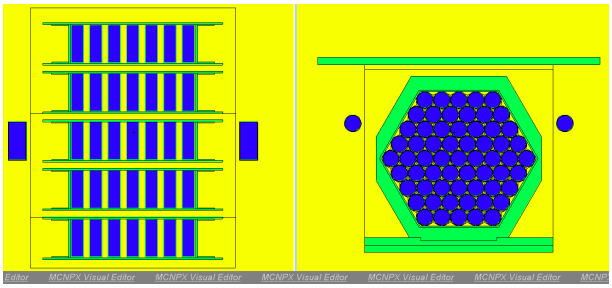

Figure 3.26: Neutron leakage monitoring by sides located ^{nat}U heating cylinders visualised by MCNPX Visual Editor [114]. The uranium cylinders are represented by blue colour, the surrounded air by yellow colour and aluminium plates by green colour. The reason of thicker hexagonal plate around the TA QUINTA cylinders is that the cut goes through the edge of hexagonal plate edge connected with front and back side of each section (see blue hexagonal plate edge in Fig. 2.9).

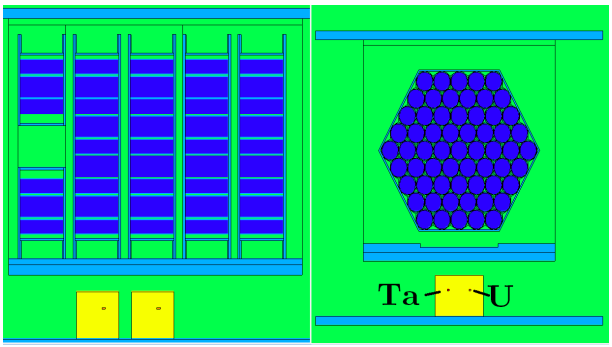

Figure 3.27: Neutron leakage monitoring by fission heating probes under the sections. The air is represented by green colour, the uranium cylinders by blue colour, the Al by light-blue colour, polystyrene by yellow colour, uranium probe for n leakage monitoring by orange colour and finally, the tantalum blank probe by red colour.

[57] By the number of generation is meant the total number of the incident particles (source) which are simulated (and tracked). So if the simulation calculates 1e7 generation, it means that 10 million of protons are transported from source and its reactions are tracked.

To perform the mesh of the certain cross section (required plane), an individual mesh must be called. In the following code is shown several variants of the certain mesh cut.

```
tmesh
 rmesh3 total
 cora3  − 18.1 180i 18.1
 corb3  − 18.1 180i 18.1
 corc3  5.6 5.8
 rmesh13 total
 cora13  − 18.1 180i 18.1
 corb13  − 18.1 180i 18.1
 corc13  18.7 18.9
 rmesh23 total
 cora23  − 25.1 250i 25.1
 corb23  − 25.1 250i 25.1
 corc23  31.8 32
 rmesh33 total
 cora33  − 18.1 180i 18.1
 corb33  − 18.1 180i 18.1
 corc33  44.9 45.1
 rmesh43 total
 cora43  − 18.1 180i 18.1
 corb43  − 18.1 180i 18.1
 corc43  58.0 58.2
 rmesh53 total
 cora53  − 18.1 180i 18.1
 corb53  − 0.1 0.1
 corc53  − 0.1 320i 64.1
 rmesh63 total
 cora63  − 25.1 250i 25.1
 corb63  7.4 7.6
 corc63   − 0.1 320i 64.1
 rmesh73 total
 cora73  − 5.1 100i 5.1
 corb73  − 25.27  − 25.17
 corc73  13.95 100i 24.05
 rmesh83 total
 cora83  − 5.1 100i 5.1
 corb83  − 25.27  − 25.17
 corc83  26.95 100i 37.05
endmd
```

The first five meshes (No. 3, 13, 23, 33, 43) are *xy* cross-sections, the rest one are cuts in the plane xz. Central target cut is performed by rmesh53 and central cut of side cylinders (neutron leakage monitoring) by rmesh63. The last two meshes deal with a central cut of fission probes located in a polystyrene. The cell coarseness is adapted to the geometry based on the expected size of the observed volume.

3.2.3 Gamma-ray spectrometry utilisation

This method was used mostly for the determination of the integral number of incident photons (widely described in following chapter 3.3). However, it was also partly used to estimate the number of fission reactions of the heating probe samples (Fig. 3.23). These samples were measured on High Purity Germanium detector (HPGe) at the YaSNaPP laboratory immediately after the experiment ends (with some delay caused by transportation). Uranium sample was safely extracted from the probe, fixed on the plastic plate, and measured by an HPGe detector. Based on the research of the uranium fission fraction and its half-life, the isotope expected to be measured has been listed and identified during the measurement. The duration of the measurement was dependent on the activity of the identified isotope, to ensure the Gaussian function integral having more than 10,000 counts, or the peak channel has more than 3,000 counts. This condition ensures the statistic error of Gaussian fit is below 1 %. Fission fragment research was carried out based on database [54] and [122], all the fission fragments of fast neutron spectrum are shown in Fig. 3.28, the selected measurable are listed in Tab. 3.3.
Gamma-ray spectrometry method is in detail described in the theses of the previous PhD researchers at JINR ADS group, primarily K. Katovský [52] and L. Závorka [49].

Table 3.3: Selected isotopes for the number of fission calculation.

Isotope	Energy [keV]	Half-life [h]
^{97}Zr	507.64	16.91
^{99}Mo	739.50	65.94
^{103}Ru	497.08	39.26
^{131}I	364.49	8.02
^{131}I	503.00	8.02
^{131}I	636.99	8.02
^{133}I	529.87	20.80
^{133}I	706.58	20.80
^{140}Ba	304.85	12.75
^{140}Ba	423.72	12.75
^{140}Ba	537.26	12.75
^{140}LaD	432.49	12.75
^{143}Ce	490.37	33.04
^{143}Ce	721.93	33.04
^{147}Nd	439.90	10.98

Figure 3.28: YASNAPP laboratory.

3.3 Proton beam monitoring

The proton beam monitoring task is a kind of challenging. It needs to be estimated as accurately as possible, because the heat generation is directly depended on the number of interacting protons. The shape of the proton beam and its centre are crucial for MCNPX simulation. It is a kind of complex problem which has been widely discussed in the thesis of A. Krása [46], or in the paper of W. Furman [123]. Both mentioned works were dealing with the Nuclotron accelerator facility, where usually other particles accelerated (such as deuterons or some light nucleuses). This work was completely performed at the Phasotron accelerator facility with proton beam irradiation. For this reason, the proton beam monitoring at this facility will be shortly discussed in the following paragraphs.

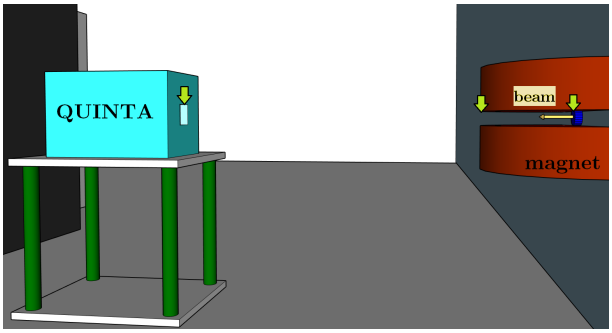

Figure 3.29: Visualisation of the proton beam extraction (yellow arrow) from the accelerator vacuum pipeline (blue - right). The beam setup is provided by several of magnets (light brown) and the beam is pointed into the centre of the QUINTA (light blue) entrance window, or other targets centre. There are three green shaded arrows with black contour, which pointed to the location of the proton beam monitors (activation foil technique and ionisation chambers).

There are two methods of proton beam monitoring plus one method for the controlling purpose. The first (online) method, the active one, uses ionisation chambers and deals with the beam geometry characteristics measurement. It is provided by accelerator operators and it is also used for the beam shape and position monitoring. The chambers are monitoring the beam centre location[58] $(x_0; y_0)$, *FWHM* (Full width at half maximum of Gaussian function) and *SUM* (it represents a relative proton flux in time) - each variable is described in both axis $(x; y)$. These values are recorded with an average frequency of 0.06 Hz, so the measurement is performed once per 17 s. The total numbers of *FWHM*, SUM and $(x_0; y_0)$ are statistically evaluated after the end of irradiation. These values are used in further for all simulations.

The second method uses the activation foil method (offline technique). The resulting isotopes in the activation foil are evaluated by gamma-ray spectrometry method. Two foil materials are used with an area of 100×100 mm^2. Several layers of aluminium foil (isotope ^{27}Al) with total mass around 6 g are usually involved. The same geometry of natural copper foil is used with a mass usually around 9 g (^{nat}Cu consist of 69.17% ^{63}Cu and 30.83%

[58] There must be mentioned the fact that based on the research of A. Baldin's group (LHE, JINR), the ionisation chambers are the most precise if the beam is located in the centre of the chamber. For this reason, the centre of the chamber was shifted to the position (1.4;0) [cm] for the QUINTA experiments, due to QUINTA rotation for 2° (widely discussed in p.45).

of ^{65}Cu). Activation foil monitors are usually located at three positions (represented by green arrows in Fig. 3.29). After the irradiation, these monitors are taken away and the reaction products are measured. Duration of the measurement on HPGe detector is usually based on the foil activation and the searched isotope characteristics. The goal is to load the gamma spectrum with good statistics for certain gamma peaks. Usually, about four or five measurements are involved and the last measurement is usually performed about a week after the experiment day. In case of aluminium foil, the reaction ^{27}Al(p,3pn)^{24}Na is observed. The reaction cross-section used for the number of proton evaluation is 10.8±0.1 mb, based on [124]. In the case of copper foil, almost 20 isotopes are routinely evaluated. Their cross-section is tabled in Tab.3.1. of A. Krása doctoral thesis [46]. For more information see [49] (English), or [52] (Czech).

Finally, the controlling part of the proton beam setting. It is performed by an empty polaroid photograph which is installed in the centre, where the beam is required. This photograph contains a cross $(x; y)$ axis with a scale. It is irradiated by several bunches of protons by reason of the fine visualisation of the proton beam real location (it is more accurate than ionisation chambers). Nevertheless, it is an analogue technique which accuracy is highly dependent on the photograph installation precision.

3.3.1 Proton beam current calculation

All other colleagues of the ADS research group typically need only the total number of protons N_p [-] when using activation foil techniques. They usually relate the results per incident particle. In the case of this thesis, the proton current must be calculated per each interval of the ionisation chamber measurement, due to the heat deposition is dynamic in time. It is evaluated based on a combination of both previously mentioned proton beam monitoring techniques. Since the total number of protons N_p is evaluated by gamma-ray spectrometry method, the relative dynamic beam intensity is calculated during the time portion (during measured 17 s intervals) by using SUM_x and SUM_y. Therefore, the total integral of protons is partitioned into time portions in which the ionisation chamber estimates the intensity. The chart of dynamic values of $FWHM$, SUM and the centre location is shown in Fig. D.7. The time portions are not equal, so the relative intensity per time portion is weighted by the time of this portion. Finally, the number of protons in the time portion is divided per total time of each time portion. The result is the number of incident protons per each second of irradiation. In the last step, it is converted to the proton beam current by multiplying by the proton charge. The current unit [nA] was chosen for this thesis purpose due to the relatively low proton beam current.

Chapter 4

Experimental research and simulation of TA QUINTA

This chapter deals with the description of the performed experiments, its measurement, simulation, and finally, a discussion about the reached results. Each experiment has a unique number assigned according to the order of irradiation[59]. This number is shown in the first column of the Tab. 3.1, where all experiments are listed, including the irradiation time, timestamp, and an integral number of protons. Only those experiments connected with the PhD thesis topic are discussed in the following paragraphs.

This chapter is divided into three parts. Each section is divided into several subsections with experimental research, simulation part, and finally the result discussion. The first section deals with a special (detail) experiment. The two ^{nat}U cylinders which TA QUINTA consists of, were irradiated in a horizontal position along the axis z by protons. It is essential for understanding the whole QUINTA target behaviour during the irradiation process. In a further section, the most critical experiments of QUINTA are discussed, primarily focused on the target total heat generation. This section contains many subsections to describe various setups (measurement with or without shielding) and techniques of measurement. The last section deals with neutron leakage monitoring, which measured by the invented fission heating probes. Neutrons were monitored by this technique at various positions outside of the QUINTA.

The QUINTA target summary

The TA QUINTA consists of 298 ^{nat}U cylinders, each with a mass of about 1.72 kg, being grouped in five sections of hexagonal geometry. It is described in detail in sub-chapter 2.3.2, and it is visualised by the accurate model in Fig. 2.9 and simplified model in Fig. 2.10. During most of the experiments, the QUINTA has been shielded by 10 cm thick Pb shielding, which unfortunately disabled sufficient access to the target. There were two possible accesses - vertical from the top of the QUINTA and horizontal from the left side of the target, as shown in Fig. 4.1.
There are six narrow upper entrances, each of dimensions about 17×120 mm^2. Each entrance is shielded by a thick lead plug. Under each of these plugs, there is a sliding aluminium plate holder designed for experimental sample irradiation requirements. These

[59]The format of the experiment labelling is e.g. *exp11* for experiment No. 11.

plugs are located between each section and in front of the first and back-side of the last section. The second access from the left side, which allows inserting an aluminium plate holder with samples horizontally across the target, has never been used for TC measurement.

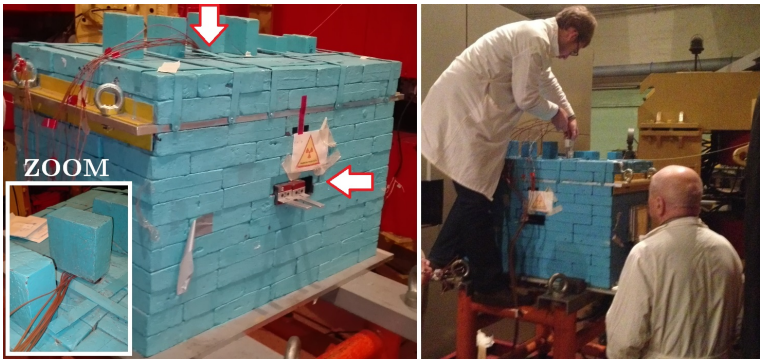

Figure 4.1: Entrances into the QUINTA target through the lead shielding are marked by white arrows. The zoom of the lead plugs and TC entrance into the target is shown on the left side. The preparation process is shown on the right side. The author is fixing there the TC inside of the QUINTA with help of Dr. J. Adam, supervisor specialist.

It was very complicated to perform experiments through the lead shielding due to the discussed narrow spaces. For this reason, it was not possible to measure all required data under these conditions reliably, especially to ensure a high-quality contact between TC and the target. Nevertheless, several measurements were performed during the colleague's experiment and finally, one experiment primarily focused on TC measurement was accomplished under these unpleasant conditions. Later, there was a possibility to perform a unique QUINTA experiment without lead shielding. Of course, it could be accomplished only under respecting strict radiation safety conditions. This experiment brought required data which in detail described the QUINTA thermal behaviour during irradiation and its responding to proton beam outage or current changes.

In short, there were two main goals of the QUINTA experiments. The first one deals with measuring the heat generation inside of the target. The second one was aimed at the experimental determination of the relative neutron flux inside and so outside (*n leakage*) of the target, by the fission probe method - ΔT measurement.

The whole experimental research started with the early first pilot experiment with the QUINTA target irradiation. It was measured by old and poorly insulated thermocouples type K with relatively low accurate electronics during November 2015. The TC measured the heat generation of the Th^{232} fission inserted inside of the QUINTA target, the backside of the 3^{rd} section. The first was located in the centre of the beam, the second one about 120 mm lower (location x=0, y=-120 mm). The fission probes were very similar to the described one in Fig. 3.23, however, without quality insulation. These thorium samples reached the temperature difference ΔT=4.5 °C during 4 hours of irradiation by 660 MeV protons ($N_p \approx 3.35 \cdot 10^{15}$). The lower positioned sample reached roughly 4.2 °C. The insulation of the measured samples was inferior. This experiment was a kind of the first survey for future needs.

4.1 Detail study of two natural uranium cylinders

It is essential to fully understand the heating process inside of the QUINTA target geometry. For this reason, a detailed heat generation study of its cylinders must be carried out. There was performed a very short experiment (20 min) where two cylinders, identical to those the QUINTA consisted of, were irradiated and measured by TC. Each cylinder contains 1 679 g of natural uranium covered by 46 g of aluminium cladding[60]. These cylinders were situated horizontally in the axis of the proton beam (axis z) with about 3 cm additional air gap between them (Fig. 4.2). This gap was equipped with cardboard insulation to ensure minimal heat transfer between them. There were fixed 13 thermocouples on the surface of the cylinder. The foil samples of ^{nat}U, Pb, and Al were installed for monitoring of the beam flux along with the cylinders (shown in Fig. 4.3). These foils were evaluated by the gamma-ray spectrometry method.

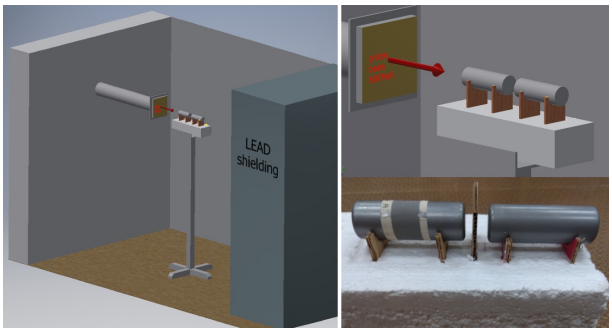

Figure 4.2: Two cylinders experimental setup model and real photo.

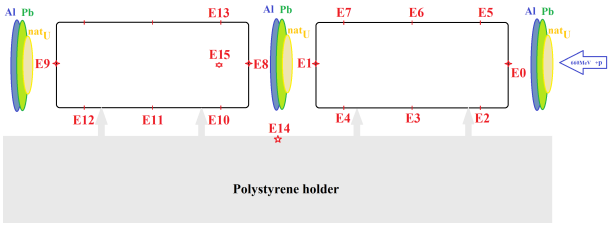

Figure 4.3: Sketch of the two ^{nat}U cylinders experiment setup with measuring positions.

The thermocouples were fixed on the surface at several positions. Thermocouples positions E2, E3, E4 and E10, E11, E12 were chosen for comparing purposes. To ensure a clear understanding of the position, they are labelled based on their distance from each front side of each cylinder, so equivalently it is 1st 1 cm, 1st 5 cm, 1st 9 cm and 2nd 1 cm, 2nd 5 cm, 2nd 9 cm respectively. This short experiment is the first part of *exp11*, therefore it will be labelled as *exp11-01*. The integral number of protons interacting with the volume of the cylinder was determined by gamma-ray spectrometry using an Al monitor (blue foil in Fig. 4.3) to be[61] $N_p \approx$ 1.17E+14.

[60] For more information about the cylinders and QUINTA geometry, see p.24.

[61] The uncertainty is expected to be $< 15\%$. The diameter of the Al monitor was equivalent to the cylinder.

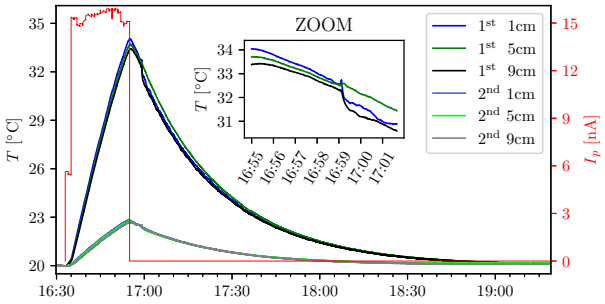

Figure 4.4: The two cylinders experimental data measured by TC, including cooling. In the upper central part is shown zoomed version of the experiment end (16:55) with further cylinders cooling. A little bit later (16:59) there is shown suddenly drop of the measured temperature caused by relocation of the target. It has happened just before the second part of *exp11* was started. If this drop is omitted, the temperature of the cylinders is slowly decreasing to the surrounded air temperature.

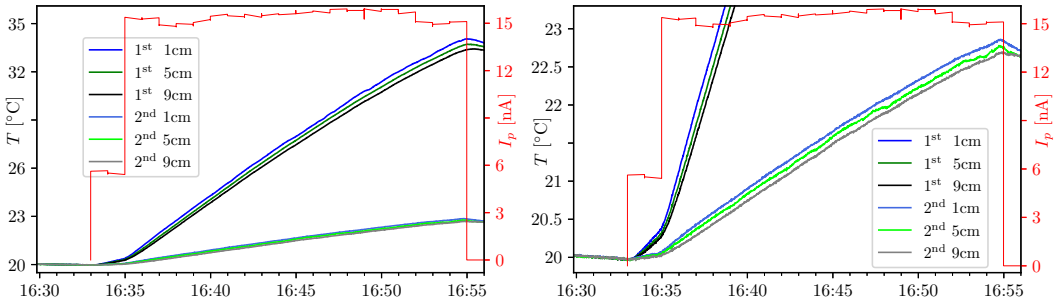

Figure 4.5: The two cylinders experiment results of the temperature measurement by TC located at the bottom part of the surface. On the right side is a zoomed version of the second cylinder. Positions are equivalent to E2,E3,E4 and E10,E11,E12 TC positions (Fig. 4.3).

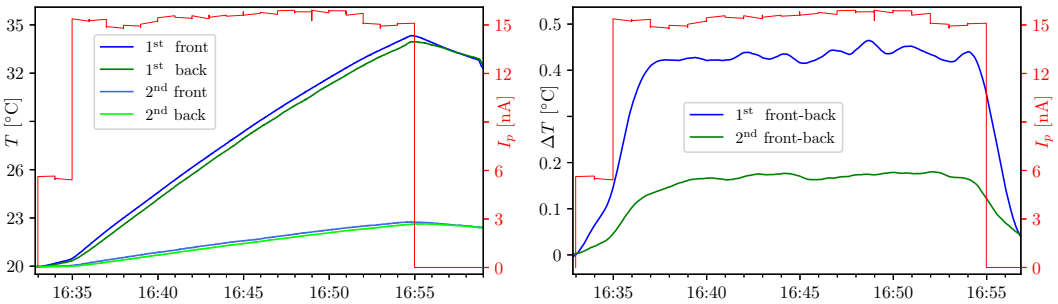

Figure 4.6: The two cylinders experimental result of the temperature measurement by TC on the front-side and back-side of each cylinder. On the right side is shown the temperature difference between each cylinder front and back sides. Positions are equivalent to E0, E1 and E8, E9 as labelled on Fig. 4.3.

The contact between the TC and the cylinder surface was not faultless, due to missing any force to press the TC to the surface. The TC fixing was carried out by plastic tape without additional insulation. It would be better to choose a more advanced approach of measurement, unfortunately, due to the very limited preparation time[62], there was no room for testing the quality of the TC contact.

[62]The decision to perform this experiment was made in less than an hour before the beam-time.

4.1.1 Simulation of two cylinders experiment by MCNPX

The heat deposition simulation was performed by MCNPX 2.7.0. Its results are used in ANSYS Transient Thermal [116] calculation for the power distribution definition. For this purpose, the experiment is simplified and the cylinders are partitioned into three symmetrical parts where the volume heat deposition is calculated (as a homogeneous distribution). The proton intensity was estimated by aluminium monitors with identical area shape as the cylinder (circular area with D=36 mm). Besides the volume tally heat deposition, the mesh heat deposition was calculated as well with a cell size of 1 mm. It is possible to figure out the power distribution function *P(x,y,z)* and use it for more precise Fluent simulation (more on p.96). It has been decided that the accuracy of the „partitioning“ method is sufficient for this simplified calculation. The uranium volume of each cylinder was virtually partitioned into three symmetrical parts, see Fig. 4.7.

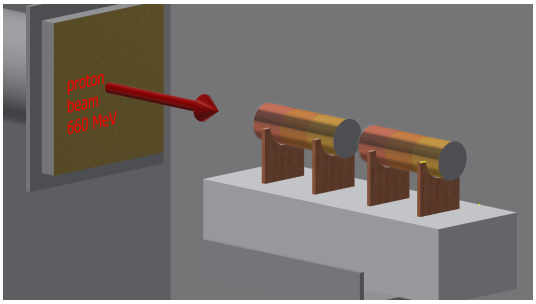

Figure 4.7: Two cylinders experiment with virtually partitioned ^{nat}U volume. The uranium is fully covered by an aluminium cladding (visualised as transparent for better clarity).

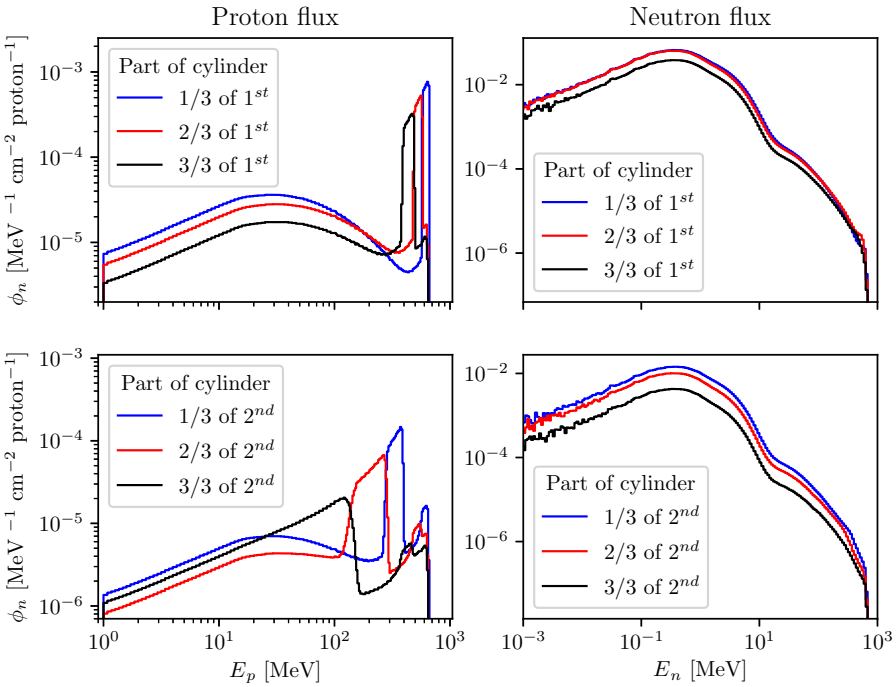

Figure 4.8: The neutron and proton relative flux calculated by MCNPX simulation for *exp11-01*. It shows spectra of n and p fluxes per each of the partitioned volume. The proton flux is decreasing, its energy spectrum is describing the ionisation looses (primarily). The neutron flux is decreasing as well, but the energy spectrum is similar.

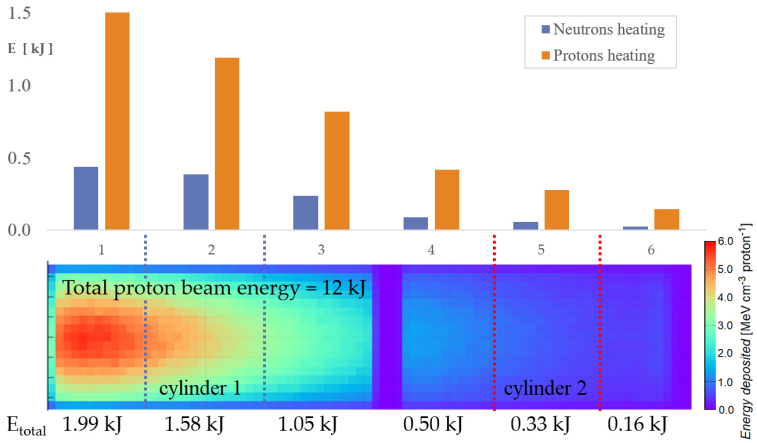

Figure 4.9: Heat deposition of two cylinders experiment, each cylinder partitioned into three parts and simulated in MCNPX. Tallies were separately calculated for protons and neutrons. In this case there were no other particles taken into account, only protons and neutrons. The most of heat is generated by proton reactions. The reason for such a smaller contribution of the neutron fission is mostly its leakage. The diameter is merely 36 mm, the most of neutrons escape. Contribution of relative neutron heat deposition relates to the proton heat deposition is 28, 32, 29, 21, 20 and 17 %, respectively from the first cylindrical part.

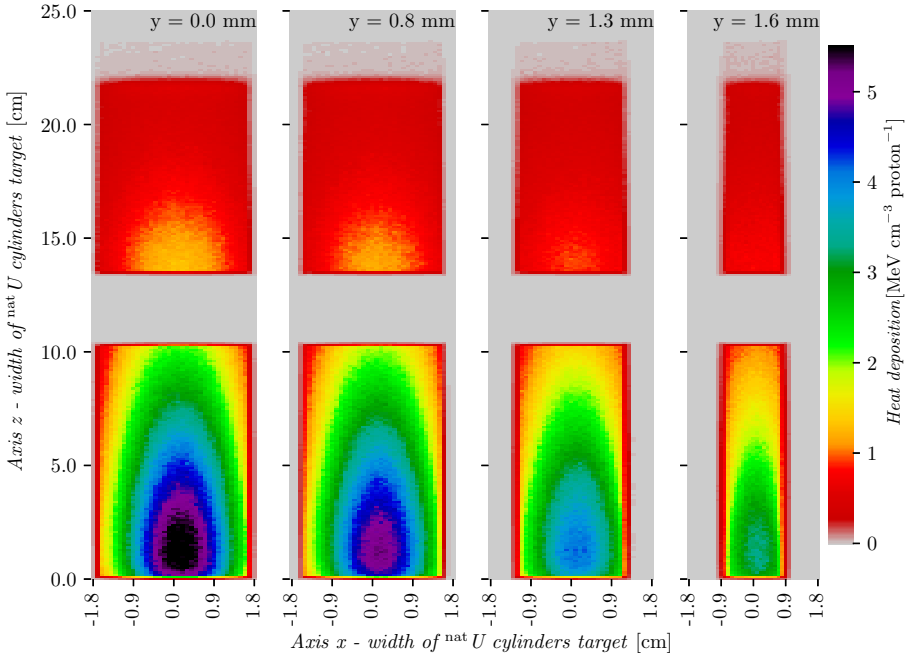

Figure 4.10: Two cylinders experiment - relative heat deposition simulation in MCNPX (mesh) for selected xz planes. Each heatmap figure has an identical colour bar (see the most right part), the maximum of this bar is 5.5 MeV·cm^{-3}·proton^{-1}. The height of the volume cut (axis y for xz plane) is displayed on top of each plot.

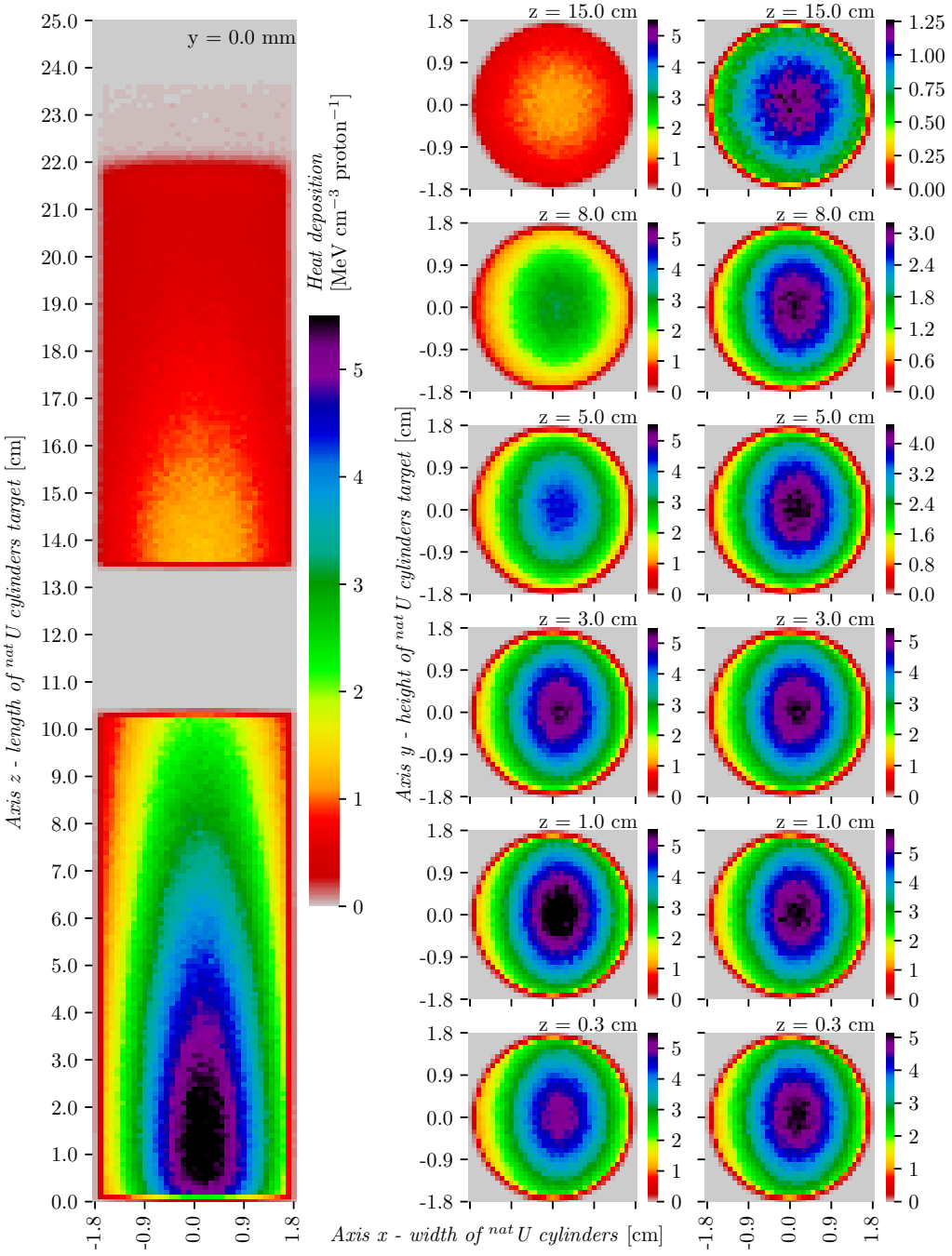

Figure 4.11: Two cylinders experiment - relative heat deposition simulated by MCNPX. On the left side, there is shown the *xz* heatmap mesh plane in the centre of both ^{nat}U cylinders (y=0 mm). In the centre part of the figure, there are displayed the *xy* cross-sections in length z specified above each plot. The heatmap colour bar of centre charts is identical with the left *xz* plane, having the maximum at 5.5 MeV·cm^{-3}·proton^{-1}. The most right column shows the same planes as the middle one, but each figure there has a modified heatmap colour bar. The black colour here represents the maximal value of each heatmap. This visualisation was chosen as the most sophisticated heat deposition description with sufficient resolution.

4.1.2 The heat transfer simulation of the two cylinders experiment

Since the relative heat deposition calculated by MCNPX, the total heat generation can be calculated. The thermal power function is variable in time according to the proton beam current. If the MCNPX rel. heat deposition is multiplied by the function of the proton beam current in time, the result is the cylinder heat deposition. The proton beam is more or less constant, as shown in Fig. 4.5 on the right axis y (red). To simplify this problem, average values were used. If multiply the volume heat deposition tally by the average proton beam current, the thermal power of the calculated volume is obtained.

Table 4.1: Results of the thermal power calculation P [W] and the power density P_{rel} [W·mm^{-3}], based on MCNPX simulation for virtually partitioned cylinders of *exp11-01*.

Cyl. part	P [W]	ΔP [W]	P_{rel} [W·mm^{-3}]	ΔP_{rel} [W·mm^{-3}]
1/3 1st	1.55	0.02	5.10E-05	6.41E-07
2/3 1st	1.23	0.02	4.04E-05	5.86E-07
3/3 1st	0.82	0.02	2.70E-05	7.91E-07
1/3 2nd	0.39	0.05	1.29E-05	1.58E-06
2/3 2nd	0.26	0.06	8.49E-06	1.89E-06
3/3 2nd	0.13	0.10	4.28E-06	3.27E-06

The temperature of the cylinder is calculated based on the constant thermal power density (constant beam current). The heat transfer by radiation was not included in this[63] calculation. The heat transfer by convection was simulated in ANSYS. The heat convection coefficient was calculated by [121] for this cylinder geometry, the result of this calculation is shown in Fig. 3.20. The results of the transient thermal analysis are shown in the following Fig. 4.12 and Fig. 4.13. Minimal and maximal temperatures are displayed in time at the bottom of these figures.

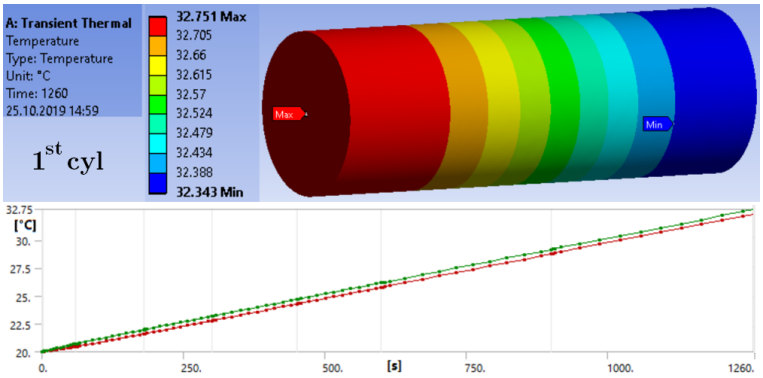

Figure 4.12: Two cylinders exp. - heat transfer simulation, T of the 1^{st} cylinder.

[63]This simplified calculation was performed by the author without any heat calculation background and without any deeper expertise or expert consultation. Other calculations were already simulated in cooperation with IMP Lanzhou, and CUT Prague, so these calculations are much more accurate. Author reached knowledge of heat transfer simulation by books [120] and [119] and e-learning courses [125].

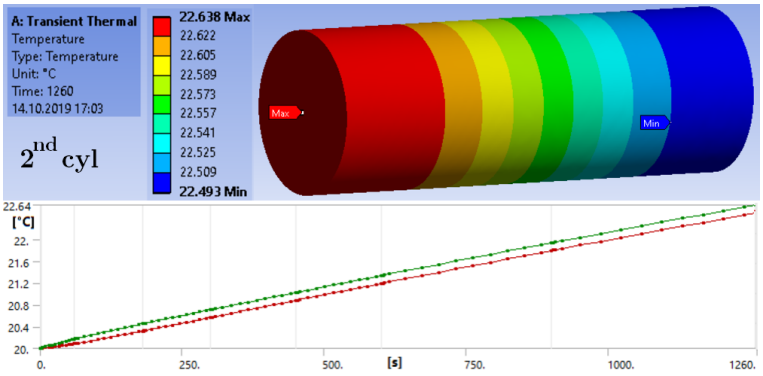

Figure 4.13: Two cylinders exp. - heat transfer simulation, T of the 2^{nd} cylinder.

4.1.3 Results discussion - two cylinders experiment

This experiment, which is originally the first part of exp11, was named as „*The two cylinders experiment*“ and labelled as *exp11-01*. Two cylinders, identical to those the TA QUINTA consisted of, were irradiated with 660 MeV protons for about 1260 s. The total number of incident protons on the cylindrical surface was determined by gamma-ray spectrometry of aluminium foil for $N_p = 1.17(10) \cdot 10^{14}$. It has been estimated by identification of ^{24}Na isotope (^{27}Al(p,x)^{24}Na reaction). There might be an error caused by the secondary particles reflection from the cylinder material. The sodium production may be caused by the photons reflection and chiefly neutrons, due to the ^{27}Al(n,α)^{24}Na reaction. Unfortunately, due to the copper foil absence and small target volume, it was not possible to estimate N_p more precisely, anyway, the uncertainty is expected to be better than 15 %.

The surface temperature of both cylinders was calculated by simplified ANSYS Transient Thermal simulation. The power density was calculated for three parts of each cylinder (see Fig. 4.2), so the ANSYS model was consisted of six similar volumes, each defined by a unique power density (constant).

To focus on the results of this experiment. The cylinders were mostly heated by ionisation loss and Coulomb collisions (elastic scattering) which caused the slowing down of the protons, by neutron fission reaction, and negligibly by gamma heating and pion reactions. The measured temperatures (experimental data) are compared with ANSYS+MCNPX simulation (see Fig. 4.5 and Fig. 4.12). The maximal measured front bottom temperature after 1260 s of irradiation (TC labelled as in Fig. 4.3) is $E2$=34.07(19) °C, back bottom is $E4$=33.51(19) °C, simulated data are E2$_{calc}$=33.17 °C and $E4_{calc}$=32.81 °C. To compare reference temperature (measured) with simulated one, $\Delta E2$=0.90(1) °C, $\Delta E4$=0.70(1) °C, so relatively $\delta E2$=6.4 %, $\delta E4$=5.2 %.
The front bottom temperature for the second cylinder in t_{irr}=1260 s is $E10$=22.77(8) °C, back bottom $E12$=22.56(8) °C, for simulation $E10_{calc}$=22.64 °C and $E12_{calc}$=22.49 °C. The error between these two methods is $\Delta E10$=0.21(1) °C, $\Delta E12$=0.21(1) °C, so relatively $\delta E10$=7.3 %, $\delta E12$=7.7 %.
The relative errors are calculated from the thermocouples measured range (the maximal measured temperature changes since the beginning of the experiment), because the temperature offset is set to surrounded temperature. The uncertainty is caused by several simplifications as described in previous paragraphs, but its accuracy is sufficient.

4.2 QUINTA target heat generation measurement

Two thermal experiments of the TA QUINTA irradiation are described here. The first one deals with the QUINTA surrounded by 10 cm of lead shielding and the second one was irradiated without shielding. Both experimental measurements are shown and discussed, although the MCNPX simulation was performed only for the version without shielding.

QUINTA with lead shielding

The QUINTA with lead shielding makes the measurement much complicated due to the narrow entrance. Special cardboard construction similar to the aluminium sample holder was created with polystyrene filling. It works as an insulation of thermocouples and primarily, it ensures a pressure between thermocouples and the QUINTA surface→better contact. The experiment was irradiated by several pulses with one long constant irradiation lasting more than four hours (Tab. 4.2).

Table 4.2: The TA QUINTA t_{irr} for *exp3*.

Plan		Real irradiation		
t_{irr}	Pause	Time of irr.		t_{irr}
[min]	[min]	start	end	[min]
5	5	17:18	17:25	7
5	5	17:35	17:40	5
10	10	17:49	17:58	9
10	10	18:08	18:18	10
250	10	18:28	22:42	254
10	10	22:54	23:04	10
10		23:14	23:24	10

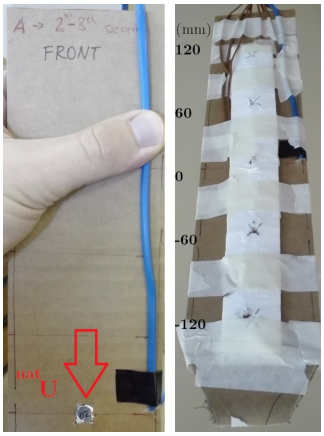

Figure 4.14: TC holder for *exp3*.

The special fissile thermal probe (similar with Fig. 3.23) was fixed in the centre of the created cardboard construction, in this case it was consisted by samples of natural uranium. It is highlighted by a red arrow in Fig 4.14 and by red-orange rectangles on the right side of Fig. 4.15. In Fig. 4.14 is shown the base construction of the TC holder (left), on the right side it is already equipped by TC with visible measuring positions +120 → -120 mm, the step between each position is 60 mm.

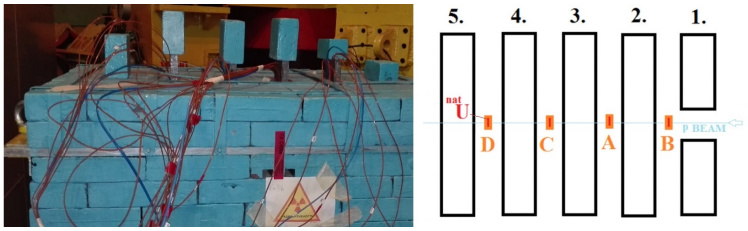

Figure 4.15: Photo of the *exp3* TC installation, and a sketch of the ^{nat}U probes location.

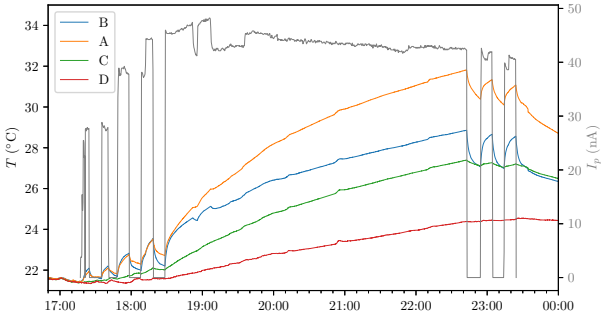

Figure 4.16: The TC measurement of the *exp3* - fissile thermal probes. Although the probes consist of fissile material, most of the heat is generated by direct proton reaction heating. It is caused by probes location just in the centre. The proton reaction heating is shown in Fig. 4.28, in principle, the relative heat deposition reflects the particle flux. Nevertheless, the probes in this figure are labelled as shown in Fig. 4.15. The probe B is located in the front of the 2$^{\text{nd}}$ section, so it is cooled by the air incoming from the beam window of the first section. For this reason, the highest temperature is reached between 2$^{\text{nd}}$ and 3$^{\text{rd}}$ section where the heat is better accumulated. Based on previous experiments and calculation, the highest neutron flux and the most proton collisions take place in the centre of 2$^{\text{nd}}$. It is not possible to partition the heat generated by the proton reaction from the neutron reaction generated. The only possibility is the changing of the probe location to the area where proton flux minor.

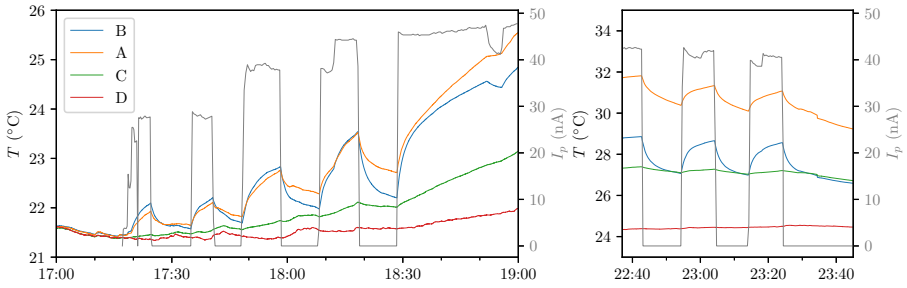

Figure 4.17: The TC measurement of the *exp3* - fissile thermal probes, zoomed. The probes B and A react very well on the proton beam occurrence, as shown by the 5 min or 10 min pulses irradiation. The temperature of probe C is smoothly increasing as well, but due to much lower proton and neutron flux, the temperature raising is primarily caused by heat transfer. Small changes of the proton beam (see time 18:52 where 15 % beam drop occurs) are very well and sharply measurable by B and A probes. As well as the beam current final decrease at 19:08 (Fig. 4.16). The C probe reacts on beam changes as well but much less significantly, due to much lower proton and neutron flux between 3$^{\text{rd}}$ and 4$^{\text{th}}$ section. There is shown on the right side, the last two 10 min pulses irradiation and its temperature response. The small temperature drop at time 23:35 is caused by picking the irradiated samples up. Basically, it is possible to rely on this measurement of the relative proton and neutron flux only in the case of higher fluxes (see Fig. 4.8 and Fig. 4.28). For measurement of lower fluxes, more sensitive probes must be used (see neutron leakage measurement - „The second method“, p.84).

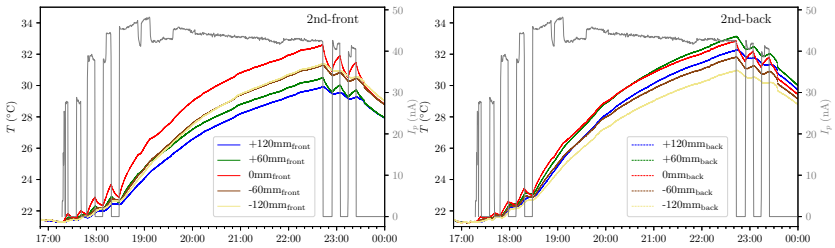

Figure 4.18: The TC measurement of the *exp3* - measuring of the front and back-side of the 2nd section. This figure is well displayed the temperature differences when passive cooling occurs. It is expected the most of the heat is released in the centre of the target. As the atmospheric air is flowing in the section by unforced (natural) convection, the upper part should be warmer than the part below. Globally this theory works well through the section, except the front of the 2nd section. Due to the first section beam window, the air is flowing not only from the lower parts to the upper one but also from the beam window. This phenomenon is well shown in this chart, on the left side where front 2nd section displayed. The upper-parts are much cooler than the lower parts. On the right side (2nd section back) the temperatures correspond with the expectation.

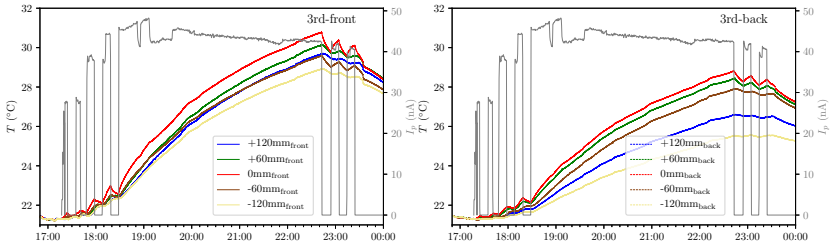

Figure 4.19: The TC measurement of the *exp3* - measuring of the front and back-side of the 3rd section. The temperature of the further sections is decreasing, due to lower proton and neutron flux and its energy (see Fig. 4.8). The distribution of the temperature reflects the heat generation distribution (if used the cooling correction). It shows that after 3rd section the T distribution is not so concentrated in the centre as in the previous section and so the heat is much better distributed, see MCNPX simulation in Fig. 4.28

.

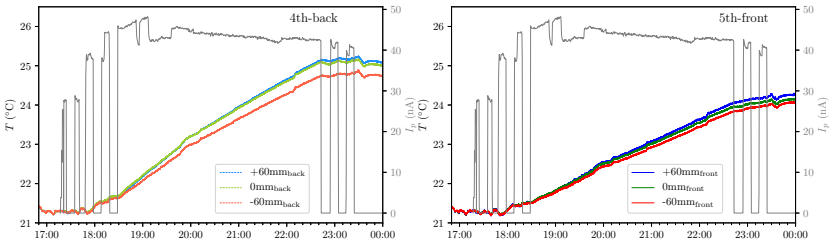

Figure 4.20: The TC measurement of the *exp3* - measuring of the 4th section back-side and the 5th section front-side. At the second half of the TA QUINTA, there is much lower proton and neutron flux, and so the heating deposition of these reactions (including gamma and pions). The target temperature there primarily consists of heat transfer from warmer parts, the particle direct heating contributes negligibly. In connection with that, the temperature does not reflect the beam changes so well.

Discussion:
The temperature measurement by TC was complicated by problematic access to the measuring positions. The thermocouples were fixed on the cardboard holder which is inserted into 17×120 mm^2. There was no room to check the contact quality. Only vertical positions were measured. Due to lack of thermocouples, since the front of 4th section, only +60,0 and -60 mm positions were measure. Unfortunately, two thermocouples located on the front side of the 4th section were destroyed during inserting into the QUINTA. For this reason, the front side of the 4th section is not plotted. It must be stated that this kind of experiment was one of the earlier, the knowledge of the experimental measuring quality was lower, and the conditions were much harder than for the QUINTA without shielding. Measured data just confirmed the expectation. It can not be stated that only temperature measurements brought out any significant or essential data. However, when the ANSYS simulation will be carried out, both experiments will be calculated - with and without shielding. The point is that the shielded target was possible to irradiate by almost double proton beam current. The measured temperature was even 2.5 higher than without shielding case due to the combination of the higher proton beam and shielding which substitute the insulation.

QUINTA without lead shielding

The experiment of QUINTA irradiation without lead shielding was performed under strict radiation safety conditions. The complex temperature distribution was monitored by 88 thermocouples. Thermocouples were fixed in the front and back side of each section in a cross-distribution (horizontally and vertically) +120 → -120 mm with the step of 60 mm (see Fig. 4.21, or full connection scheme with all labels in Fig. D.1).

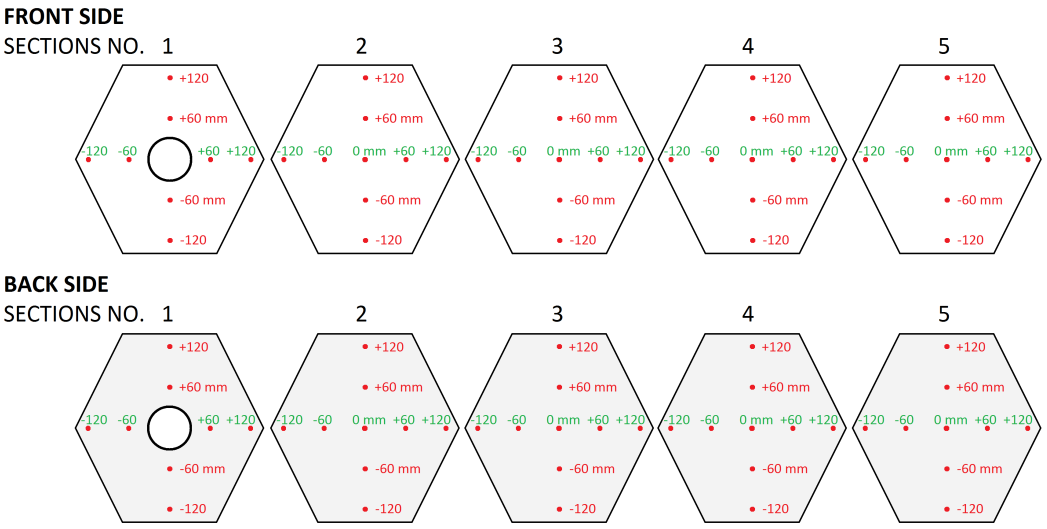

Figure 4.21: The TC positions of the *exp10*. Unfortunately, there were destroyed three TC during the manipulation and testing measurement. These three measuring position were not evaluated (shown in Fig. D.1).

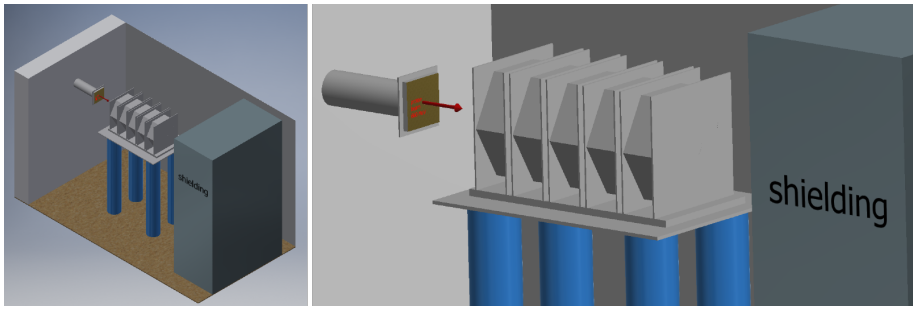

Figure 4.22: Model of the TA QUINTA irradiation without shielding.

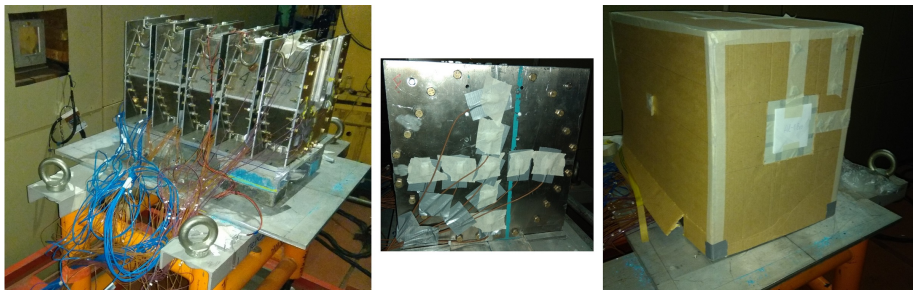

Figure 4.23: The setup of the *exp10*. On the left side is shown the whole TA QUINTA without shielding with already fixed thermocouples. The thermocouples were fixed directly to the aluminium cover for the front and back side of each section by highly adhesive tape. There was 5 mm thermal insulation over this tape fixed by paper tape. It works as thermal insulation, and even more important, it presses the thermocouple to the surface of the measured position (see the middle figure). On the right side, there is a pictured setup just before the experiment. The QUINTA was covered by a cardboard box to provide a thermal boundary to limit the convection.

4.2.1 Temperature measurement of TA QUINTA heat generation

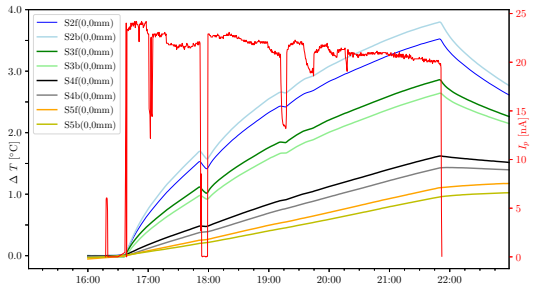

Figure 4.24: TA QUINTA temperature measurement without shielding in the centre of each section. This chart shows the problematic combination of the direct heating process and surface cooling. Most of the heat is released in the second section, but either, the second section is cooled the most from the front side due to a hole in the first section (discussed in Fig. 4.16). For this reason, the second section front side is cooler than the back side. If the first section without the beam window, hypothetically, the front side of all displayed section would be warmer than the back side.

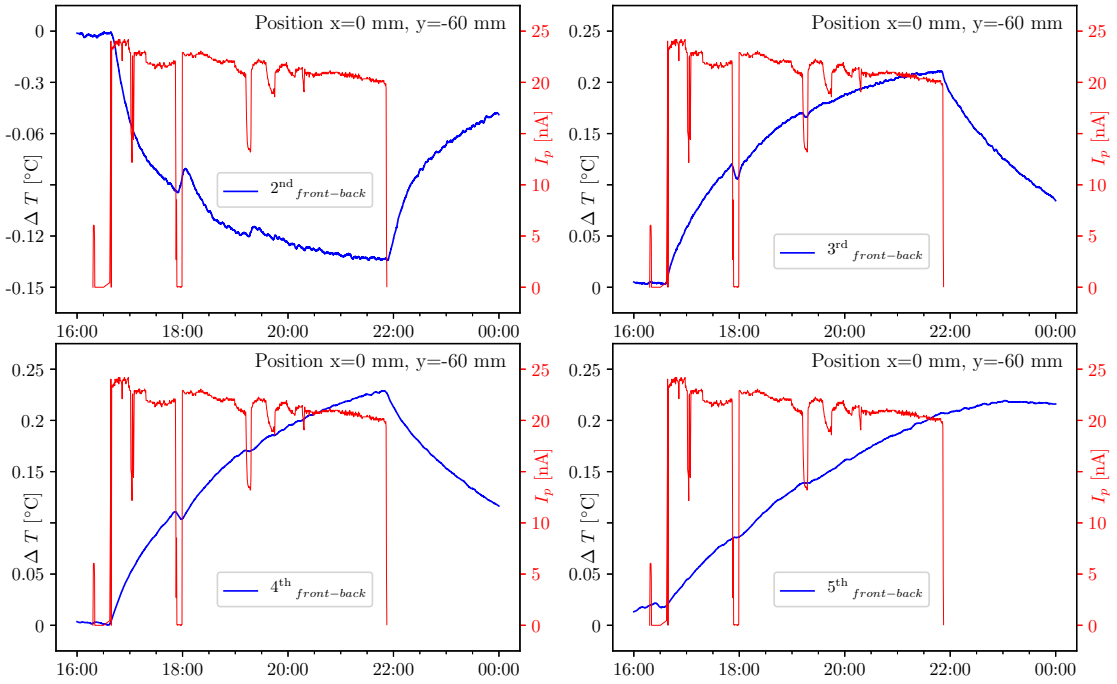

Figure 4.25: TA QUINTA temperature measurement without shielding with front-back difference at position x=0 mm; y=-60 mm. This figure describes the problem of the different cooling of each section. Basically for each section, the front side should be warmer than the back one, due to more reactions appear there. The second section was affected as in the previous paragraph discussed.

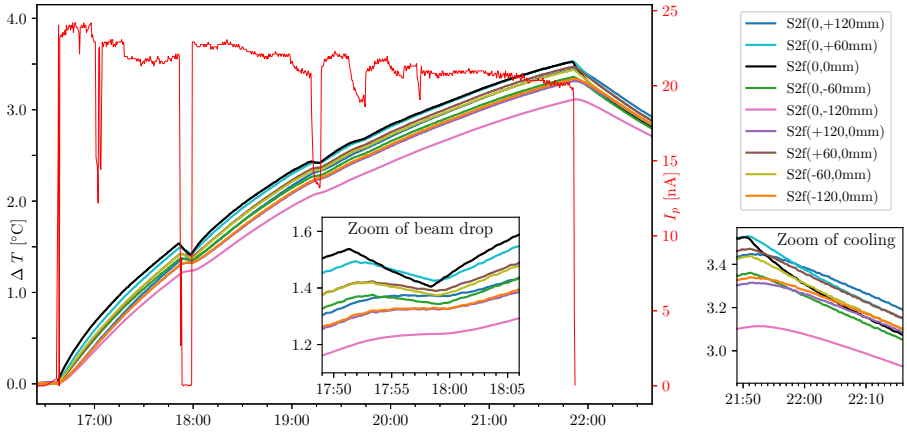

Figure 4.26: TA QUINTA temperature measurement without shielding, the front side of the 2nd section. All measured positions are displayed. The chart consists of two additional zoomed windows. Firstly, it is the first beam drop, and the second zoomed window below the legend shows the end of irradiation (only cooling process and heat transfer occurs there without any direct heating). All measured position of the QUINTA are analysed in this form to be able to easily compare them (see Appendix D.2, D.3 and D.4).

4.2.2 MCNPX simulation of TA QUINTA without shielding

There were two methods of heat deposition calculation. The first method uses the volume heat deposition tally. Each cylinder is defined as a tally volume and separately calculated for each particle reaction contribution. It allows to separate the heat deposition of the target (uranium cylinders with cladding, in total 298 pcs) and the heat deposition released by the Al construction of the QUINTA target (see Fig. 4.22).
The second method calculates the heat deposition mesh tally for each particle contributing to heat deposition. It is very suitable for visualisation purposes and for better understanding the target behaviour. The input code is enclosed on p.172. The last mesh definition in this code (rows 301-306), was used for controlling purposes. It consists of only one cell, which contains the whole QUINTA volume. It calculates the average value of this volume relative heat deposition density.

The MCNPX code and its utilisation have been already discussed (p.45), as well the visualisation methods by Python Seaborn (p.48). In these results will be shown only the final heatmap charts, cylinders heating visualisation and tables with important data. Usually, it is expected to share the MCNPX input file for control purposes. It is enclosed in appendix, p.172. The Python visualisation script was very similar to the script used for other targets plotting (enclosed in the appendix, p.181). To make this dissertation more „open-access“, all MCNPX results are enclosed on the cloud of Google Disk accessible for all BUT students or employees, see appendix F, items 1, 2 and 3.

The first method results:
The relative heat deposition of each cylinder was simulated for proton, neutron, photon, pion reactions, and finally their summary per each section. Unfortunately, it is very tricky to perform a clear visualisation of all cylinders heating. The best way is to use the heatmap (which already used for the meshing). Another visualisation by 3D chart was performed in Gnuplot for neutrons and protons only, see Fig. D.6. The summary per each section is shown in the following 2D chart with added visualisation of the total ratio by a pie chart.

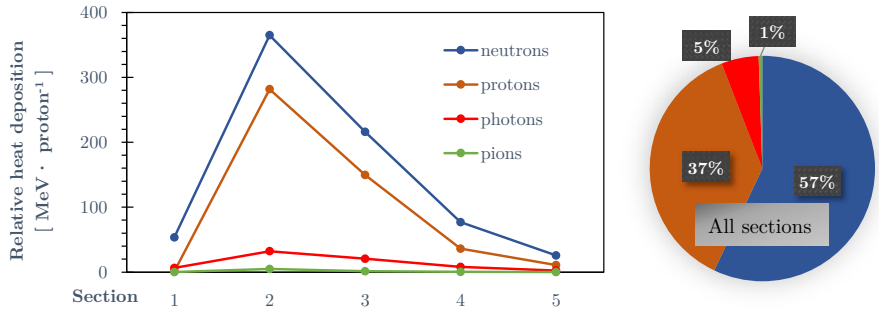

Figure 4.27: This chart shows the relative heating of the uranium cylinders with Al cladding per individual sections. Four sources of the heat are separated, based on the particle of the heating reaction (protons, neutrons, photons, and pions). The left chart represents the absolute values of data listed in Tab. 4.3 (highlighted by blue colour). On the right side is shown a chart describing the whole target heating ratio by individual contributors. The pie chart is based on data listed in Tab. 4.4 (highlighted by green colour). Absolute values of all section contribution per each particle is listed in Tab. 4.4.

Table 4.3: The ratio of the heating reactions partitioned by the contributing particle is listed by two way of comparison. It deals only with heat deposition of uranium cylinders with its Al cladding without construction parts heating (actually, it contributes by less than 3 % - see Tab. 4.4). The data highlighted by blue colour shows the ratio of heat deposition caused by a chosen particle in selected section to the total heat deposition of a chosen particle in the whole target (so the heat deposition in the first section by neutron reaction is 7 % of the total neutron reaction heat deposition in the whole target). On the other hand, the data highlighted by green colour shows the ratio of each particle heating contribution per total heat deposition of chosen section (so the neutron reactions contributes by 87 % of the first section total heat deposition).

Sec.	neutron	proton	photon	pion	neutron	proton	photon	pion	all
1	7%	0%	9%	2%	87%	2%	11%	0%	100%
2	50%	59%	46%	73%	53%	41%	5%	1%	100%
3	29%	31%	29%	19%	56%	39%	5%	0%	100%
4	10%	8%	11%	5%	63%	30%	6%	0%	100%
5	3%	2%	4%	1%	66%	28%	7%	0%	100%
all	100%	100%	100%	100%					

Table 4.4: Relative heat deposition of the individual QUINTA target parts. The heat deposition is related to the 660 MeV incident proton. These simulation results show the total gain of the QUINTA target G≈2.02. The energy gain is usually a very important value for ADS project concepts. It describes the energy multiplication factor of the target (rather reactor or demo reactor). Anyway, the accelerator energy consumption for proton acceleration must be included in that calculation. Due to dealing with experimental targets, the gross gain is calculated only.

Simulation method, part and source particle		
Mesh tally, whole QUINTA, all particles	1330.67	MeV·proton^{-1}
Volume tally, all cylinders, neutrons	737.58	MeV·proton^{-1}
Volume tally, all cylinders, protons	479.55	MeV·proton^{-1}
Volume tally, all cylinders, photons	69.60	MeV·proton^{-1}
Volume tally, all cylinders, pions	6.74	MeV·proton^{-1}
Volume tally, all cylinders, all particles	1293.48	MeV·proton^{-1}
Calculation - heating by Al constriction	37.19	MeV·proton^{-1}

The second method results:
Following heatmap charts describe the distribution of the heat deposition inside of the QUINTA target. Enlarged version of *xz* heatmap planes is enclosed in appendix Fig. D.5. The charts are shown in vector graphics. It can be widely zoomed to observe in detail the behaviour of each TA QUINTA part.

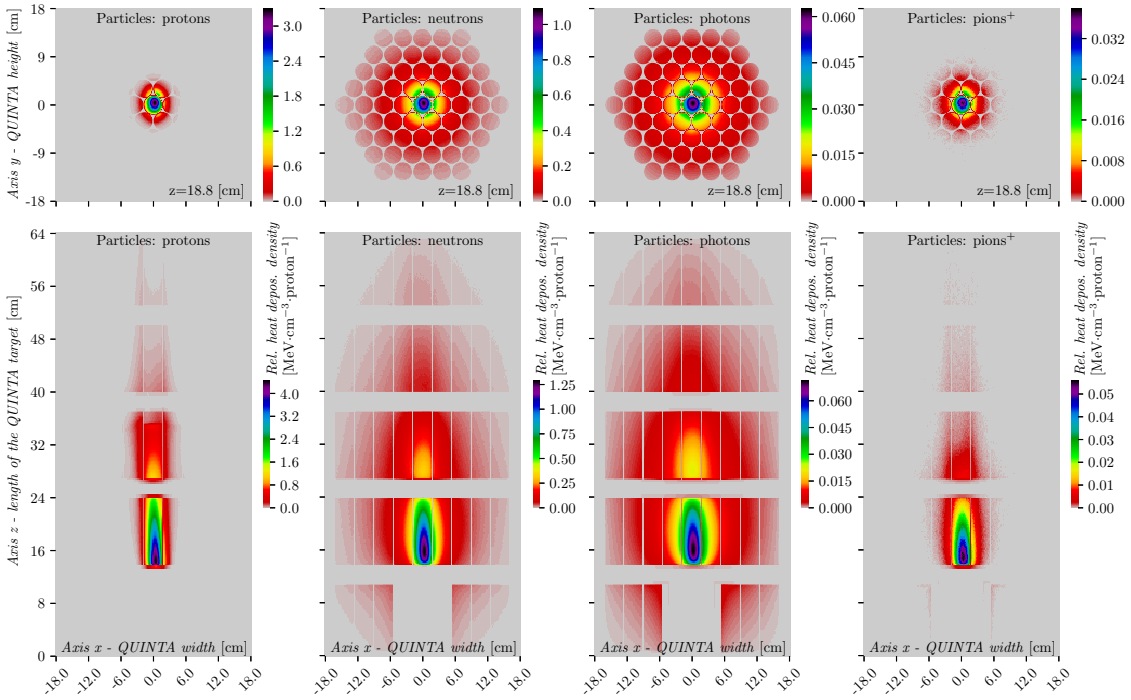

Figure 4.28: TA QUINTA - MCNPX simulation of relative heat deposition density separated into individual particles whose reactions contribute to heat deposition. Each chart has a unique maximum of the heatmap bar to show the heat generation distribution per each participating particle on a detailed scale. The upper part of the figure shows *xy* planes. The *xz* planes are displayed at the bottom. The proton reaction causes very concentrated heating due to ionisation loss and inelastic scattering (the secondary hadrons continue in direction of the primary particle for an intra-nuclear cascade of spallation reaction). Neutrons are released from spallation reaction randomly in all directions. The neutron heating is concentrated the most in the centre due to the highest neutron flux concentration (the most of reactions), but it is much better distributed to surrounded target parts. The heat generated by neutron reactions (mostly uranium fission) is radially decreasing up to the target border. The gamma heating is well distributed through the target but it has a much smaller total heat contribution. Finally, the pion heating reactions. They are similarly spread as the proton heating reactions due to their origin from the spallation reaction, in contrast with the proton reaction heating, the pion reactions contribution is merely negligible.

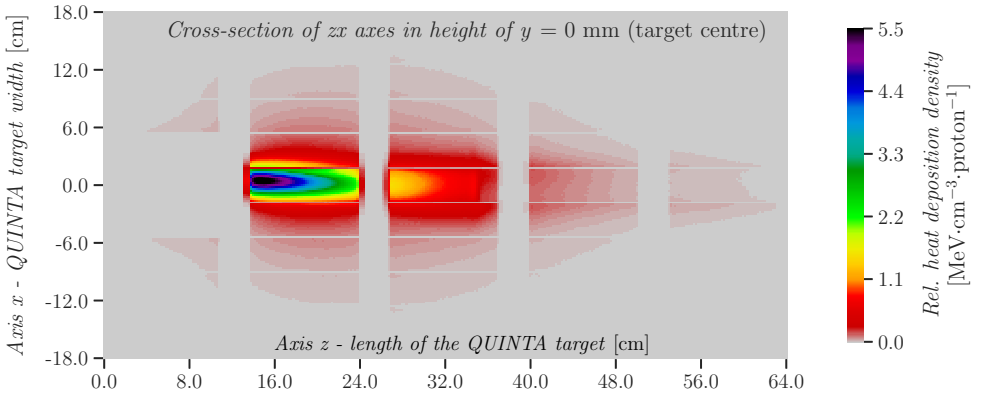

Figure 4.29: TA QUINTA MCNPX simulation of the total (all particles included) relative heat deposition density for *exp10*, *xz* plane for y=0 mm. The bar maximal of the heatmap is set to 5.5 MeV·cm^{-3}·proton^{-1}. The cell edge size of the calculated mesh is 2 mm.

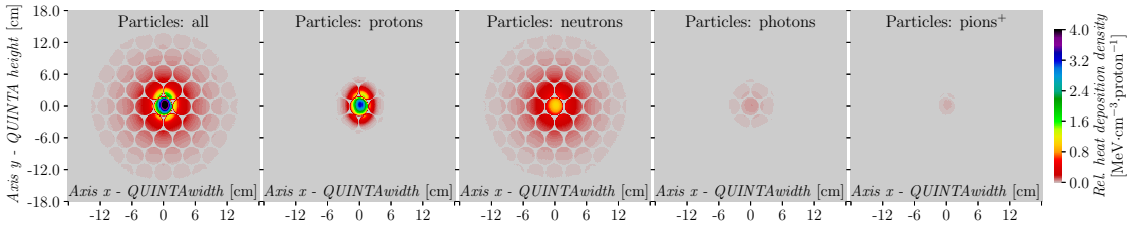

Figure 4.30: TA QUINTA - MCNPX simulation of the relative heat density distribution by each contributing particle (*xy* plane). Each chart has the same heatmap bar maximum (4 MeV·cm^{-3}·proton^{-1}) to show easily comparable results. On the top of each chart is displayed the heating particle name (or rather the particle whose reaction causes the heat generation). The z distance of the *xy* plane is equivalent for all charts z=18.8 cm (roughly a middle of the second section).

4.2.3 Results discussion - TA QUINTA

Experimental measurement:

Relative temperature measurement reflects changes of the target internal energy state, so it allows to observe the relative heat changes. These heat changes are caused primarily by three phenomenons. The first one is the direct heating by nuclear reactions in the volume of the measured surface (this one is required to be monitored). The other two are caused by heat transfer - increasing of the internal energy state by the heat accumulation from warmer parts, and decreasing by releasing accumulated heat from the surface to surrounding colder parts. While the heat transfer of the solid is primarily caused by conduction, the solid surface is cooled chiefly by convection and negligibly by radiation. The amount of transferred heat depends on the surrounding objects internal energy state, fluid characteristics, and finally on the outer boundary conditions. They can accumulate the transferred heat or reflect it (if radiation occurs). It is tricky to separate these three phenomenons by simple temperature change measurements.

For this reason, there is shown chart (Fig. 4.26) with very important temperature decreasing monitoring (when outage, or the beam current changes, or the irradiation ends). It allows separating the heat transfer from direct heating. The target direct heating is caused by the proton flux occurrence, so its outage or changes affect the heat deposition directly. Due to good conduction, this phenomenon can be observed where direct heating is a major contributor to internal energy changes (sharp temperature changes). On the other hand, if the internal heat changes are chiefly caused by heat transfer, the beam outage is not affecting the changes of internal energy → the temperature changes are very smooth, the changes are visible with a delay which depends on the heat transfer rapidity.

To summary, the most directly heated parts are in the centre cylinders of each section, see the black line as sharply decreasing since the beam drop (in Fig. 4.26). It is chiefly caused by proton heating. Similar sharp trends with lower slope are shown in the positions ±60 mm - as vertically so horizontally, mostly in the second and third section. In essence, the direct heating of the central target's uranium cylinder depends on the beam position and its flux. It is suitable to expect that the upper parts will be heated by heat transfer of the warmer central part by natural convection, but of course, all of the three heat transfer processes occur. Due to the larger size of these charts, all measurements are placed in Appendix D.2, D.3 and D.4. Temperature measurement is chiefly affected by the proton beam window, which causes the front 2nd section cooling. This measurement is essential for future ANSYS Fluent simulations.

MCNPX simulation:

The MCNPX simulation allows to simulate the heat deposition caused by various nuclear reactions. Particles whose reactions caused the chief portion of direct target heating were neutrons and protons. Besides these two, there were simulated minor contributors, the reactions caused by photons (so-called gamma heating), and pions$^+$. The MCNPX simulation calculated the heat deposition of cylinders by each contribution particle reaction. Most of the heat was released by neutron reactions (mostly fission), about 57 %, followed by proton reactions which contribute by about 37 %. The gamma heating contributes only by 5 % and pions$^+$ merely less than 1 %.

Based on simulation, the total heat deposition of the TA QUINTA was 1330.67 MeV per each interacting 660 MeV proton. It means that the gross energy gain is 2.02. More than 97 % of the heat is released in uranium cylinders with aluminium cladding, the rest of the heat is released in construction parts. Most of the heat is released in the second and third section due to the highest concentration of reaction (highest proton and neutron flux). The first section generates about 61 MeV·proton^{-1}, the second section 684 MeV·proton^{-1}, third section 387 MeV·proton^{-1}, fourth section 121 MeV·proton^{-1}, and finally, the last fifth section generates only 39 MeV per incident protons. The total number of incident protons was estimated to $1.52 \cdot 10^{15} \pm 16 \cdot 10^{13}$ by gamma-ray spectrometry. The total heat generated in the target is estimated to about 374 kJ.

Due to the high importance of these results, the zoomed figure of each particle reaction distribution can be found in the appendix in Fig. D.5. The summary chars in Fig. 4.27 and data in Tab. 4.3 and Tab. 4.4. The 3D thermal power generation per each cylinder is shown in Fig. D.6 for neutrons and protons.

Heat transfer simulation of TA QUINTA[64] is planned to be finished during the year 2021.

[64] During the cooperation with group of Dr. Xuezhi Zhang, IMP Lanzhou, it was planned that the highly accurate model of the QUINTA target will be calculated with their computation facility. The cooperation began on February 2020 and the 3D CAD models ready for simulation with all material constants were sent with several explaining email during May 2020. In total, three models should be simulated until the end of 2020. Unfortunately, this cooperation failed due to a new complicated project of Dr. Zhang's team which made them very busy. Due to this fact, it has been decided that only two simulations - the LEAD and CARBON will be calculated by the author in the frame of this research. The QUINTA target simulation is planned to be finished based on fulfilling the cooperation agreement with Dr. Zhang's group in the short future. However, it will not be part of this dissertation, it will be published separately with the author experimental data.

4.3 Neutron leakage monitoring of the QUINTA target

The neutron leakage monitoring of the QUINTA target is described in section 3.2. Only results and pictures from this experiment are shown here, excluding already described measuring details. Before reading the following pages have a look at the mentioned methodology. For the TA QUINTA were studied two different methods of neutron leakage monitoring.
The first method - monitoring of neutron leakage by natural uranium cylinder (mass of 1.72 kg). Cylinders were located on both sides of the TA QUINTA at a height of 75 mm, see Fig. 4.31, and in detail in Fig. 3.24. Due to the utilisation of natural uranium in distant locations, lower specific heat was expected.

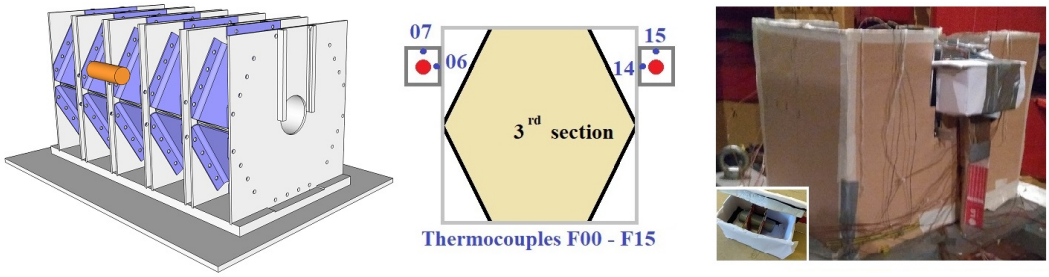

Figure 4.31: Neutron leakage setup for both sides cylinders experiment of TA QUINTA. Two cylinders are located on both sides symmetrically, in the centre of the QUINTA length, fitted by basic thermal insulation. Thermocouples measure temperature on the surface of the cylinder at several symmetrical positions. The insulation wall heated by QUINTA heat transfer was measured as well for the comparison reason.

The second method deals with comparing two geometrically identical tiny probes (described in Fig. 3.23), one contains a fissile sample (enriched uranium), the other one a blank sample (tantalum). The distance of these probes from the QUINTA target centre is great enough, so the neutron particle reactions are the major (negligible proton heating). The heat deposition is therefore chiefly caused by the neutron fission reaction which occurs exclusively in the fissile sample. This measurement was performed at two positions, under the second and the third section, see Fig, 4.32.

Figure 4.32: Neutron leakage setup for under the QUINTA target measurement. On the left side is displayed the insulation box with samples under the third section. On the right side, there is shown a similar measurement under the second section where was expected larger neutron flux. It was expected to measure sharp but small temperatures change caused by direct heating of n leakage fission reactions due to thick insulation which suppress the heat transfer from the QUINTA target. These photographs show the measurement setup before the final position fixation, so it looks orderless.

4.3.1 Temperature measurement of neutron leakage heating

The temperature was measured by TC type T for both measurements. This experiment *(No.11)* consisted of three irradiation stages. The first one dealt with the two cylinders irradiation for 20 min (see section 4.1 and Fig. 4.4). During this irradiation, the QUINTA target was moved for about 1 m left (from the point of beam axis view). Since the first stage of irradiation has been finished, the QUINTA target was shifted into the irradiation position (time 17:00) and the controlling beam pulses (several proton bunches around 17:05) were shut. About a minute later, the photograph of the beam was removed (the target near the measuring objects was visited by a group of researchers). After the short irradiation (17:10-17:30), the first batch of samples was removed (colleagues research), and the long irradiation was started. Each visit of the target influenced the temperature measurement of the outside cylinders, see the temperature peaks in visiting times in Fig. 4.33.

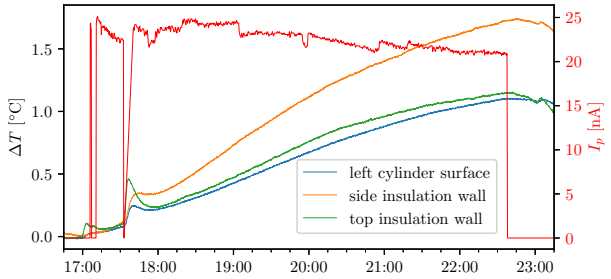

Figure 4.33: Neutron leakage monitoring by ΔT measurement of outside ^{nat}U cylinder heating. On the figure is shown only the left cylinder due to its similar behaviour with the right one. Surface ΔT is represented by blue colour, and the insulation ΔT is represented by orange and green colours, respectively for the side wall (shared with the QUINTA target) and the top wall. The measurement positions are shown in the centre of Fig. 4.31 (thermocouple positions „06“ and „07“). Unfortunately, the ΔT measured on the insulation wall was higher for both cases (orange, green) in comparison with the ΔT of the cylinder surface. It is primarily caused by two facts. The cylinders are located in the upper part of the TA QUINTA far from the centre and the insulation quality is poor. The second reason is that the cylinder consists of natural uranium (the tiny probes are made from enriched uranium, so the reaction cross-section is different).

The specific heat of the natural uranium cylinder at such a distant location is too low to be measured in these experimental conditions. On the other hand, the neutron leakage monitoring under the TA QUINTA brought interesting results. The idea of comparing the blank sample with the heating sample (uranium) is very powerful. It allows sufficient sensitivity and due to the comparison of two almost identical TCs eliminates many uncertainties. It should be noticed that the displayed data are already filtrated. The comparison of raw data with the filtrated data is located in the appendix, p.179.

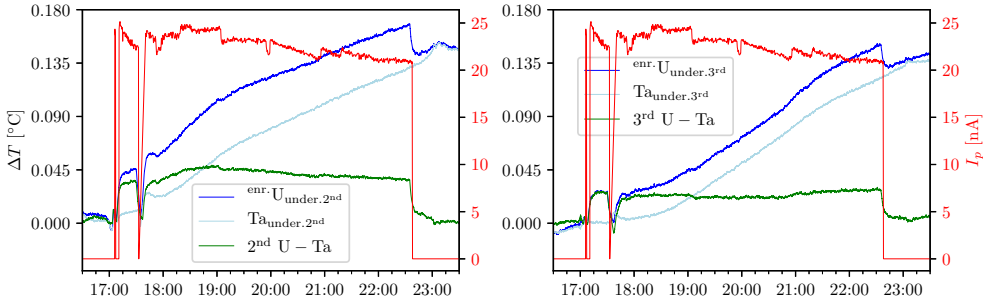

Figure 4.34: Neutron leakage monitoring under the QUINTA target by tiny heating probes. The neutron flux is estimated by comparing the blank sample and the fissile sample. A tiny volume of enriched uranium is safely encased and measured by TC on the cladding surface (blue colour). Tantalum blank sample of the same geometry was symmetrically located with similar insulation. The background temperature was increasing during the irradiation time due to heat transfer from the QUINTA heating. The heat transfer rapidity and quantity was very effectively decreased by advanced thermal insulation. However, some amount of this transferred heat was accumulated by the measuring probes. This phenomenon was neglected by comparing these two samples together (represented by green colour). There was a difference between insulation materials under the second and third section (the difference of the thermal resistance was about 20 %).

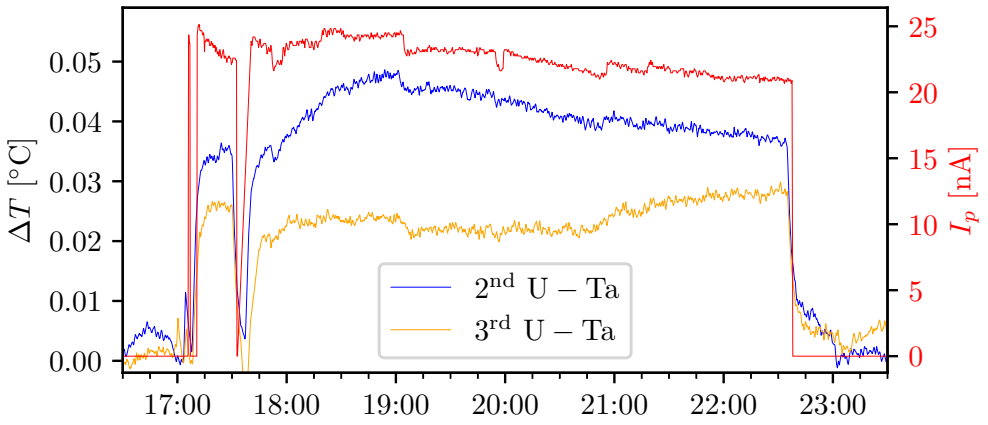

Figure 4.35: Comparison of the neutron leakage monitoring under the QUINTA target by the tiny heating probes. Both of the green characteristics from the previous Fig. 4.34 are compared together. Accuracy of the measurement may be affected by slightly different cold junction temperature of each thermocouple, however, it has been monitor by two different methods (described in Fig. 3.10 and above). Moreover, it was minimised by measuring methodology with electronics insulation and long pre-experimental measurement testing. Anyway, it is probably the cause of the slightly different characteristics of these cases. Also different insulation material and geometries imperfection plays its role. For longer measurement, imperfection of this method is highlighted due to complicated heat transfer delay based on many variables. The same figure of raw data (without filtering) is shown in appendix, Fig. D.8

4.3.2 MCNPX simulation of neutron leakage heating

Neutron leakage heating was calculated by MCNPX to determine the absolute value of direct heating inside of the observed object and to separate individual heating reactions. It was expected that the major heating contributor is going to be neutron reactions caused by leaking neutrons from the target. On the Fig. 4.36 is shown the heat deposition distribution for various particle reactions in the plane xz in the middle of monitoring cylinder y=75 mm. The cell edge of the mesh is 2 mm. The earlier idea was to plot here also the heat distribution mesh of the under quinta leakage monitoring. Due to very tiny probe size its visualisation is not suitable. It was calculated by volume heat deposition tally, see the results in Tab. 4.5. The probe heat distribution is uniform, due to large distance from the target where the n flux is uniformly distributed.

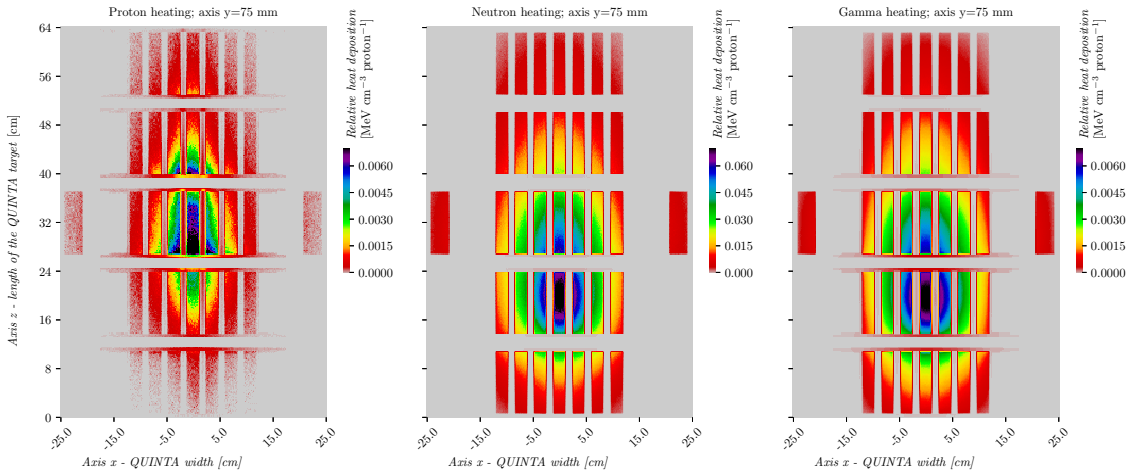

Figure 4.36: Visualisation of the neutron leakage simulation by MCNPX heat depositions mesh tally for side ^{nat}U cylinders monitoring. The centre of the cylinders are at a height of 75 mm from the target QUINTA centre (which in x=0 mm; y=0 mm). The secondary protons almost not occurring in such a distant location from the centre. Its maximum relative heat deposition densities are in similar values as photons. It shows that the proton flux is much lower and its maximum is shifted into the third section at this plane distance. It is primarily caused by the direction of secondary particles from the spallation. The gamma heating is much better distributed and it is releasing heat in various materials equivalently based on material properties (primarily the mass density). For this reason, the aluminium construction is slightly highlighted in heatmap visualisation in comparison with the neutron heating visualisation. The maximum of the neutron reactions heating is about an order of magnitude higher and similarly distributed as the gamma heating. So it could be expected that the gamma heating contributes by more or less 10 % of neutrons contribution. Due to vector graphic, the visualised pixel is one simulated cell. The whole volume of one cylinder consists of about 13,300 cells so the calculation of the total volume tally is sufficiently precious. Comparison of figures with various heatmap bar maximum is shown in appendix in Fig. D.11 (including pions heating which skipped here).

Table 4.5: The MCNPX results of the QUINTA target n leakage heating. These results were calculated by volume tallies. For simulation output and setting, see p.196 item 3.

$\mathbf{E}_{\mathrm{depos}}$ [J]	$^{\mathrm{enr}}\mathrm{U}^{2\mathrm{nd}}_{\mathrm{probe}}$	$^{\mathrm{enr}}\mathrm{U}^{3\mathrm{rd}}_{\mathrm{probe}}$	$\mathrm{Ta}^{2\mathrm{nd}}_{\mathrm{probe}}$	$\mathrm{Ta}^{3\mathrm{rd}}_{\mathrm{probe}}$	$^{\mathrm{nat}}\mathrm{U}^{\mathrm{left}}_{\mathrm{cyl}}$	$^{\mathrm{nat}}\mathrm{U}^{\mathrm{right}}_{\mathrm{cyl}}$
total	9.95	8.38	0.03	0.03	110.67	109.73
protons	0.00	0.00	0.00	0.00	2.42	2.60
neutrons	9.85	8.30	0.00	0.00	98.66	97.69
photons	0.09	0.08	0.00	0.00	9.52	9.38
pions$^+$	0.00	0.00	0.00	0.00	0.06	0.06

4.3.3 Results discussion - QUINTA leakage

Neutron leakage monitoring is essential for spallation targets. It was measured on the QUINTA target by using the offline gamma-ray spectrometry technique. This temperature measurement was performed as an independent measurement. Unfortunately, the side cylinder measurement did not bring sufficient results. It was caused primarily by the very low specific heat of the natural uranium in such a distant location. The 1,720 g of natural uranium cylinder generates about 110 J during the experiment. In contrast to the enriched uranium sample under the QUINTA target with a mass about 2 g generate in the same time about 10 J. The specific heat of the measured natural uranium cylinder is very roughly about 1 % of the enriched uranium probe. It explains the reason the measuring failed.

Results of the under QUINTA neutron leakage measurement are very interesting. It reflects the proton beam changes during the irradiation. However, the differences between these two positions do not reflect well the difference of the total direct heat deposition. There are three possible explanations. The first one - it is caused by the different shape and material of insulation (under the third section the insulation has contact with the lower plate of the QUINTA → better heat transfer). Second one - cold junction effect (described on p.37). And finally, it may be caused by the uncertainty of the sample position fixation (low dependency expected). Most probably it combines somehow all of these mentioned deficiencies. Important to be listed, that only about half of the usually used proton beam flux was used in this irradiation to fulfil the radiation safety.

Based on MCNPX simulation, the side cylinders are primarily heated by neutron reactions (for about 89.2 % of total heat). The next most significant contributor is the gamma heating (about 8.6 %), and finally, the proton reaction (about 2.2 %).
The energy released from enriched uranium probes (located under the TA QUINTA) is chiefly caused by neutron fission reactions (about 99 %). It was planned to measure these samples by HPGe detector to determine the total number of fission reactions. Unfortunately, it was not possible due to the lower importance of this measurement. There were a large number of irradiated samples in this experiment measured by other researchers. Nevertheless, the benchmark of MCNPX simulations of similar geometric settings is discussed widely in [79], p.69. In summary, this temperature measurement of neutron leakage was successful. In the future, this kind of measurement could be supported by gamma-ray spectrometry measurement.

Chapter 5

Other targets research

In the frame of this dissertation, another two targets were researched besides the QUINTA target. These targets were irradiated and studied by several methods by reason to prepare the most suitable target for sub-critical blanket BURAN, described in section 2.3.2. Prolonged targets of lead and carbon were constructed and finally irradiated by 660 MeV protons at Phasotron irradiation facility. These materials were chosen for detail study due to their varied neutron spectra. The LEAD target produces dozens of fast neutrons, while the CARBON target produces fewer neutrons at much higher energies. Based on the simulation, the lead material stops the 660 MeV protons in a distance of 30.7 cm (without air gap) and for the carbon material it is in distance of 112.5 cm. By a combination of these two materials can be prepared the most suitable target for future BURAN experiments.

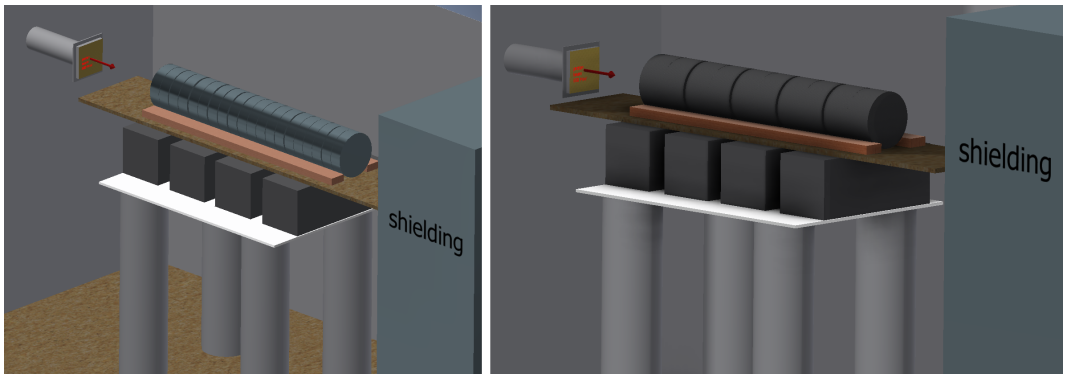

Figure 5.1: Model of the LEAD (left) and the CARBON (right) target irradiation.

5.1 LEAD target

The LEAD target consists of twenty cylinders, each with diameter 19 cm and length 5.2 cm. There was a problem with the lead material that the geometry is not easy to machine, so the cylinder geometry has 1 mm tolerance, however, the cylinders contain small fragments on the surface causing roughness up to 2 mm. Between each two neighbour cylinders, there was an air gap for measuring purposes. If only thermocouple measurement was involved, the air gap was minimal (primarily caused by rough geometry). After 2^{nd}, 4^{th}, 6^{th} and 8^{th} cylinder, there were a larger air gaps where copper and lead activation foils are installed. Mass density of the lead was ρ_{Pb}=11.35 g·cm^{-3}. The total target length was 108.1 cm. It was consisted of 104 cm of the lead and 4.1 cm of several air gaps. In principle, only first 6 cylinders significantly interact with protons. The target was irradiated by 660 MeV protons for 265 min excluding several of the planned beam pauses (purpose of cooling observation), see Tab. 5.1.

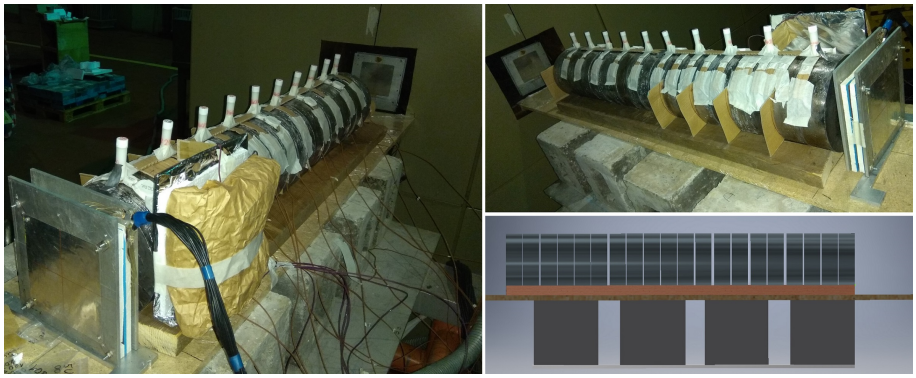

Figure 5.2: Prolonged lead target setup, real pictures and simulation. On the left side is shown the proton beam camera in the front of the target. Between every two cylinders are connected thermocouples. On the top of cylinders, there are ampules with solid salt which is a part of other research. On the surface are glued various activation foils for purpose of neutron monitoring by the gamma-ray spectrometry method. Finally, in the front part of the target, there is a thermal insulation (consisted of paper, polystyrene and aluminium) for purpose of neutron leakage monitoring which is a part of this research. On the right upper side of the figure is shown the opposite side view, where shown the copper and lead activation foils on cardboard holder. Below this figure, there is the 3D Inventor simulation of the target air gap which were actually vary for each measured position.

Table 5.1: The irradiation time of the LEAD target experiment

Short irradiation		T_{irr}	**Long irradiation**		T_{irr}
Beam start	Beam stop		Beam start	Beam stop	
15:34:13	15:39:30	0:05:17	16:45:25	20:34:41	3:49:16
15:44:31	15:49:27	0:04:56	**Total long irradiation**		**3:49:16**
15:54:29	16:04:26	0:09:57			
16:09:29	16:19:29	0:10:00			
16:29:33	16:34:38	0:05:05	**Total short irradiation**		**0:35:15**

5.1.1 Temperature measurement of the LEAD target

The temperature was measured by thermocouples on back-side of each cylinder.

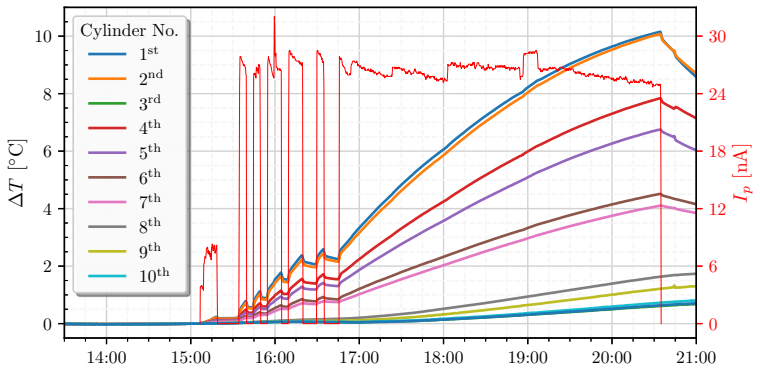

Figure 5.3: Thermocouples temperature measurement of the LEAD target (*exp13*). Only front 6 cylinders are significantly contributing on heat generation (discussed on page 92). This phenomenon is confirmed by experimental temperature measurement. If the cylinder generates significant heat, the increasing temperature should correspond with the proton beam occurrence. On the other hand, beam outage should causes the target cooling → temperature should decrease when beam absence. If these conditions are visible by ΔT measurement, the measured temperature increase is caused by any of the heat deposition reactions. If the cylinder temperature is increasing very slowly and does not respond to beam occurrence, the increased temperature is probably caused by heat transfer from surrounding parts (cylinders heated by particle reactions). It is represented by cylinders 7-10. Other cylinders are not displayed for better clarity (negligible ΔT).

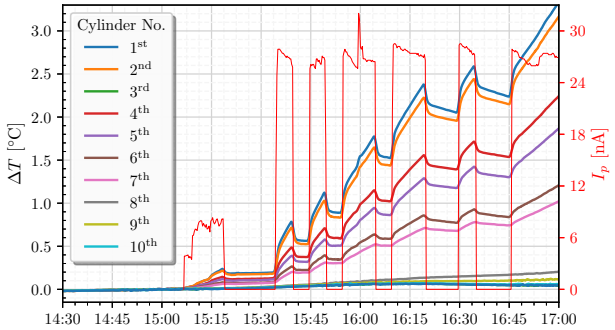

Figure 5.4: Zoomed part of the LEAD target temperature measurement (*exp13*). The best way of the heat deposition monitoring is during the short irradiation pulses (5 or 10 minutes length), see Tab. 5.1. Temperature characteristics are reflecting the beam current, which represented by axis *y2* on the right side (red colour). If both processes are happening (the direct heating by particle reaction heat deposition and heat loss by transfer to surrounded parts), the ΔT measurement describes both of these processes. For this reason, it can not be simply verified by MCNPX simulation - the ANSYS Fluent simulation must be added. Widely discuss in section 5.2.2.

5.1.2 Simulation of the LEAD target by MCNPX

Two methods of heat deposition calculation were chosen. **The first method** deals with a mesh tally, where the LEAD target was „cut“ in the *zx* plane, right in the centre of the target height (y=0 mm). In principle, the plane was partitioned into squares with edge equal to 2 mm (in principle it is cube 8 mm^3) where was the heat deposition calculated. Mesh tally was calculated for all particle whose reaction participates on heating, such as protons, neutrons, photons, and pions$^+$. The result of this simulation is shown in Fig. 5.6. Nevertheless, the most crucial for further calculation is the total heat deposition → sum of all reaction contributors, it is displayed in Fig. 5.5. The MCNPX input code with Python script for visualisation are shown in appendix[65] and MCNPX output (which contents the input code at the beginning) is uploaded to cloud, see p.196 item 6.

Due to most of the heating reactions are situated in the first 6 cylinders, there is no reason to simulate the whole target. There is no heating and almost no reaction in the second half of the target, see Fig. 5.10. The mesh tallies were calculated along the length of 45 cm. Farther locations generate negligible heat (total heat deposition < 0.01%), mostly generated by gamma heating. This phenomenon is shown in Fig. 5.5, please carefully watch the heat deposition density units, each particle contribution has own maximum. The heat deposition density of the whole target is reasonable to be plotted up to 6$^{\mathbf{th}}$ cylinder, there is generated about 99.7% of heat, see Fig. 5.7 and each cylinder heat deposition contribution in Fig. 5.8.

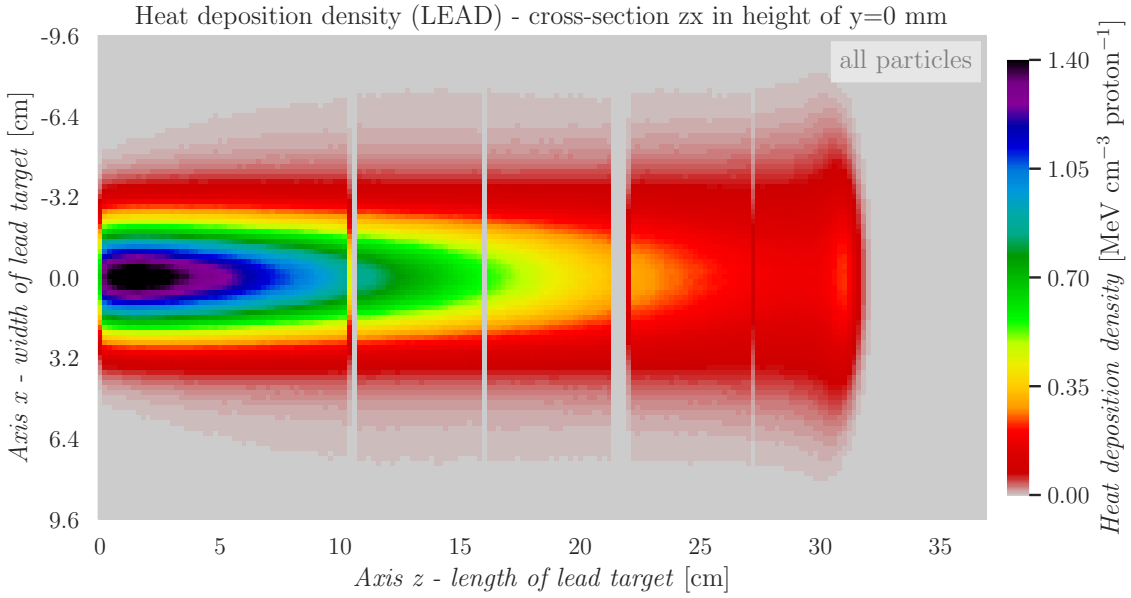

Figure 5.5: Heat deposition mesh tally simulation of the LEAD target by MCNPX. The sum of all contributed particles reactions (proton, neutron, photon and pion$^+$) is shown. Between the first and the second cylinder, there is not simulated any air gap. The coarse resolution is 2 mm.

[65] The Python script manual for MCNPX tally mesh visualisation is uploaded to YouTube.com, see: https://youtu.be/R6P4zrUihkQ. All scripts are located in the appendix, see Python visualisation code on page 181.

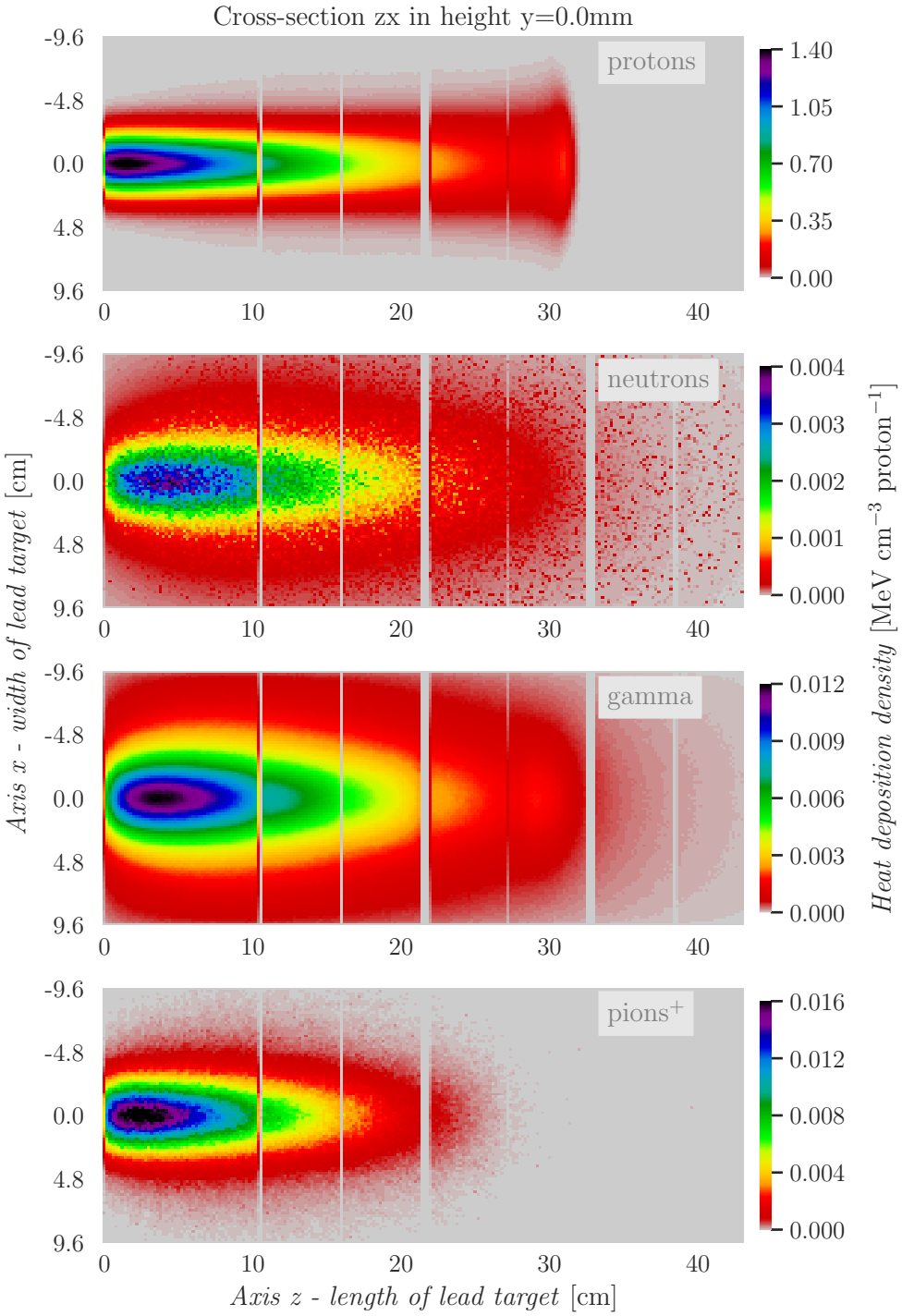

Figure 5.6: Heat deposition mesh tally simulation of the LEAD target by MCNPX. Charts display heat deposition density of each participated particles → proton, neutron, photon and pion$^+$. Each chart has own heatmap distribution, the max value of each chart is represented by black colour, carefully watch the units. This figure describes well the distribution of each particles heating but does not allow to compare them easily each together. By this purpose there are comparing charts in appendix, see Fig. E.1.

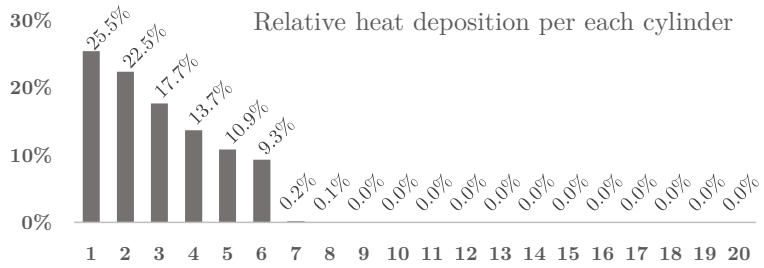

Figure 5.7: Relative total heat deposition per each cylinder of the LEAD target (proton, neutron, photon and pion$^+$ reactions included). Axis x represents the number of cylinder, axis y represent relative heat deposition of each cylinder to the total target heat deposition.

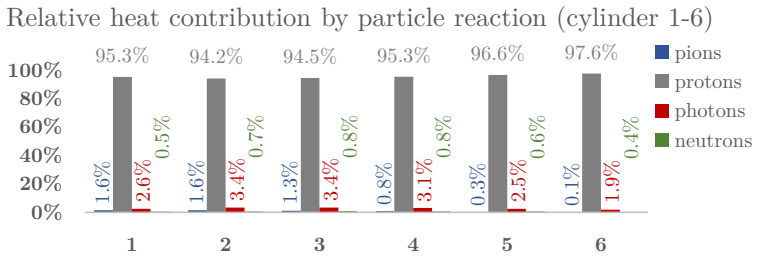

Figure 5.8: Relative heat deposition contribution of all contributing particles per each cylinder. Due to first 6 cylinders contributes up to 99.7% of total heat deposition, other cylinders are not displayed. Axis x represents the cylinder number, axis y represents relative heat deposition of particle contributor to the total cylinder heat deposition. In summary, 95.12 % of the total target heat was generated by protons reaction, 3.03 % by photons (gamma heating), 1.17 % by pion$^+$, and about 0.68 % of the total heat was generated by neutron reactions.

The second method of heat deposition calculation was performed by virtual target partitioning into 360 cylindrical annulus and 20 cylinders. For each of these geometries, the heat deposition volume tally was calculated. This method was chosen for the heat source definition potentially usable in ANSYS calculation. In principle, each cylinder was partitioned into 19 pieces - one cylinder and 18 cylindrical annulus (rings). The inner cylinder has radius 5 mm and was surrounded by cylinder rings with a stepping radius growth of 5 mm. Either inner r, so the outer R is increased by 5 mm each step (annulus with inner radius $\mathrm{r_{increased}} = \mathrm{R_{previous}}$, and $\mathrm{R_{increased}} = \mathrm{r_{increased}} + 5$ mm).

It is important to have a look at normalised data results per gram of mass. The highest relative heat deposition is located in the centre, with almost linear decreasing to the surrounding area, see Fig. 5.9. Since multiply these normalised data by the mass of each geometry (the combination of colourful step data with the mass visualisation by grey stepping line), the heat deposition by an annulus cylinder is calculated, see Fig. 5.10.

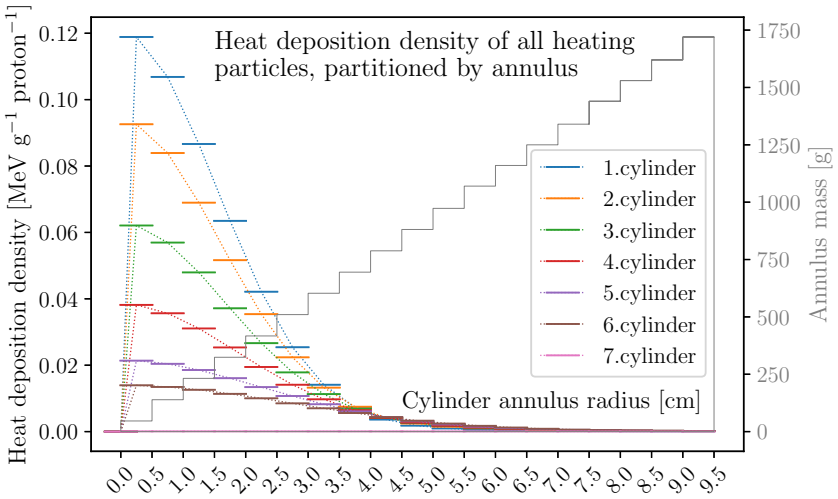

Figure 5.9: MCNPX simulation of the LEAD target total heat deposition. Each cylinder of the target is partitioned by annulus - described in previous paragraph. Axis x represent cylinder radius boundaries [inner r, outer R]. Axis y (left side) represents the relative heat deposition normalised per mass and incident proton. Due to the 7$^{\text{th}}$ cylinder generates merely about 0.2 % of total heat generation, the data representing it (pink characteristics) looks like limited to zero → further cylinders are not displayed by this reason. Finally, the second y-axis (right one) represents the mass of each cylindrical annulus (grey colour) - characteristic is grey as well and looks like stairs from lower left to upper right.

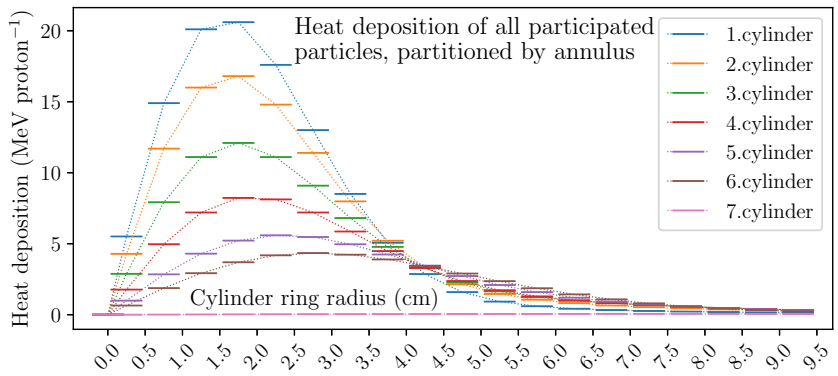

Figure 5.10: MCNPX simulation of the LEAD target total heat deposition. Each cylinder of the target is partitioned by annulus - described in previous paragraph. Axis x represent cylinder radius boundaries [inner r, outer R]. Axis y represents the heat deposition per incident proton of each annulus cylinder. In principle, it is other variation of previous chart in Fig. 5.9, with a difference that axes y_{left} and y_{right} are multiplied each together. It shows that the most of heat is released in the first cylinder, specifically in the cylinder ring of r=1.0 cm & R=1.5 cm, followed by r=1.0 cm & R=1.5 cm. Essentially, the chart also shows that by increasing target distance, the relative heat deposition peak is shifting radially far from the centre of the target. It is caused by primary photons track length.

5.1.3 Heat transfer simulation of the LEAD target by ANSYS

The earlier heat transfer simulations of the LEAD target were performed in cooperation with IMP Lanzhou, China, namely Dr. Xuezhi Zhang. He performed the first 2D simulation (based on the author 3D CAD model), wrote the first User Defined Function (UDF), and in principle, brought the know-how to this problem. This simulation results as well as the CARBON target, are a part of the research project between BUT and IMP. Unfortunately, the results were totally wrong and the cooperation was stopped.

The author provided data of total heat generation per each cylindrical ring of each cylinder. Heat generation input file consisted of 380 source definitions. In essence, it was sufficient to calculate the heat transfer only for the first 7 cylinders of the target (it means 133 sources of exact geometry definition). This definition is already approximated because the proton beam has an elliptical shape, however the cylindrical rings are partitioned by an annulus shape. Nevertheless, each cylinder is defined independently.

After discussion about computation time and its complexity, another source definition was chosen to simplify computation. It is based on the symmetrical source power description. It has been done by a 2D curve (described by equation) which is practically rotated along the z axis to receive the spatial layout of the power source density. To verify this method, this power source curve was calculated in Dr. Zhang's team at IMP and these results were compared with MCNPX heat deposition mesh tally calculated by the author. The equations are divided into two parts, the first one describes the target in the distance 0→29.5 cm, the second one describes target in the distance 29.5→32.3 cm (calculated for 50 mm ideal Pb cylinders with air gaps). These equations along 32.3 cm target length describe about 99.7 % of the total heat deposition.

The target heat flux definition by IMP Lanzhou

$$\begin{aligned} a_{\ 0\rightarrow 29.5\mathrm{cm}} &= 1.43 - z \cdot 0.03202 - z^2 \cdot 0.00225 + z^3 \cdot 6.47 \cdot 10^{-5} \\ c_{\ 0\rightarrow 29.5\mathrm{cm}} &= 2.145 + 0.01202 \cdot z + 5.9210 \cdot 10^{-5} \cdot z^2 + 5.356 \cdot 10^{-5} \cdot z^3 \end{aligned} \tag{5.1}$$

$$\begin{aligned} a_{\ 29.5\rightarrow 32.3\mathrm{cm}} &= 0.1697 - z \cdot 0.0369 + z^2 \cdot 0.04848 - z^3 \cdot 0.01148 \\ c_{\ 29.5\rightarrow 32.3\mathrm{cm}} &= 3.993 + z \cdot 0.166 + z^2 \cdot 0.053 - z^3 \cdot 0.029 \end{aligned} \tag{5.2}$$

$$\rho_{E_{rel}} \ = \ a \cdot \mathrm{e}^{-\frac{r^2}{c^2}} \ [\mathrm{MeV} \cdot \mathrm{cm}^{-3} \cdot \mathrm{proton}^{-1}] \tag{5.3}$$

$$P_{static} \ = \ a \cdot \mathrm{e}^{\frac{-r^2}{c^2}} \cdot 10^6 \cdot \mathrm{I_p} \cdot 10^6 \ [\mathrm{W} \cdot \mathrm{m}^{-3}] \tag{5.4}$$

$$\frac{dp}{dt} \ = \ a \cdot \mathrm{e}^{\frac{-r^2}{c^2}} \cdot 10^6 \cdot \frac{i_p}{dt} \cdot 10^6 \ [\mathrm{W} \cdot \mathrm{m}^{-3}] \tag{5.5}$$

In these equations, the length distance is represented by z, the radius by r, the relative heat deposition density by a $\rho_{E_{rel}}$, the uniform power density P_{static} and finally variable power density dp. To calculate the power, $\rho_{E_{rel}}$ is multiplied by constant 10^6 to get eV from MeV, by proton beam current variable $\mathrm{I_p}$ in units of [A] and another constant 10^6 to transform [cm^{-3}] to [m^{-3}]. If the static state calculation is involved, the proton beam is represented by constant. If this result is in further multiplied by irradiation time, the total heat deposition in units of [J] is obtained. If calculate the dynamic state, where the beam is not uniform (this research case), the calculation must be performed over time → $\frac{dp}{dt}$.

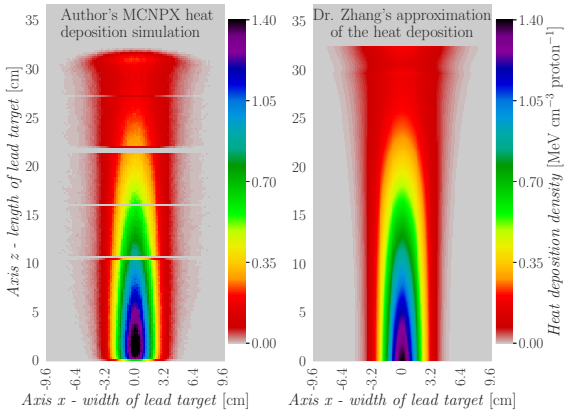

Figure 5.11: The heat deposition density mesh comparison between the symmetrical approximation calculated by IMP Lanzhou (Dr. Zhang) vs author's MCNPX. This comparison shows the whole heat distribution in 3-dimensional system, because it is symmetrical. Anyway, more important is the real heat generation comparison per each cylinder, which is shown in Fig. 5.12. To see this comparison along the length of the target, see Fig. 5.13.

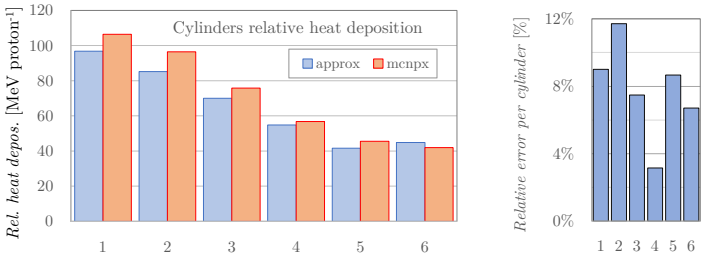

Figure 5.12: Relative heat deposition for each cylinder - comparison between approximated calculation by IMP Lanzhou and author's MCNPX calculation, on the left side. On the right side is shown the relative error of approximation per each cylinder in percent. These results should be understand in context with Fig. 5.7.

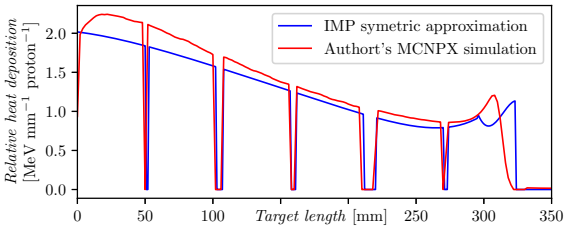

Figure 5.13: Heat deposition per incident 660 MeV proton along the full cylindrical volume of length = 1 mm. The whole volume is partitioned by 1 mm in axis z (length). Comparison of IMP's approximation vs author's simulation in MCNPX, calculated by written Python script attached in p.184.

Based on the author's MCNPX simulation, the relative heat deposition in the whole target is 420.33 MeV per one incident 660 MeV proton. For the approximated heat generation source, it is 393.31 MeV·proton^{-1}. In the approximated calculation is released about 7 % less energy than simulated by MCNPX. In essence, it could be a sufficient result. Due to trying the corresponding results based on hard data, the author decided to create a special script to perform this calculation more accurately.

Python script for 3D thermal power distribution approximation by equations

The approximation results based on eq. 5.1 and eq. 5.2 are not sufficient enough. In the following lines is described the author's method of 3D thermal power approximation by several of equations. It can be useful for other applications, or following MCNPX mesh tally calculations.

Step 1^{st} - since the MCNPX calculation of any mesh tally is performed (for example see the heat mesh definition in eq. 3.6), the xz cross-section of the target centre (y=0 mm) must be created → data as visualised in Fig. 5.5 are received. Actually, it does not matter which units are used, the author prefers the relative heat deposition density.
Extract these data without statistical errors. The columns are representing the length along the axis z, rows are radius r, or globally target width. Delete the lower half of the width - in case the beam interacts in the centre (let the centre be equal to width=0 mm), so the extracted data are going to be rows from the maximum x width, down to the centre equal to 0 mm. For each length portion, calculate the maximum value of the relative heat deposition → the data of the parameter a are received. Then calculate the values of parameter c, based on equation 5.3. To calculate c for each value of the matrix, the following equation was used.

$$c = \sqrt{\frac{r^2}{\ln(\frac{\rho_{E_{rel}}}{a})}} \tag{5.6}$$

Now, it is a tricky part, because by eq. 5.6 calculates a matrix of values based on r and $\rho_{E_{rel}}$, or z *axis*, respectively. Values of the final parameter c (one value per each length portion) are received by a specific median calculation along the specific radius. As eq. 5.3 describes, the a parameter influences the absolute value (maximum) for each portion of length. On the other side, the c parameter influences distribution along the radius, therefore the result of the exponential part of the equation is a ratio (number $\mathbf{R} \in [0, 1]$). Boundaries of specific medians are based on all data, excluding the statistically incorrect one. From this, *„Step 1"* is received a matrix of 3 rows → z (length portion), a parameter and c parameter. In the case of the LEAD target heating, it is following:

z_{cm}	0.0	0.2	0.4	0.6	0.8	1.	0	1.2	1.4	1.6	1.8	2.	0	2.2	2.4	2.6	2.8	...
$a_{parameter}$	1.000	1.353	1.398	1.421	1.428	1.441		1.455	1.462	1.460	1.459	1.448		1.444	1.420	1.419	1.413	...
$c_{parameter}$	2.160	2.175	2.174	2.185	2.213	2.220		2.210	2.235	2.260	2.276	2.308		2.297	2.316	2.333	2.319	...

Step 2^{nd} - fit these data by polynomial functions of suitable boundaries, it is essential to ensure the data are fitted as accurately as possible. Then calculate a new matrix of approximated data based on eq. 5.3. Plot these data and compare them with MCNPX calculation. It is recommended to compare the relative heat deposition of the whole volume partitioned by length. Than compare each cylinders contribution, and finally, perform a visual comparison of zx plane heatmap. This method, described by *Step* 2^{nd}, is performed by written Python script enclosed in Appendix E.2, page 184 and script output text file (p.188). For these complicated calculations in the script, the YouTube manual[66] was recorded.

$$\begin{aligned} a_i &= A_{i_a} \cdot z_{i_a} + B_{i_a} \cdot z_{i_a}^2 + C_{i_a} \cdot z_{i_a}^3 + D_{i_a} \\ c_i &= A_{i_c} \cdot z_{i_c} + B_{i_c} \cdot z_{i_c}^2 + C_{i_c} \cdot z_{i_c}^3 + D_{i_c}, \end{aligned} \tag{5.7}$$

where: i is $\mathbf{Z} \in$ (1,total number of fit boundaries); z represents the length.

[66] A video manual of this script utilisation was created, available at https://youtu.be/RRqtm1FfxJU.

Values of a and c parameters were fitted by 5 polynomial functions for the a curve and 3 polynomial functions for the c curve by this script. These functions are described based on eq. 5.7 by the following parameters (see script output on p.188):

$z_{a_1} = \mathbf{R} \in (0, 2.2)$; $z_{a_2} = \mathbf{R} \in [2.2, 10)$; $z_{a_3} = \mathbf{R} \in [10, 29.6)$;
$z_{a_4} = \mathbf{R} \in [29.6, 30.8)$; $z_{a_5} = \mathbf{R} \in [30.8, 32.8)$
$z_{c_1} = \mathbf{R} \in (0, 28.4)$; $z_{c_2} = \mathbf{R} \in [28.4, 30)$; $z_{c_3} = \mathbf{R} \in [30, 32.8)$

For i_a equal to $\mathbf{Z} \in [1, 5]$:
$A_{i_a} = [0.21909, -0.018913, -0.08793, -110.080344, 276.293819]$,
$B_{i_a} = [-0.104531, -0.007767, 0.000851, 3.611824, -8.760729]$,
$C_{i_a} = [0.014078, 0.00038, 0.000013, -0.03948, 0.092521]$,
$D_{i_a} = [1.318461, 1.514514, 1.704485, 1117.918602, -2902.101152]$.

For i_c equal to $\mathbf{Z} \in [1, 3]$:
$A_{i_c} = [0.027177, -160.147586, 203.784897]$,
$B_{i_c} = [-0.000221, 5.506333, -6.104596]$,
$C_{i_c} = [0.000048, -0.063012, 0.060292]$,
$D_{i_c} = [2.203768, 1554.274309, -2243.107934]$.

Final fits may be described as $fit_a = \sum_{i=1}^{5} a_i$ and $fit_c = \sum_{i=1}^{3} c_i$.

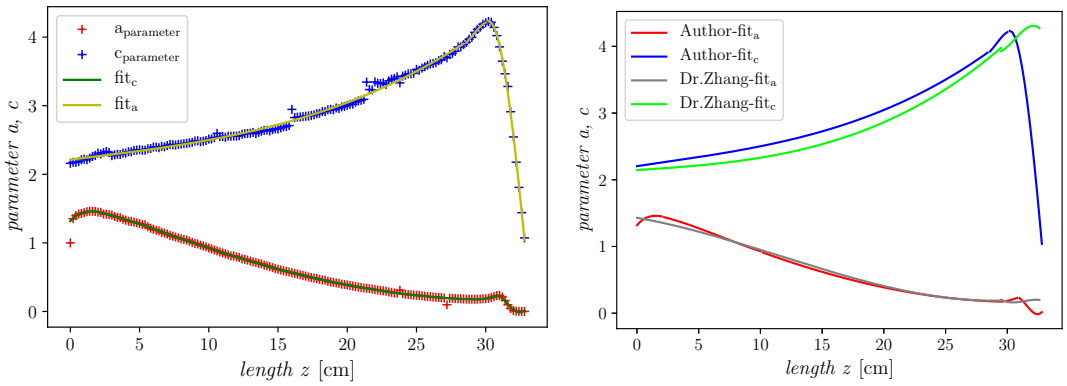

Figure 5.14: Displayed values of a and c parameters were calculated by author based on description „*Step* 1^{st}“ (p.98). These values are represented by blue and red „+“ marks on the left side of the figure with it's respective polynomial fits. To compare both fitting methods, author's vs Dr. Zhang, see the chart on the right side. Polynomial fits provided by Dr. Zhang were calculated by eq. 5.1 and eq. 5.2. Parameters a and c have different units, therefore only numbers displayed. Parameter a have identical units with calculated MESH quantity unit. In this case, the heat deposition density related to incident proton (where coulombs are represented by A·s) → a parameter unit is [MeV·cm^{-3}·A·s]; the c parameter represents the length → [cm].

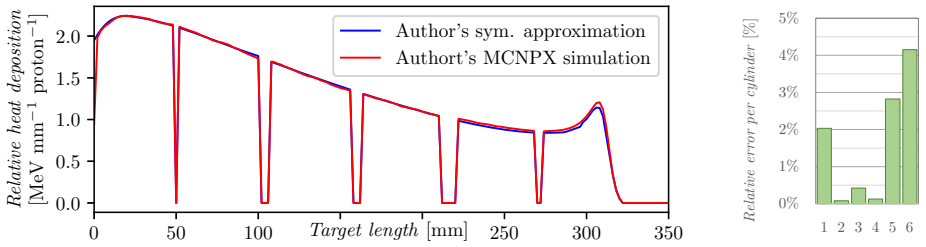

Figure 5.15: Displayed figures on the left side is identical with the Fig. 5.13 but the approximation was provided more accurately by author's script (see p.98). It fits much better to MCNPX simulation, as shown on the right side of the figure, where the relative error displayed (same method as in Fig. 5.12).

The relative heat deposition in the whole LEAD target is equal to 419.99 MeV per incident 660 MeV proton, based on the symmetrically approximated equations calculated by the author. The total integral number of incident protons was determined by activation foil method to $2.30(18)\cdot10^{15}$. The total heat deposition in the target is calculated by multiplication of the relative heat deposition with the integral number of incident protons.

Table 5.2: The LEAD target heat deposition results, divided by computation method

Author's MCNPX simulation	154.87 kJ
Dr. Zhang's symmetrical approximation	144.92 kJ
Author's symmetrical approximation	154.75 kJ

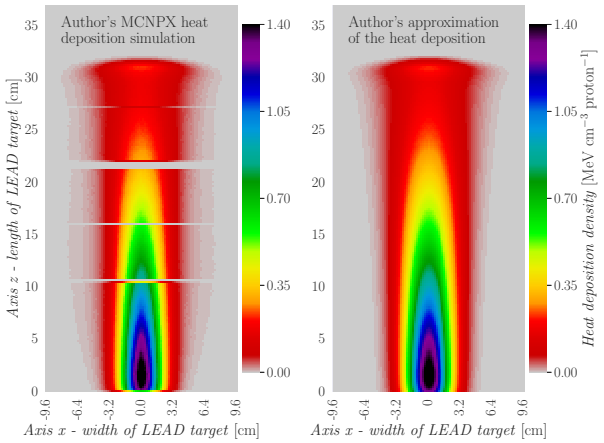

Figure 5.16: The heatmap mesh comparison of relative heat deposition density between the symmetrical approximation by calculated equation (p.98) vs MCNPX simulation. Principe of this comparison is equivalent to Fig. 5.11. The air gaps shown in the left side are not displayed in right side figure, due to the equations describe the symmetric distribution. The air gaps will be created after the source is assigned to the relevant cylinders in ANSYS Fluent. Where the air is define, there is no heating involved.

ANSYS-FLUENT simulation setting and results

The geometry of the LEAD target was simulated only for the first 10 cylinders due to most of the energy (over 99 %) being deposited in the first 6 cylinders. For this reason, the simulated volume is about half in comparison with the CARBON target simulation. It allows to use much softer mesh, however, the air gaps between cylinders are much smaller and the heat production is much higher, so the requirement for the mesh quality is much higher. In principle, due to higher requirements and lover volume, the limit of student licence is as problematic as for the CARBON target. The ANSYS Fluent setting and calculation problems are widely discussed in the CARBON target section due to it has been simulated and irradiated earlier, see section 5.2.3.

The process of geometry creation, meshing, and Fluent simulation setting of the LEAD target was recorded and is available on YouTube[67]. dissertation channel. The created mesh is displayed in the following Fig. 5.17. Very soft meshing was used for close cylinder volume due to the high temperature gradient expected. Due to that, there was not enough free cells for softer meshing of more distant volume.

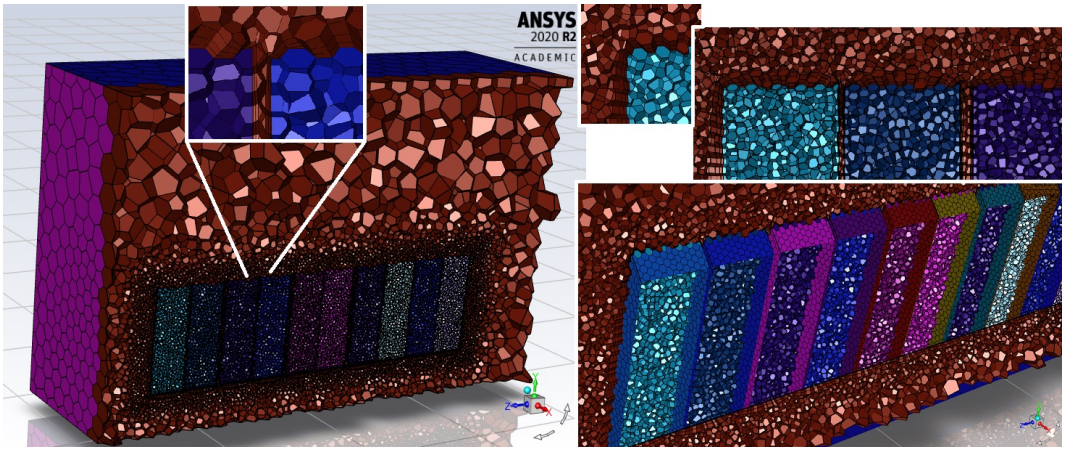

Figure 5.17: 3D model of the LEAD target with surrounding fluid volume. The mesh was created by author in Fluent meshing tool and it consist of 479,222 cells. Visualisation shows the surface mesh as well as the internal volume mesh. On the left side of the figure is shown the 3D cut through the volume in yz plane with chosen zoomed part of the meshed interfaces. The outside of the solid (interface solid-fluid) is increased number of cells by purpose of better transfer simulation accuracy. The problem of this created mesh is the limitation of 512,000 cells - more distant cells are too rough. For further research it is recommended to decrease the maximum volume of cells and growth rate of the mesh (more distant cells layer to the previous one).

[67] To watch the video, visit: https://youtu.be/oOjEZQ1Rqso

The Fluent simulation settings of the LEAD target: In principle, all not mentioned setting was used by default. The simulation was based on the same setting condition as CARBON simulation, only the lead material constant and operating conditions were different. The Fluent simulation setting is listed in p.122. The Fluent simulation case file is located in dissertation cloud, see p.197 *Fluent files*, item 3. The simulation is simplified, only lead material and fluid are simulated.

- lead material constants:
  - ▷ Density = 11,350 kg/m^3
  - ▷ Specific heat = 130 J/kg/K
  - ▷ Thermal conductivity = 34.7 W/m/K
- Physics-Operating Conditions:
  - ▷ Operating Pressure = 97,800 Pa
  - ▷ Operating Density = 1.192 kg/m^3

The exact positions of the experimental measurement of temperature were in the centre of each cylinder back side surface, the z axis distant is written in the chart (Fig. 5.21). The thermocouples were fixed by paper tape with negligible thermal insulation. The temperature probes simulated by the Fluent were defined in the centre of the cell distant -0.5 mm from the LEAD cylinder back side surface (listed in the chart as well).

Power source definition:
The power source has been defined based on the described equations, see equations 5.1, with using the calculated parameters for the LEAD target listed in p.99. The UDF was firstly written in the same principle as for CARBON target on p.123, however, since the power was assigned to the cylinders and visualised the User Defined Memory (UDM) where the power distribution is allocated, an error occurs. The reason of this behaviour was not detected, despite the written UDF was discussed with the Fluent specialists, visualised in Fig. 5.18. This UDF is attached in cloud, p.197 item 4. Nevertheless, the solution of the problem has been found. A single UDF was created per single cylinder, all of them (6 UDF for 6 cylinders) were compiled, and finally allocated one by one. The total heat generation by Fluent simulation was 159.4 kJ based on monitoring per each time step. The ratio of each cylinder contribution was for cylinders 1→8: 27.85 %, 24.14 %, 15.54 %, 13.36 %, 10.63 %, 8.16 %, 0.21 %, 0.11 %, respectively. For comparison, see Tab. 5.2 and Fig. 5.7.

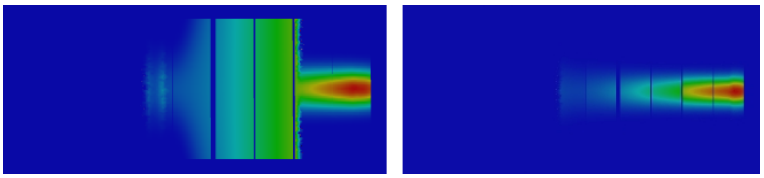

Figure 5.18: Visualisation of the thermal power source defined by UDF. On the left side is shown the problematic UDF, on the right side is shown the correct one - each cylinder defined by own UDF as described in previous paragraph (the colour bar is not identical, only for the problem illustration).

Fluent simulation results

The fluid temperature (target cooling by natural convection) was monitored over the irradiation time. The solution animations were created and are available on YouTube[68]. The static visualisation of the heat transfer simulation are shown in Fig. 5.19.

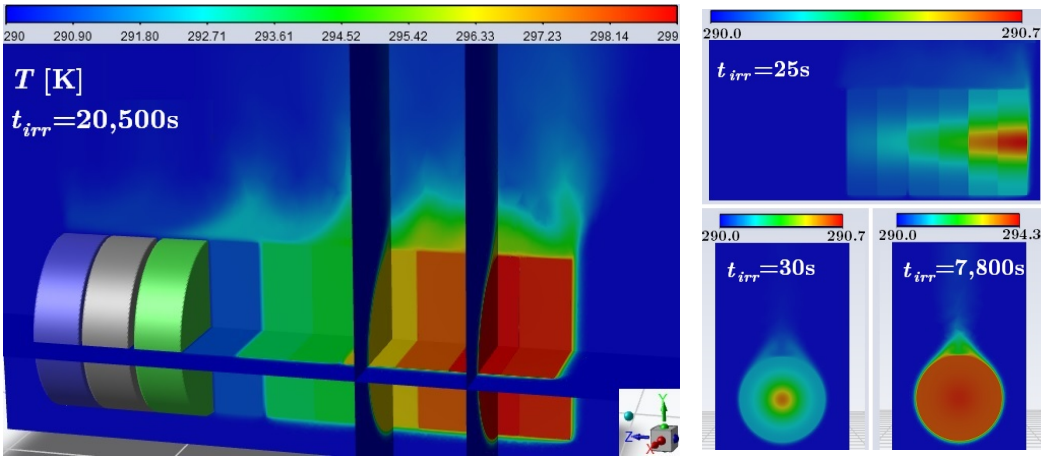

Figure 5.19: Fluent simulation results of the LEAD target temperature distribution in various irradiation time and various planes. On the left side is shown the 3D temperature visualisation in irradiation time 20,500 s. The solid of cylinders 8,9,10 is visualised. The right side of the figure shows yz plane on the top and two xy planes at bottom part. The irradiation times are listed in the respective figure screen.

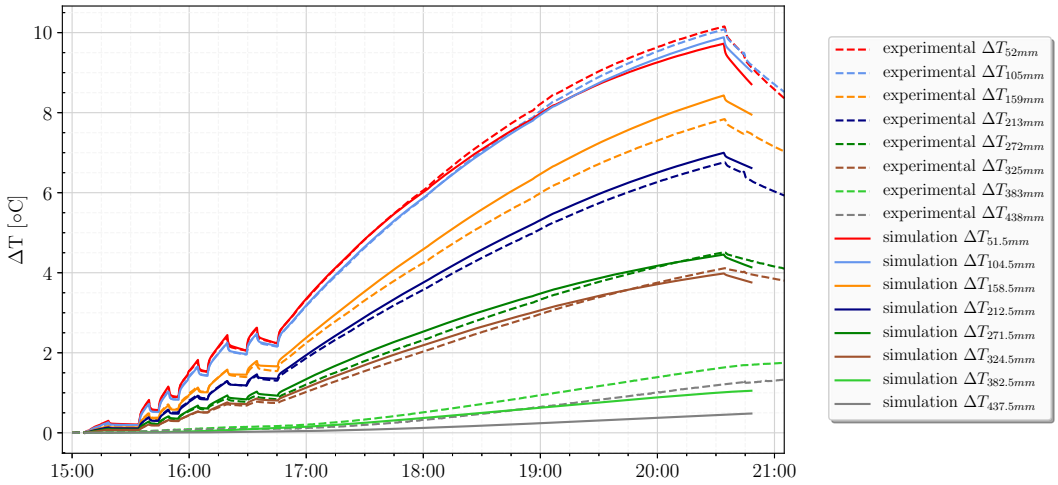

Figure 5.20: Comparison of the ΔT for ANSYS Fluent simulation and experimentally measured data.

[68]The YZ plane animation is available here: https://youtu.be/4zxb4y1UdhE,
XY plane animation for z=186mm: https://youtu.be/QevlUmI2gzU,
XY plane animation for z=75mm: https://youtu.be/jYHtHNRO9TU,
3D animation: https://youtu.be/C_KKmKTbOR4, and finally,
XZ plane animation: https://youtu.be/uVRbrjrYu0c.

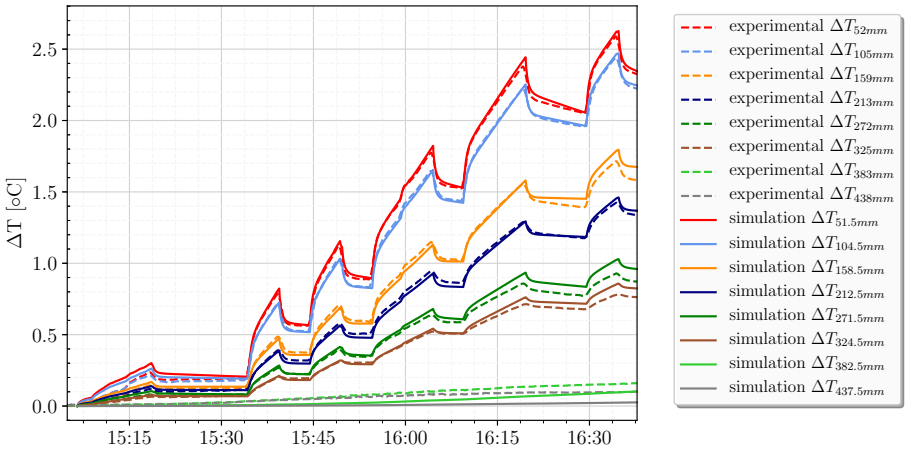

Figure 5.21: Comparison of the ΔT for simulation and measured data - zoomed version of the experiment beginning.

5.1.4 Neutron leakage monitoring on LEAD target

The neutron leakage probes were installed outside of the LEAD target at a radial distance R=13 cm in two different axial z distances. The first measuring distance was chosen 6 cm (beginning of the second cylinder), the second one at distance 13.5 cm (centre of the third cylinder). For each measuring position, there were two probes for comparison - blank probes from tantalum material, and a fission probe from enriched uranium. These probes were thermally insulated from the target (heat source) to decrease the heat transfer ratio and from the opposite side where the probes were cooled by air. Beside this insulation, individual probes were inserted in the centre of a thermal foam insulation block with dimensions 6x4x3 cm^3 The measurement was performed on the right side of the LEAD target, see the following Fig. 5.22.

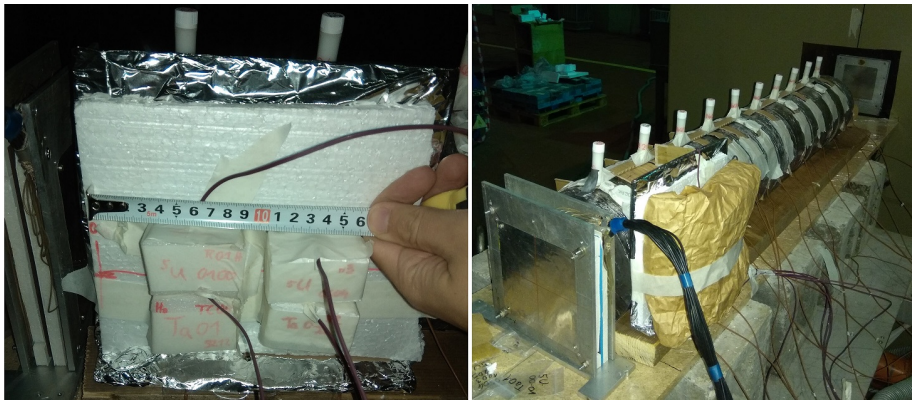

Figure 5.22: Neutron leakage probes installation on the LEAD target. On the right side picture is shown the whole target with already insulated neutron leakage probes (light brown insulation on the right side of the LEAD target).

Results of relative temperature measurement

The temperature of the neutron leakage probes was measured by thermocouple type E by using the NI9212 card. The sample masses were not identical, anyway, its difference was lower than 30 % (it does not affect the results proportionally). The uncertainty of insulation shape causes some small divergences in heat transfer as well as the uncertainty of correct sample fixation. The uncertainty of thermocouple measurement is identical to other measurements of this thesis (already discussed in the section 3.1.1). The relative neutron flux can be estimated based on this measurement, however several simplifications must be taken in consideration. Based on Fig. 5.24 the neutron flux at the first location (z=6 cm) is very approximately about 40 % higher than the neutron flux at position z=13.5 cm. This comparison method is widely discussed in the section below Fig. 5.31.

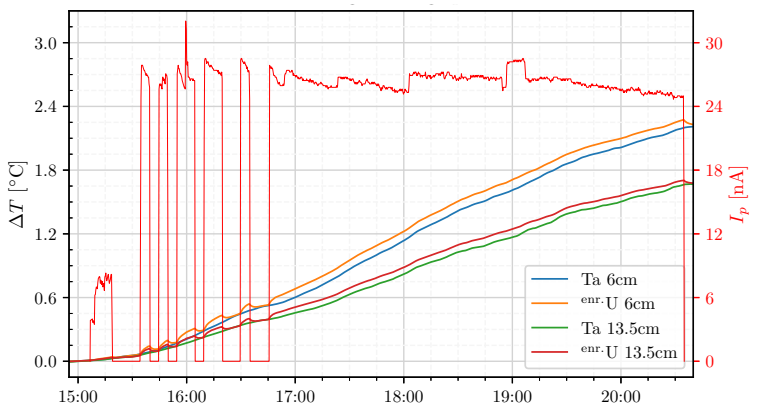

Figure 5.23: Temperature differences of neutron leakage probes, experiment with the LEAD target. The chart shows on left y axis the temperature difference of blank (Ta) and fission ($^{\text{enr.}}$U) probes at two different locations. On the right axis y is shown the proton beam current. The neutron leakage is proportional to number of reactions inside of the target and it decreases quadratic with radius increase. The radius is identical, only axial distances are various (6 cm and 13.5 cm). The background temperature is caused by heat transfer from the LEAD target (described in 5.1.2), slowed by thermal insulation between probes and target (previous picture). It shows that the heat is directly releasing inside of the fission sample, while the blank sample increase is caused only by background heat. By this reason it is suitable to subtract these two probes temperature to display direct heat (rather temperature) caused by fission reaction. It is shown on following chart Fig. 5.24.

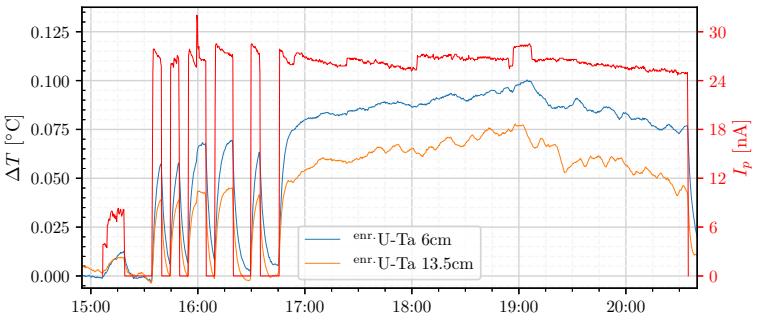

Figure 5.24: Direct ΔT increase of neutron leakage fission probes - LEAD target. The chart shows the difference temperature between blank Ta probe and fission $^{\text{enr.}}$U probe for two measured axial z distances. The neutrons are produced directly based on spallation reaction caused by protons from accelerator. It shows the beam outages where probes detect no direct heating caused by absence of leaking neutron. Due to identical insulation, the relative neutron flux difference may be approximately estimated by ratio of these two measurements. However it is very tentative due to various temperature background and several simplifications. Earlier temperature peaks are not so affected by target heat transfer due to its delay.

5.1.5 Results discussion - LEAD target

The lead material is widely used as a spallation target due to its suitable characteristics. It has a high neutron yield per proton which grows with the proton beam energy (Fig. 2.5). For this reason, the heat production per produced neutron decreases with the growing energy of the incident proton. For this reason, the higher proton beam energy is better (the goal of the spallation target is to generate neutrons, not heat). The heat production inside of the spallation target is proportional to the beam current. The target must be actively cooled for higher proton fluxes. For this cooling reason, the molten spallation targets are rather used for future ADS design than the solid targets. The spallation target heat study is very crucial for accelerator-driven reactor design. For example, the MYRRHA project uses LBE target with specific maximal power 350 W·cm^{-3} per mA, where the simulated temperature maximum is about 525 °C [126].

The LEAD target experiment was in principle very similar to the MYRRHA project spallation target, however, the target was solid (cooled by air) and the proton current was about 0.001 % of the MYRRHA design. It allows studying similar reactions with less radiation and thermal stress exposure. Similar simulation techniques (MCNPX simulation for particle transportation, combined with heat transfer simulation by ANSYS Fluent) were used and experimental measurement was performed by accurate thermocouple measurement. The neutron production was monitored on the surface by the offline gamma-ray spectrometry method (studied by other ADS group researchers) and by an independent online method of fission probes ΔT measurements. Tiny samples producing heat proportionally to the neutron flux were compared with a similar geometry of blank samples.

The LEAD target was irradiated by 660 MeV protons for 5 hours including several irradiation pauses for target cooling monitoring and for monitoring heat transfer through the thermal insulation. The temperature measurement reflects the proton flux without extra delay. Such a tiny proton beam current changes as 0.6 nA (from 2.6→3.2 nA) lasting less than 20 s was reliably detected by TC probes, see irradiation time 16:00 in Fig. 5.4. Temperature changes were measured in the back-side surface centre of each Pb cylinder. Due to negligible ΔT changes of more distant cylinders, only the first 10 cylinders are shown in charts. About 99.7 % of the heat was released in the 30.7 cm of the lead. In summary, 95.12 % of the total target heat was generated by protons reaction, 3.03 % by photons (gamma heating), 1.17 % by pion$^+$, and about 0.68 % of the total heat was generated by neutron reactions. The thermal power distribution in the cylindrical volume was calculated by MCNPX, approximated with a Python script by several equations, including its dynamic changes caused by proton current instability during the whole irradiation time. These equations were written in C language to User Defined Function (UDF) and used as a dynamic source definition for ANSYS Fluent heat transfer simulation. The current of the proton beam over the irradiation time was calculated based on relative current monitoring by gas-filled ionisation chambers, combined with the estimated total number of interacting protons acquired by the activation foil technique (Cu and Al foils evaluated). The frequency of the proton beam current monitoring is about 0.06 Hz.

The simplified 3D geometry of the LEAD target with surrounding fluid was created in ANSYS SpaceClaim Geometry and the created volume was meshed by the ANSYS Fluent Meshing tool. Due to the utilisation of the student licence of ANSYS, only 512,000 cells could be simulated (the academic licence is limited by the perimeter distance from the institute). For this reason, the simulation of natural convection is not perfect. The

interface solid-fluid is equipped with a quality mesh to ensure the interface heat transfer, however, the more distant cells of the fluid are too large and cause simulation uncertainties.

The final comparison between the experimental data and simulation is shown in Fig. 5.20. The simulation fits very well the experimental measurement. The maximal simulation error is about 7.5 % for the third cylinder measurement. It is caused by several factors. On the surface of the target was fixed the experimental samples by paper tape and a cardboard construction was inserted between cylinders. It influences the heat transfer a lot, see Fig. 5.2. The construction parts which were holding the target are not simulated, as well as the ionisation chamber on the front side of the target. It changes the fluid cooling behaviour in the real experiment. The roughness of the Pb cylinder geometry and sharp surface fragments cause the uncertainty of the volume for simulations in MCNPX and Fluent. Finally, there are ANSYS Fluent model uncertainties caused by the approximated heat source definition (uncertainty up to 5 %) and the mesh roughness in more distant parts. The ΔT measurement uncertainty also slightly contributes to the total experiment vs. simulation error.

The experiment of neutron flux monitoring shows very interesting results. The two geometrical similar probes of Ta and $^{\text{enr.}}$U materials were placed at similar neutron flux, covered by thermal insulation and its heating was monitored by very accurate TC measurement. The dependency of ΔT to proton beam current changes were monitoring. These results are shown in Fig. 5.24. This measurement is very dependent on the thermal insulation quality, data acquisition setting, and surrounding fluid conditions. The direct heating can be determined due to several beam outages - heat transfer from the warmer target has a delay, and is suppressed by thermal insulation. By this measuring method is even visible (detectable) such a small proton current change as mentioned 600 pA. This method is suitable for short irradiation pulse monitoring. Tiny volume probes are very sensitive, however, the measurement sensitivity should be studied in laboratory conditions with unified neutron source utilisation. It was planned to compare the experimental results with the MCNPX simulation of the heat deposition and the neutron flux of the neutron leakage to discuss the sensitivity and accuracy of the measurement. Finally, it has been decided to publish these results directly in the prepared publication.

5.2 CARBON target

The CARBON target consists of ten cylinders, each with diameter 19 cm and length 10 cm. The air gap realised for measuring purposes (for the thermocouples measurement and activation foil installation) was about 1 cm thick, located after each even cylinder. Mass density of the carbon was ρ_c=1.8 g·cm^{-3}, based on the manufacturer data sheet. The total mass of the whole CARBON target was about 51 kg. The total target length was 104 cm (consisted of 10×100 mm of the carbon cylinders and 4×10 mm of air gap). Due to a low reaction cross-section of carbon, some particles are going through the target (the proton beam Bragg peak would be located in the carbon length of 112.5 cm, based on MCNPX simulation). The target was irradiated by 660 MeV protons for 277 min excluding several unplanned beam outages caused by beam instability, see the Fig. 5.26. Actually, the beam instability had a positive effect for the target cooling monitoring, to estimate the direct heating caused by beam occurrence, and finally, for the comparison of experimental vs. simulated dynamic data. The total experiment duration was about 336 min and the total number of incident protons was determined to N_p= 2.40(19) · 10^{15}. The beam parameters were: $FWHM_x$=35.1 mm, $FWHM_y$=34.6 mm, x_0=-5.1 mm, y_0=-0.1 mm.

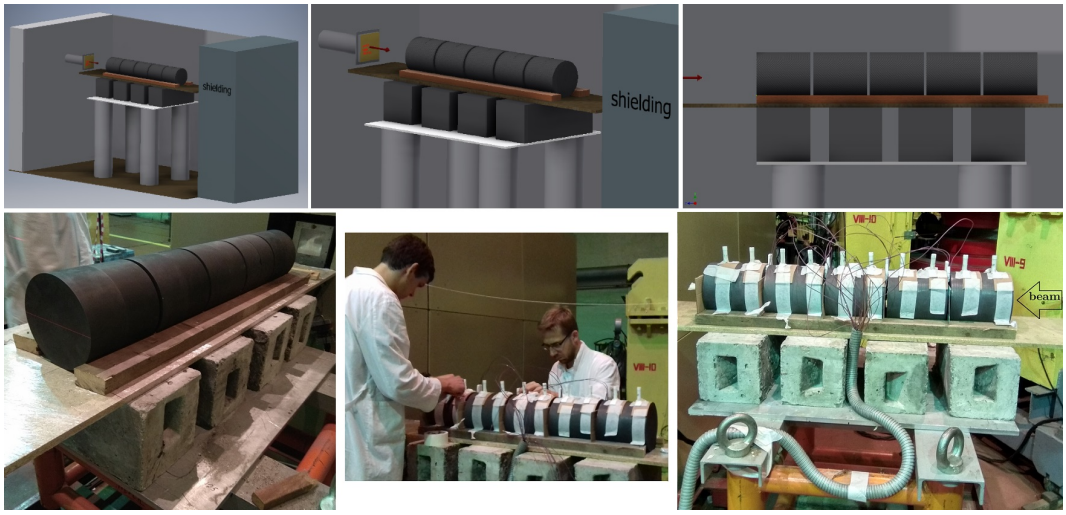

Figure 5.25: The 3D CAD model visualisation of the CARBON target is shown on the top of this figure. At the bottom part, there are real photographs from the experiment preparation. The final installation of the target is shown on the most left side, the thermocouples and activation foil installation by author (wearing glasses) and salt ampules samples by D. Král (black hair) is shown in the centre, and finally the CARBON target ready to be irradiated on the most right side (with the proton beam direction label).

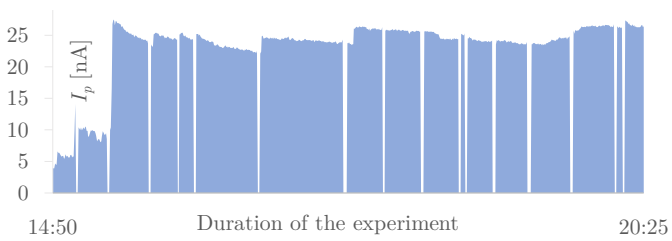

Figure 5.26: The proton beam current during the CARBON target irradiation.

5.2.1 Temperature measurement of the CARBON target

The temperature was measured on the back-side surfaces of each even cylinder at three positions (positions „A“, „B“ and „C“ - marked by green, red, and yellow colours, respectively - in Fig. 5.27). The measuring position length was accordingly 20, 41, 62, and 83 cm (it corresponds to 2nd, 4th, 6th and 8th cylinder). In total, there were 12 measuring positions. Due to the copper activation foil sample (total size of 50x50mm) located in the centre of each measured cylinder, the TC could not be installed in the centre where most of the heat was produced. In following, the locations of each position are described by $(x_i; y_i)$ in [mm] (i=position label), based on the blue axes coordination system labelled on Fig. 5.27, left. The centre of the target is located at position (0,0); position „A“ (40,-15); position „B“ (40,15); position „C“ (0,50). The polystyrene holder width was 25 mm and the thickness 10 mm. The thorium samples sizes were 10×10×1 mm^{-3}, equipped by TC in the centre.

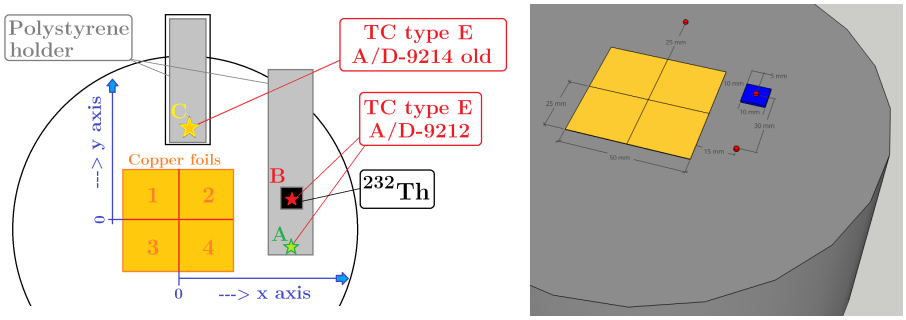

Figure 5.27: The CARBON target measuring positions. On the left side is shown the 2D sketch with description marks. The 3D CAD model with real dimensions is shown on the right side (Th sample = blue coloured volume, TC locations = red coloured volume).

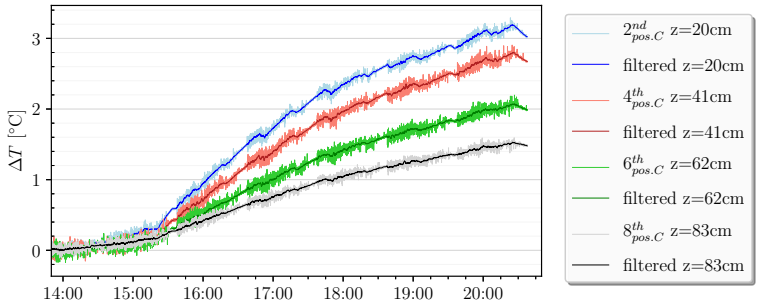

Figure 5.28: During the testing measurement before the experiment, a problem with an older A/D converter NI2914 has occurred. Measured data were very noisy. It was caused by new measuring setup in LabView with wrong data storage method. During data saving on NI9214, the electronics was wrongly evaluating the data. It took about 50 minutes to correct the data evaluation, but due to an one hour saving interval, data were noisy almost all the time. This fact was found only several hours before the experiment installation so there were no time for troubleshooting. By this reason, important positions were measured by second card NI9212 and these noisy measurement was install to the position „C“, only for controlling purposes. Data measured by NI9414 (noisy) are displayed by light colours. Filtered version of these data is displayed by respective darker colour.

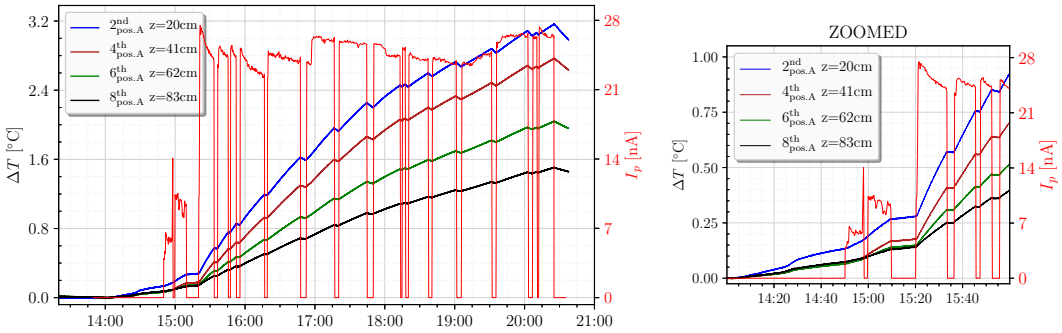

Figure 5.29: The main temperature measurement at the position „A“ of the CARBON target is displayed on the left axis y together with the proton beam current on the right $y2$ axis. Based on the temperature measurement results analysing it must be stated that the heat is distributed quite evenly, as in the radial direction, so along the target length. As the protons interact with the target along whole length, the temperature is uniformly and slowly decreasing along the target length. The maximum of measured temperature differences reaches about 3-time lower values in comparison with the LEAD target. It is caused mostly by lower proton interaction of carbon, therefore the Pb target releases the heat in much smaller volume, and generally there is different specific heat constant. Zoomed part of the experiment beginning is shown on the right side by reason to discuss the temperature measurement sensitivity of surrounded conditions. The experiment was prepared in advanced. The instruments were installed and the measurement was started about 24 hours before the experiment has begun, to get steady temperature of target and electronics. Unfortunately, one of our colleague was installing some instrument during 14:15-14:30 → T of the 2^{nd} pos. increased.

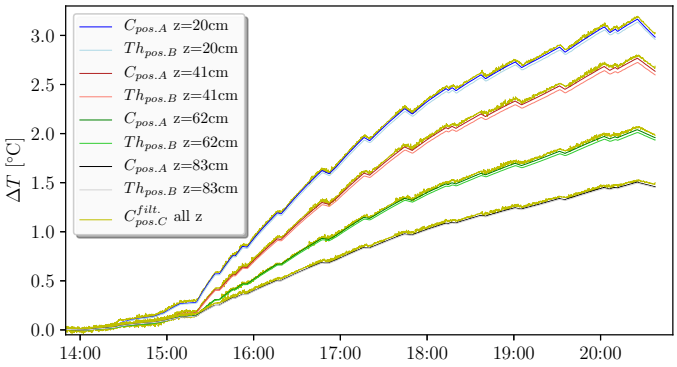

Figure 5.30: All measured positions by TC type E (totally twelve) are displayed. The main position „A“ = dark colour, labelled as $C_{pos.A}$ (where the first letter describes measured material) → $Th_{pos.B}$ is used for the Th sample at position „B“ = light colours. To simplify the figure, the „C“ position is represented by yellow colour for all lengths, and only filtrated data are displayed (for raw data see previous Fig. 5.28). The thorium sample temperature is slightly lower than the carbon temperature at the position „A“. It is causes by tiny thermal insulation between carbon and thorium (the heat resistance decreasing the heat transfer rapidity from the CARBON target to the Th sample). It seems the „C“ position reaches slightly higher temperatures, but not significantly (position is above the centre). This position „C“ is no more important (were used only for controlling purpose).

The reason the thorium sample was installed inside of the CARBON target is based on the expectation that Th sample reaches higher direct thermal power density than the carbon material if the proton means occurs (higher heating reaction cross-section). If look very carefully on the differences between the light and dark characteristics in the Fig. 5.30, it is slightly noticeable that there are some tiny trend changes during the beam occurrence. These two characteristics have been subtracted (*pos.A-pos.B*) to reach zoomed version of this phenomenon. For the position z=20cm, see the Fig. 5.31; other positions are shown in appendix (Fig. E.2). To see the real temperature growth caused by direct particle heating (proton beam occurrence), the increasing temperature background must be subtracted. It may be done manually peak by peak by linear approximation of the temperature background in the peak boundaries. Due to many peaks for each of measuring position, the Python script containing the visualisation was created (see appendix p.189).

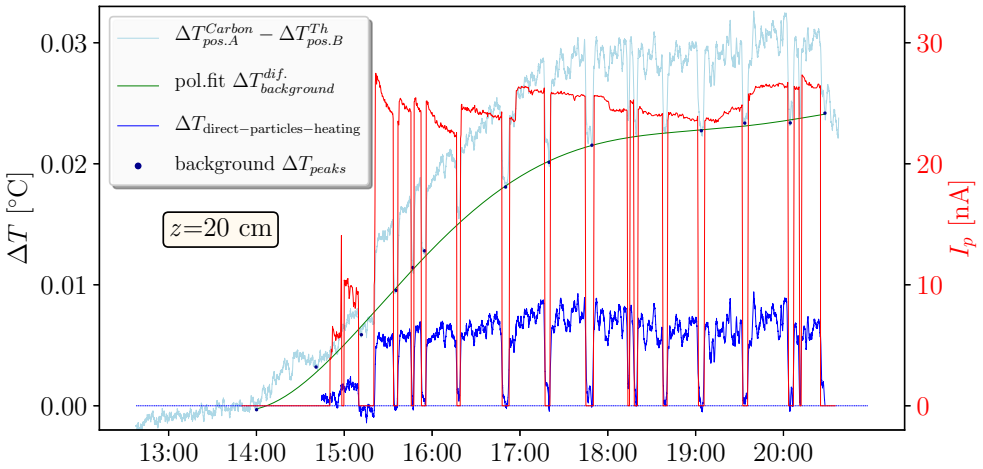

Figure 5.31: Calculation of the thorium sample direct temperature responses, based on proton beam occurrence. Phenomenon described in previous paragraph. The increasing thorium temperature background is fitted by polynomial function of 6^{th} order (green) and subtracted from the light-blue characteristic. The final ΔT caused by direct particle heating is represented by blue colour. Other measuring positions are located in appendix p.191 due to larger dimensions.

Since the direct temperature difference was calculated, the boundaries of individual temperature peaks must be located and their values approximated (due to noise). The idea was based on expectation that the direct heating of Th sample could be representing the number of reactions - only relatively. Finally, each temperature peak was defined and its maximum was approximated by a linear regression calculated by Python script - attached in appendix, p.192. For both mentioned scripts, the video manuals were recorded[69]. The comparison of data enhanced by the linear regression is shown in Fig. 5.32, with displaying the proton beam current as well. Due to many subtractions, really small measured values are involved. In essence, such small values are measured in the range of TC+electronics sensitivity and can be seriously given only by respecting several measuring conditions.

[69] See at https://youtu.be/bxQp_vvTLIY manual for data subtraction of pos.A with pos.B + direct Th ΔT background polynomial fits + direct temperature calculation, and https://youtu.be/9XoYIU1r0Rk for the direct temperature peaks location and their linear regression.

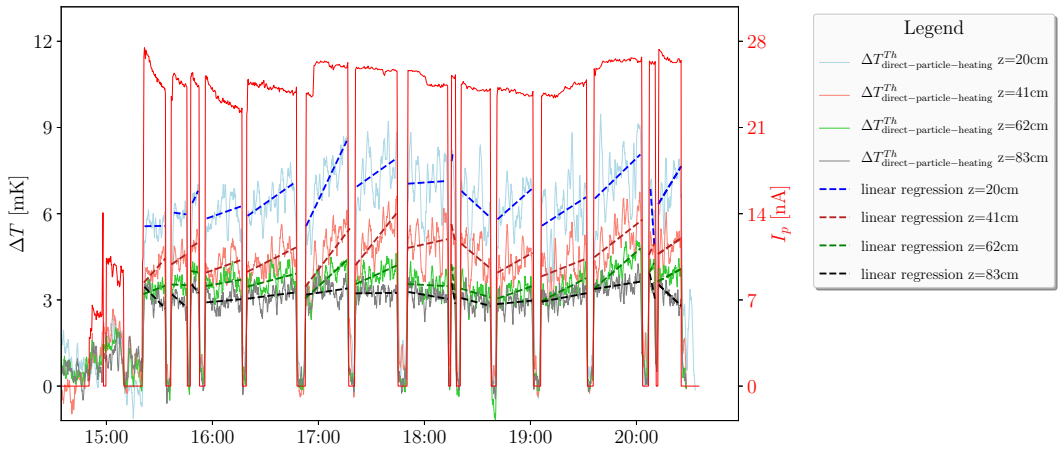

Figure 5.32: Direct particle reactions heating of the Th samples, monitored by temperature measured by highly accurate TC type E for the CARBON target irradiation.

Finally, the linear regressions of each ΔT peaks are compared together and the median of all peaks is calculated per each position. Peak boundaries and the beam current are not important due to the calculation of relative values. Results are presented in the following Tab. 5.3, including the data from MCNPX simulation, which are widely discussed in the next section. The full version of the measured data is enclosed in Tab. E.1.

Table 5.3: Relative comparison of the thorium sample direct heating

Method of the Th direct heating comparison	z=20cm	z=41cm	z=62cm	z=83cm
Relative ΔT measurement by TC type E	100%	70%	55%	48%
Relative heat deposition, MCNPX simulation	100%	78%	58%	46%

The comparison of ΔT relative values with rel. heat deposition values calculated by MCNPX can bring interesting ideas for future more detail study. If the beam changes are rapid enough (heat transfer delay is much longer) → temperature probes with a suitable sample might be very cheap detectors of the relative flux changes. In this case the thorium sample has been used, but in principle more common materials can be utilised as listed in Tab. 5.5. This phenomenon was planned to be a study in further experiments during the end of 2019 or 2020. Unfortunately, due to the combination of several complications, this planned experimental irradiation was not performed yet. More information about direct heat deposition inside of the thorium sample and the carbon target generally are widely discussed in the following subsection 5.2.2.

5.2.2 Simulation of the CARBON target by MCNPX

At the beginning of this chapter, the previously discussed problem of thorium sample direct heating and its possibility of wide utilisation, is going to be finished. The proton reactions on the CARBON target produce very hard neutron spectra of lower flux. Thorium sample heat deposition was simulated by MCNPX to determine the total heat deposition $E_{dep.}^{total}$ [J] per each measured position and contribution of all particles. These data are shown in Tab. 5.4, particles contribution is represented by the ratio values of total amount ($E_{rel.}^{particle}$ [%]) and their median is calculated through all positions. The relative values across positions are shown in comparison to the first position (z=20cm) on the right side highlighted by the green colour. The values are very small but so is the sample volume. In short, it is detectable only due to very accurate measurements, as described in Chap. 3. Also it would be not possible without an accurate analysing technique in Python which involves some filtering methods.

Table 5.4: The thorium sample heat deposition.

	$E_{rel.}^{n}$	$E_{rel.}^{\gamma}$	$E_{rel.}^{p}$	$E_{rel.}^{\pi^+}$	$E_{dep.}^{total}$ [J]	$E_{rel.}^{total}$ [%]
z=20cm	6.4%	0.3%	89.6%	3.8%	1.928	100%
z=41cm	6.2%	0.3%	90.8%	2.7%	1.499	78%
z=62cm	4.6%	0.2%	93.6%	1.6%	1.120	58%
z=83cm	3.4%	0.2%	95.7%	0.7%	0.883	46%
median	**5.4%**	**0.2%**	**92.2%**	**2.2%**		

Due to most of the direct heat in thorium is released by proton reactions, there were and idea to use also other materials for further experiments. Such as iron or lead, which are more common and abundant. Together with already used thorium and more exotic natural uranium, the simulation was performed. MCNPX simulation with a centred beam of symmetrical shape has been calculated. Four geometries of identical samples with dissimilar material were symmetrically located in radial positions. Each sample volume was identical to the previous Th sample (10×10×1 mm^{-3}) but nowadays, the proton beam was set right in the centre. Positions were (x,y) in [mm]: Pb(40,15), Fe(-40,15), ^{nat}U(40,-15), and finally Th(-40,-15). The result of this comparison is shown in Tab. 5.5. The results show that the iron sample releases merely about 22 % less energy than thorium. It means it could be a very simple and cheap probe. Full table of these results is placed in the appendix, see Tab. E.2. On the same page, there is a placed Tab. E.3, where compared results calculated by two different libraries (ENDF70 - which used for all performed simulations vs LA150N (LANL)). The results show that only uranium has noticeably different reaction cross-section. However, the library diversity is already out of this thesis topic.

Table 5.5: Direct heating of various samples - CARBON target, MCNPX

	$E^{total}_{deposition}$ [J] - per sample			
material	Pb	Fe	^{nat}U	Th
z=20cm	2.35	2.27	5.14	2.90
z=41cm	1.86	1.79	4.09	2.40
z=62cm	1.42	1.38	3.07	1.77
z=83cm	1.13	1.11	2.45	1.39

More appropriate unit to value the heating processes is **the relative power per mass**. If the average beam power is considered, for z=20cm, the results are: $p^{Pb}_{rel.}$=124.77 μW·g^{-1}, $p^{Fe}_{rel.}$=173.50 μW·g^{-1}, $p^{^{nat}U}_{rel.}$=161.80 μW·g^{-1}, and finally $p^{Th}_{rel.}$=148.87 μW·g^{-1}. The sample density plays its role as well as the reaction cross-section.

Surrounded parts heating

During the experiment planning, there was an thought that the surrounding construction materials could influence the total heat of the whole target. As shown in Fig. 5.1, there is a wooden base with two side holders under the target, which are held by four concrete bricks. These materials are crucial for heat deposition studies due to their close location under the target. The MCNPX simulation results are shown in Tab. 5.6.

Table 5.6: Heat deposition of the CARBON target's surrounded materials, MCNPX

	wooden base			concrete blocks			
	base	left	right	1st	2nd	3rd	4th
mass [kg]	6.2	1.4	1.4	38.5	37.9	39.1	38.5
$E^{total}_{deposition}$ [kJ]	1.1	0.4	0.4	0.7	2.7	3.1	2.3
$E^{proton}_{rel.}$ [%]	86.3	85.8	85.8	68.8	86.0	90.6	93.0
$E^{neutron}_{rel.}$ [%]	8.5	8.7	8.7	12.2	6.4	5.3	5.0
$E^{photon}_{rel.}$ [%]	0.4	0.3	0.3	2.6	1.0	0.7	0.6
$E^{pion^+}_{rel.}$ [%]	4.9	5.2	5.2	16.5	6.5	3.3	1.4

Generated heat is already reaching the units of kJ, but the mass must be considered. As in the previous case, the relative power per mass is going to be used. The wooden base reaches 10.64 μW·g^{-1}, side wooden holder - each 15.59 μW·g^{-1} and the concrete bricks only 1.15 μW·g^{-1}, 4.34 μW·g^{-1}, 4.82 μW·g^{-1} and 3.55 μW·g^{-1} in respective order. Power of these materials might be neglected because it does not noticeable contribute to the carbon power.

MCNPX heat deposition simulation - MESH

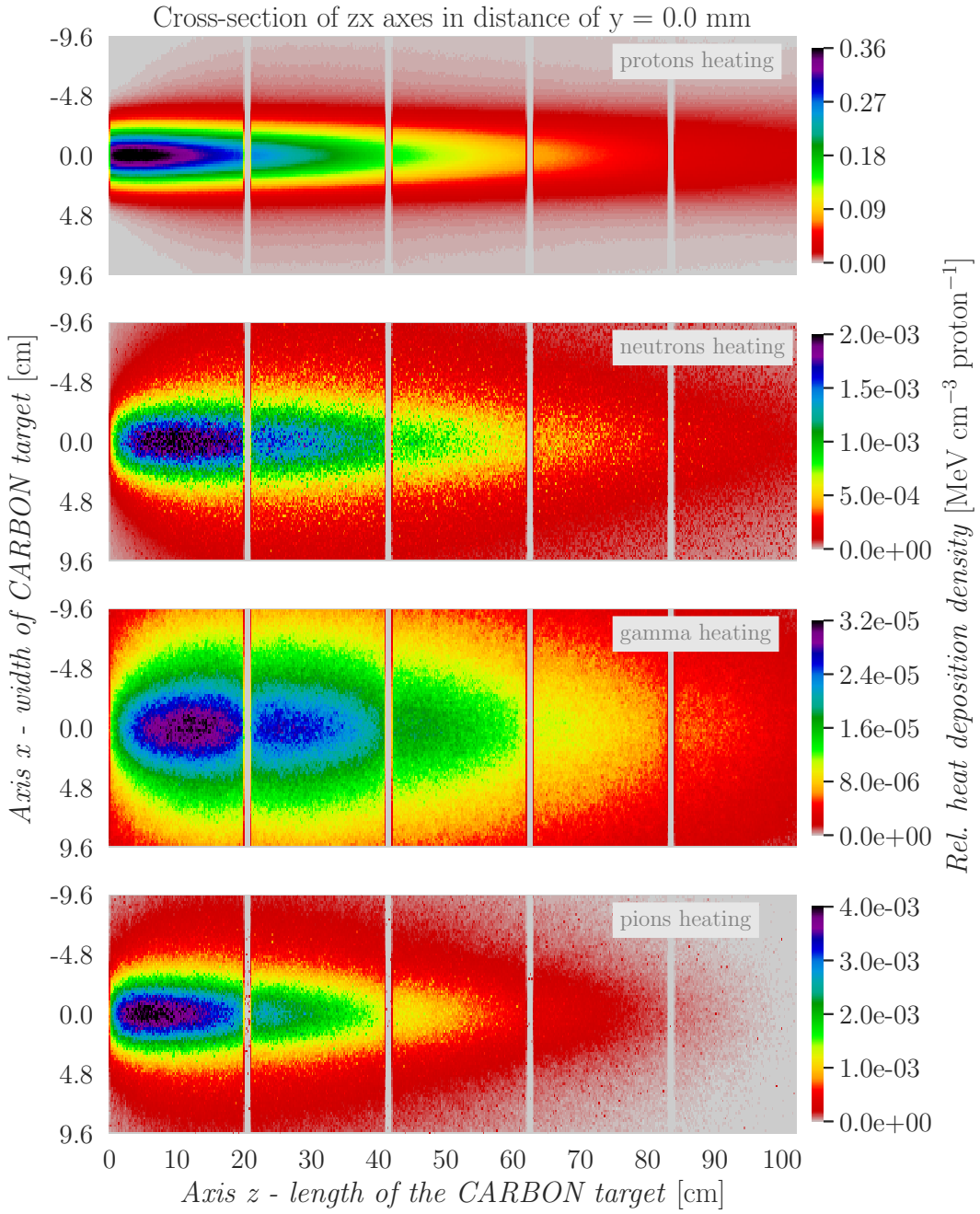

Figure 5.33: Relative heat deposition density mesh tally of the CARBON target simulated by MCNPX. Charts display rel. heat deposition density of each participated particles → proton, neutron, photon and pion^{+}. Each chart has own heatmap distribution, the max value of each chart is represented by black colour, carefully watch the units. This figure describes well the distribution of each particles heating but does not allow to compare them easily each together. By this purpose there are comparing charts in appendix, see Fig. E.3.

Previous figure shows that the major heat deposition is caused by proton reactions. All other particle heating values are at least about 2 orders of magnitude lower. The total heat deposition is therefore very similar to the proton heating one. It is shown in Fig. 5.34. Relative heat deposition density was recalculated to the total heat deposition inside of the target, it is E_{total}^{CARBON}=140.16 kJ. Relative heat generation contribution per each cylinder is shown in Fig. 5.35. Although the proton heating portion is major, the other particles contribution is also plotted in Fig. 5.36. All these charts are equivalent to the LEAD target description in p.94.

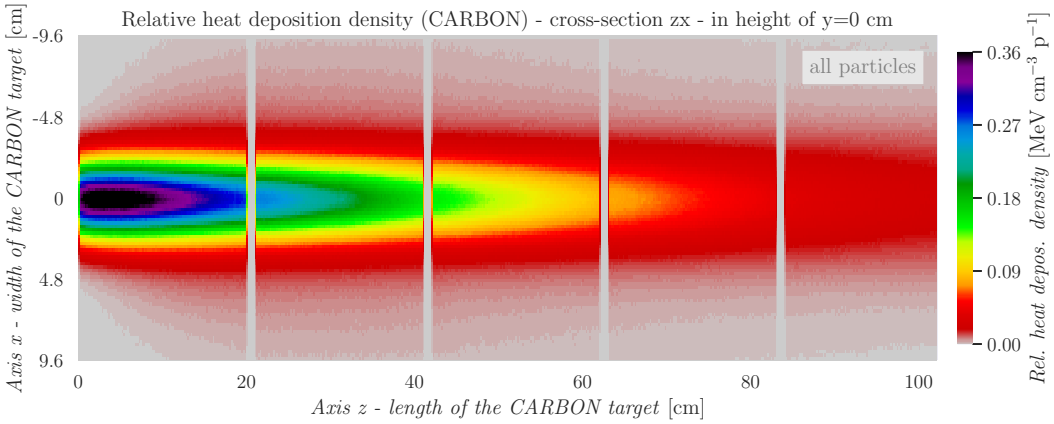

Figure 5.34: Relative heat deposition density of the CARBON target simulated by MCNPX - all heating particles are involved.

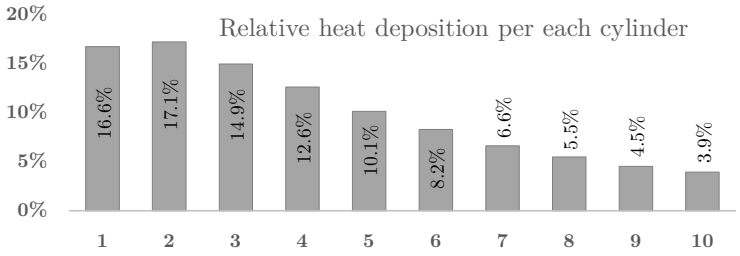

Figure 5.35: Relative heat generation per CARBON target cylinder.

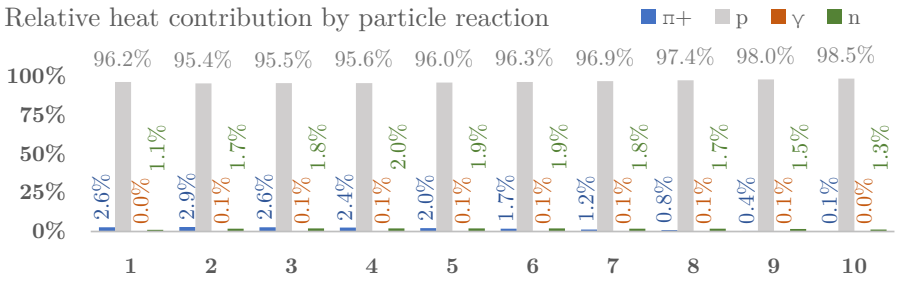

Figure 5.36: Comparison of the relative heat deposition by particle reactions per cylinder.

To perform an identical target description with the LEAD target, the CARBON target was virtually partitioned into a cylindrical annulus (method described in p.95) and each geometry heating was calculated. Due to the beam is not centred well, the heating does not reach an identical maxim as for the LEAD target.

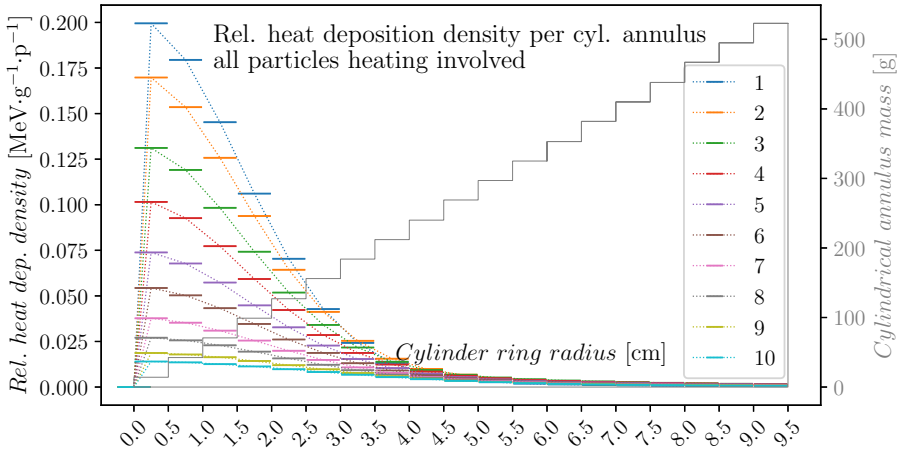

Figure 5.37: Relative heat deposition density of the CARBON target's cylindrical annulus. The mass of cylindrical annulus is displayed on the left y axis. The numbers in the legend represents the order of cylinder from the front side. The axis x is from both charts on this page used form describing area between inner and outer radium of the annulus. This topic is discussed in Fig. 5.9, and section above it.

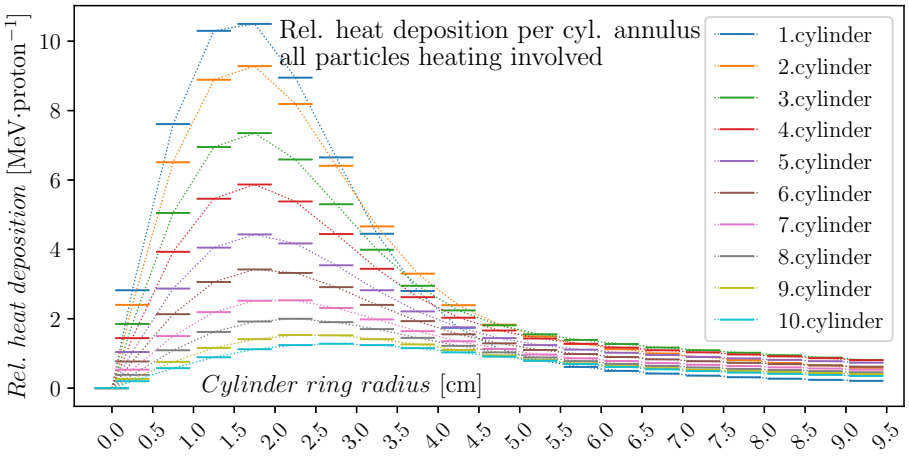

Figure 5.38: Relative heat deposition of the CARBON target's cylindrical annulus. Results reached by multiplying left and right axis data of Fig. 5.37, per each cylindrical annulus.

5.2.3 Heat transfer simulation of the CARBON target by ANSYS

The earlier heat transfer calculation has been carried out by Dr. Zhang's team from IMP Lanzhou. The relative power was estimated by this team by the following equations.

$$\begin{aligned}
a_{\ 0\to 9.5\text{cm}} &= 0.02635 \cdot z - 4.937 \cdot 10^{-3} \cdot z^2 + 2.427 \cdot 10^{-4} \cdot z^3 + 0.3264 \\
a_{\ 9.5\to 104\text{cm}} &= -7.955 \cdot 10^{-3} \cdot z + 4.61 \cdot 10^{-5} \cdot z^2 - 4.985 \cdot 10^{-8} \cdot z^3 + 0.4094 \\
c_{\ 0\to 9.5\text{cm}} &= 0.05383 \cdot z - 7.929 \cdot 10^{-3} \cdot z^2 + 4.583 \cdot 10^{-4} \cdot z^3 + 2.072 \\
c_{\ 9.5\to 104\text{cm}} &= 4.087 \cdot 10^{-3} \cdot z + 1.97 \cdot 10^{-5} \cdot z^2 + 1.286 \cdot 10^{-6} \cdot z^3 + 2.223
\end{aligned} \tag{5.8}$$

The power calculation is performed by the same equations as used for the LEAD target, eq. 5.3, eq. 5.4 and eq. 5.5. Results of this calculation were not sufficient, as shown by several comparisons in the following Fig. 5.39.

The author performed an own approximation in the same way as for the LEAD target (p.98). Values of a and c parameters were fitted by 3 polynomial functions for the a curve and 2 polynomial functions for the c curve by Python script (Section 5.1.3). These polynomial functions are written in the following eq. 5.9.

$$\begin{aligned}
a_{\ 0\to 2.4\text{cm}} &= 4.8728 \cdot 10^{-2} \cdot z - 2.3833 \cdot 10^{-2} \cdot z^2 + 4.255 \cdot 10^{-3} \cdot z^3 + 0.3399 \\
a_{\ 2.4\to 25\text{cm}} &= 2.701 \cdot 10^{-3} \cdot z - 6.93 \cdot 10^{-4} \cdot z^2 + 1.5 \cdot 10^{-5} \cdot z^3 + 0.3773 \\
a_{\ 25\to 104\text{cm}} &= -9.894 \cdot 10^{-3} \cdot z + 7.596 \cdot 10^{-5} \cdot z^2 - 1.99 \cdot 10^{-7} \cdot z^3 + 0.4533 \\
c_{\ 0\to 20\text{cm}} &= 3.7955 \cdot 10^{-2} \cdot z - 1.232 \cdot 10^{-3} \cdot z^2 + 2.7 \cdot 10^{-5} \cdot z^3 + 2.1865 \\
c_{\ 20\to 104\text{cm}} &= 3.415 \cdot 10^{-3} \cdot z + 1.445 \cdot 10^{-4} \cdot z^2 + 1.464 \cdot 10^{-7} \cdot z^3 + 2.6103
\end{aligned} \tag{5.9}$$

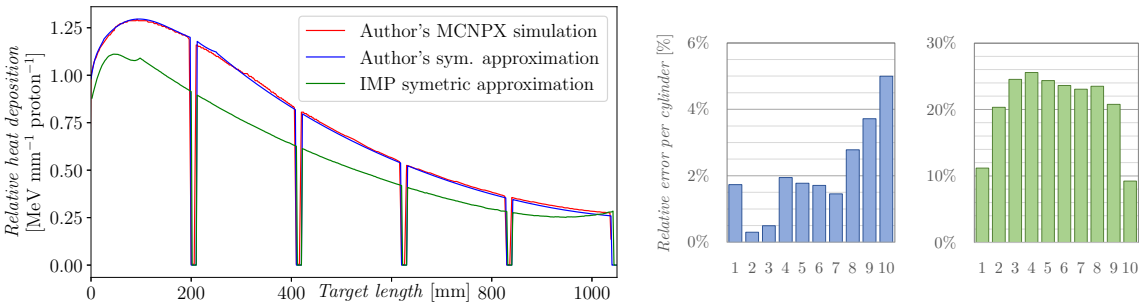

Figure 5.39: Relative heat deposition [MeV·mm^{-1}·proton^{-1}] along the whole CARBON target by three different method of calculation is shown on the left side of the figure. MCNPX simulation is declare to be reference, because other two methods are based on its approximation. The chart shows the reliability of both approximation methods. Their relative errors are plotted on the right side charts with respecting the curve colours. It has been calculated by written Python script, which recalculated whole volume power density (for each cell).

Table 5.7: The CARBON target heat deposition results by computation method.

Author's MCNPX simulation	140.63 kJ	365.78 MeV·p^{-1}
Dr. Zhang's symmetrical approximation	111.51 kJ	290.03 MeV·p^{-1}
Author's symmetrical approximation	138.34 kJ	359.82 MeV·p^{-1}

To compare the energy amount deposited per incident 660 MeV proton, the relative heat deposition is shown in the right column of the Tab. 5.7. It is the statistical average amount of energy released inside of the CARBON target per one incident proton. The comparison of both approximation techniques results is shown in Fig. 5.40.

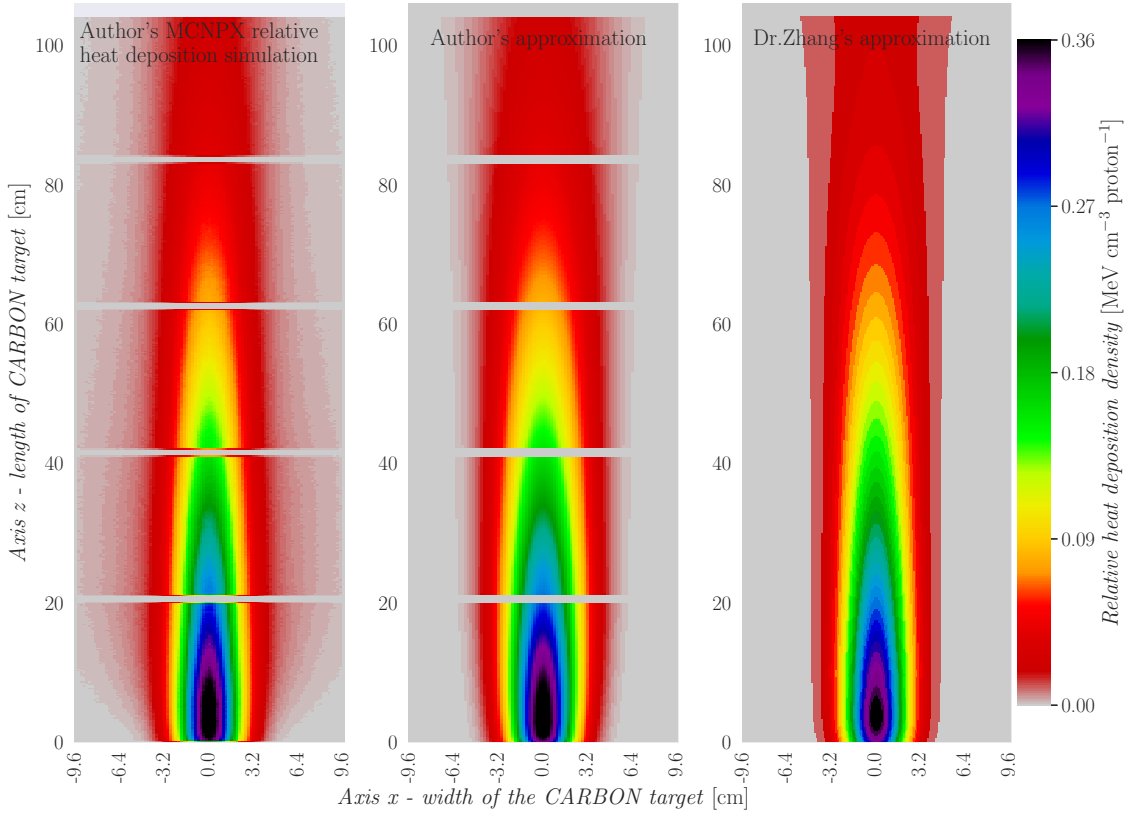

Figure 5.40: Both approximated methods are compared by heatmap charts of relative heat deposition density mesh. The MCNPX simulation is shown on the left side, the author's approximation in the middle, and finally, the IMP's approximation on the right side. It shows, that author's simulation is much more precious also in 2D. Moreover, there are much smoother distribution transition (contours without visible border) which better respond to the reality. The heat deposition of more distant radius, where minor heat is deposited, are neglected in both of approximation. This fact could slightly affect the results.

ANSYS-FLUENT simulation setting and results

The constants of CARBON material were taken from the manufacturing company data sheet and those not included were taken from [127] based on this company recommendations. The CARBON target was calculated earlier than the LEAD target, so the details are widely discussed here. It have been calculated about 60 variants of 2D model to understand the behaviour of the calculation and sensitivity of simulation based on constants uncertainty, and the mesh quality. Due to the calculation was performed by student licence[70], only 512,000 mesh cells could be employed. In the next step the 3D model of the structured mesh was created by Yafeng Shu (IMP Lanzhou), see Fig. 3.21. Several calculations were performed with additional mesh adaption, however, the quality of the mesh was not sufficient (especially in the front side of the first cylinder) and unfortunately, it was not possible to adapt it due to cells over-limit[71]. Finally, the author created a mew geometry with more advanced mesh which deals with the natural convection more appropriately, see Fig. 5.41. The Fluent calculation setting (step by step from the meshed geometry) is described in recorded video[72]. This fluent model is attached in cloud files, see p.197 *Fluent files*, item 1.

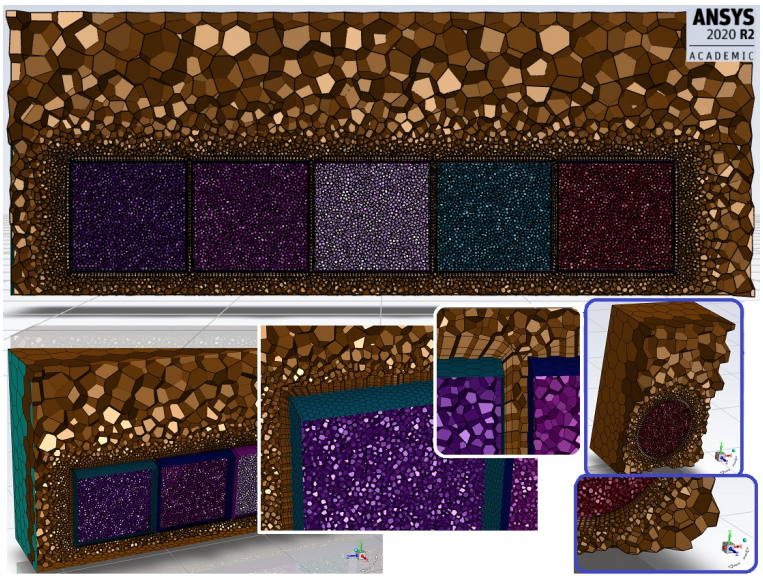

Figure 5.41: 3D model of the CARBON target with mesh created by author in Fluent meshing tool. Above is displayed yz plane of the mesh in the x=0 mm, below are shown zoomed parts. On the right side is displayed xy plane to visualise the meshing around the cylinder. It is very important for natural convection to use interface fine meshing, to ensure correct calculation (see the cells partition close to the cylinders walls). The fluid around is asymmetrical to decrease number of mesh cells. Due to the heated air goes up, the lower fluid volume does not have to be simulated.

[70] Calculations performed during internship in Dubna (Russia) and full academic licence was not possible to use due to perimeter limitation from the BUT (location of calculation must be in perimeter 50 km).

[71] There is also coarsening option, however, it allows to coarse only already adapted cell, do not allow to coarse performed mesh. For this reason, there was not other option than perform a new geometry and mesh.

[72] Available on YouTube, see: https://youtu.be/C85XIkuw4GY.

The Fluent simulation settings of the CARBON target:

- target front face centre = x_0=0 m, y_0=0 m, z_0=0 m
- viscous model = „laminar“
- boundaries conditions = „pressure outlet“

- fluid constants:
  - Density → incompressible-ideal-gas
  - Specific heat = 1026.43 J/kg/K
  - Thermal conductivity = 0.0256 W/m/K
  - Viscosity = 0.0184 g/m/s
- carbon constants:
  - Density = 1800 kg/m^3
  - Specific heat = 710 J/kg/K
  - Thermal conductivity = 129 W/m/K
- solution methods:
  - Pressure-Velocity Coupling = SIMPLE
  - Spatial Discretization - all defaults except „Pressure“=„Body Force Weighted“
- Physics-Operating Conditions:
  - Operating Pressure = 100,300 Pa
  - Operating Density = 1.212 kg/m^3
- Calculation setting:
  - Number of Time Steps = 4,500
  - Time Step Size = 5 s
  - Max Iterations/Time Step = 10
- Temperature probe positions (x,y,z):
  - ΔT_{20cm}=(0.04, -0.02, 0.195) m
  - ΔT_{41cm}=(0.04, -0.02, 0.405) m
  - ΔT_{62cm}=(0.04, -0.02, 0.615) m
  - ΔT_{83cm}=(0.04, -0.02, 0.825) m

Power source definition:
The power source has been defined based on the described equations, see equations 5.9, however, slightly suppressed. The power distribution was saved to User Defined Memory (UDM), which has been simultaneously visualised (YZ plane, x=0 mm) to confirm the correctness (the power source was defined as symmetrical, $x;y$ defined by circle → rotating z axis). This visualisation is shown in Fig. 3.22, figure (A). Moreover, each cylinder power was monitored per each calculation Time Step. Total internal heat production was calculated per cylinder and compared with MCNPX simulation (shown in Fig. 5.35 and Tab. 5.7). It has been found that the relative mesh distribution fits visually well as well as the heat ratio production per each cylinder, however, the absolute target heat generation is overestimated. The same comparison has been performed for the UDF created by IMP Lanzhou (based on equations 5.8). In this case, the visualisation does not fit well, such as the cylinder heat ratio and moreover, the total heat production is under estimated. All these problems are described in Fig. 5.42 and Tab. 5.8.

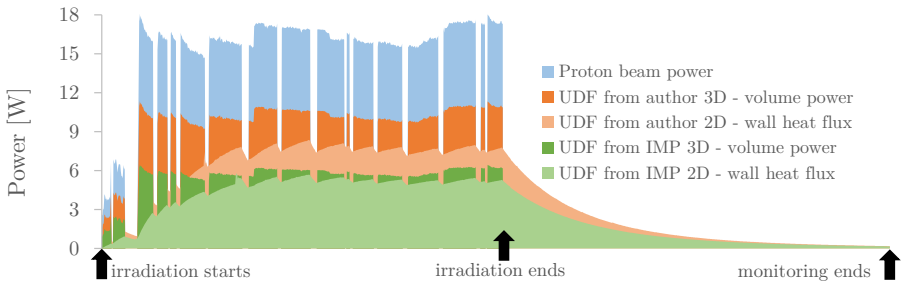

Figure 5.42: Comparison of two techniques dealing with confirming the target power assigned from UDF. This figure shows the CARBON target power distribution during the time, based on used monitoring technique for two different UDF. The left vertical axis represents power, the bottom horizontal axis represents time. The blue colour represent the proton beam power. Dark orange and dark green represent volume power of all cylinders (3D model) in irradiation time for the author's UDF based on eq. 5.9 and the IMP's UDF based on eq. 5.8 respectively. These three values are proportionally dependent on proton beam occurrence. The second way of the UDF accuracy monitoring is suitable for 2D models where the previous volume monitoring cannot be used. It deals with monitoring of the cylinder walls heat transfer represented by lighter colours in the figure. It must be monitoring until the target is cooled to surrounding air temperature (labelled on time axis as „monitoring ends“).

Table 5.8: Monitoring of the CARBON target heat generation assigned from UDF definition. The 2D model lower values are caused by the monitoring ended earlier than the target was fully cooled to surrounding temperature. To shorten the table, the 2D and 3D are listed in single line (2D = wall heat flux / 3D = volume power)

	E [kJ]	E/E_{tot} [%]
Total proton beam energy (E_{tot})	259.8	100.00
UDF from author 3D / 2D volume power	163.1 / 161.9	62.78 / 62.32
UDF from IMP 3D - volume power	116.1 / 112.0	44.69 / 43.11
MCNPX calculation	140.0	53.90
Used 3D author correlated UDF	*142.4*	*54.82*

The previous data shows that the assigned power by UDF is overestimated by 15.6 %. By this reason, there was an added correlation coefficient in the UDF source definition which decreases the assigned power by 0.865. Calculated total heat released by this assigned power distribution was 142.4 kJ, see the last *italic* line of Tab. 5.8. The UDF thermal power distribution was not assigned as accurately as estimated by Python script. Ration of the thermal power distribution per doubled CARBON cylinder was 33.3 %, 27.2 %, 18.5 %, 12.4 % and 8.5 % The power of each cell is assigned based on the centre cell position. Since the mesh is slightly changed, the total released target energy can be changed significantly if the mesh is coarse. Used UDF is attached on cloud, p.197 item 2.

Fluent simulation results

It is important to monitor the heat transfer to the surrounding fluid area to estimate the model correctness. The solution animations were created and are available on YouTube[73]. Earlier wrong calculations are shown in Fig. 3.19 and in appendix C.6 with additional discussion about calculation sensitivity. The temperature distribution for T_{irr}=18,300 s is displayed in Fig. 5.43 and final comparison of the ΔT between experimental data and simulation in Fig. 5.45.

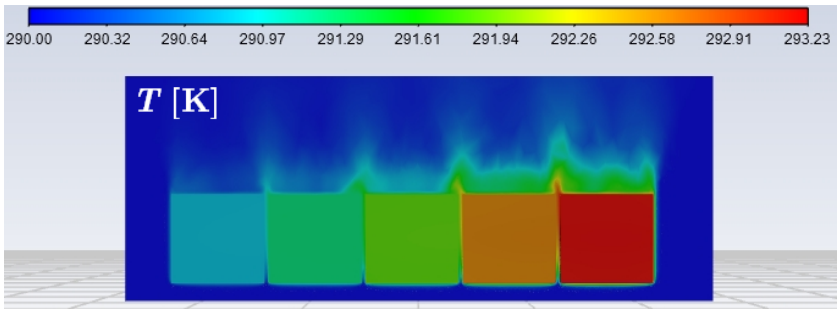

Figure 5.43: Fluent simulation results of the CARBON target temperature distribution in irradiation time 18,300 s for YZ plane. In principle, it show that more fine mesh and larger fluid volume would be suitable.

[73]The YZ plane animation is available here: https://youtu.be/anKJ9XiD6zk, XY plane animation: https://youtu.be/nvnVIsJm2tY, and finally, XZ plane animation: https://youtu.be/iWAwPP3YseM.

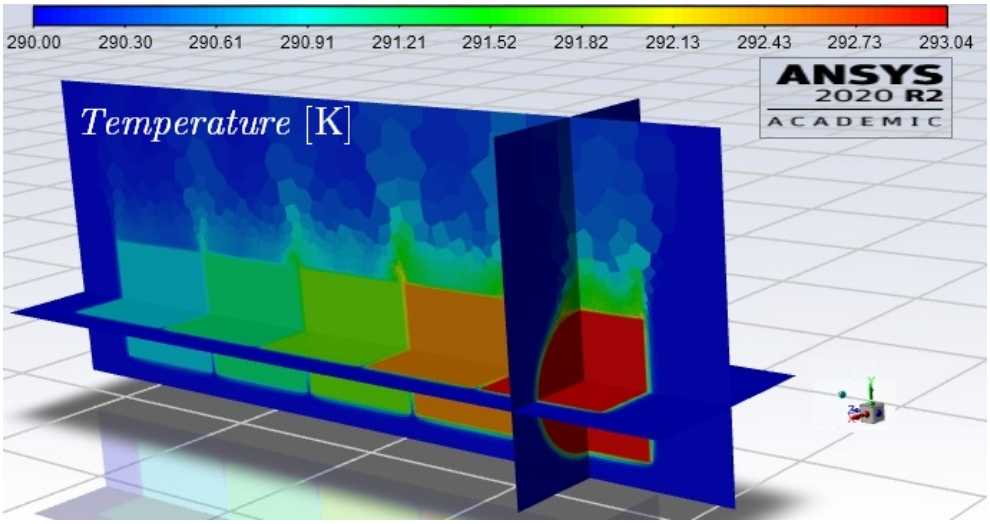

Figure 5.44: Visualisation of 3D CARBON temperature per cell mesh without smoothing (smoothed version is shown in Fig. 5.43), $T_{irr.} = 15{,}200$ s. The coarseness of the more distant region causes the heat do not transfer to upper parts correctly. It would be suitable to decrease the mesh cell size in more distant regions. However, it would not be possible to use student licence which allows to work in maximum with 512,000 cells.

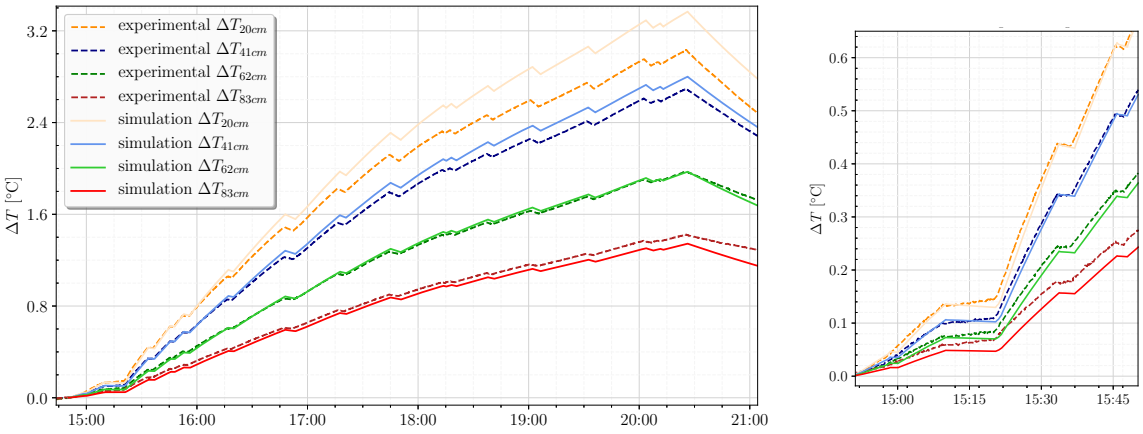

Figure 5.45: Comparison of the ΔT for simulation and measured data. On the left side is shown whole experiment time, right side figure shows zoomed part of the irradiation beginning. This simulation suffer of several inaccuracies, such as missing small block of thermal insulation between cylinders at measuring positions, slightly overestimated heat source, neglected experimental other samples and materials installed on the target surface, and primarily, neglected surrounding air temperatures changing during the experiment. For comparing purposes, the measured ΔT was offset to the beginning irradiation time, how ever it was not steady state, see zoomed part of Fig. 5.29. Results are widely described in the following discussion.

5.2.4 Results discussion - CARBON target

The CARBON target experiment consisted of several measurements. On the one side, there were offline monitoring of the neutron flux and its spectrum by an activation foil method (colleague research). On the other side, there were experiments based on very accurate temperature measurements. Unfortunately, the first-mentioned measurement affected the accuracy of the temperature measurement due to its requirement to have quick access to the target. For this reason, it was impossible to create ideal measuring conditions. However, this experiment was successful and brought many interesting results.

The proton beam instability was used for detailed monitoring of dynamical changes in the experimental setup, such as target cooling when the beam outage occurs, and primarily, the direct Th sample heating placed inside of the target. This part of the experiment studied a very cheap method of proton flux monitoring by accurate temperature measurement of two different materials. The ΔT of the CARBON target and thermally insulated Th samples were measured in a similar position at four different target lengths (different proton flux) and compared to the first measuring position. Based on the temperature measurement, which suffers from several simplifications, the relative proton flux was 70 %, 55 %, and 48 % for second, third, and fourth measuring positions. Based on the MCNPX simulation, the relative proton flux was 78 %, 58 %, and 46 % with respecting the previous order. It is a very interesting result of base research and should be more detailed studied in laboratory conditions. It can find usage in specific applications of proton or neutron flux occurrence monitoring. This method has many disadvantages, however, due to modern electronics, suitable utilisation can be found. The following research of this topic should be aimed at sensitivity analyses and experimental comparison of various materials in laboratory conditions with unified p/n flux source.

The heat generation monitoring of the cylindrical CARBON target irradiated by 660 MeV protons was carried out by accurate temperature measurement. These results were later compared with MCNPX simulation and ANSYS Fluent calculation. The utilisation of these tools is common - heat transfer simulations (ANSYS Fluent, OpenFOAM, Autodesk CFD, COMSOL Multiphysics, or others) are widely using in the industry, design and many other branches as well as particle transporting codes (MCNPX, Fluka, GEAT, or others), which are primarily used in medicine, science, industry and others. There are also applications, however, not so often, where these two totally different simulations are employed together, such as nuclear reactor design, spallation target experiments, or similar problems. In these cases, the heat is deposited by particle reactions in the simulated object and its transfer is monitored to ensure the limits of destruction (for experiments or testing) or to simulate transfer efficiency, structure stress, or others values. The CARBON target experiments (as well as the LEAD target) combine slightly complicated parts of these simulation possibilities - asymmetrical volume heat deposition which is various over irradiation time in combination with the simulation of natural convection heat transfer at lower temperature differences. Asymmetrical heat deposition was approximated by several equations generated from the written Python script, the variable behaviour over time was defined by Fluent User Defined Function (with using gamma-ray spectrometry method to estimate the total number of interacting protons, and accelerator ionisation chamber for relative proton beam monitoring over time). The most problematic part was the Fluent simulation. It took plenty of time, several consultations with ANSYS Fluent experts and a high number of sensitivity analyses to set the model and outer conditions accurately. Heat transfer simulation was also depen-

dent on outside weather condition, which has been taken into account as well. Finally, the comparison of experimentally measured data with purely simulated data was performed. There is one more problem in temperature measurement because one of our colleagues was carelessly installing some instruments on the front side of the experimental target, so the already stabled target temperature was interrupted. The whole target temperature increased for 0.06 °C, however, the first measuring section increased for 0.14 °C. It complicates the comparison due to the irradiation was not started in the target temperature steady-state. This problem is shown in zoomed Fig. 5.29 on the right side. For this reason, the ΔT offset is set to the time just before the irradiation starts.

The simulation reaches the maximal error during the irradiation of 11.1 % (in principle lower due to the discussed offset setting) for the highest temperature at the end of irradiation, see Fig. 5.45 (measured 3.0 °C, simulated 3.36 °C). For the second position, the maximal relative error is 3.9 %, for the 3rd position it is 1.85 % and finally, for the 4th 5.7 %. It is a very good result, moreover, if having in mind the complexity of this simulation placed in limited experimental conditions. The ANSYS Fluent simulation should be recalculated with a softer mesh, primarily in the upper target region (cells in the upper part are too large, the quality of the heat transfer simulation is not ensured). The mesh coarseness problem is clearly shown in the 3D temperature results visualisation (without smoothing) in Fig. 5.44. The model should be more accurate - thermal insulation and irradiation samples between sections are not simulated, which can increase the measured temperature in the lower temperature region. The approximated thermal power distribution is slightly overestimated. The internal thermal power distribution should be rather directly mapped from the MCNPX mesh tally results - it will be much more accurate and it includes asymmetrical power distribution. Unfortunately, this method (mapping) was unknown to the author at the beginning of the simulation process. The utilisation of approximated equations and UDF definition was very laborious, complicated, and finally, less accurate.

In summary, the used technique brought very interesting and pretty accurate results. It is possible to compare pure experimental data with the advanced simulation (a combination of several simulation + experimental methods).

Chapter 6

Conclusion

The extensive research performed in the frame of this PhD thesis goes through several topics. Experimental measurements were performed at JINR in Dubna and dealt with neutron and proton flux monitoring, gamma-ray spectrometry method, and accurate ΔT for the purpose of target heat generation monitoring. Research compares the experimental measurement with simulation. Data acquisition was performed by LabView. Experimental data were analysed by advanced Python scripts with various libraries usage - *pandas* and *numpy* for data manipulation and *matplotlib* and *seaborn* for visualisation, and other commonly used libraries. Irradiated samples and foils processed by gamma-ray spectrometry were measured by HPGe detectors in YaSNaPP laboratory at JINR.

Irradiated experiments were simulated by the particle transportation code MCNPX. The heat deposition was estimated per volume and as a volume mesh to estimate its distribution. The total number of protons interacting with the target was estimated by Cu and Al activation foil (gamma-ray spectrometry). Due to the proton beam being dynamic over time and the power distribution is proportional to the beam current, the dynamic power distribution was calculated based on the relative proton current monitored by gas-filled ionisation chambers. The transfer of the generated heat was simulated by ANSYS Fluent. The 3D specific heat distribution was approximated by several equations and interpreted by UDF to the Fluent. Time dependent experimental results were compared with the simulations. Although several simplifications are used, the experimental vs simulation uncertainty is about 11 % for the CARBON target and about 7.5 % for the LEAD target. If the simulation complexity is taken into consideration, the results are very sufficient. Moreover, the ANSYS Fluent calculation is going to be improved since academic licence is available. Based on the experience of 2D simulation, it is expected that the 3D Fluent simulation improvement by softening the mesh will be significant. When the MCNPX results will be mapped into the ANSYS and the source asymmetry will be taken into account, the uncertainty of simulation vs experiment is expected to be better than 5 % (with softer mesh of larger fluid volume).

This conclusion describes a global research summary, the individual data of the experiment results are listed in *Results discussion* which located at the end of each experimental section. For TA QUINTA heat generation see p.82, detail experimental study of its cylinders heating results are shown on p. 71, for the TA QUINTA neutron leakage results see p.88, the LEAD target experiment results are summarised on p.107, and finally, the CARBON experiment on p.126. This conclusion will only shortly highlight these results.

During the PhD studies were performed 13 thermal experiments, however, only the most important four of them are listed in this thesis. Besides the experimental target heat generation study, the neutron and proton flux was measured by the invented tiny volume heating probes. All experimental targets researched by the ADS group in Dubna during the years 2015-2020 were in detail studied by the author's thermal methodology.

Small proton beam current changes (such as 600 pA) for the LEAD target experiment were detected by the target ΔT measurement, as well as by neutron leakage heating probes. It means that the ΔI_p=600 pA causes a measurable change of the neutron flux in the radial distance 13.5 cm. Generally, the neutron leakage flux monitoring was carried out by $^{\mathrm{nat}}$U or $^{\mathrm{enr}}$U probes for the TA QUINTA and the LEAD target, where spallation neutron leakage occurs. For the TA QUINTA short irradiation, the direct internal heat increase comparison between the under third and second section was about 77 %, see Fig. 4.35. For long irradiation, the measurement is affected by several errors caused by the heat transfer from the TA QUINTA (difference thermal insulation) and the problem with TC connection - they were not connected to neighbour channels (CJ could reach slightly different temperature during the irradiation) due to the author mistake. Based on MCNPX simulation, the ratio of the heat deposition between these two positions is 84 %. It is very good correlation. The repetition of this experiment without the mentioned mistakes was planned but unfortunately, has not been performed yet. The lead neutron leakage monitoring by a similar technique reaches very good results.

The proton flux was measured by a similar method inside of the CARBON target. The relative proton flux was estimated by four tiny volume thorium probes. Probes were placed at four distances inside of the CARBON target. The uncertainty between the relative temperature comparison with MCNPX heat deposition simulation is about 11 % (if the MCNPX simulation reference), see p.113. The reached sensitivity was very high, the maximal measured ΔT was in this case merely 9 mK (with using a statistic function and data filtration). It must be stated that all of these experimental data comes from base experimental research and it should be studied in detail at laboratory conditions with unified sources. In principle, these results are a kind of parallel product of the main experimental heat generation research.

Unfortunately, the most interesting experiments are still in anticipation. The BURAN sub-critical blanket irradiation should use a combination of studied LEAD and CARBON targets. Hopefully, the experiment will be carried out in 2021.

In summary, this kind of research was unique in the JINR ADS research group and brought important data about the opportunities and limits of these measurements. The author tested several methods and prepared a complete methodology of the measurement. There is included the thermocouples manufacturing, testing, and calibration. There are described troubles with data acquisition and its solutions. Due to larger data packages of measured and simulated data, there is a widely discussed Python scripting language utilisation. Most of the used scripts are enclosed, including a detail video manual enclosed on YouTube dissertation channel. Simulation by MCNPX, volume meshing, its visualisation, and primarily the method of 3D heat deposition distribution approximation by equations are widely discussed. The final solution is shared (uploaded to this thesis cloud). There is discussed the ANSYS Fluent simulation and its challenges. Due to dealing with natural convection in a large volume experimental hall, it is a very sensitive simulation. Detail manual of the model creation and setting is enclosed on YouTube as well. Many 3D models, simulations, and codes were made during this thesis processing - they are available on the Google Cloud Platform, based on BUT - Google cooperation. These files are accessible to all BUT students and academic staff. All links are listed in the last three pages of the appendix. These open access data hopefully help students to boost the learning process rapidity or help researchers to use the described programs and tools more easily due to enclosed tutorials.

The author's goal of this thesis processing was based on data open accessing. This research was too long primarily due to the lack of detailed information in accessible sources. For this reason, this PhD thesis is quite more extensive than recommended and discusses the problem from the beginning up to the final solution.

List of Abbreviations

ADB ADS Burner.

adh. adhesive.

ADRUF Accelerator Driven Recycle Used Fuel.

ADS Sub-critical Accelerator-Driven Systems.

BESS battery energy storage system.

BP The British Petroleum Company plc.

BURAN Bolshoy URAN (Russian abbreviation) // Bigger URAN.

BUT Brno University of Technology.

BWR Boiling Light-Water Cooled and Moderated Reactor.

CERN The European Organization for Nuclear Research.

CERN-PS The Proton Synchrotron at CERN.

CiADS China Initiative Accelerator Driven System.

CJ cold junction.

CJC cold junction compensation.

CO_2 carbon dioxide.

CS cross section.

cyl. cylinder.

DEPE Department of Electrical Power Engineering.

DLNP Dzelepov Laboratory of Nuclear Problems.

E&T RAW Energy and Transmutation of Radioactive Waste.

eq. equation.

EU European Union.

FBR Fast Breeder Reactor.

FEEC Faculty of Electrical Engineering and Communication.

FP fission products.

GCR Gas Cooled, Graphite Moderated Reactor.

GHG greenhouse gas.

HJ hot junction.

HPGe High Purity Germanium detector.

HTGR High Temperature Gas Cooled Reactor.

IMP The Institute of Modern Physics.

JINR Joint Institute for Nuclear Research.

LBE Lead-Bismuth Eutectic.

LHE Veksler and Baldin Laboratory of High Energies.

LWGR Light-Water Cooled, Graphite Moderated Reactor.

MCNPX 2.7.0. Monte Carlo N-Particle Transport Code.

NI National Instrument.

pcs pieces.

PHWR Pressurized Heavy-Water Moderated and Cooled Reactor.

PV photo-voltaic.

PWR Pressurized Light-Water Moderated and Cooled Reactor.

QUINTA Quasi-Infinite Targets.

RTD resistance temperature detector.

SAD The Subcritical Assembly in Dubna.

SMR small modular reactor.

SNF spent nuclear fuel.

TA target assembly.

TC thermocouple.

UDF User Defined Function.

UDM User Defined Memory.

UNO United Nations Organization.

WMO World Meteorological Organization.

WoS Web of Science.

YaSNaPP Nuclear Spectroscopy on Proton Beam - laboratory name (Russian abbreviate).

List of Symbols

$\Delta \boldsymbol{T}$ temperature difference.

$\Delta \boldsymbol{V}_{gain}$ relative voltage gain.

t_{irr} irradiation time.

$\mathrm{I_p}$ Current of proton beam [A].

$\rho_{E_{rel}}$ Relative heat deposition density.

N_p Integral number of interacting protons [-].

$\boldsymbol{G}$ energy gain.

$\boldsymbol{T}$ temperature.

$\boldsymbol{V}$ voltage.

gCO$_2$e gram of carbon dioxide equivalent.

GW$_\mathrm{e}$ gigawatt (of electricity).

GWd·t$_{\mathrm{HM}}^{-1}$ Burn-up describes the amount of energy extracted from the fuel mass.

kWh kilowatt-hour.

min minute(s).

tCO$_2$e ton of carbon dioxide equivalent.

$\mathbf{V}_{meas}$ measured voltage (EMF).

Bibliography

[1] NASA. *Global Climate Change* [online]. 2020 [cit. 2020-02-15]. Available at: https://climate.nasa.gov/.

[2] Ritchie, H. and Roser, M. CO_2 and Greenhouse Gas Emissions. *Our World in Data*. 2020. Available at: https://ourworldindata.org/co2-and-other-greenhouse-gas-emissions.

[3] Smil, V. *Energy: A Beginner's Guide*. 2nd ed. Oneworld Publications, 2017. ISBN 1-786-07133-9.

[4] Smil, V. *Energy and Civilization: A History*. 1st ed. MIT press, 2017. ISBN 0-262-03577-4.

[5] Verma, V. K. and Katovsky, K. *Spent Nuclear Fuel and Accelerator-Driven Subcritical Systems*. 1st ed. Springer, 2019. ISBN 978-981-10-7503-2.

[6] Smil, V. Energy (r)Evolutions Take Time. *World Energy*. 2019, no. 44, p. 10–14. Available at: https://www.eni.com/static/en-IT/world-energy-magazine/rethinking-energy.html.

[7] Smil, V. *Energy Transitions*. 1st ed. Praeger, 2010. ISBN 978–0–313–38178–2.

[8] UNO. World energy requirements in 1975 and 2000. In: *Proceedings of the International Conference on the Peaceful Uses of Atomic Energy*. New York: UNO, 1956, p. 3–33. Atomic Energy.

[9] UNO. *World energy supplies 1950–1974*. 1st ed. New York: Department of Economic and Social Affairs, Statistical Office, United Nations, 1976. 825 p.

[10] BP. *Statistical Review of World Energy 2009* [online]. Data Report. London: The British Petroleum Company plc, 2009. 48 p. [cit. 2020-02-18]. Available at: https://www.bp.com.

[11] BP. *BP Statistical Review of World Energy 2019* [online]. Data Report. London: The British Petroleum Company plc, 2019. 64 p. [cit. 2020-02-25]. Available at: https://www.bp.com/content/dam/bp/business-sites/en/global/corporate/pdfs/energy-economics/statistical-review/bp-stats-review-2019-full-report.pdf.

[12] NCEE. *Greenhouse Gases* [online]. 2020 [cit. 2020-02-19]. Available at: https://www.ncdc.noaa.gov/monitoring-references/.

[13] University Of Oxford. *CO_2 and Greenhouse Gas Emissions* [online]. 2020 [cit. 2020-02-17]. Available at: https://ourworldindata.org.

[14] Energy Research Institute of Academy of Macroeconomic Research. *China Renewable Energy Outlook 2018*. Energy Outlook. Peking: China National Renewable Energy Centre, 2018. 390 p. Available at: www.chinaenergyviewpoint.com/wp-content/uploads/2019/01/CREO-2018-EN-web.pdf.

[15] Carbon Brief. *Clean on Climate* [online]. 2020 [cit. 2020-02-20]. Available at: https://www.carbonbrief.org.

[16] Schlömer, S., Bruckner, T. et al. *2014: Annex III: Technology-specific cost and performance parameters. In: Climate Change 2014: Mitigation of Climate Change*. Technology Report. United Kingdom and New York: Cambridge University Press, 2014. 28 p. Available at: https://www.ipcc.ch/site/assets/uploads/2018/02/ipcc_wg3_ar5_annex-iii.pdf.

[17] Sovacool, B. K. Valuing the greenhouse gas emissions from nuclear power: A critical survey. *Energy Policy*. 2008, no. 36, p. 2950–2963. Available at: https://doi.org/10.1016/j.enpol.2008.04.017.

[18] Sovacool, B. K., Andersen, R. et al. Balancing safety with sustainability: assessing the risk of accidents for modern low-carbon energy systems. *Journal of Cleaner Production*. 2016, vol. 112, p. 3952 – 3965. Available at: https://doi.org/10.1016/j.jclepro.2015.07.059. ISSN 0959-6526.

[19] Ziegler, M. S. et al. Storage Requirements and Costs of Shaping Renewable Energy Toward Grid Decarbonization. *Joule*. 2019, no. 3, p. 2134–2153. Available at: https://doi.org/10.1016/j.joule.2019.06.012.

[20] IRENA(2017). *Electricity Storage and Renewables: Costs and Markets to 2030*. Energy Outlook. Abu Dhabi: International Renewable Energy Agency, 2017. 132 p. Available at: https://www.irena.org/-/media/Files/IRENA/Agency/Publication/2017/Oct/IRENA_Electricity_Storage_Costs_2017.pdf.

[21] Mongird, K. et al. *Energy Storage Technology and Cost Characterization Report*. Energy Report. Washington: U.S. Department of Energy - Hydrowires, 2019. 120 p. Available at: https://energystorage.pnnl.gov/pdf/PNNL-28866.pdf.

[22] IEA. *Will pumped storage hydropower expand more quickly than stationary battery storage?* [online]. 2019 [cit. 2020-02-23]. Available at: https://www.iea.org/articles/will-pumped-storage-hydropower-expand-more-quickly-than-stationary-battery-storage.

[23] Group, T. U. *TeX Live* [online]. 2019 [cit. 2020-05-22]. Available at: https://www.tug.org/texlive/.

[24] Hammersley, J. and Lees Miller, J. *OverLeaf* [online]. 2019 [cit. 2020-01-19]. Available at: https://www.overleaf.com/.

[25] Castro, J. *Writefull* [online]. 2020 [cit. 2020-11-19]. Available at: https://writefullapp.com/.

[26] *Pixlr (free)*. 2020. Available at: https://pixlr.com/x/.

[27] Adobe. *Photoshop CS3*. Trial version. Available at: https://www.adobe.com/products/photoshop.

[28] PDFresizer.com. *Crop PDF files*. Available at: https://pdfresizer.com/crop.

[29] *SketchUp (free)*. 2020. Available at: https://app.sketchup.com/.

[30] Autodesk. *Inventor Professional*. Student version. Available at: https://www.autodesk.com/products/inventor/overview.

[31] Microsoft Corporation. *Microsoft Excel*. Available at: https://office.microsoft.com/excel.

[32] Foundation, P. S. *Python Language Reference* [http://www.python.org]. June 2018.

[33] Suchopar, M. *Study of neutron production and transport in systems based on spallation reactions*. Prague, 2016. 185 p. Dissertation. Czech Technical University in Prague.

[34] Siemer, D. *Nuclear Power: Policies, Practices, and the Future*. John Wiley & Sons, 2019.

[35] Ball, P. Ancient nuclear power controlled by water. *Springer Nature*. 2004.

[36] Raymond, M. and Keith, H. *Nuclear Energy*. 7th ed. Addison-Wesley Publishing Company, 2015. ISBN 978-0-12-416654-7.

[37] IAEA. *The Power Reactor Information System (PRIS)* [online]. 2019 [cit. 2020-02-06]. Available at: https://pris.iaea.org/PRIS.

[38] World Nuclear Association. *Outline History of Nuclear Energy* [online]. 2020 [cit. 2020-10-18]. Available at: https://www.world-nuclear.org/information-library/current-and-future-generation/outline-history-of-nuclear-energy.aspx.

[39] Khan, S. U.-D. and Nakhabov, A. *Nuclear Reactor Technology Development and Utilization*. Elsevier, 2020.

[40] IAEA. *Nuclear Power Reactors in the World (RDS-2)*. IAEA, 2020. Available at: https://www.iaea.org/publications/14756/nuclear-power-reactors-in-the-world.

[41] IAEA. *Energy, Electricity and Nuclear Power Estimates for the Period up to 2050*. IAEA, 2020. Available at: https://www.iaea.org/publications/14786/energy-electricity-and-nuclear-power-estimates-for-the-period-up-to-2050.

[42] Jevremovic, T. and Kraus, M. Advanced Large Water Cooled Reactors. *IAEA Advanced Reactors Information System (ARIS)*. 2020. Available at: https://aris.iaea.org/Publications/20-02619E_ALWCR_ARIS_Booklet_WEB.pdf.

[43] Bouchet, S., Reitsma, F., Subki, M. and Kiuchi, H. Advances in small Modular Reactor Technology Developments. *IAEA Advanced Reactors Information System (ARIS)*. 2020. Available at: https://aris.iaea.org/Publications/SMR_Book_2020.pdf.

[44] GenerationIV International Forum. *GIF 2019 Annual Report-final - Chap4 full* [online]. 2019 [cit. 2020-10-22]. Available at: https://www.gen-4.org/gif/jcms/c_119076/gif-2019-annual-report-final-chap4-full.

[45] Nifenecker, H., David, S., Loiseaux, J. and Meplan, O. Basics of accelerator driven subcritical reactors. *Nuclear Instruments and Methods in Physics Research Section A: Accelerators, Spectrometers, Detectors and Associated Equipment.* Elsevier. 2001, vol. 463, no. 3, p. 428–467.

[46] Krasa, A. *Neutron Emission in Spallation Reactions of 0.7 – 2.0 GeV Protons on Thick, Lead Target Surrounded by Uranium Blanket.* Prague, 2008. 164 p. Dissertation. Czech Technical University in Prague.

[47] Bowman, C., Arthur, E., Lisowski, P., Lawrence, G., Jensen, R. et al. Nuclear energy generation and waste transmutation using an accelerator-driven intense thermal neutron source. *Nuclear Instruments and Methods in Physics Research Section A: Accelerators, Spectrometers, Detectors and Associated Equipment.* Elsevier. 1992, vol. 320, 1-2, p. 336–367.

[48] Rubbia, C. *Energy amplifier for nuclear energy production driven by a particle beam accelerator.* Google Patents, june 30 1998. US Patent 5,774,514.

[49] Závorka, L. *Transmutation of Actinides Using Spallation Reactions.* Prague, 2015. 168 p. Dissertation. Czech Technical University in Prague.

[50] Asquith, N. *Fast and thermal Accelerator Driven Systems: Studies of secondary particle production and transport.* Sydney, 2015. 246 p. Dissertation. The University of Sydney, Faculty of Science.

[51] Borger, J. J. *Studies of the Particle Field of an Accelerator Driven System.* Sydney, 2012. 256 p. Dissertation. The University of Sydney, Faculty of Science.

[52] Katovský, K. *Studium sekundarních neutronů a jader vznikajících při reakcích protonů a neutronů v terči z uranu a plutonia.* Prague, 2008. 230 p. Dissertation. Czech Technical University in Prague.

[53] Vrzalova, J. *Experimental determination of neutron reaction cross sections relevant for accelerator-driven transmutation systems.* Prague, 2015. 136 p. Dissertation. Czech Technical University in Prague.

[54] S.Y.F. Chu, L. E. and Firestone, R. *The Lund LBNL Nuclear Data Search* [online]. February 1999 [cit. 2020-05-22]. Version 2.0. Available at: http://nucleardata.nuclear.lu.se/toi/.

[55] Wilson, P. D. The nuclear fuel cycle from ore to wastes. 1996.

[56] Feiveson, H., Mian, Z., Ramana, M. and Hippel, F. von. Managing spent fuel from nuclear power reactors: Experience and lessons from around the world. *International Panel on Fissile Materials, available at: http://fissilematerials. org/library/rr10. pdf.* 2011.

[57] IAEA. *Costing Methods and Funding Schemes for Radioactive Waste Disposal Programmes*. IAEA Nuclear Energy Series, 2020. Available at: https://www-pub.iaea.org/MTCD/Publications/PDF/PUB1900_Web.pdf. ISBN 978–92–0–111720–5.

[58] IAEA. Finland's Spent Fuel Repository a „Game Changer" for the Nuclear Industry. IAEA News Center. 2020, [cit. 2021-02-25]. Available at: https://www.iaea.org/newscenter/news/finlands-spent-fuel-repository-a-game-changer-for-the-nuclear-industry-director-general-grossi-says.

[59] Filges, D. and Goldenbaum, F. *Handbook of spallation research: theory, experiments and applications*. Wiley, 2009.

[60] Shen, B. S. P. and Merker, M. *Spallation nuclear reactions and their applications*. Springer Science & Business Media, 2012.

[61] Oxford University Press. *Oxford Dictionaries API* [online]. 2019 [cit. 2020-06-24]. Available at: https://www.lexico.com/.

[62] Carpenter, J. M. Pulsed spallation neutron sources for slow neutron scattering. *Nuclear Instruments and Methods*. Elsevier. 1977, vol. 145, no. 1, p. 91–113.

[63] Bartholomew, G. A., Fraser, J. S. and Garvey, P. *Accelerator breeder concept*. Atomic Energy of Canada Ltd., 1978.

[64] World Nuclear Association. *Accelerator-driven Nuclear Energy* [online]. 2019 [cit. 2020-02-08]. Available at: https://www.world-nuclear.org/information-library/current-and-future-generation/accelerator-driven-nuclear-energy.aspx.

[65] World Nuclear Association. *Status of Accelerator Driven Systems Research and Technology Development* [online]. 2015 [cit. 2020-03-11]. Available at: https://www-pub.iaea.org/MTCD/Publications/PDF/TE-1766_web.pdf.

[66] Yoshioka, R., Furukawa, K., Kinoshita, M., Degtyarev, A. M., Myasnikov, A. A. et al. 15 - Accelerator-driven systems. In: Dolan, T. J., ed. *Molten Salt Reactors and Thorium Energy*. Woodhead Publishing, 2017, p. 495–521. Available at: https://www.sciencedirect.com/science/article/pii/B9780081011263000154. ISBN 978-0-08-101126-3.

[67] ESS. *European Spallation Source-webside* [online]. 2020 [cit. 2020-10-22]. Available at: https://europeanspallationsource.se/.

[68] SKC·CEN. *MYRRHA project* [online]. 2020 [cit. 2020-10-22]. Available at: https://www.sckcen.be/en/projects/myrrha.

[69] SKC·CEN. *MYRRHA* [online]. 2020 [cit. 2020-10-22]. Available at: https://www.myrrha.be/.

[70] IMP. *Introduction to ADANES Research in China* [online]. 2020 [cit. 2020-10-22]. Available at: http://english.imp.cas.cn/Work2017/CI2017/.

[71] Google. *Scholar*. 2021. [Online]. Available at: http://scholar.google.com.

[72] Hunter, K. ScienceDirect™. *The Serials Librarian*. Taylor & Francis. 1998, vol. 33, 3-4, p. 287–297.

[73] Clarivate Analytics. Web of science. *Clarivate Analytics*. 2019.

[74] Moed, H. F., Bar Ilan, J. and Halevi, G. A new methodology for comparing Google Scholar and Scopus. *Journal of informetrics*. Elsevier. 2016, vol. 10, no. 2, p. 533–551.

[75] JPARS. *Japan Proton Accelerator Research Complex* [online]. 2020 [cit. 2020-10-22]. Available at: https://j-parc.jp/c/en/facilities/index.html.

[76] JINR members. *Energy and Transmutation of Radioactive Waste* [online]. 2008 [cit. 2021-03-20]. Available at: http://e-t.jinr.ru/.

[77] Shvetsov, V., Broeders, C., Golovnin, I., Gonzalez, E., Gudowski, W. et al. The Subcritical Assembly in Dubna (SAD)—Part I: Coupling all major components of an Accelerator Driven System (ADS). *Nuclear Instruments and Methods in Physics Research Section A: Accelerators, Spectrometers, Detectors and Associated Equipment*. 2006, vol. 562, no. 2, p. 883–886. Proceedings of the 7th International Conference on Accelerator Applications. Available at: https://www.sciencedirect.com/science/article/pii/S0168900206003718. ISSN 0168-9002.

[78] Batin, V. I. et al. Temperature Measurement of the Uranium Sample Irradiated with Secondary Neutrons. In: *JINR Rapid Communications No.5,6[97]-99*. Dubna, Russia: JINR, 1999, p. 33–41. Nuclear Physics. In Russian language.

[79] Tichý, P. *Study of Accelerator-Driven Subcritical Setups Determined for Testing of Transmutation Possibilities*. Prague, 2020. 154 p. Dissertation. Czech Technical University in Prague.

[80] Tumendelger, T. et al. Calorimetry of an Electronuclear Target for Uranium-Lead Assembly at Proton Energy 1.5 GeV. *JINR preprint*. Dubna, RF: [b.n.]. 1999, P1, p. 22. In Russian language.

[81] Krivopustov, M. I. et al. Calculative Analisys For an Experiment of Thermomeasuring the Massive Target, Irradiated by a Beam of Relativistic Protons. *Preprint, Inst. Appl. Math., the Russian Academy of Science*. Moscow, RF: [b.n.]. 2000, no. 2000, p. 18. In Russian language. Available at: https://library.keldysh.ru/preprint.asp?id=2000-76.

[82] Krivopustov, M. I. et al. On a First Experiment on the Calorimetry of an Uranium Blanket Using the Model of the U/Pb Electro-Nuclear Assembly «Energy Plus Transmutation» on a 1.5 GeV Proton Beam from the Dubna Synchrophasotron. *JINR preprint*. Dubna, RF: [b.n.]. 2000, P1, p. 32. In Russian language.

[83] Andriamonje, S., Angelopoulos, A. et al. Experimental determination of the energy generated in nuclear cascades by a high energy beam. *Physics Letters B*. Elsevier. 1995, vol. 348, 3-4, p. 697–709.

[84] Calero, J., Cennini, P. et al. Experimental temperature measurements for the energy amplifier test. *Nuclear Instruments and Methods in Physics Research Section A: Accelerators, Spectrometers, Detectors and Associated Equipment*. Elsevier. 1996, vol. 376, no. 1, p. 89–103.

[85] Bitter, R., Mohiuddin, T. and Nawrocki, M. *LabVIEW: Advanced programming techniques*. Crc Press, 2006.

[86] OMEGA. *Properties of PFA and FEP Insulation* [online]. Product Report. Stamford, CT, USA, 2019. 2 p. [cit. 2020-03-29]. Available at: https://br.omega.com/omegaFiles/temperature/pdf/teflon_insul.pdf.

[87] Williams, T., Kelley, C. and many others. *Gnuplot 5.2: an interactive plotting program* [http://gnuplot.sourceforge.net/]. September 2017.

[88] Hunter, J. D. Matplotlib: A 2D graphics environment. *Computing in science & engineering*. IEEE Computer Society. 2007, vol. 9, no. 3, p. 90–95.

[89] McKinney, W. et al. Pandas: a foundational Python library for data analysis and statistics. *Python for High Performance and Scientific Computing*. Seattle. 2011, vol. 14, no. 9.

[90] Oliphant, T. E. *A guide to NumPy*. Trelgol Publishing USA, 2006.

[91] Waskom, M., Botvinnik, O., O'Kane, D., Hobson, P., Lukauskas, S. et al. Mwaskom/seaborn: v0. 8.1 (September 2017). *Zenodo, doi*. 2017, vol. 10.

[92] OMEGA. *TL-WELD* [online]. 2016 [cit. 2020-12-22]. Available at: https://br.omega.com/omegaFiles/heaters/pdf/TL_WELD.pdf.

[93] Metalle, T. S. M. P. der. Und Erze durch Temperatur-Differenz. *Abh. Akad. Wiss. Berlin*. vol. 182021, no. 1822, p. 289346.

[94] OMEGA. *Platinum RTD Capsules* [online]. Product Report. Stamford, CT, USA, 2017. 2 p. [cit. 2020-04-07]. Available at: https://assets.omega.com/pdf/test-and-measurement-equipment/temperature/sensors/rtds/RTDCAP.pdf.

[95] OMEGA. *Advanced Design Surface Mount RTD - Class A Accuracy* [online]. Product Report. Stamford, CT, USA, 2018. 2 p. [cit. 2020-04-26]. Available at: https://assets.omega.com/pdf/test-and-measurement-equipment/temperature/sensors/rtds/SA1-RTD.pdf.

[96] Koning, A., Hilaire, S. and Duijvestijn, M. TALYS-1.2 A nuclear reaction program, User manual. *NRG, Netherlands*. 2009, p. 16–18.

[97] Savitzky, A. and Golay, M. J. Smoothing and differentiation of data by simplified least squares procedures. *Analytical chemistry*. ACS Publications. 1964, vol. 36, no. 8, p. 1627–1639.

[98] National Instrument. *DATASHEET NI9212 and TB-9212* [online]. 2018 [cit. 2020-05-01]. Available at: http://www.ni.com/pdf/manuals/374358c_02.pdf.

[99] National Instrument. *DATASHEET NI9214 and TB-9214* [online]. 2018 [cit. 2020-05-01]. Available at: https://www.ni.com/pdf/manuals/375138a_02.pdf.

[100] National Instrument. *NI 9212 (FPGA Interface)* [online]. 2017 [cit. 2020-05-18]. Available at: http://zone.ni.com/reference/en-XX/help/373197K-01/criodevicehelp/crio-9212/.

[101] National Instrument. *NI 9214 (FPGA Interface)* [online]. 2017 [cit. 2020-05-18]. Available at: https://zone.ni.com/reference/en-XX/help/370984T-01/criodevicehelp/crio-9214/.

[102] National Instrument. *DATASHEET NI9217* [online]. 2018 [cit. 2020-05-01]. Available at: https://www.ni.com/pdf/manuals/374187a_02.pdf.

[103] OMEGA. *Revised Thermocouple Reference Tables, type T* [online]. Product Report. Stamford, CT, USA, 2018. 1 p. [cit. 2020-04-02]. Available at: https://www.omegaeng.cz/temperature/Z/pdf/z207.pdf.

[104] OMEGA. *Revised Thermocouple Reference Tables, type K and E* [online]. Product Report. Stamford, CT, USA, 2018. 3 p. [cit. 2020-04-06]. Available at: https://assets.omega.com/pdf/tables_and_graphs/thermocouple-type-k-celsius.pdf.

[105] Mosaic Industries. *Efficient Thermocouple Calibration and Measurement* [online]. 1993 [cit. 2020-05-25]. Available at: http://www.mosaic-industries.com/embedded-systems/microcontroller-projects/temperature-measurement/thermocouple/calibration-table#t-type-thermocouple-calibration.

[106] Los Alamos National Laboratory. *Monte Carlo Methods, Codes, & Applications Group* [online]. 2019 [cit. 2020-05-03]. Available at: https://mcnp.lanl.gov/.

[107] Chadwick, M., Herman, M., Obložinskỳ, P., Dunn, M. E., Danon, Y. et al. ENDF/B-VII. 1 nuclear data for science and technology: cross sections, covariances, fission product yields and decay data. *Nuclear data sheets*. Elsevier. 2011, vol. 112, no. 12, p. 2887–2996.

[108] Chadwick, M., Obložinskỳ, P., Herman, M., Greene, N., McKnight, R. et al. ENDF/B-VII. 0: next generation evaluated nuclear data library for nuclear science and technology. *Nuclear data sheets*. Elsevier. 2006, vol. 107, no. 12, p. 2931–3060.

[109] Junghans, A., De Jong, M., Clerc, H.-G., Ignatyuk, A., Kudyaev, G. et al. Projectile-fragment yields as a probe for the collective enhancement in the nuclear level density. *Nuclear Physics A*. Elsevier. 1998, vol. 629, 3-4, p. 635–655.

[110] Khushvaktov, J., Tichy, P., Adam, J., Baldin, A., Baznat, M. et al. Study of the residual nuclei generation in a massive lead target irradiated with 660 MeV protons. *Nuclear Instruments and Methods in Physics Research Section A: Accelerators, Spectrometers, Detectors and Associated Equipment*. Elsevier. 2020, vol. 959, p. 163542.

[111] Khushvaktov, J. H. *Study of secondary neutron interactions with 232Th, 129I, and 127I nuclei at the uranium assembly quinta irradiated by 2, 4, 6, and 8 GeV deuterons*. Tashkent, 2019. 108 p. Dissertation. Institute of Nuclear Physics. Available at: http://www.inp.uz/en/dissertations.

[112] Tichy, P., Adam, J., Baldin, A., Chudoba, P., Furman, W. et al. Experimental investigation and Monte Carlo simulations of radionuclide production inside the Uranium spallation target QUINTA irradiated with a 660-MeV proton beam. In: EDP Sciences. *EPJ Web of Conferences*. 2019, p. 04003.

[113] Zeman, M., Adam, J., Katovsky, K., Stastny, O., Svoboda, J. et al. Experimental investigation of the radionuclides produced in massive spallation target. In: IEEE. *2018 19th International Scientific Conference on Electric Power Engineering (EPE)*. 2018, p. 1–6.

[114] Pelowitz, D. B. *MCNPXTM USER'S MANUAL, version 2.7.0* [part of software package]. Manual. LANL, New Mexico 87545, USA, 2011. 645 p. [cit. 2020-05-08].

[115] Gurecky, W. L. *Development of an MCNP6 - ANSYS FLUENT Multiphysics Coupling Capability*. Austin, 2015. 114 p. Dissertation. The University of Texas at Austin. Available at: https://repositories.lib.utexas.edu/handle/2152/46994.

[116] ANSYS. *Ansys, Workbench*. Academic version. Available at: https://studentcommunity.ansys.com/thread/19-1-free-student-products-are-released/.

[117] ANSYS. *ANSYS Fluent Heat Transfer Modelling, Lecture 04: Natural Convection* [presentation]. 2017 [cit. 2021-04-11]. Available at: 18.2Release-offline.

[118] ANSYS Innovation course. *Natural Convection* [online]. 2020 [cit. 2021-03-18]. Available at: https://courses.ansys.com/index.php/courses/natural-convection/.

[119] Lee, H.-H. *Finite Element Simulations with ANSYS Workbench 2019*. SDC Publications, 2019.

[120] Lienhard, J. H. *A heat transfer textbook*. Courier Dover Publications, 2019. Available at: http://www.mie.uth.gr/labs/ltte/grk/pubs/ahtt.pdf.

[121] Quick Field. *Natural convection coefficient calculator* [online]. 2019 [cit. 2020-04-30]. Available at: https://quickfield.com/natural_convection.htm.

[122] IAEA. *Nuclear Data Service* [online]. 2008 [cit. 2020-05-22]. Available at: https://nds.iaea.org/.

[123] Furman, W., Adam, J., Baldin, A., Berlev, A. and Gundorin, N. Recent results of the study of ADS with 500 kg natural uranium target assembly QUINTA irradiated by deuterons with energies from 1 to 8 GeV at JINR NUCLOTRON. In: *XXI International Baldin Seminar on High Energy Physics Problems*. 2012, p. 10–15.

[124] Morgan, G., Alrick, K., Saunders, A., Cverna, F., King, N. et al. Total cross sections for the production of 22Na and 24Na in proton-induced reactions on 27Al from 0.40 to 22.4 GeV. *Nuclear Instruments and Methods in Physics Research Section B: Beam Interactions with Materials and Atoms*. Elsevier. 2003, vol. 211, no. 3, p. 297–304.

[125] Udemy. *Ansys course* [online]. 2019 [cit. 2020-01-19]. Available at: https://www.udemy.com/topic/ansys/.

[126] Keijers, S., Fernandez, R., Stankovskiy, A., Kennedy, G. and Van Tichelen, K. *Design of the MYRRHA spallation target assembly.* 2015.

[127] Stankus, S. V., Savchenko, I., Agadzhanov, A. S., Yatsuk, O. S. and Zhmurikov, E. Thermophysical properties of MPG-6 graphite. *High Temperature.* Springer. 2013, vol. 51, no. 2, p. 179–182.

[128] WMO. *The State and the Variations of Greenhouse Gases in the Atmosphere* [online]. Data Report. Geneva: World Meteorological Organization, 2020. 13 p. [cit. 2020-02-17]. Available at: https://library.wmo.int/doc_num.php?explnum_id=10074.

[129] Friedlingstein, P., O'Sullivan, M., Jones, M. W., Andrew, R. M., Hauck, J. et al. Global carbon budget 2020. *Earth System Science Data.* Copernicus GmbH. 2020, vol. 12, no. 4, p. 3269–3340.

[130] Le Quéré, C., Peters, G. P., Friedlingstein, P., Andrew, R. M., Canadell, J. G. et al. Fossil CO 2 emissions in the post-COVID-19 era. *Nature Climate Change.* Nature Publishing Group. 2021, vol. 11, no. 3, p. 197–199.

[131] Pehnt, M. Dynamic lifecycle assessment of renewable energy technologies. *Renewable Energy.* 2006, no. 31, p. 55–71. Available at: https://doi.org/10.1016/j.renene.2005.03.002.

[132] Gaglon, L. et al. Life-cycle assessment of electricity generation options: The status of research in year 2001. *Energy Policy.* 2006, no. 30, p. 1267–1278. Available at: https://doi.org/10.1016/S0301-4215(02)00088-5.

[133] Fthenakis, V. M. et al. Emissions from Photovoltaic Life Cycles. *Environ. Sci. Technol.* 2008, no. 42, p. 2168–2174. Available at: https://doi.org/10.1021/es071763q.

[134] Gulevich, A., Kalugin, A., Ponomarev, L., Seliverstov, V. and Seregin, Comparative study of ADS for minor actinides transmutation. *Progress in Nuclear Energy.* Elsevier. 2008, vol. 50, 2-6, p. 359–362.

List of publications

2020

Král, D.; Zeman, M.; Adam, J.; Katovský, K.; Svoboda, J.; Šťastný, O.; Vrzalová, J.; Tichý, P.; Khushvaktov, J.; Solnyshkin, A. Measurement of Activation Products in Chloride Salts Irradiated by Spallation Neutrons. In Proccedings of the 2020 21th International Scientific Conference on Electric Power Engineering (EPE). 2020. p. 1-6. ISBN: 978-1-7281-9479-0.

Svoboda, J.; Adam, J.; Foral, Š.; Gustov, S.; Katovský, K.; Kushvatov, J.; Král, D.; Solnyshkin, A.; Tichý, P.; Tyutyunnikov, S.; Zeman, M. Generated heat by different targets irradiated by 660 MeV protons. INDIAN JOURNAL OF PURE & APPLIED PHYSICS, 2020, vol. 58, no. 4, p. 246-254. ISSN: 0975-1041.

Khushvaktov, J.; Adam, J.; Baldin, A.; Katovský, K.; Král, D.; Furman, W.; Solnyshkin, A.; Svoboda, J.; Závorka, L.; Zeman, M.; Wagner, V. et al. Study of the residual nuclei generation in a massive lead target irradiated with 660 MeV protons. NUCLEAR INSTRUMENTS & METHODS IN PHYSICS RESEARCH SECTION A-ACCELERATORS SPECTROMETERS DETECTORS AND ASSOCIATED EQUIPMENT, 2020, vol. 959, no. 903, p. 1-8. ISSN: 0168-9002.

Tichý, P.; Adam, J.; Gustov, S.; Kushvatov, J.; Solnyshkin, A.; Svoboda, J.; Tyutyunnikov, S.; Zeman, M.; et al. Monitoring mixed neutron-proton field near the primary proton and deuteron beams in spallation targets. INDIAN JOURNAL OF PURE & APPLIED PHYSICS, 2020, vol. 58, no. 4, p. 282-293. ISSN: 0975-1041.

2019

Tichý, P.; Adam, J.; Baldin, A.A.; Chudoba, P.; Furman, W.; Suchopár, M.; Svoboda, J.; Vrzalová, J.; Wagner, V.; Závorka, L.; Zeman, M. et al. Experimental investigation and Monte Carlo simulations of radionuclide production inside the Uranium spallation target QUINTA irradiated with a 660-MeV proton beam. In EPJ Web of Conferences Volume 204 (2019) XXIV International Baldin Seminar on High Energy Physics Problems "Relativistic Nuclear Physics and Quantum Chromodynamics" (Baldin ISHEPP XXIV). EPJ Web of Conferences. Les Ulis: EDP Sciences, 2019. p.4003-4009. ISSN: 2100-014X.

2018

Zeman, M.; Adam, J.; Katovský, K.; Svoboda, J.; Šťastný, O.; Vrzalová, J. et al. Experimental Investigation of the Radionuclides Produced in Massive Spallation Target. In Proccedings of the 2018 19th International Scientific Conference on Electric Power Engineering (EPE). 1. 2018. p. 532-537. ISBN: 978-1-5386-4611-3.

Svoboda, J.; Adam, J.; Brunčiaková, M.; Katovský, K.; Solnyshkin, A.; Zeman, M. et al. Process of heat generation and its transfer monitoring at uranium spallation target QUINTA. In Proccedings of the 2018 19th International Scientific Conference on Electric Power Engineering (EPE). 1. Brno: Brno University of Technology, 2018. p. 522-526. ISBN: 978-1-5386-4611-3.

Khushvaktov, J.; Adam, J..; Svoboda, J.; et al. Monte Carlo simulations and experimental results on neutron production in the uranium spallation target QUINTA irradiated with 660 MeV protons. APPLIED RADIATION AND ISOTOPES, 2018, no. 137, p.102-107. ISSN: 0969-8043.

2017

Zeman, M.; Adam, J.; Katovský, K.; Svoboda, J.; Vespalec, R.; et al. Comparison Between Simulation and Measurement of Neutron Flux Using 59Co at the Spallation Target QUINTA. In The XX International Scientific Conference of Young Scientists and Specialists (AYSS-2016). Dubna, JINR: JINR, 2017. p. 234-238. ISBN: 978-5-9530-0416- 9.

Svoboda, J.; Katovský, K.; Adam, J.; Zeman, M.; Vespalec, R.; et al. High Accurate Measurement of Temperature Differences at The Massive Spallation Uranium Target to Determine The Neutron Flux. In The XX International Scientific Conference of Young Scientists and Specialists (AYSS-2016). Dubna, JINR: JINR, 2017. p. 230-233. ISBN: 978-5-9530-0416-9.

Katovský, K.; Slančík, T.; Ševanka, K.; Zeman, M.; Svoboda, J.; Varmuža, J.; Šťastný, O. Liquid fuel accelerator driven subcritical reactor - the only spent fuel transmutor option?. Proceedings of the ICHERA-2017: international conference on high energy radiation and applications; Vadodara (India); 10-13 Oct 2017. 1. Vadodara, India: Physics Department, The Maharaja Sayajirao University of Baroda, 2017. p. 42-43.

Svoboda, J.; Katovský, K.; Zeman, M.; Adam, J.; et al. Neutron Flux Determination By High Accuracy Temperature Measurement. In 26th International Nuclear Physics Conference, INPC 2016; Adelaide Convention Centre; Australia; 11 September 2016 through 16 September 2016. Proceedings of Science. Trieste - Italy: Sissa Medialab srl Partita IVA: 01097780322, 2017. p. 1-8. ISSN: 1824-8039.

Tichý, P.; Adam, J.; Svoboda, J.; Zeman, M.; et al. Determination and Monte Carlo Simulations of Neutron Flux Inside Spallation Target Quinta. In 26th International Nuclear Physics Conference, INPC 2016; Adelaide Convention Centre; Australia; 11 September 2016 through 16 September 2016. Proceedings of Science. Trieste - Italy: Sissa Medialab srl Partita IVA: 01097780322, 2017. p. 1-8. ISSN: 1824-8039..

2016

Svoboda, J.; Katovský, K.; Zeman, M.; Adam, J.; Solnyshkin, A. et al. Determination of the neutron flux by the temperature differences at the massive spallation uranium target QUINTA. In Proceedings of the 2016 17th International Scientific Conference on Electric Power Engineering (EPE). 1. Praha: Czech Technical University in Prague, 2016. p. 582-585. ISBN: 978-1-5090-0907- 7.

Svoboda, J.; Katovský, K. MOŽNOSTI VYUŽITÍ THORIA V JADERNÉ ENERGETICE SOUČASNOSTI. In Jaderná energetika v pracích mladé generace – 2015. Praha: Česká nukleární společnost, 2016. p. 216-221. ISBN: 978-80-02-02647- 1.

Zeman, M.; Katovský, K.; Svoboda, J.; Vespalec, R.; et al. Current research on ADS at the Joint Institute for Nuclear Research. In PoS- 4th Workshop on ADS and thorium. Proceedings of Science. Huddersfield, Anglie: 2016. p. 1-12. ISBN: 9785953003957. ISSN: 1824-8039.

Varmuža, J.; Vojáčková, J.; Katovský, K.; Foral, Š.; Zeman, M.; Svoboda, J.; Novotný, F. Nuclear Education Programme Development as the Response to the NPP Personnel Retirement. Warsaw: European Nuclear Society, 2016. p. 317-322.

Appendix A

Introduction sub-data

This appendix contains sub-data in charts or tables supporting the author claims in the primary text. They are located in the appendix to do not disturb the primary text, due to its large size. The author sees a lack of information about Global Warming and Climate Change phenomena in lately published theses in energy sector topics. Due to fake news attacking the readers seeking present information in energy topics, base overlook of the current situation was processed.

A.1 Global warming and climate change

Beside of CO_2 ([74]1) mostly produced by combustion of fossil fuels in the energy sector, transport and residential sector, there are methane CH_4 ([75]28) produced by agriculture, energy sector and waste, and finally, the nitrous oxide N_2O ([75]265), primarily produced by agriculture. This three GHG (see Fig. A.2) are concentrated in the atmosphere the most (Fig. A.3), and in particular contribute to climate change ([75]Fig. A.4). The group of „F-gases“, in particular PFC-14 ([75]6,630) or SF_6 ([75]23,500) is regulated by law.

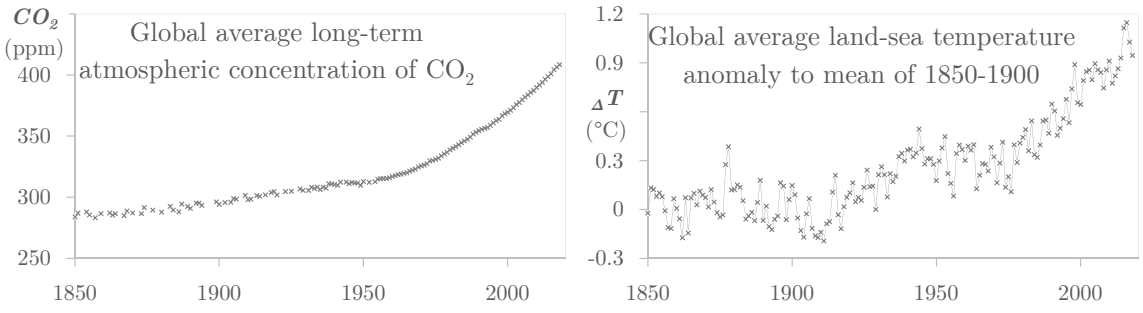

Figure A.1: Global atmospheric CO_2 concentration and temperature anomaly, data [2].

[74] Global warming relative potential to CO_2, based on potential for 100 years.

[75] According to the research of the European Commission, Joint Research Centre and Netherlands Environmental Assessment Agency based on data of the Emission Database for Global Atmospheric Research.

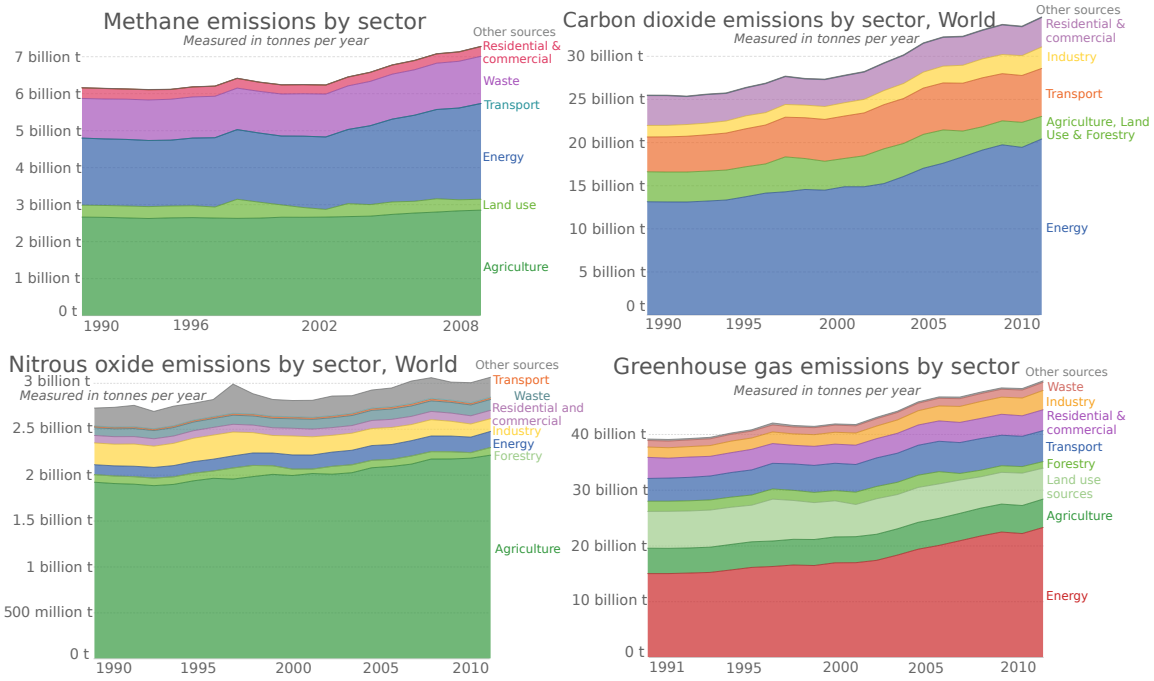

Figure A.2: Greenhouse gas annual emissions by sector, (tCO_2e) [128]

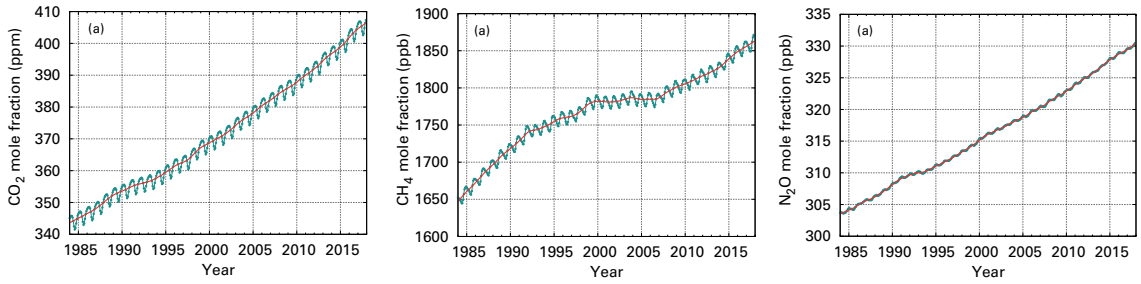

Figure A.3: Global averaged mole fractions for the major greenhouse gases [128]

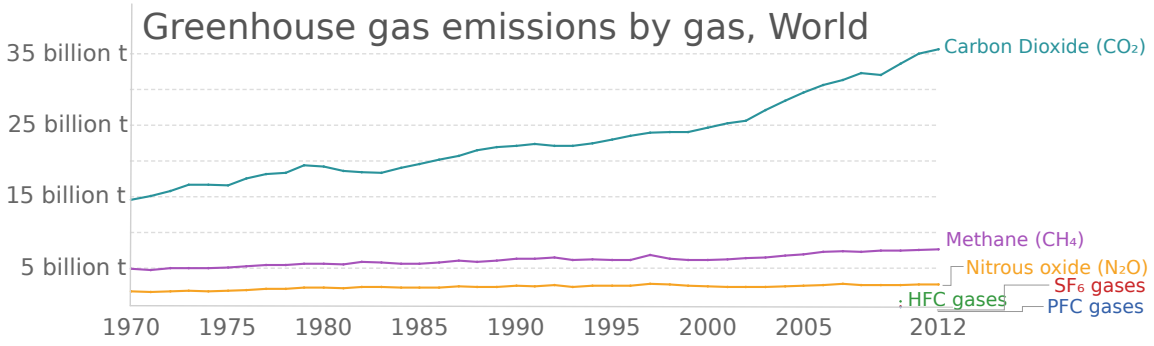

Figure A.4: Greenhouse gas annual emissions in tonnes of CO_2 equivalents (tCO_2e) [128]

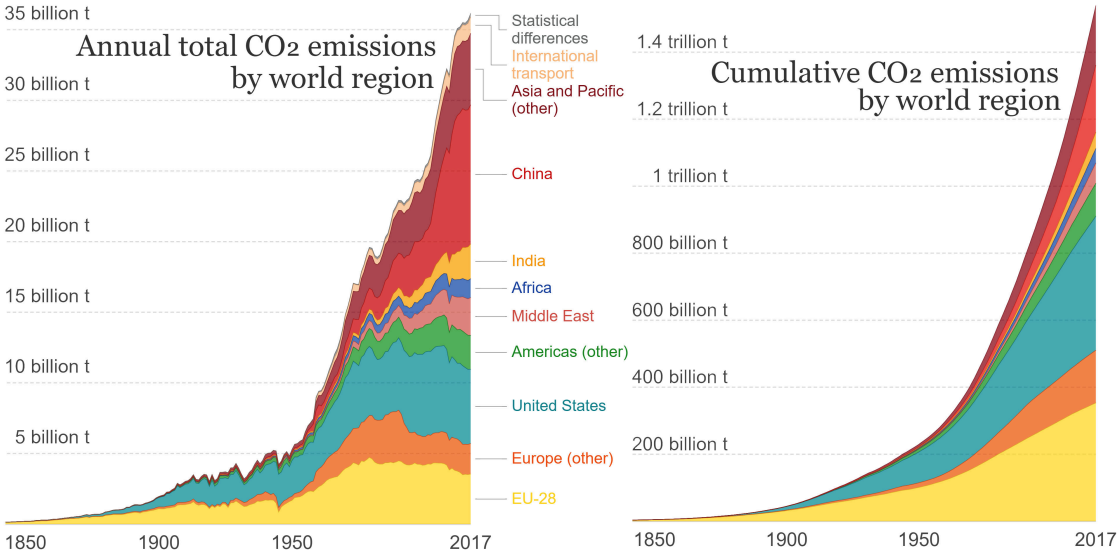

Figure A.5: Annual and cumulative total CO_2 emissions by world region [2].

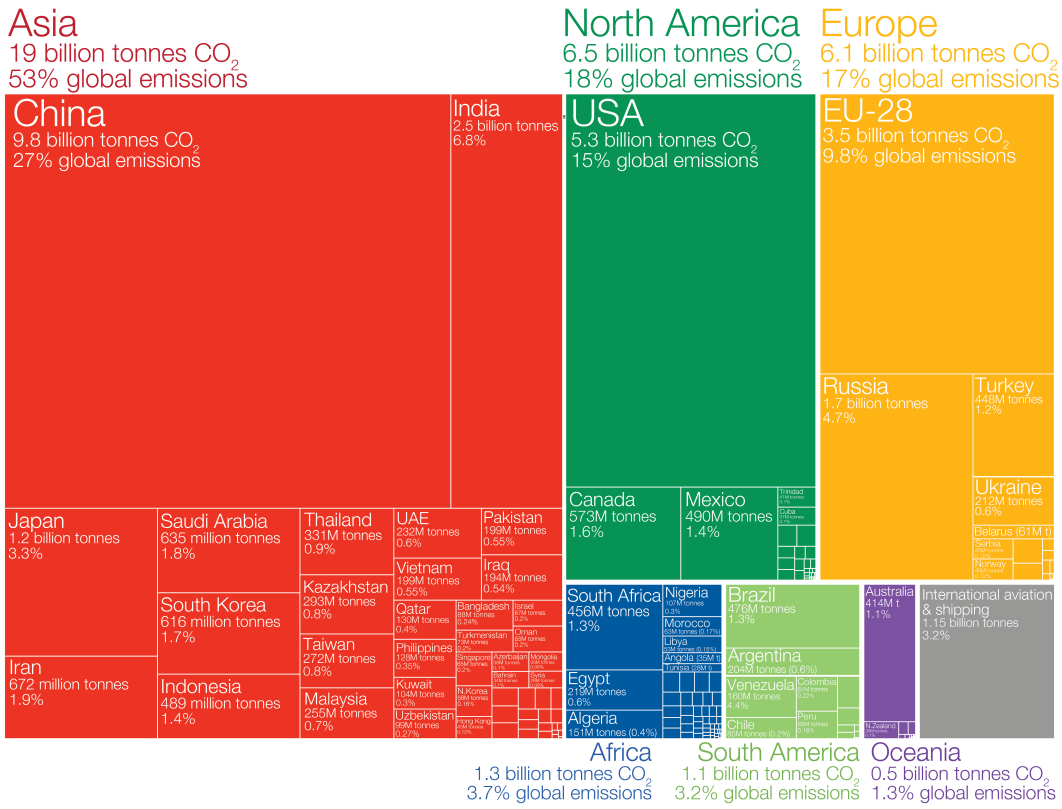

Figure A.6: Annual CO_2 contribution by country in 2017 [2].

A.2 Balance of CO_2 sources and sinks

Where does the carbon go after its emission? As the previous figures in detail described the sources of its emission, finally, on this page is shown its sink. Historically, it is shown in Fig. A.7. Year average detail (2010-2019) of the carbon dioxide balance is shown in Fig. A.8.

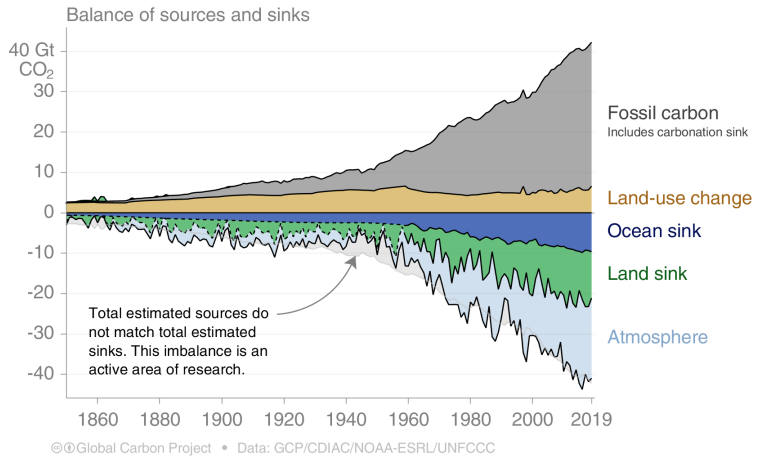

Figure A.7: Historical balance of worldwide CO_2 sources and sinks [129].

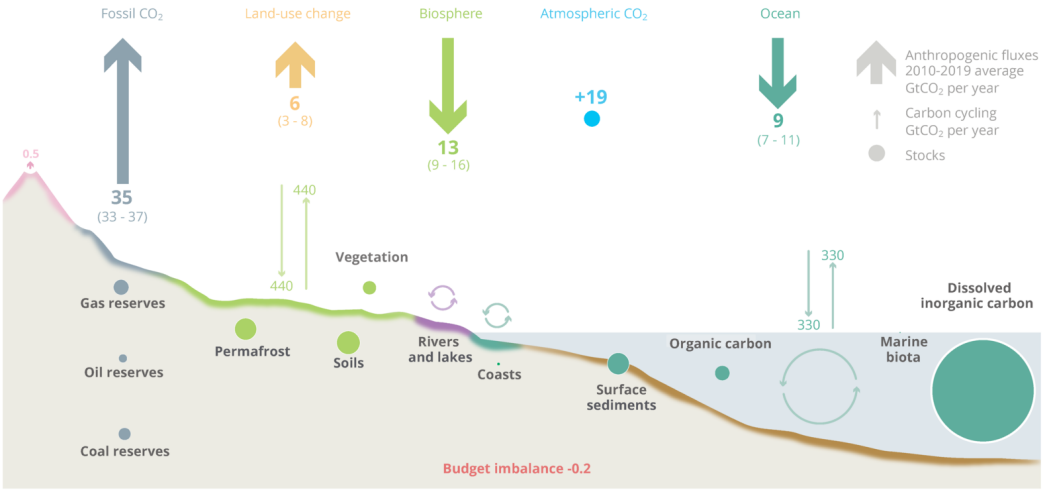

Figure A.8: Detail of global CO_2 sources balance [129], average data for 2010-2019.

A.3 Renewable sources and electricity accumulation

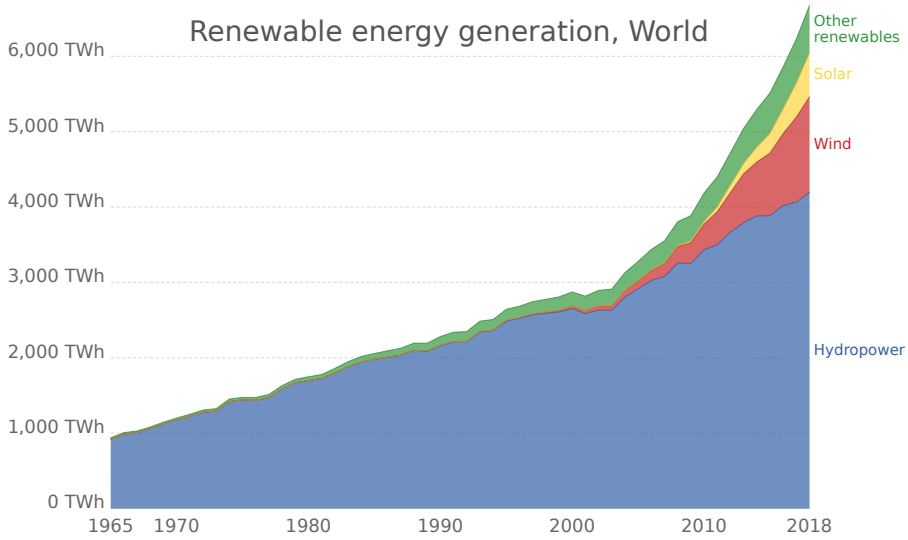

Figure A.9: Electricity generated by renewable sources [2].

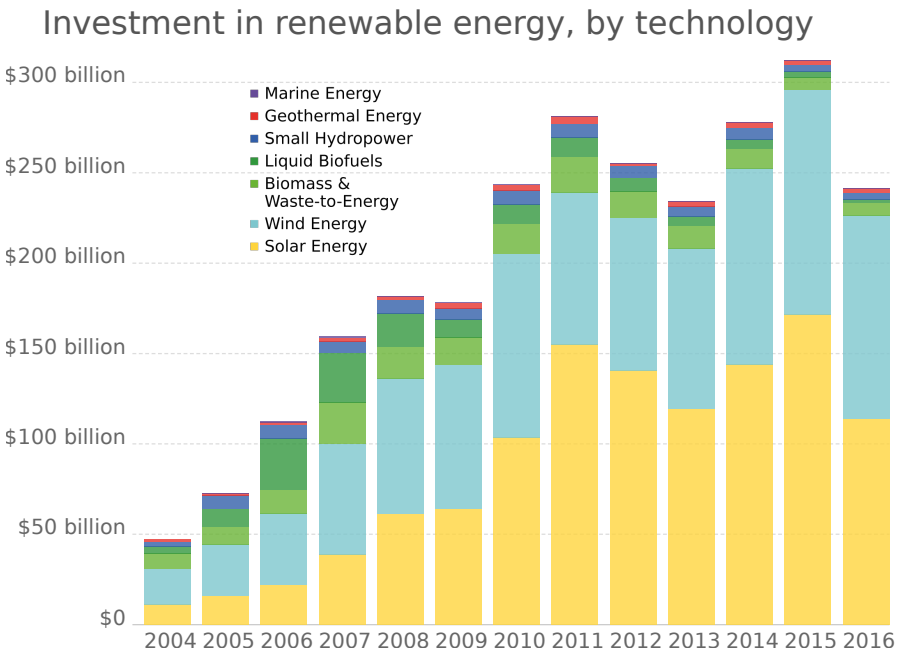

Figure A.10: Investment in renewable energy by source [2].

Shorts used on this page (not included in *List of acronyms*): LA = lead-acid; VRLA = valve-regulated lead-acid; NaS = sodium sulphur; NaNiCl = sodium nickel chloride; VRFB = vanadium redox flow battery; ZBFB = zinc bromine flow battery; NCA = nickel cobalt aluminium; NMC/LMO = nickel manganese cobalt oxide/lithium manganese oxide; LFP = lithium iron phosphate; LTO = lithium titanate [20].

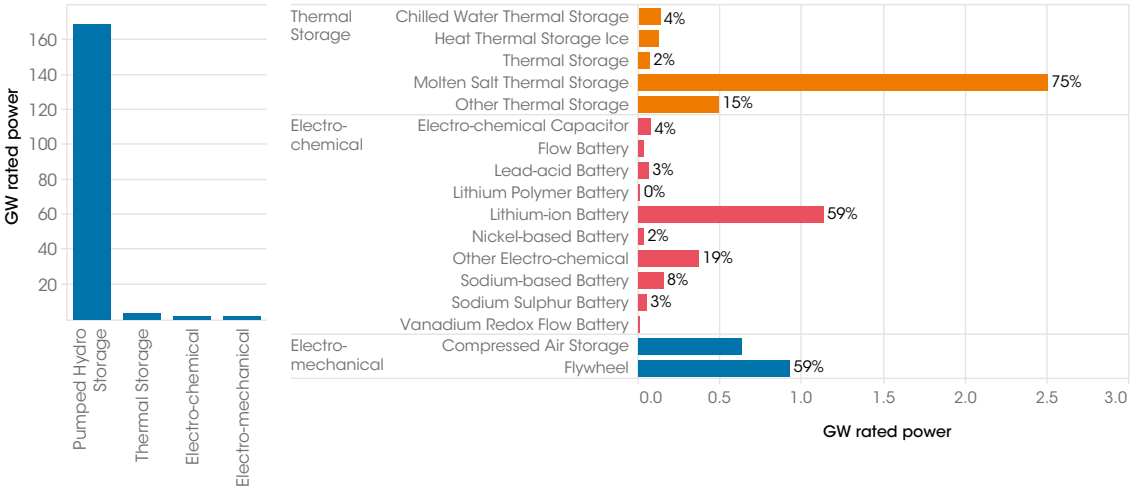

Figure A.11: Electricity power capacity storage worldwide by technology in mid-2017 [20]

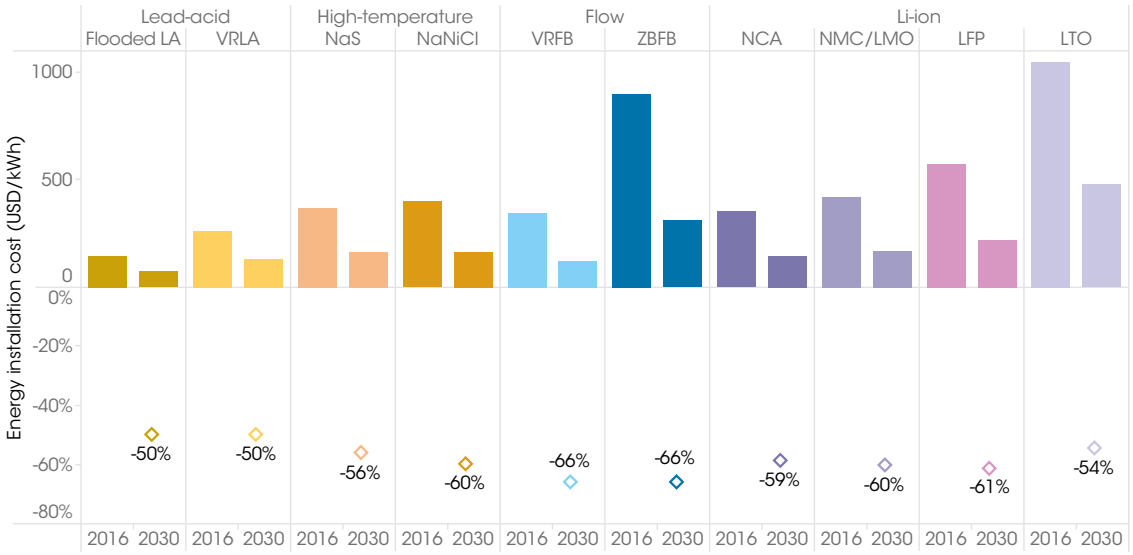

Figure A.12: Install energy cost reduction potential for various battery, outlook to 2030 [20]

A.4 Global warming 2021 update (COVID-19 data)

The section about global warming was written at the end of 2019 when the whole planet has no idea about the coming epidemic. The Asian people wearing masks were targets of jokes, the only problem of aviation was Boeing 737 MAX and the fossil CO_2 emissions should increase based on the expected scenario. The COVID-19 pandemic shook the world. Due to countries lock-downs, the carbon emissions decreased much more than any previous crisis.

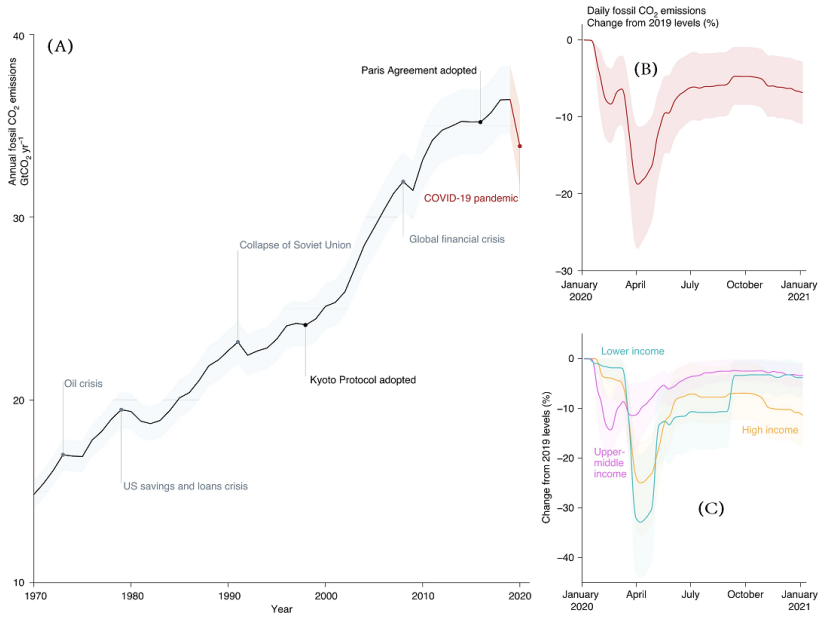

Figure A.13: On the figure (A) is shown an annual fossil carbon emission during 1970-2019 (with 2020 projection) in $GtCO_2 \cdot year^{-1}$. Figure (B) shows the detail of daily changes during 2020 compared to 2019. Finally, figure (C) shows a comparison of various countries grouped by their income (economy) [130].

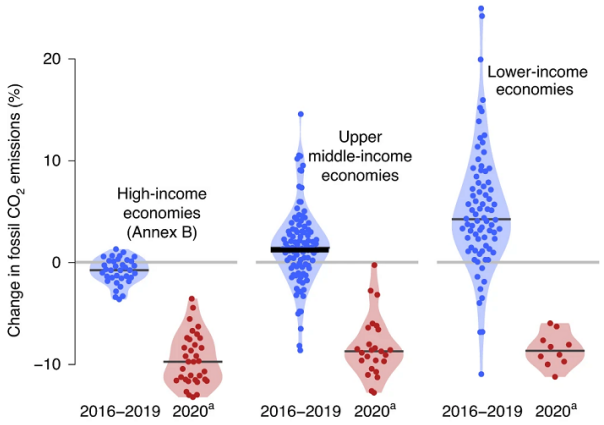

Figure A.14: Comparison of yearly average emission during 2016-2019 with pandemic year 2020 for 3 groups of country divided by its income [130].

A.5 Relative CO_2 equivalent emission per sources

Table A.1: Estimation of the relative CO_2 equivalent emission for various sources. Two different data sources, 2014 [16] and 2008 [17].

Technology	**Capacity/configuration/fuel**	**Estimate (/kWh)**
Wind	2.5MW, offshore	9
Hydroelectric	3.1MW, reservoir	10
Wind	1.5MW, onshore	10
Bio-gas	Anaerobic digestion	11
Hydroelectric	300kW, run-of-river	13
Solar thermal	80MW, parabolic trough	13
Biomass	Forest wood Co-combustion with hard coal	14
Biomass	Forest wood steam turbine	22
Biomass	Short rotation forestry Co-combustion with hard coal	23
Biomass	Forest wood reciprocating engine	27
Biomass	Waste wood steam turbine	31
Solar PV	Poly-crystalline silicone	32
Biomass	Short rotation forestry steam turbine	35
Geothermal	80MW, hot dry rock	38
Biomass	Short rotation forestry reciprocating engine	41
Nuclear	Various reactor types	66
Natural gas	Various combined cycle turbines	443
Fuel cell	Hydrogen from gas reforming	664
Diesel	Various generator and turbine types	778
Heavy oil	Various generator and turbine types	778
Coal	Various generator types with scrubbing	960
Coal	Various generator types without scrubbing	1050

Wind, hydroelectric, bio-gas, solar thermal, biomass, and geothermal data were taken from [131]. Diesel, heavy oil, coal with scrubbing, coal without scrubbing, natural gas, and fuel cell data from [132]. Solar PV estimates taken from [133]. Nuclear is taken from [17]. Estimated values have been rounded to integers. Due to the progress in renewable technologies, the numbers are expected to be slightly different (lower) nowadays. Unfortunately, the reliable updated source was not found.

Appendix B

Chapter 2 sub-data

B.1 History of interested ADS research projects worldwide

Table B.1: History of interested ADS research projects worldwide, data from [134].

Project	Beam power [MW]	k_{ef}	Blanket power [MW]	*n* flux spectra [$n \cdot cm^{-2}$]	Target material [-]	Fuel
ABC-ADDT-ATW-AFCI (USA)	4.8 (800 MeV, 6 mA)	0.95	250	thermal	Pb	ThU
OMEGA (Japan 1997)	58 (1.5 GeV, 39 mA)	0.9	820	4×10^{15} fast	W	Np/5Pu/30Zr
JAERI-ADS (Japan 2004)	27 (1.5 GeV, 18 mA)	0.97	800	fast	Pb–Bi	MA/Pu/ZrN
HYPER (S. Korea)	15 (1 GeV, 10–16 mA)	0.98	1000	fast	Pb–Bi	MA/Pu
XADS Design A (Italy)	3.6 (600 MeV, 3–6 mA)	0.95–0.97	80	10^{15} fast	Pb–Bi	U/Pu/MOX
XADS Design B (France)	3.6 (600 MeV, 3–6 mA)	0.95–0.97	80	10^{15} fast	Pb–Bi	U/Pu/MOX
Design C (Belgium)	1.75(5 mA, 350 MeV)	0.95	50	3×10^{15} fast	Pb–Bi	U/Pu/MOX
INR (Russia)	0.15 (10 mA, 500MeV)	0.95–0.97	5	fast	W	MA/MOX
NWB (Russsia)	3 (380 MeV, 10 mA)	0.95–0.98	100	10^{14}–10^{15} fast	Pb–Bi	UO2/UN U/MA/Zr
CSMSR (Russia)	10 (1 GeV, 10 mA)	0.95	800	5×10^{14} epitherm.	Pb–Bi	Np/Pu/MA Melted salt

Appendix C

Chapter 3 sub-data

C.1 Python script - merging and filtering

```
from scipy import signal
from scipy.signal import savgol_filter
import matplotlib.dates as mdates
import os, glob, sys, xlrd
import pandas as pd
# patch to your folder
path = "c:\\Clouds\\owncloud\\vut-jinr\\PhD\\_Dubna\\experimenty\\calibration"
# want merging?
merging = True
# ------------------------------ merging ---------------------------
if merging:
    all_files = glob.glob(os.path.join(path+"\\calibration_*.xlsx"))
    all_df = []
    for f in all_files:
        df = pd.read_excel(f)
        all_df.append(df)
    merged_df = pd.concat(all_df, ignore_index=True, sort=True)
    print(merged_df)
    merged_df.to_csv(path+"\\merged.csv", sep=";")

content_all = pd.read_csv(path + "\\merged.csv", sep = ";", parse_dates=["Time"], index_col ="Time")
RTD=content_all.iloc[14000:22500,[0:4]] # ready for calibration
tc=content_all.iloc[14000:22500,[4:]] # ready for calibration
tc_all=content_all.iloc[:,[4:]] # all_thermocouples data

def filter(x):
    return savgol_filter(x, 11, 1)
smoothed_TC = tc.apply(filter)
smoothed_RTD = RTD.apply(filter)
smoothed_TC_all = tc_all.apply(filter)

def MED(x):  # definition of min-max function
    return pd.Series(index=['median'], data=[x.median()])
RTDmedian_beg = smoothed_RTD.iloc[0:50,:].apply(MED)
tcmedian_beg = smoothed_TC.iloc[0:50,:].apply(MED)
RTDmedian_end = smoothed_RTD.iloc[8400:8450,:].apply(MED)
tcmedian_end = smoothed_TC.iloc[8400:8450,:].apply(MED)

smoothed_TC_all.plot() # to plot smoothed data
tc_all.plot() # to plot raw data
plt.show()
```

Figure C.1: Python code of basics data manipulation - merging and filtering.

```
import numpy as np; import scipy as sp; import sys      # Josef Svoboda, BUT v Brně
import pandas as pd; from scipy.integrate import quad   # josef.svoboda @ vutbr.cz
# change following 5 lines
RTD = 30.1 # units °C === T at the beginning of experiment, the thermocouples are calibrated to it
TC_type = "E" # choose here which TC type want to calibrate
path = "c:\\Clouds\\owncloud\\vut-jinr\\PhD\\_Dubna\\experimenty\\z_DzP"
cal_file = pd.read_csv(path + "\\thermocouples_calibration.csv", sep=";") # data reading
content_all = pd.read_csv(path + "\\data001.csv", sep=";", parse_dates=["Time"], index_col="Time")
# to distinguish thermocouple type T and E, the column name must include "T_" or "E_"
if TC_type == "T":          # choosing rows of TC_T or TC_E
    cols = [col for col in content_all.columns if 'T_' in col]; type = 1
elif TC_type == "E":
    cols = [col for col in content_all.columns if 'E_' in col]; type = 2
else:
    print("\nERROR occurred!!!\n\n---Wrong variable TC_type set. Ensure the TC_type is 'T' or 'E'!!!---")
    sys.exit()
df_TC = content_all.loc[:, cols];   colum = []  # makes new DF of selected type of thermocouples (E or T)
for col in df_TC.columns:   #  it makes list of the selected column names
    colum.append(col)       # thermocouples choosing is finished ---
def minMax(x):  # definition of min-max function
    return pd.Series(index=['min_dV(uV)', 'max_dV(uV)'], data=[x.min(), x.max()])
stats = df_TC.apply(minMax)  # makes new DF of min max for selected thermocouples file
# ---------------------------------- voltage gain polynomial calibration based on data-sheet data ---|||
y_ = np.array(cal_file.iloc[50:76, type])   # reading x data -10->15°C
x_ = np.array(cal_file.iloc[50:76, 0])      # reading y data -10->15°C
z = np.polyfit(x_, y_, 2)  # making fit
p = np.poly1d(z)  # return parameters of calculated fit

A_abs = np.ndarray.tolist(z)[0] # parameter A of the polynomial function
B_abs = np.ndarray.tolist(z)[1] # parameter B of the polynomial function
C_abs = np.ndarray.tolist(z)[2] # parameter C of the polynomial function
fce = A_abs * x_ * x_ + B_abs * x_ + C_abs  # calculate rel. gain from polynomial fit
#difference_polynom_vs_data = (((fce - y_) / (y_)) * 100)
#print("differences (in % ) are:\n\n",difference_polynom_vs_data)

voltage_cal_min = stats.iloc[0, :].to_numpy() / 1000 # searching min Emf (mV)
voltage_cal_max = stats.iloc[1, :].to_numpy() / 1000 # searching max Emf (mV)
# makes absolute voltage equal to 0°C compensation cold junction
voltage_cal = np.column_stack((voltage_cal_min, voltage_cal_max))

C_abs_ = C_abs - voltage_cal  # move y axis from ZERO to voltage_cal to find positive root of function
# following x2 calculated all absolute Temp based on measured !ABSOLUTE! voltage by polyfit
x2 = np.array((-B_abs + (B_abs * B_abs - 4 * A_abs * C_abs_) ** 0.5) / (2 * A_abs)) #second root of |dT|
one_df = pd.DataFrame(x2, columns=['minT(°C)', "maxT(°C)"], index=colum).T # writes min and max |dT| measured by HJ
save_abs_V_cal=pd.concat([one_df,stats],axis=0) # it is saved in the end on code
# ---------------------------- end of absolute polynomial calibration based on RTD temperature --------|||

# ccccccccccccccccccccccccccccccc calibration based on polynomial fit of V gain per degree C  -------- |||
x_list = []; y_list = []
for i in range(49, 75):  # choose temperatures -10->+15°C, and its equal voltage gain (voltage difference)
    y_list.append(cal_file.iloc[i + 1, type] - cal_file.iloc[i, type])  # load gain per °C to y axis
    x_list.append(cal_file.iloc[i + 1, 0]) # load temperature
y = np.asarray(y_list, dtype=np.float32)
x = np.asarray(x_list, dtype=np.float32)
print("temperature (°C):\n",x,"\nrelVgain calculated from data-sheet (uV/°C):\n",y*1000)

z_perC = np.polyfit(x, y, 2)  # it makes 2nd poly fit of voltage gain per degree celsius
p_perC = np.poly1d(z_perC)  # return gain per °C for "z" temperature according to fit
A_perC = np.ndarray.tolist(z_perC)[0] #parameters
B_perC = np.ndarray.tolist(z_perC)[1]
C_perC = np.ndarray.tolist(z_perC)[2]
fce_perC = np.round((A_perC * x **2 + B_perC * x + C_perC)*1000,2)  # y axis calculated from polynomial fit
print("\npoly fit of relVgain (uV/°C)\n",fce_perC)
linFIT= np.polyfit(x, y, 1)  # it makes lin fit of voltage gain per degree celsius
lin_perC = np.poly1d(linFIT)  # return gain per °C for "z" temperature according to fit
A_lin_perC = np.ndarray.tolist(linFIT)[0] #parameters
B_lin_perC = np.ndarray.tolist(linFIT)[1] #parameters
fce_lin_perC = np.round((A_lin_perC*x+B_lin_perC)*1000,2)
print("\nlin fit of relVgain (uV/°C)\n",fce_lin_perC)
difference_polynom_perC_vs_data = (((fce_perC - y) / (y)) * 100) # calc. difference to fit
lin_regression_perC_vs_data = (((fce_lin_perC - y) / (y)) * 100) # calc. difference to fit
print("\nlinear regression   slope:",A_lin_perC,"offset",B_lin_perC)
print("\n rel. diff. of lin.vs.poly.(ref) fit:\n",np.round((fce_perC-fce_lin_perC)/fce_perC*100,2))

# to find measured voltage if know RTD and measured temperature -> fill in following temperature ||
down = RTD
up   = 19.74 # change here known temperature to calculate the measured voltage
print("\nNow calculating the integral (V_meas.) between temperature limits", down, "and", up, "°C")
a=A_perC; b=B_perC; c=C_perC
```

Figure C.2: Code of automatic calibration (1/2) in Python 3.7. [32].

```
 80 def integrand(x, a, b, c):
 81     return a * x ** 2 + b * x + c
 82 I = sp.integrate.quad(integrand, down, up, args=(a, b, c))
 83 print("\nMeasured voltage on thermocouples is (Integral): ",round(I[0],4), "mV")
 84 # -------  calculation of integral manually  ---------------- if require for up&down boundaries
 85
 86 # the temperature is calculate based on gain per °C polynomial calibration,
 87 # integer is known (measured voltage) a one of boundaries is seeking temperature
 88 calculated_T = []; measured = (np.array(stats)/1000) # is calculates min and max of measured V
 89 for q in np.nditer(measured): # it is iterating by columns !!!
 90     if q >= 0:
 91         up = np.roots([a / 3, b / 2, c, +q]) #move integral about q to find dT = root
 92         calculated_T.append(round(up[2],5))
 93     elif q < 0:
 94         down = np.roots([a / 3 , b / 2 , c , - q]) # for negative Emf
 95         calculated_T.append(round(down[2], 5))
 96 minlist=[]; maxlist=[];i=0
 97 while i < len(calculated_T):
 98     minlist.append(calculated_T[i]);  i=i+1
 99     maxlist.append(calculated_T[i]);  i=i+1
100 calculated_T_pd = pd.DataFrame([minlist,maxlist], index=["min","max"], columns = colum)
101 T_g=stats.loc['max_dV(uV)']-stats.loc['min_dV(uV)'] #calculate diff. measured voltage max-min
102 TC_gain=calculated_T_pd.loc['max']-calculated_T_pd.loc['min'] #the same for temperature
103 cal=pd.DataFrame(T_g/TC_gain, columns=["av.cal_gain(uV)"]).T #simply divide to reach average slope
104 # each thermocouple was measured for certain dT (-10°C) a its gain difference was calculate
105 gain_cal= pd.read_csv(path + "\\cal_thermocouple_E_gain.csv", sep=";") # loading gain difference
106 final_gain_cal=pd.DataFrame((cal.iloc[0,:].sub((gain_cal.iloc[0,:]),axis=0)),columns=["final_calibrated"])
107 save_all=pd.concat([save_abs_V_cal,cal,final_gain_cal.T],axis=0) # merging of DataFrames to save together
108 if TC_type == "T":
109     save_all.to_csv(path+"\\cal_thermocouple_T.csv")
110 elif TC_type == "E":
111     save_all.to_csv(path+"\\cal_thermocouple_E.csv")
```

Figure C.3: Code of automatic calibration (2/2) in Python 3.7. [32].

The previous code is described by comments of the code. To make it easier to clearly understand, a summary of the code is written here. Lines need to be changed (4-8, 105) where the patch name of the used files is written. The program deals separately with TC types T and E, so it is specified in line 5. Lines 10-22 deal with separating TC which will be calibrated (if type E is chosen, only columns that contain the label $E\_$ are used) and further the minimal and maximal measured voltage are found. Lines 23-45 deal with the calibration based on the polynomial fit of the absolute voltage (Emf) gain of data-sheet data. Lines 48-55 calculate the relative voltage gain (derivative function of absolute voltage gain) and save data to arrays x and y. It is used by rows 57-73 to make polynomial and linear fits, it checks the relative error and prints it (see in results Fig. C.4). There is also the calculation of integral for the case if know the measured temperature and want to calculate the measured voltage based on relative voltage gain. Finally, the most important part of the code is shown in rows 88-111. It calculates average gain slope for measured range by TC (^{max}dV-^{min}dV). All calculated data are merged (line 107) and saved to the csv file by the type of TC.

The results from the previous code is shown in following lines, the table is extracted from the csv file.

temperature (°C):
[-10. -9. -8. -7. -6. -5. -4. -3. -2. -1. 0. 1. 2. 3. 4. 5. 6. 7. 8. 9. 10. 11. 12. 13. 14. 15.]

relVgain calculated from data-sheet (uV/°C):
[57. 58. 58. 58. 58. 58. 58. 58. 59. 58. 59. 59. 59. 58. 59. 59. 60. 59. 59. 60. 59. 60. 60. 59. 60. 60.]

poly fit of relVgain (uV/°C)
[57.51 57.63 57.75 57.86 57.98 58.09 58.2 58.31 58.42 58.52 58.62 58.72 58.82
58.92 59.01 59.1 59.19 59.28 59.36 59.44 59.52 59.6 59.68 59.75 59.82 59.89]

lin fit of relVgain (uV/°C)
[57.62 57.71 57.81 57.9 58. 58.09 58.19 58.28 58.38 58.47 58.57 58.66 58.76
58.86 58.95 59.05 59.14 59.24 59.33 59.43 59.52 59.62 59.71 59.81 59.9 60.]

linear fit: slope: 9.5385e-05 offset 0.05857

rel. difference of linear vs. polynomial fit (poly=ref):
[-0.19 -0.14 -0.1 -0.07 -0.03 0. 0.02 0.05 0.07 0.09 0.09 0.1 0.1
0.1 0.1 0.08 0.08 0.07 0.05 0.02 0. -0.03 -0.05 -0.1 -0.13 -0.18]

Now calculating the integral (measured V) between temperature limits 30.1 and 19.74 °C

Measured voltage on thermocouples is (Integral): -0.6262 mV

Finally, the csv file of calibration is saved based on TC type. It contains following data format:

	$^{converter}\mathbf{E_{H0}}$	$^{converter}\mathbf{E_{H1}}$	$\mathbf{E_{H2}}$	$\mathbf{E_{H3}}$	$^{shielded}\mathbf{E_{H4}}$	$^{shielded}\mathbf{E_{H5}}$
min_dT(°C)	0.313	0.526	-9.600	-9.583	-9.422	-9.182
max_dT(°C)	0.328	0.540	-9.329	-9.311	-9.124	-8.883
minV(uV)	18.356	30.864	-558.691	-557.723	-548.447	-534.542
maxV(uV)	19.241	31.684	-543.082	-542.048	-531.198	-517.294
average$_{cal}^{gain}$(uV)	58.593	58.540	57.570	57.571	57.592	57.622
final$_{cal}^{gain}$(uV)	58.493	58.188	57.869	57.768	56.821	55.399

Figure C.4: Results from automatic calibration program (Fig.C.2 and Fig.C.3).

C.2 Python script - visualisation of subplots & zoom

```
import os, glob, sys, xlrd
import pandas as pd
import matplotlib.pyplot as plt
from matplotlib import rc
rc('font', **{'family': 'serif', 'serif': ['Computer Modern']})
rc('text', usetex=True)

# patch to your folder and files
path = "c:\\Clouds\\owncloud\\vut-jinr\\PhD\\_Dubna\\experimenty\\calibration"
smoot=pd.read_csv(path + "\\dataa_.csv", sep = ",", parse_dates=["Time"], index_col ="Time")
smootRTD=pd.read_csv(path + "\\dataaRTD.csv", sep = ";", parse_dates=["Time"], index_col ="Time")
RTD_zoom=pd.read_csv(path + "\\RTD6_8lin.csv", sep = ",", parse_dates=["Time"], index_col ="Time")
RTD_dif=RTD_zoom.iloc[:,1:].sub(RTD_zoom.iloc[:,0].tolist(), axis=0)
RTD_dif.columns=["$\Delta$T$_{RTD_{1}-RTD_{0}}$","$\Delta$T$_{RTD_{2}-RTD_{0}}$","$\Delta$T$_{RTD_{3}-RTD_{0}}$"]
TC_diff_cal=pd.read_csv(path + "\\TC_calibrated.csv", sep = ",", parse_dates=["Time"], index_col ="Time")
all_together=pd.concat([TC_diff_cal,RTD_dif.iloc[:,:]], axis=1, sort=False)
all_together_zoom = all_together.iloc[8200:8400,:]

f = plt.figure(figsize=(14,6)) # figure size

ax1 = f.add_subplot(231) # first subplot and following others
ax1.plot(smoot.index, smoot)
ax1.set_ylabel(r'Measured voltage ($\mu$V)')
ax1.xaxis.set_major_locator(mdates.HourLocator(interval = 2))
ax1.xaxis.set_major_formatter(mdates.DateFormatter('%H:%M'))
ax1.xaxis.set_minor_locator(mdates.MinuteLocator(byminute=[0,15,30,45], interval = 1))
ax1.legend(smoot.columns.tolist(), loc="center")
plt.setp(ax1.get_xticklabels(), visible=False)

ax2 = f.add_subplot(234, sharex=ax1)
ax2.plot(smootRTD.index, smootRTD)
ax2.set_xlabel("Time")
ax2.set_ylabel(r'Measured temperature ($^{\circ}$C)')
ax2.xaxis.set_major_locator(mdates.HourLocator(interval = 2))
ax2.xaxis.set_major_formatter(mdates.DateFormatter('%H:%M'))
ax2.xaxis.set_minor_locator(mdates.MinuteLocator(byminute=[0,15,30,45], interval = 1))
plt.subplots_adjust(hspace=0)
plt.gca().xaxis.set_label_coords(0.5, 0.07)
ax2.legend(smootRTD.columns.tolist(), loc="center")

ax3 = f.add_subplot(133)
ax3.plot(all_together.index, all_together)
ax3.set_xlabel("Time")
ax3.set_ylabel(r'Temperature change trend ($^{\circ}$C)')
ax3.xaxis.set_major_locator(mdates.HourLocator(interval = 1))
ax3.xaxis.set_major_formatter(mdates.DateFormatter('%H:%M'))
ax3.xaxis.set_minor_locator(mdates.MinuteLocator(byminute=[0,15,30,45], interval = 1))
plt.subplots_adjust(wspace=0.2)
ax3.legend(all_together.columns.tolist(), loc="best")
plt.gca().xaxis.set_label_coords(0.3, 0.03)
# zoom chart will be input in last chart down
ax6 = plt.axes([0.79, 0.17, 0.1, 0.28])
ax6.plot(all_together_zoom.index, all_together_zoom)
ax6.xaxis.set_major_locator(mdates.MinuteLocator(interval = 1))
ax6.xaxis.set_major_formatter(mdates.DateFormatter('%H:%M'))

ax4 = f.add_subplot(232)
ax4.plot(RTD_zoom.index, RTD_zoom)
ax4.set_ylabel(r'RTD temperature increase ($^{\circ}$C)')
ax4.xaxis.set_major_locator(mdates.HourLocator(interval = 1))
ax4.xaxis.set_major_formatter(mdates.DateFormatter('%H:%M'))
ax4.xaxis.set_minor_locator(mdates.MinuteLocator(byminute=[0,15,30,45], interval = 1))
ax4.legend(RTD_zoom.columns.tolist(), loc="best")

ax5 = f.add_subplot(235)
ax5.plot(RTD_dif.index, RTD_dif)
ax5.set_ylabel(r'RTD HJs-CJ $\Delta$T ($^{\circ}$C)')
ax5.xaxis.set_major_locator(mdates.HourLocator(interval = 1))
ax5.xaxis.set_major_formatter(mdates.DateFormatter('%H:%M'))
ax5.xaxis.set_minor_locator(mdates.MinuteLocator(byminute=[0,15,30,45], interval = 1))
ax5.legend(RTD_dif.columns.tolist(), loc="best")
plt.gca().xaxis.set_label_coords(0.5, 0.07)
# setting labels and tics size
plt.rcParams['ytick.labelsize'] = 12
plt.rcParams['xtick.labelsize'] = 12
plt.rcParams['axes.labelsize'] = 13
plt.savefig(path+'\\plot3.pdf')
```

Figure C.5: Python code of data plotting - subplot with zoom of chart.

C.3 Python script - visualisation of MESH; any chosen plane

```
# program for plotting mesh from MCNPX output
# author    : Josef Svoboda;
# aff.      : Joint Institute for Nuclear Research // Brno University of Technology;
# email     : svoboda@jinr.ru // Josef.Svoboda@vutbr.cz
# Must DO: 1) clean data file only with data = all_data_
# Must DO: 2) boundaries of mesh in three lines as datafile = all_data_axis

import numpy as np, import pandas as pd, import matplotlib.pyplot as plt, from matplotlib import cm
import seaborn as sns, from matplotlib.colors import ListedColormap, LinearSegmentedColormap
cut_xy=None, cut_xz=None, cut_yz=None # don't change
#change target name (shows in charts)
target_name = "Carbon"
# set the patch here:
path = "d:\\Clouds\\ownCloud\\vut-jinr\\PhD\\_Dubna\\experimenty\\Carbon\\"
# what cross-section (CS) do you want:  (comment lines you don't use)
cut_xy = [5, 10, 20, 30, 50, 60, 70, 90]  # number 1 means xy1 ->first cubes in mesh
cut_xz = [1,5,10,20]
cut_yz = [2,7, 15, 21]
# load files prepared in point 1 and 2 (lines 3 & 4)
content = pd.read_fwf(path+"all.data", header=None)
name = pd.read_fwf(path+"all_data_axis", header=None)
# ---- now it will create new folder where the results will be saved
if not os.path.exists(path + "mplot"):
    os.mkdir(path + "mplot")
# locating name of lines and columns, deleting NaN and convert to list, after make it float
name_x = name.iloc[[0]].dropna(axis=1).values.tolist()[0]
# open DF "name", line 0, drops NaN for axis in line and save values to list
namex = [float(i) for i in name_x]
name_y = name.iloc[[1]].dropna(axis=1).values.tolist()[0]
namey  = [float(i) for i in name_y]
name_z = name.iloc[[2]].dropna(axis=1).values.tolist()[0]
namez  = [float(i) for i in name_z]
# now it is preparing variable with total number of elements in each axis
CSx=len(namex)-1 # number of possible CS (Cross-Sections) in axis x
CSy=len(namey)-1 # number of possible CS (Cross-Sections) in axis y
CSz=len(namez)-1 # number of possible CS (Cross-Sections) in axis z

# makes average of boundaries -> boundaries to mesh cube center, round to 2 decimals
namex_real = [], namey_real = [], namez_real = []
for x in range(0, len(namex) - 1):
    namex_real.append(float((namex[x] + namex[x + 1]) / 2))
namex_real = [round(x,1) for x in namex_real]
for x in range(0, len(namey) - 1):
    namey_real.append(float((namey[x] + name_y[x + 1]) / 2))
namey_real = [round(x,1) for x in namey_real]
for x in range(0, len(namez) - 1):
    namez_real.append(float((namez[x] + namez[x + 1]) / 2))
namez_real = [round(x,1) for x in namez_real]
# setting white color for heat 0-0,01% to see the shape
max=1000, OrgRed = cm.get_cmap('OrRd', max)
newcolors = OrgRed(np.linspace(0, 1, max))
white = np.array([1, 1, 1, 1])
black = np.array([max, max, max, 1])
newcolors[:1, :] = white
newcmp = ListedColormap(newcolors)

if cut_xy != None:
    # ------------------------------------------------ cut_xy ------------------------------------------------
    for i in range (0,len(cut_xy)):
        xy=content.iloc[(cut_xy[i]-1)*CSx:cut_xy[i]*CSx]
        xy.index = [namey_real]
        xy.columns = [namex_real]
        xy = xy.rename_axis(index="Axis y - height of "+target_name+" target [cm]",
                            columns="Axis x - width of "+target_name+" target [cm]")
        yticks = np.linspace(-9, 9, 7)
```

Figure C.6: Python code - MCNPX MESH plotting various MESH cross-sections (1/2).

```
        sns.set(font_scale=2)
        fig, ax = plt.subplots(figsize=(12,9))          # Sample figsize in inches
        plt.title("Cross-section of xy axes in distance of z = "+str(namez_real[cut_xy[i]])+" mm", y=1.08)
        g=sns.heatmap(xy, cmap=newcmp, xticklabels=3, yticklabels=3, vmin=0)
        g.set_xticklabels(g.get_xticklabels(),rotation=90)
        g.set_yticklabels(g.get_yticklabels(),rotation=0)
        g.collections[0].colorbar.set_label("Heat deposition [MeV cm$^{-3}$ proton$^{-1}$]", labelpad=20)
        g.xaxis.labelpad = 20
        g.yaxis.labelpad = 20
        # g.set_yticks(yticks*ax.get_ylim()[1])
        plt.tight_layout()
        plt.savefig(path+"mplot\\xy"+str(cut_xy[i])+"plot.png")
        plt.close()
    print("\n\n","All works fine, xy cross-sections files has been saved to DIR:\n\n  - - - >  ",path + "mplot")
if cut_xz != None:
    # ------------------------------------------------ cut_xz ------------------------------------------------
    for i in range (0,len(cut_xz)):
        rows_needy = []
        for z in range(0,CSz):
            rows_needy.append((z*CSy+cut_xz[i])-1)
        xz=content.iloc[rows_needy]
        xz.index = [namez_real]
        xz.columns = [namex_real]
        xz = xz.rename_axis(index="Axis y - length of " + target_name + " target [cm]",
                            columns="Axis x - width of " + target_name + " target [cm]")

        fig, ax = plt.subplots(figsize=(12,18))         # Sample figsize in inches
        plt.title("Cross-section of xz axes in distance of y = " + str(namey_real[cut_xz[i]]) + " mm",y=1.08)
        g=sns.heatmap(xz, cmap="OrRd", xticklabels=3, yticklabels=10, vmin=0)
        g.collections[0].colorbar.set_label("Heat deposition [MeV cm$^{-3}$ proton$^{-1}$]", labelpad=20)
        g.set_xticklabels(g.get_xticklabels(),rotation=90)
        g.set_yticklabels(g.get_yticklabels(),rotation=0)
        g.xaxis.labelpad = 20
        g.yaxis.labelpad = 20
        sns.set(font_scale=2)
        # plt.show()
        plt.savefig(path+"mplot\\xz"+str(cut_xz[i])+"plot.png")
        plt.close()
    print("\n\n","All works fine, xz cross-sections files has been saved to DIR:\n\n  - - - >  ",path + "mplot")

if cut_yz != None:
    # ------------------------------------------------ cut_yz ------------------------------------------------
    for i in range(0, len(cut_yz)):
        df_yz=pd.DataFrame()
        for z in range(0,CSz):
            calcul = np.add(z*CSy, np.arange(0,CSy)).tolist()
            if z==0:
                nparray = content.iloc[calcul, [cut_yz[i]]]
                nparray.columns = [namez_real[z]]
                nparray.index = [namey_real]
                df_yz = nparray
            else:
# if use pd.append so indexing is not possible to change and data consist of full matrix of mostly NaN
                nparray=content.iloc[calcul, [cut_yz[i]]].to_numpy()
                df_yz[namez_real[z]]=nparray

        df_transposed = df_yz.T # have to transpose matrix due to z axis is in columns
        df_transposed.index = [namez_real]
        df_transposed.columns = [namey_real]
        df_transposed = df_transposed.rename_axis(index="Axis y - length of " + target_name + " target [cm]",
                                                  columns="Axis x - hight of " + target_name + " target [cm]")
        fig, ax = plt.subplots(figsize=(12, 18))  # Sample figsize in inches
        plt.title("Cross-section of yz axes in distance of x = " + str(namex_real[cut_yz[i]]) + " mm")
        g = sns.heatmap(df_transposed, cmap="OrRd", xticklabels=3, yticklabels=10, vmin=0)
        g.collections[0].colorbar.set_label("Heat deposition [MeV cm$^{-3}$ proton$^{-1}$]", labelpad=20)
        g.set_xticklabels(g.get_xticklabels(),rotation=90)
        g.set_yticklabels(g.get_yticklabels(),rotation=0)
        g.xaxis.labelpad = 20
        g.yaxis.labelpad = 20
        sns.set(font_scale=2)
        # plt.show()
        plt.savefig(path + "mplot\\yz" + str(cut_yz[i]) + "plot.png")
        plt.close()
    print("\n\n","All works fine, yz cross-sections files has been saved to DIR:\n\n  - - - >  ",path + "mplot")
```

Figure C.7: Python code - MCNPX MESH plotting various MESH cross-sections (2/2).

C.4 Gnuplot script - visualisation of MESH

```
 1 reset
 2 set palette model RGB rgbform 33,13,10 positive
 3 set grid front
 4 set terminal pngcairo size 550,1200
 5 set title "{/:Italic Lead heat deposition \n[MeV cm^-^3 proton^-^1]" font "Arial,28"
 6 set xlabel "{/:Italic Lead target width} [cm]" font "Arial,24" offset 0,-0.5
 7 set ylabel "{/:Italic Axis y - length of Lead target} [cm]" font "Arial,24" offset -1
 8 set cblabel "{/:Italic Energy deposited} [MeV cm^-^3 proton^-^1]" font "Arial,24" offset 3.5
 9 set xtics font "Arial,19"
10 set ytics font "Arial,19"
11 set cbtics font "Arial,19" offset -.1
12 # set format cb "%.1f"
13 set size 0.85,0.97
14 set origin 0.02,.018
15 set autoscale cb
16 set yrange [0:105]
17
18 set output 'c:\Clouds\owncloud\vut-jinr\PhD\DzP_Lead\pics\xz.png'
19 plot [:][:] "xz.tec" using 1:2:3 notitle with image
20 set output 'c:\Clouds\owncloud\vut-jinr\PhD\DzP_Lead\pics\yz.png'
21 plot [:][:] "yz.tec" using 1:2:3 notitle with image
22
23
24 unset yrange
25 set xtics font "Arial,16"
26 set ytics font "Arial,16"
27 set cbtics font "Arial,16" offset .1
28 set xlabel "{/:Italic Axis x - width of Lead target} [cm]" font "Arial,20"
29 set ylabel "{/:Italic Axis y - height of Lead target} [cm]" font "Arial,20" offset -0.2
30 set cblabel "{/:Italic Energy deposited} [MeV cm^-^3 proton^-^1]" font "Arial,20" offset 3.4
31 set format x "%.0f"
32 set format y "%.0f"
33 set format cb "%.2f"
34 set size 0.95,0.99
35 set origin 0.005,0.017
36 # or offset graph 0,0,0,0 #left,right,top,bottom
37 set terminal pngcairo size 800,700
38 set title "{/:Italic Lead heat deposition} \n[MeV cm^-^3 proton^-^1]" font "Arial,22" offset 0,0.2
39
40 set format cb "%.2f"
41 set output 'c:\Clouds\owncloud\vut-jinr\PhD\DzP_Lead\pics\xy5.png'
42 plot [:][:] "xy5.tec" using 1:2:3 notitle with image
43
44 set output 'c:\Clouds\owncloud\vut-jinr\PhD\DzP_Lead\pics\xy14.png'
45 plot [:][:] "xy14.tec" using 1:2:3 notitle with image
46
47 set output 'c:\Clouds\owncloud\vut-jinr\PhD\DzP_Lead\pics\xy24.png'
48 plot [:][:] "xy24.tec" using 1:2:3 notitle with image
49
50 set output 'c:\Clouds\owncloud\vut-jinr\PhD\DzP_Lead\pics\xy35.png'
51 plot [:][:] "xy35.tec" using 1:2:3 notitle with image
52
53 .
54 .
55 .
56
57 set terminal pdf size 9,4
58 set yrange [-10:10]
59 set xrange [0:36]
60 set title "{/:Italic Lead heat deposition} [MeV cm^-^3 proton^-^1]" font "Arial,24" offset 0,-0.5
61 set xlabel "{/:Italic Lead target width} [cm]" font "Arial,20" offset 0
62 set cblabel "{/:Italic Energy deposited} [MeV cm^-^3 proton^-^1]" font "Arial,20" offset 2
63 set ylabel "{/:Italic Axis z - length of Lead target} [cm]" font "Arial,20" offset -.1
64 set xtics font "Arial,16"
65 set ytics font "Arial,16"
66 set cbtics font "Arial,16" offset -.2
67 set output 'c:\Clouds\owncloud\vut-jinr\PhD\DzP_Lead\pics_\Pb_xy.pdf'
68 plot [:][:] "xz.tec" using 2:1:3 notitle with image
69
70 .
71 .
72 .
73
```

Figure C.8: Gnuplot script for plotting MCNPX mesh tallies. The binary mdata file was converted into certain cuts e.g. (line 42) xy5 means the target cross-section in plane XY with distance z=5·$CellSize$ mm, where cell size defined by *corc3* definition in MCNPX input (see mesh definition in equation 3.6). In rows 1-56 is shown plotting of png output (easier manipulation and results check). There are many variants of vector graphical outputs but for basic purposes is used the most suitable PDF plot (shown in rows 57-68). The axes x and z are switched into zx for more clear visualisation (row 68). This visualisation is shown in Fig. 3.17. Lines 53-55 and 70-72 represent equivalent repetition for other chosen cuts.

C.5 MCNPX demonstration input (simplified Pb target)

```
c  ------------------------------------------------------------------
c | simple Pb target - demonstration example - Josef Svoboda, BUT |
c  ------------------------------------------------------------------
c                                                        MCNPX 2.7.0
c  ------------------------------------------------------------------
c             beginning of cell cards                              |
c  ------------------------------------------------------------------
400 2 -11.35 110 -111 -1   $ Pb cylinder definition                 |
110 1 -1.292e-3 -99 #400   $ spherical air definition except Pb     |
998 0 99                   $ rest of universe                       |
999 1 -1.292e-3 -2 21 -22  $ cookie cutter    (CCC)                 |
c  ------------------------------------------------------------------
c               end of cell card                                   |
c  ------------------------------------------------------------------

c  ------------------------------------------------------------------
c             beginning of surface card                            |
c  ------------------------------------------------------------------
  1   cz   9.5           $ cylinder with  r=9.5cm                  |
110   pz   0.0           $ plane xy where z=0  cm                  |
111   pz   35            $ plane xy where z=35 cm                  |
2     cz   10            $ cylinder with  r=10 cm (cookie cutter)  |
21    pz  -10            $ plane xy where z=-10cm     - || -       |
22    pz   40            $ plane xy where z= 40cm     - || -       |
99 sz 17 50 $ shifted centre sphere;inside air+target,outer UNIV.  |
c  ------------------------------------------------------------------
c               end of surface card                                |
c  ------------------------------------------------------------------

c  ------------------------------------------------------------------
c             beginning of control card                            |
c  ------------------------------------------------------------------
mode n p h / $ transport of neutrons,photons,protons and pions(+)  |
imp:n,h,/ 1 1 0 1 $ importance for cells except cell "998"         |
phys:n 700 3j -1  $ Upper limit for n E_n=700MeV,tabl=-1 (cutoff)  |
phys:h 700 j -1   $          - || -       the same for protons     |
phys:h 700        $ Upper energy limit for photons                 |
phys:/ 700        $ Upper energy limit for pions(+) = 700MeV       |
c materials (ZZZAAA=007014) (if neg.->mass density ratio=-0.755)   |
m1 7014 -0.755 8016 -0.232 18000 -0.013                      $     |
     hlib=70h nlib=70c $ air --- 70h or 70c is endf library $     |
m2 82204 1.4 82206 24.1 82207 22.1 82208 52.4                $     |
     hlib=70h nlib=70c $ Pb rho=11.35g                       $     |
c                                                                  |
c tallies definition                                               |
f16:n 400 $ tally of heat deposition caused by neutron reactions   |
f26:h 400 $ tally of heat deposition caused by proton reactions    |
+f36: 400 $ tally of total heat deposition caused                  |
f17:n 400 $ tally of heat deposition caused by neutron fission     |
c                                                                  |
c mesh of total heat deposition, comments not allowed in mesh def  |
tmesh
 rmesh3 total
 cora3 -9.7 96i 9.7
 corb3 -9.7 96i 9.7
 corc3 -0.1 175i 35.1
endmd
c                                                                  |
c physics models INCL4+ABLA                                        |
lca 6j 1 j 2 $ definition of INCL4/ABLA                            |
lea 6j 2     $ definition of INCL4/ABLA                            |
c ----- problem termination card                                   |
stop nps 2e7 $ stop calculation after 2e7 particle histories       |
prdmp 5e6 j 5e6 $ printing dump:tally(5e6) runpe(none) mctal(5e6)  |
c                                                                  |
c 660 MeV proton beam, gaussian spatial profile description        |
c beam in axis z, beam position z=-1cm, cutter cookie=999          |
sdef dir 1 vec 0 0 1 x d1 y d2 z -1 ccc 999 tr 3 par h erg 660   $|
sp1 -41 3.38 0 $ Gaussian beam FWHMx=3.38cm                      $|
sp2 -41 3.71 0 $ Gaussian beam FWHMy=3.71cm                      $|
tr3  0 0 0  1 0 0  0 1 0  0 0 1 $ center beam shifting=none(000) $|
c _________________________________________________________________|
```

Figure C.9: MCNPX input file of simplified LEAD target for demonstration purpose

C.6 Tips and fails in ANSYS Fluent simulation

In this section are discussed common problems and tips for 2D Fluent simulation which were used for testing before the 3D simulation was performed. The main problem of the 2D simulation is that it does not used fluid gravity well (see Fig. 3.18). Nevertheless, it is sufficient for trend change observation (sensitivity analysis).

Geometry and mesh of 2D model

The beginning of the 2D target geometry was placed at a length of z=30.0 cm due to surrounding fluid volume defined from z=0 cm. For this reason, the heat source definition in UDF must be Only 2D model was used, so to upper half of the target was simulated and finally rotated. The whole meshed model is spread from x_{beg}=0 cm, y_{beg}=0 cm to x_{end}=160 cm, y_{end}=30 cm, the target spreads (including air gap between cylinders «in total 4 cm») from x_{beg-T}=30 cm, y_{beg-T}=0 cm to x_{end-T}=134 cm, y_{end-T}=9.5 cm. The rest of the model area is filled by air. The first model simulation (including the mesh) is shown in Fig. C.10. The mesh softness was not sufficient, the updated version is shown in Fig. C.11.

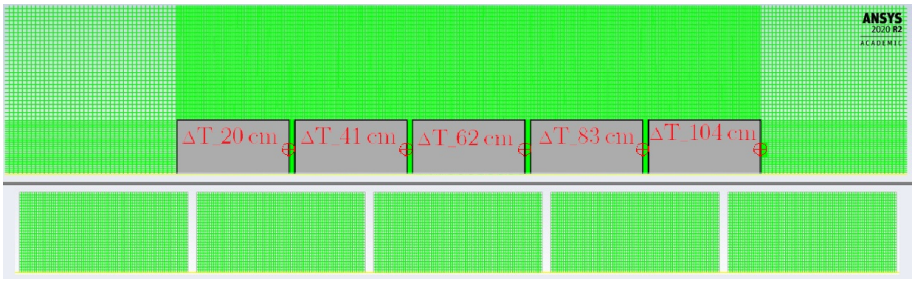

Figure C.10: ANSYS Fluent 2D model of the CARBON target, carried out in cooperation with Y. Shu, IMP. Upper part, above the thick grey line, shows the fluid mesh and solid CARBON with measuring positions. The figure below the line shows zoomed version of the meshed target model (solid) without fluid. The yellow line at the bottom of the figure represents the z axis.

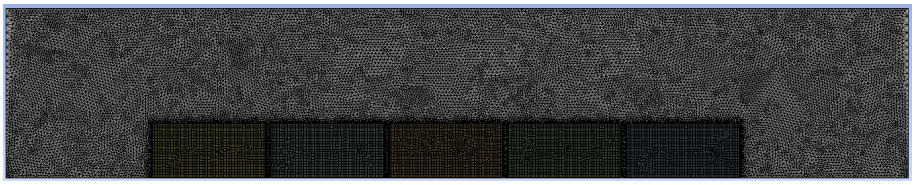

Figure C.11: The same geometry as previous figure with more suitable mesh.

The tricky part is to define the heat source. The heating is calculated in MCNPX and has to be converted as an input for the ANSYS simulation. The most simple way to do it is to calculate some selected volume (for example, whole cylinder) and define this heating power to the cylinder in the ANSYS simulation. This method was used in the previously discussed simulation (Two horizontal cylinder experiment), although the cylindrical volume was partitioned into three symmetrical pieces. Unfortunately, it is not suitable for this case. The heat flux is not well distributed in the CARBON cylinder (see Fig. 5.33), the cylinder diameter is 19 cm and the most of the heat is generated in the centre of each cylinder (more than 80 % heat is released by less than 20 % of the cylinder volume). It brings the idea to

partition each cylinder into several volumes by an annulus (cylindrical rings), calculate each volume heating power, and finally, define this cylindrical annulus in ANSYS. This method was used earlier and it is widely described in p.94 (paragraph „Second method“).
There are two other possible methods. If the heat source is symmetrical, it is possible to simplify the 3D heat source to the symmetrical 2D (with further rotation) by several of the equations, which described and widely discussed on p.96 and following. This method was chosen for the CARBON and LEAD targets, due to simplification reasons. Equation preparation is challenging task, but since it has been done, the ANSYS simulation is much quicker than 3D simulation.
The last discussed option of the heat source definition is based on so-called „mapping“ the results from MCNPX into ANSYS. It is suitable for ANSYS 3D simulations. The heat mesh must be calculated in MCNPX (described in p.47 and following). In further, it must be converted from MCNPX binary code to the *csv* file which is containing the Cartesian coordinate system (x,y,z, each per one column; units [m]) and the heat flux [W·m^{-2}] (the uncertainty should be inserted either). After importing this file into the ANSYS, there is an interface to assign data (columns) in the right order. It is also allowed to change some of the units.

Dynamic heat source definition

The previous heat source definition expected the constant heat source in time. Due to the accelerator outage and proton current changes in time (see Fig. 5.26), it is necessarily to change this static heat source setting to the dynamic one. There are probably more options, but for this work it has been chosen to set the time step, in which the heat flux is constant. It has been mentioned that the information about the proton beam were recorded once per 16.5 seconds, so the time step was chosen to double of this recording time by reason to eliminate any random fluctuations (an average of two measurements was used).

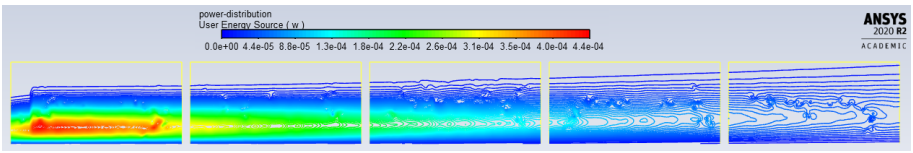

Figure C.12: Visualisation of the power source of CARBON target in Fluent 2D. The units are in W but related to the calculated volume, so better use it as relative. At the first sight, this visualisation does not seem to respond with MCNPX calculation where the highest power in the centre (close to rotation axis). It is caused by relative units in MCNPX calculation related to volume (rotating model), the volume of the 2D rotating mesh grows with the radius.

Duration of the ANSYS simulation longed for the same time as the experimental irradiation. The dynamic of the heat flux behaviour was sampling per 33 s. The heat flux was calculated for each time step by appointing the average current (variable I_p in unit [A]) for each time step to equation 5.3, together with all other variables described by equations 5.9. It described the behaviour of the heat flux during the whole simulated time. The file which described all of these settings for ANSYS simulation is attached in appendix, page 168. The first version of this code was prepared in cooperation with Dr. Zhang.

Even more complicated part of this simulation is to suitably set the outer condition. Due to the target located at a large experimental hall, the surrounding temperature was usually not changing much - for simplified calculations, it is expected to be constant.

In essence, all experiments were irradiated with similar surrounding conditions, anyway, the absolute temperature of the air in the experimental hall was for each experiment different, based on the weather season.

Due to natural convection with lower temperature changes ($\Delta T^{max} = 10$ °C), the laminar viscous mode is expected to be used. The following figures are showing the results and discussing the boundary conditions of the simulation. All constants were set as described on p.122 but the difference was that Operating Density was not specified. It causes problems with calculation. The results were totally out of the expected range and the continuity residuals were not converged. Based on consultation with Fluent experts, it was recommended to change the mesh, change the viscous model, and finally, change the outlet conditions to ensure the converge of the continuity residuals. In total, it was calculated about 50 models with various settings than the error was found.

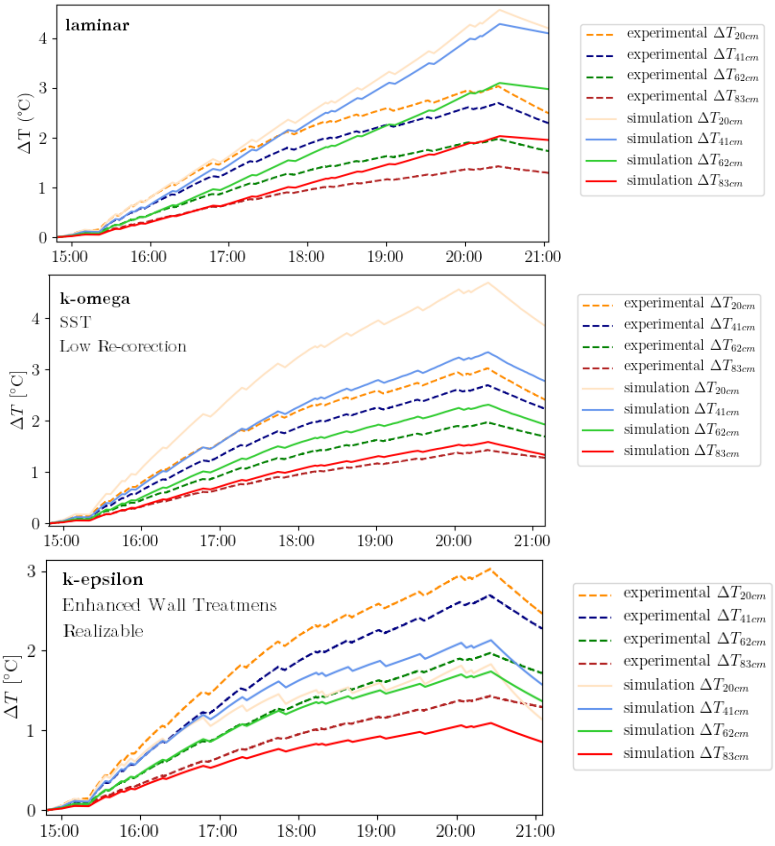

Figure C.13: Fluent simulation results without specified Operation Density for laminar, k-omega and k-epsilon viscous model.

The necessity of specifying the operating density has been found due to consultation with TechSoft company. Since the model is set correctly, the residuals converge. Operating conditions are set based on barometric pressure, temperature, and humidity. The result of the correct simulation is shown in Fig. 5.45.

C.6.1 Fluent UDF for 2D CARBON simulation

Power distribution UDF for the CARBON target, function name=„power_ww“

```
#include "udf.h"
DEFINE_SOURCE(power_ww,c,t,dS,eqn)
{
double source=0.0;
double xc[2];
double poz = 0.0 ;
double pox = 0.0 ;
double poy = 0.0 ;
double aa1 = 0.0;
double bb1 =0.0 ;
double aa2 =0.0 ;
double bb2 =0.0 ;
double aa3 =0.0 ;
double bb3 =0.0 ;
double aa4 =0.0 ;
double bb4 =0.0 ;
int i=0;
double time=0.0;
double T = 33.0;
double a[700]={3.95324E-09,3.86339E-09,4.67201E-09,4.49231E-09,6.33416E-09,... (continuing)
};

 time = RP_Get_Real("flow-time");

i= floor (time/T);

C_CENTROID(xc,c,t);

pox = xc[0]*100-30.0 ;
poy = xc[1]*100;
poz = xc[2] ;

if ( xc[0] < 0.024 )
{
        C_UDMI(c,t,0)= a[i];
        aa1 = 0.339849+4.8728e-2*pox-2.3833e-2*pow(pox,2)+4.255e-3*pow(pox,3);
        bb1 = 2.186492+3.7955e-2*pox-1.232e-3*pow(pox,2)+2.7e-5*pow(pox,3);
        source= aa1*exp(-pow(poy/bb1,2))*1e6*a[i]*1e6;
        dS[eqn]=0.0;

        return source;
}

else if (0.024 <= xc[0] < 0.20)
{
        C_UDMI(c,t,1)= a[i];
        aa2 = 0.377280+2.701e-3*pox-6.93e-4*pow(pox,2)+1.5e-5*pow(pox,3);
        bb2 = 2.186492+3.7955e-2*pox-1.232e-3*pow(pox,2)+2.7e-5*pow(pox,3);
        source= aa2*exp(-pow(poy/bb2,2))*1e6*a[i]*1e6;
        dS[eqn]=0.0;

        return source;
}

else if (0.20 <= xc[0] < 0.25)
{
        C_UDMI(c,t,2)= a[i];
        aa3 = 0.377280+2.701e-3*pox-6.93e-4*pow(pox,2)+1.5e-5*pow(pox,3);
        bb3 = 2.610334+3.415291e-3*pox+1.444670e-4*pow(pox,2)+1.464088e-7*pow(pox,3);
        source= aa3*exp(-pow(poy/bb3,2))*1e6*a[i]*1e6;
        dS[eqn]=0.0;

        return source;
}

else if (0.25 <= xc[0] < 1.04)
{
        C_UDMI(c,t,3)= a[i];
        aa4 = 0.4532772-9.893612e-3*pox+7.596158e-5*pow(pox,2)-1.989548e-7*pow(pox,3);
        bb4 = 2.610334+3.415291e-3*pox+1.444670e-4*pow(pox,2)+1.464088e-7*pow(pox,3);
        source= aa4*exp(-pow(poy/bb4,2))*1e6*a[i]*1e6;
        dS[eqn]=0.0;

        return source;}

else
{
        source = 0.0 ;
        dS[eqn]=0.0;
        return source;
}
}
```

Appendix D

Chapter 4 sub-data

D.1 Temperature measurement of the QUINTA target

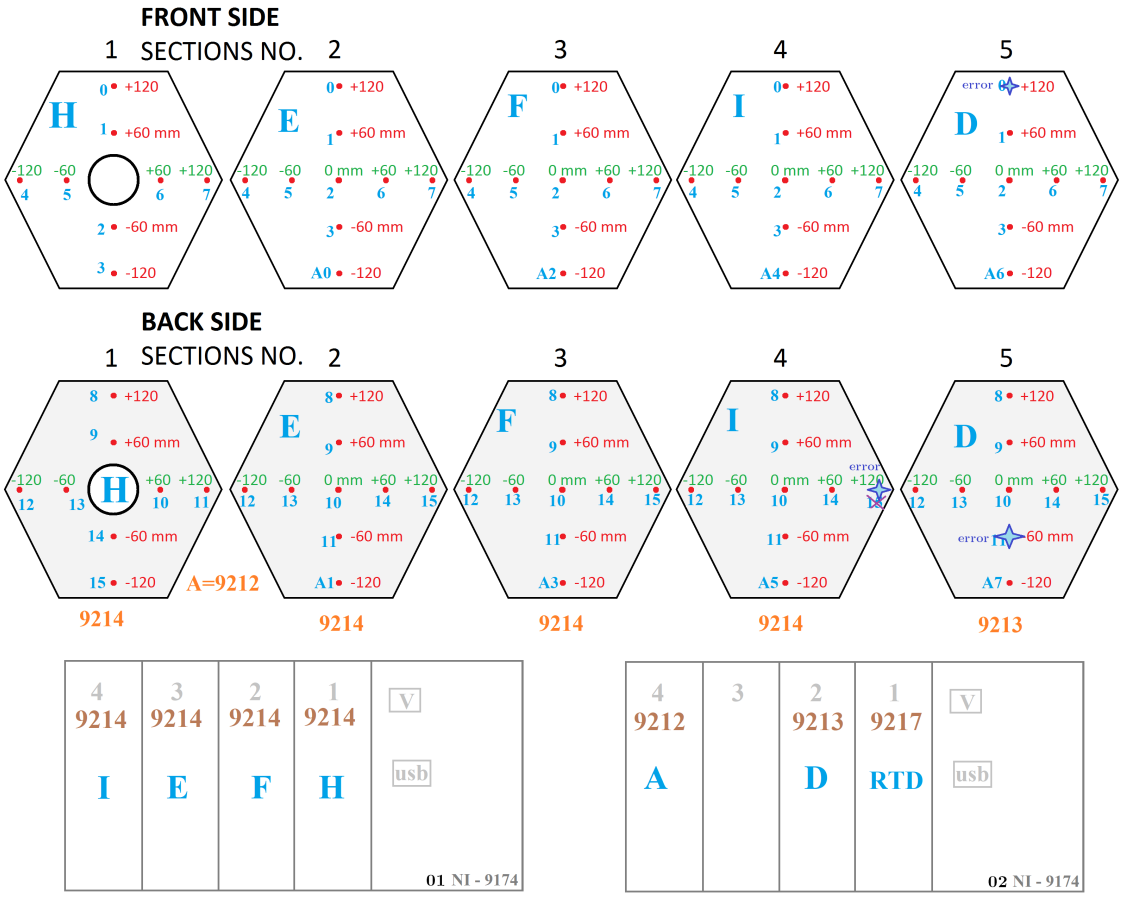

Figure D.1: TC connection of the *exp10*.

All measured data for the *exp10* located in the appendix due to the larger size. The most important parts of the measurement are zoomed in. Charts are described in the main text on the page 77.

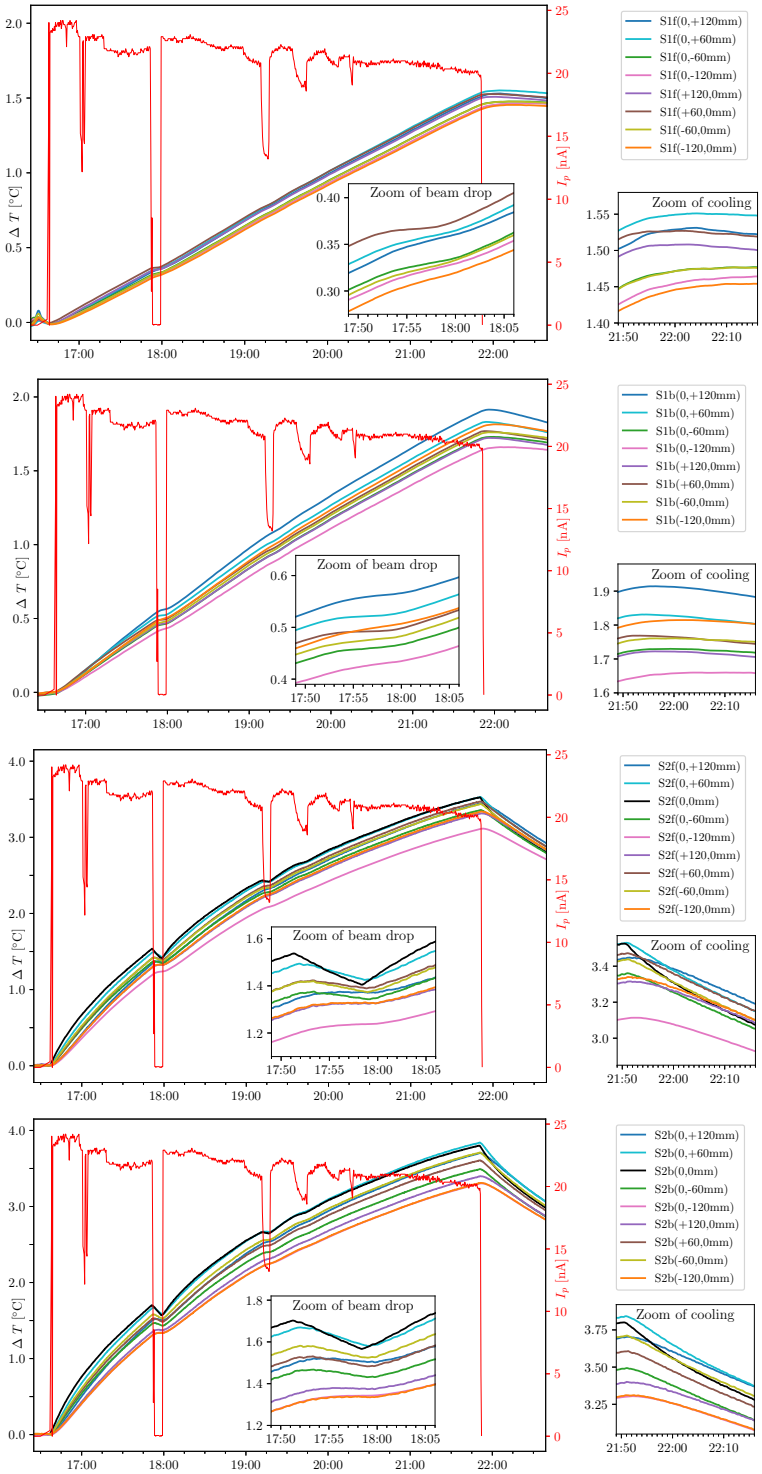

Figure D.2: TA QUINTA temperature measurement without shielding, sections 1-2.

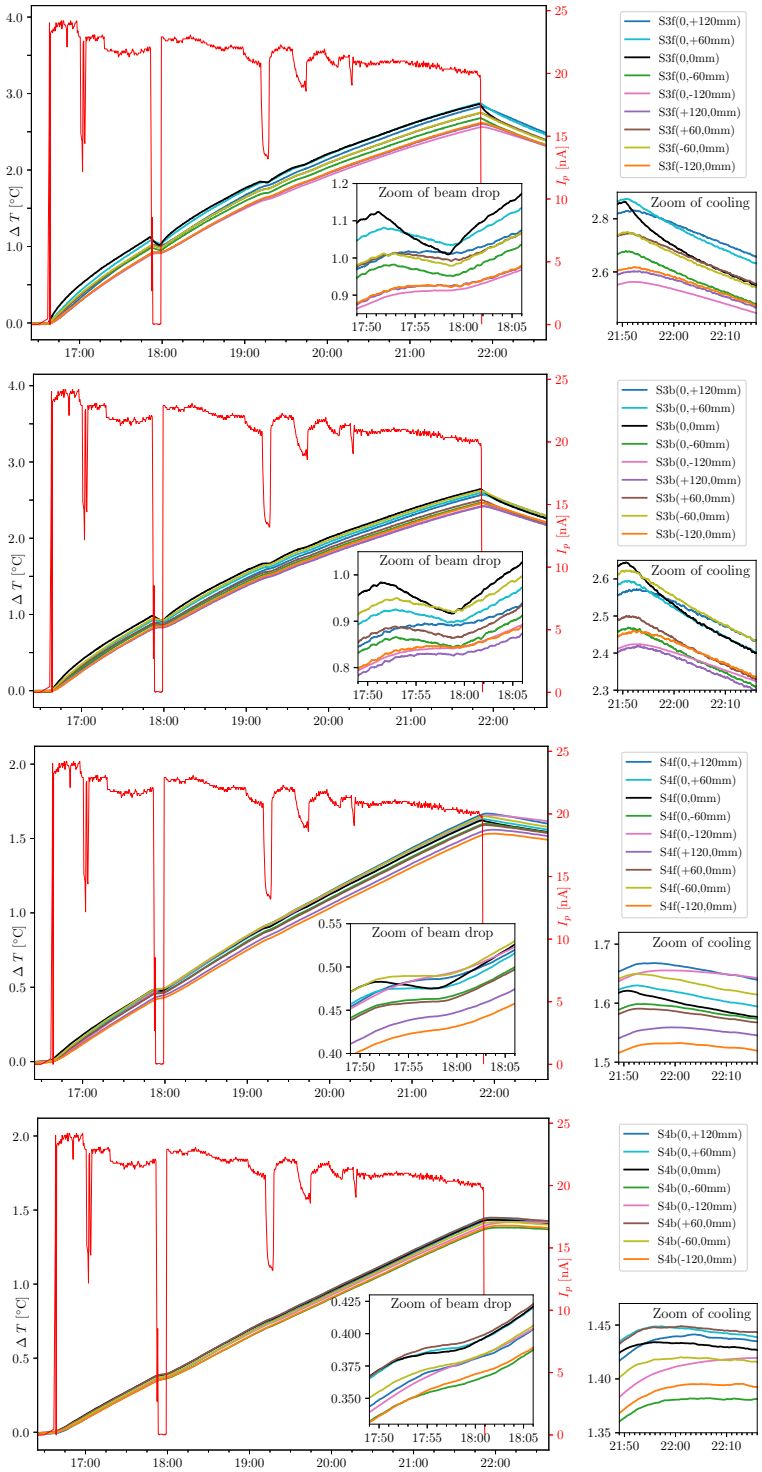

Figure D.3: TA QUINTA temperature measurement without shielding, sections 3-4.

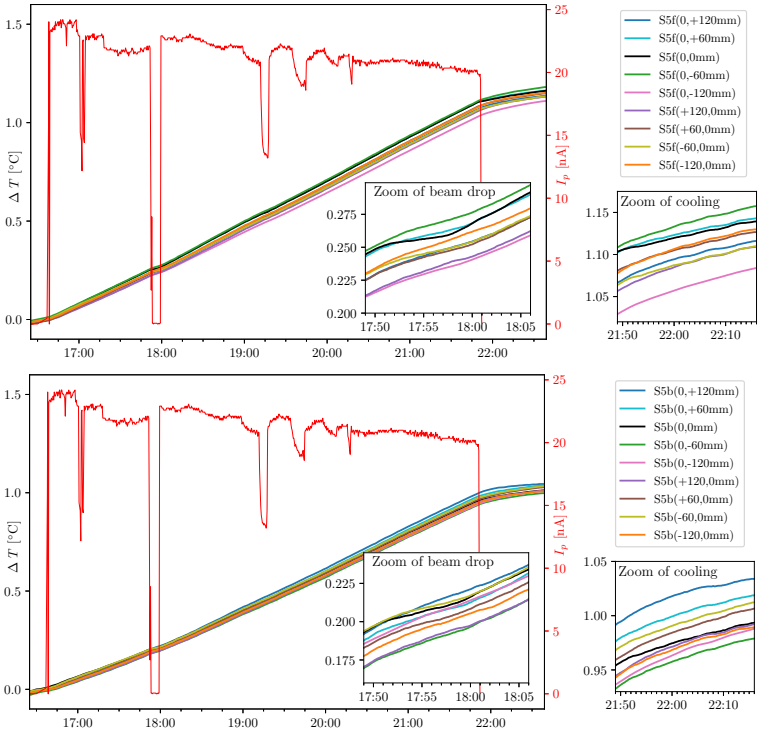

Figure D.4: TA QUINTA temperature measurement without shielding, sections 5.

D.2 MCNP input code of the QUINTA target

```
c Quinta setup based on M.Suchopar ver 1.5 with Pb shielding DEC 2013
c ------------------------------------------------------------------------------
c Changes performed by Josef Svoboda for Phasotron accelerarot (660MeV protons)
c Pb shielding is removed and special probes for neutron leakage monitoring
c are simulated (fission and blank probes).
c Model is equivalent to Exp11 (label in J.Svoboda PhD thesis) 2017−06−29
c
c cell card
1 0 −20 fill=1 $ 2nd section of the target
2 0 −2 3 −4 5 −6 7 u=1 lat=2 trcl=(0 0 13.6) $ U rod lattice
       fill=−5:5 −5:5 0:0
       3 3 3 3 3 3 3 3 3 3 3
        3 3 3 3 3 2 2 2 2 2 3
         3 3 3 3 2 2 2 2 2 2 3
          3 3 3 2 2 2 2 2 2 2 3
           3 3 2 2 2 2 2 2 2 2 3
            3 2 2 2 2 2 2 2 2 2 3
             3 2 2 2 2 2 2 2 2 3 3
              3 2 2 2 2 2 2 2 3 3 3
               3 2 2 2 2 2 2 3 3 3 3
                3 2 2 2 2 2 3 3 3 3 3
                 3 3 3 3 3 3 3 3 3 3 3
101 0 101 −120 fill=4 $ 1st section of the target with hole for beam
102 0 −2 3 −4 5 −6 7 u=4 lat=2 trcl=(0 0 0.5) $ U rod lattice with hole
       fill=−5:5 −5:5 0:0
       3 3 3 3 3 3 3 3 3 3 3
        3 3 3 3 3 2 2 2 2 2 3
         3 3 3 3 2 2 2 2 2 2 3
          3 3 3 2 2 2 2 2 2 2 3
           3 3 2 2 2 3 3 2 2 2 3
            3 2 2 2 3 3 3 2 2 2 3
             3 2 2 2 3 3 2 2 2 3 3
              3 2 2 2 2 2 2 2 3 3 3
               3 2 2 2 2 2 2 3 3 3 3
                3 2 2 2 2 2 3 3 3 3 3
                 3 3 3 3 3 3 3 3 3 3 3
3 1 −18.90 (−14 11 −12) u=2 $ U rod
4 2 −2.7 (14 −15 11 −12):(−15 10 −11):(−15 12 −13) u=2 $ Al envelope
5 3 −1.292e−3 (15:−10:13) u=2 $ air
6 3 −1.292e−3 −16 u=3 $ air
7 2 −2.7 (20 −21) $ Al hex side plates for 2nd section
8 2 −2.7 (−19 21 90 −26 27 37):(−19 90 35 −34 29 −37)
9 2 −2.7 (22 −23 −26 27 −28 37):(22 −23 35 −34 29 −37) $ Al front plate 2nd
10 2 −2.7 (24 −25 −26 27 −28 37):(24 −25 35 −34 29 −37) $ Al rear plate 2nd
```

```
107 2 −2.7 (120 −121) $ Al hex side plates for 1st section (front,rear)
108 2 −2.7 (−119 121 109 −26 27 37):(−119 109 35 −34 29 −37)
109 2 −2.7 (102 10 −123 −26 27 −28 37):(10 −123 35 −34 29 −37) $ Al front
110 2 −2.7 (102 124 −125 −26 27 −28 37):(124 −125 35 −34 29 −37) $ Al rear
11 like 1 but trcl=(0 0 13.1) $ 3rd section of the target
12 like 7 but trcl=(0 0 13.1)
13 like 9 but trcl=(0 0 13.1)
14 like 10 but trcl=(0 0 13.1)
103 like 8 but trcl=(0 0 13.1)
15 like 1 but trcl=(0 0 26.2) $ 4th section of the target
16 like 7 but trcl=(0 0 26.2)
17 like 9 but trcl=(0 0 26.2)
18 like 10 but trcl=(0 0 26.2)
104 like 8 but trcl=(0 0 26.2)
111 like 1 but trcl=(0 0 39.3) $ 5th section of the target
112 like 7 but trcl=(0 0 39.3)
113 like 9 but trcl=(0 0 39.3)
114 like 10 but trcl=(0 0 39.3)
105 like 8 but trcl=(0 0 39.3)
115 2 −2.7 (−30 33 −31 32 36 −29):(−30 33 32 −35 29 −37):(−30 33 34 −31 29 −37)
130 2 −2.7 (−31 32 −36 130 33 −30) $ Al lower plate 2
c
c
c pillars of QUINTA (under Al lower plate) so called Pb legs
c
300 4 −11.35 (−302 32 −130 135 33 −303) $ first leg under AL plate
301 4 −11.35 (301 −31 −130 135 33 −303) $ first leg under AL plate
302 4 −11.35 (−302 32 −130 135 −30 300) $ first leg under AL plate
303 4 −11.35 (301 −31 −130 135 −30 300) $ first leg under AL plate
c
c
c polystyrene with Ta and U235 − leakage monitors under QUINTA
c
402 6 −18.95 (415 −414 413 −412 410 −411) $ U leakage monitor with TC 1st
404 like 402 but trcl=(−4.55 0 0) MAT=7 RHO=−16.654 $ Ta blank monitor 1st
400 5 −1.06 (405 −404 135 −402 401 −400) #402 #404 $polystyrene insulation 1st
403 like 402 but trcl=(0 0 13.1) $ U leakage monitor with TC 2nd
405 like 402 but trcl=(−4.55 0 13.1) MAT=7 RHO=−16.654 $ Ta blank monitor 2nd
401 5 −1.06 (405 −404 135 −402 417 −416) #403 #405 $polystyrene insulation 2nd
c
c
c Definition of U cylinders outside (with Al cladding) for purpose
c of n leakage monitoring by heating measurement
c
304 3 −1.292e−3 (−14 128 −129) $ U rod − air
305 like 304 but trcl=(22.5 7.5 26.2) MAT=1 RHO=−19.5 $ U cyl fis monitor 1st
306 3 −1.292e−3 (14 −15 128 −129):(−15 123 −128):(−15 129 −124)
307 like 306 but trcl=(22.5 7.5 26.2) MAT=2 RHO=−2.7 $ Al cladding of U 1st
308 like 304 but trcl=(−22.5 7.5 26.2) MAT=1 RHO=−19.5 $ U cyl fis. monitor 2nd
309 like 306 but trcl=(−22.5 7.5 26.2) MAT=2 RHO=−2.7 $ Al cladding of U 2nd
c
c
131 2 −2.7 (139 −140 −135 136 137 −138) $ Al lower plate big
132 2 −2.7 (139 −140 141 −142 137 −138) $ Al upper plate
133 3 −1.292e−3 (−31 32 −30 33 59 −141) $ upper air
173 2 −2.7 (−101 102 123 −124) $ beam hole Al cover in 1st section
174 3 −1.292e−3 (−102 10 −125) #304 #306 $ beam hole in 1st section
c
c
94 3 −1.292e−3 (33 −30 −31 32 36 −59 −125) $ air
      #101 #107 #108 #109 #110 #115 #173 #174 #304 #306
95 3 −1.292e−3 (33 −30 −31 32 36 −59 125 −126)
      #1 #7 #8 #9 #10 #11 #12 #13 #14 #103 #115
96 3 −1.292e−3 (33 −30 −31 32 36 −59 126)
      #15 #16 #17 #18 #111 #112 #113 #114 #104 #105 #115
97 3 −1.292e−3 −1 (−33:30:−32:31:−130:142) #131 #132 #999 $ air outside
      #300 #301 #302 #303 #305 #307 #308 #309 #400 #401 #402 #403 #404 #405
999 3 −1.292e−3 (−99 −1 −137 100) $ cookie cutter cell
998 0 1

c surface card
1 sz 32.75 75.0
2 px 1.8
3 px −1.8
4 p 0.5 0.8660254 0 1.8
5 p 0.5 0.8660254 0 −1.8
6 p −0.5 0.8660254 0 1.8
7 p −0.5 0.8660254 0 −1.8
c definition of U rod inside the lattice
10 pz 0
11 pz 0.1119
12 pz 10.2881
13 pz 10.4
14 cz 1.6881
15 cz 1.7999
16 cz 3.6
c definition of hole for beam entrance
101 cz 4.3
102 cz 4.0
c definition of Al hex side plates
90 rhp 0 0 13.9 0 0 9.8 0 17.5 0
19 rhp 0 0 13.6 0 0 10.4 0 17.5 0
```

```
20 rhp 0 0 13.6 0 0 10.4 0 14.3 0
21 rhp 0 0 13.6 0 0 10.4 0 14.6 0
109 rhp 0 0 0.8 0 0 9.8 0 17.5 0
119 rhp 0 0 0.5 0 0 10.4 0 17.5 0
120 rhp 0 0 0.5 0 0 10.4 0 14.3 0
121 rhp 0 0 0.5 0 0 10.4 0 14.6 0
c definition of Al front and rear plates
22 pz 13.1
23 pz 13.6
24 pz 24.0
25 pz 24.5
26 px 17.5
27 px −17.5
28 py 17.5
29 py −17.5
123 pz 0.5
124 pz 10.9
125 pz 11.4
126 pz 39.3
c geometry of base cylinder (air) to be shifted and modified as U cyl outside
128 pz 0.6119
129 pz 10.7881
c definition of Al lower plate
30 pz 67.75
31 px 20.0
32 px −20.0
33 pz −2.25
34 px 8.1
35 px −8.1
36 py −18.4
37 py −16.8
130 py −20.0
c definition of under Quinta Pb (legs) holding TA
300 pz 47.75
301 px 10
302 px −10
303 pz 17.75
c
c
c polystyrene and Ta and U235 for leakage monitoring
400 pz 24
401 pz 14
402 py −22.6
404 px 5
405 px −5
410 pz 20
411 pz 20.86
412 py −25.1
413 py −25.34
414 px 2.5
415 px 2.05
416 pz 37.1
417 pz 27.1
c
c
c definition of Al lower plate big
135 py −30.0
136 py −31.6
137 pz −12.25
138 pz 77.75
c definition of Al upper plate
139 px −30.0
140 px 30.0
141 py 20.0
142 py 21.6
c
59 py 19.0 $ upper air surface
75 px −4.2
76 px 4.2
c
99 cz 10.0
100 pz −25.0

c data card
mode n h p /
imp:n,h,/,p 1 58r 0
phys:n 700 3j −1 $ for MCNPX −1=table mix match
phys:h 700 j −1 $ for MCNPX
phys:p 700
phys:/ 700
m1 92238 −0.992739 92235 −0.007204 92234 −0.000057 nlib=70c hlib=70h$U rho=18.9
m2 13027 1 nlib=70c hlib=70h $ Al rho=2.7g/cc
m3 7014 −0.755 8016 −0.232 18000.42c −0.013 nlib=70c hlib=70h $ air
m4 82204 1.4 82206 24.1 82207 22.1 82208 52.4 nlib=70c hlib=70h $ Pb rho=11.35
m5 1001 −0.077421 6012 −0.922579 nlib=70c hlib=70h $ polystyrene, rho=1.060g/cc
m6 92235 −0.952 92238 −0.048 nlib=70c hlib=70h $ enrichment 95.2% +−0.4%
m7 73181 −1 nlib=70c hlib=70h $ tantalum rho=16.654 g/cc
c
c energy spectrum for neutron leakage monitors 235−U, Ta, nat−U
f14:n 402 403 404 405 305 308
e14 1e−6 1e−3 179log 1e3
f24:h 402 403 404 405 305 308
```

```
e24 1e−6 1e−3 179log 1e3
c
c tallies for neutron leakage monitors 235−U, Ta, nat−U
+f6: 402 403 404 405 305 308
f16:h 402 403 404 405 305 308
f26:n 402 403 404 405 305 308
f36:p 402 403 404 405 305 308
f46:/ 402 403 404 405 305 308
f17:n 402 403 404 405 305 308
c
c MESH definition − heat deposition by particles
tmesh
 rmesh3 total
 cora3 −18.1 180i 18.1
 corb3 −18.1 180i 18.1
 corc3 18.7 18.9
 rmesh53 total
 cora53 −18.1 180i 18.1
 corb53 −0.1 0.1
 corc53 −0.1 320i 64.1
 rmesh63 total
 cora63 −25.1 250i 25.1
 corb63 7.4 7.6
 corc63 −0.1 320i 64.1
 rmesh111:h pedep
 cora111 −18.1 180i 18.1
 corb111 −18.1 180i 18.1
 corc111 18.7 18.9
 rmesh511:h pedep
 cora511 −18.1 180i 18.1
 corb511 −0.1 0.1
 corc511 −0.1 320i 64.1
 rmesh611:h pedep
 cora611 −25.1 250i 25.1
 corb611 7.4 7.6
 corc611 −0.1 320i 64.1
 rmesh121:n pedep
 cora121 −18.1 180i 18.1
 corb121 −18.1 180i 18.1
 corc121 18.7 18.9
 rmesh521:n pedep
 cora521 −18.1 180i 18.1
 corb521 −0.1 0.1
 corc521 −0.1 320i 64.1
 rmesh621:n pedep
 cora621 −25.1 250i 25.1
 corb621 7.4 7.6
 corc621 −0.1 320i 64.1
 rmesh131:p pedep
 cora131 −18.1 180i 18.1
 corb131 −18.1 180i 18.1
 corc131 18.7 18.9
 rmesh531:p pedep
 cora531 −18.1 180i 18.1
 corb531 −0.1 0.1
 corc531 −0.1 320i 64.1
 rmesh631:p pedep
 cora631 −25.1 250i 25.1
 corb631 7.4 7.6
 corc631 −0.1 320i 64.1
 rmesh141:/ pedep
 cora141 −18.1 180i 18.1
 corb141 −18.1 180i 18.1
 corc141 18.7 18.9
 rmesh541:/ pedep
 cora541 −18.1 180i 18.1
 corb541 −0.1 0.1
 corc541 −0.1 320i 64.1
 rmesh641:/ pedep
 cora641 −25.1 250i 25.1
 corb641 7.4 7.6
 corc641 −0.1 320i 64.1
C controling of the total heat per whole volume
 rmesh33 total
 cora33 −18.1 18.1
 corb33 −18.1 18.1
 corc33 −0.1 64.1
endmd
c
c
c
c physics models INCL4+ABLA
lca 6j 1 j 2
lea 6j 2
stop nps 3e8
prdmp 3e8 1e8 3e8
c 660 MeV proton beam, gaussian spatial profile
sdef dir 1 vec −0.0349 0 0.9994 x d1 y d2 z −12.3 ccc 999 tr 3 par h erg 660
sp1 −41 2.39 0
sp2 −41 3.32 0
tr3 1.4 0.38 0 1 0 0 0 1 0 0 0 1
```

D.3 QUINTA heat deposition visualisation, enlarged figure

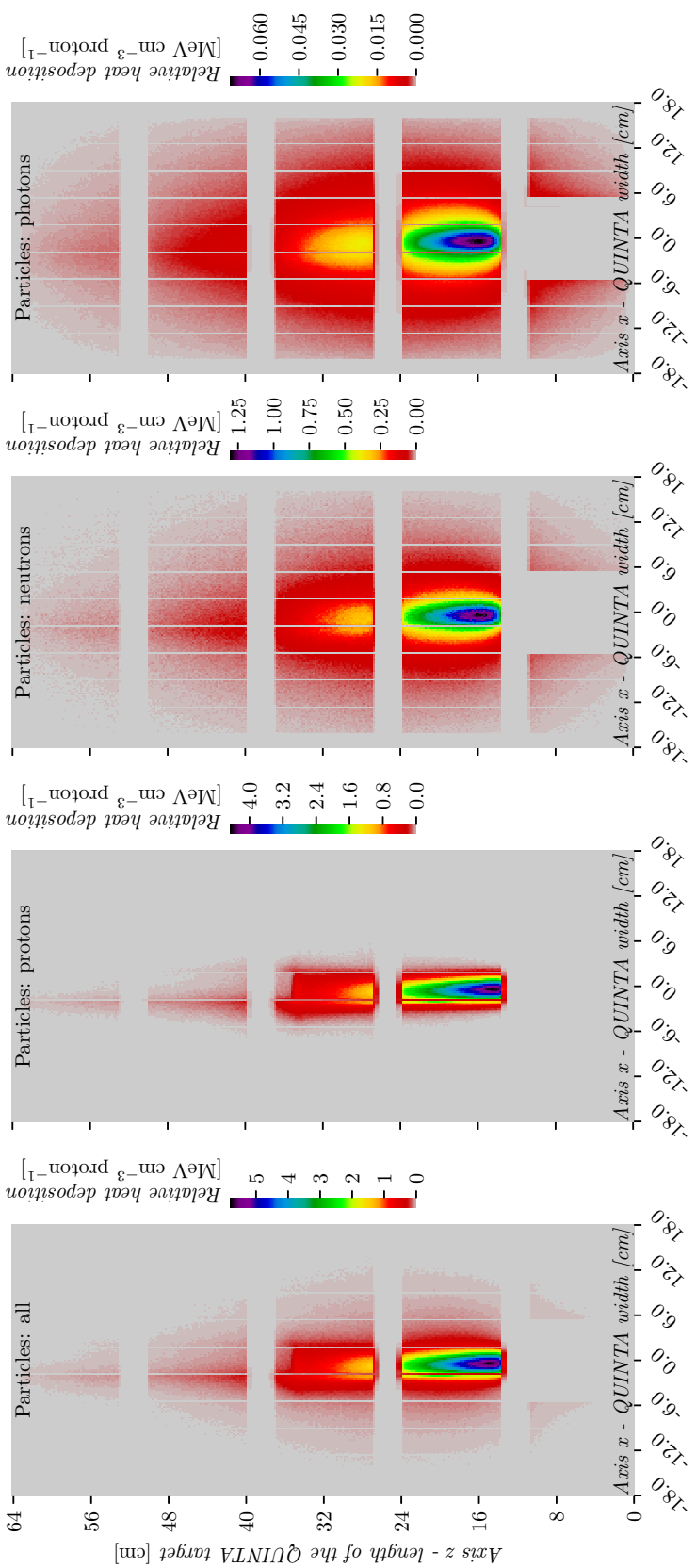

Figure D.5: MCNP simulation of QUINTA heat generation, by each participate particle (*exp10*). This figure is an extended and zoomed version of Fig.4.28.

D.4 Thermal power visualisation of each QUINTA cyl.

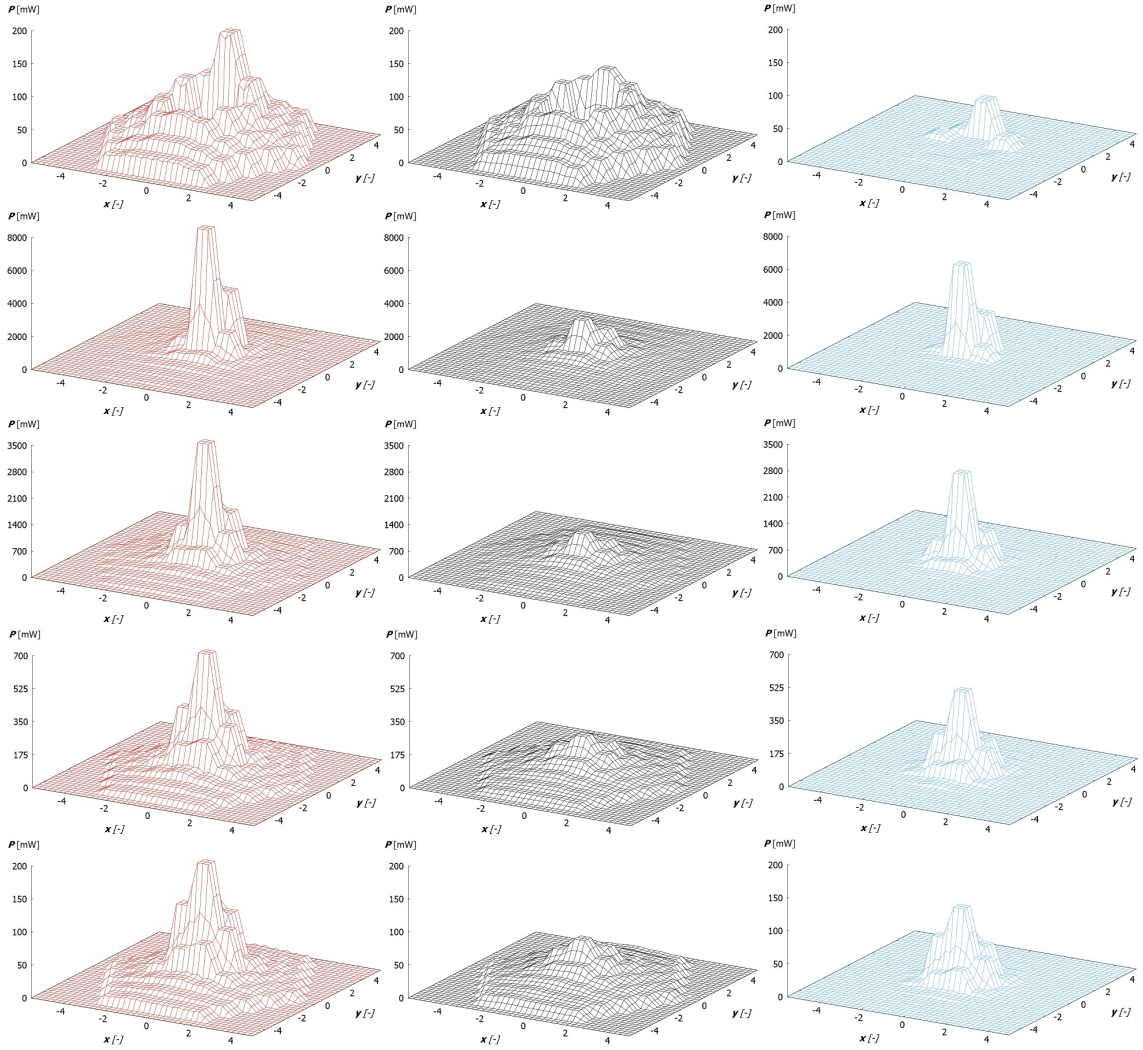

Figure D.6: Heat generation per each cylinder of the QUINTA for *exp10*. On the left side (red) is displayed total heat deposition per each cylinder. In the middle (black) is shown the neutron heating and finally, on the right size is displayed heat deposition caused by proton s reactions (blue colour).

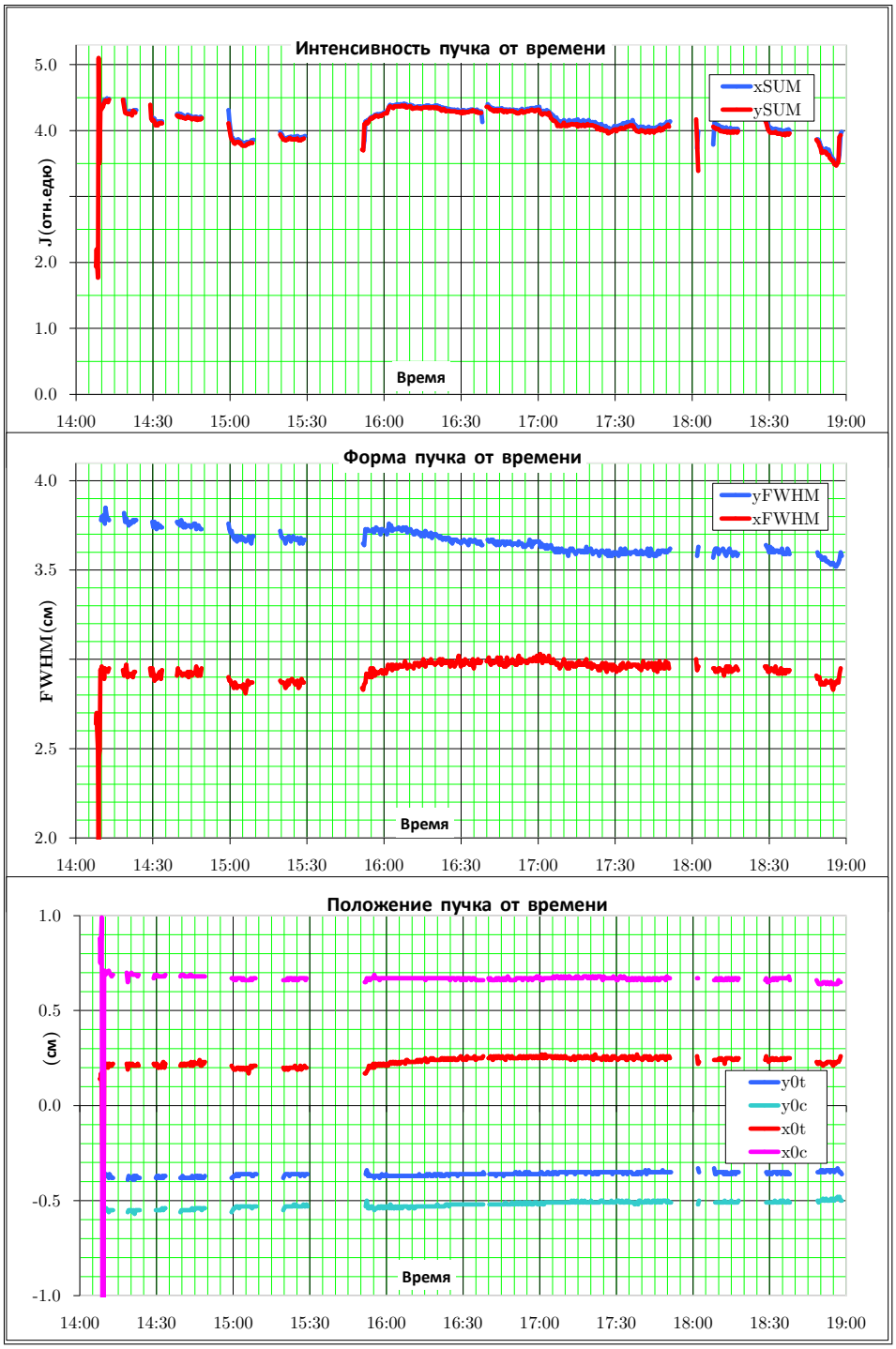

Figure D.7: Proton beam data received from the Phasotron accelerator manager, *exp11* (24.6.2017). The first chart describes so-called „relative proton beam intensity“, basically, it is the relative proton current sum in x and y directions. The middle chart is the FWHM shape for both axis in [cm] and finally, the bottom chart is the centre and so-called „centre of gravity“ of the beam [cm]. Unfortunately, the time is shifted from real-time, so the axis was synchronised based on TC measurement.

D.5 Neutron leakage sub data

The following chart shows a comparison between raw and filtrated data. In further, there are discussed less significant measurement results.

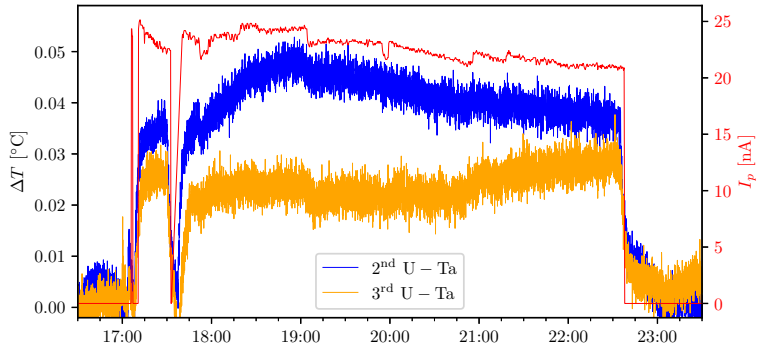

Figure D.8: Identical data as shown in Fig. 4.35, but in this case without any filtering.

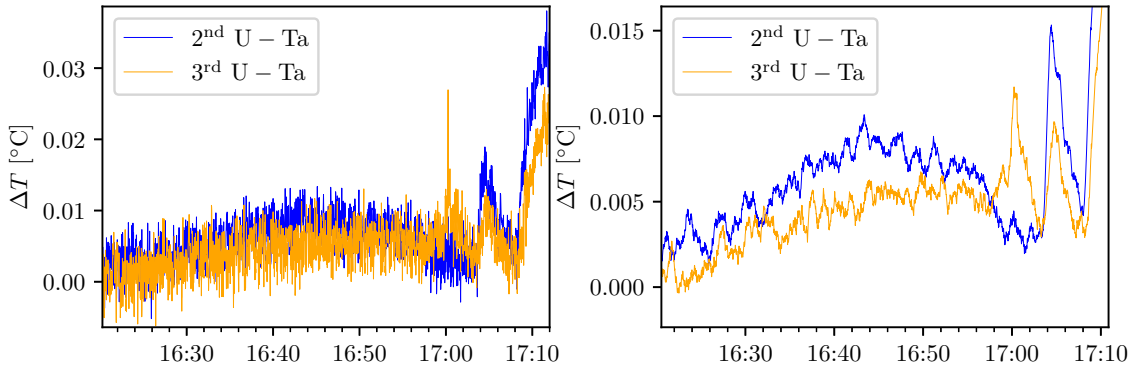

Figure D.9: Before the experiment with the QUINTA target, the Two cylinder irradiation experiment was performed. During this time, the QUINTA has been moved about 1 m aside. There was no direct interaction with the proton beam, but leaking neutrons from the spallation reaction of the two-cylinder experiment slightly interacted with QUINTA. In this chart is shown a zoomed version of previous Fig. D.8 at the time before the QUINTA experiment. The neutron reaction heating is slightly visible, but it is so negligible changes that can not be really discussed as results in these conditions. This figure description including phenomenons highlighting is shown in Fig. D.10.

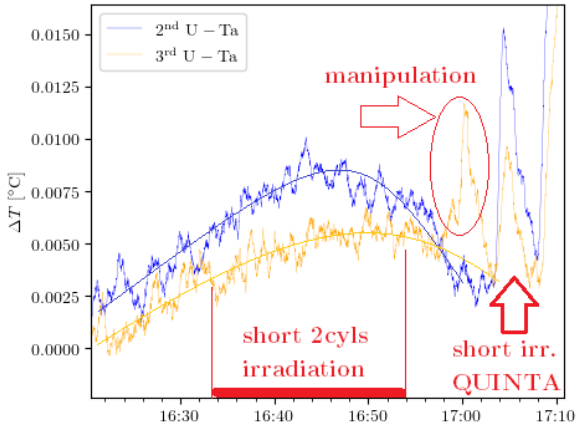

Figure D.10: Some ΔT are highlighted with description of its expected reason.

D.5.1 Neutron leakage of QUINTA target - side cylinders

Due to the larger scale and size of this visualisation in vector graphics, the comparing images in the appendix are already converted to „.png“ files. Lower image quality is caused by 10 times data compression.

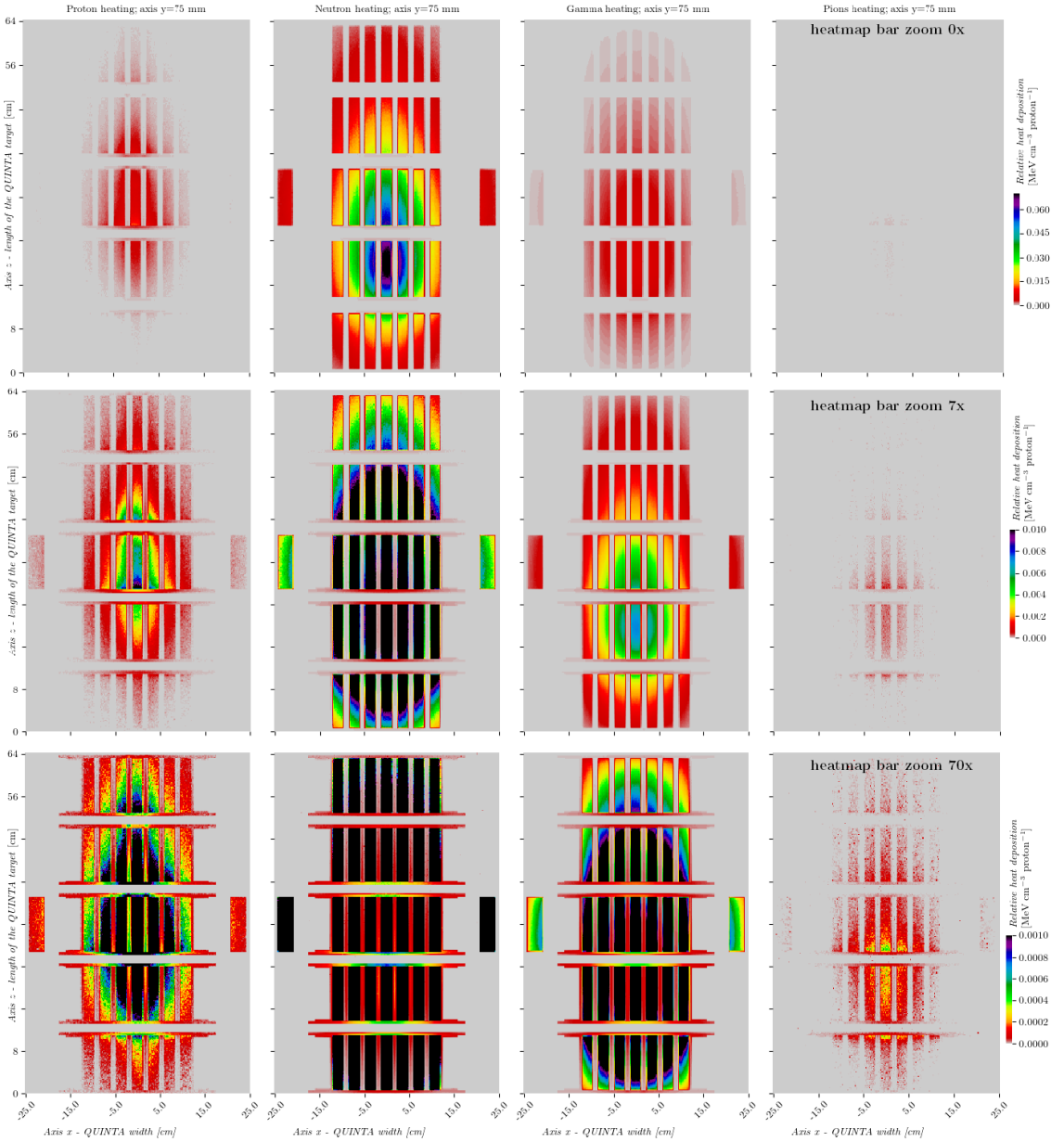

Figure D.11: MCNP simulation of the QUINTA side cylinders relative heating (neutron leakage), including pions heating. The high-quality vector image is shown without pions in Fig. 4.36. Charts are comparing all particles which participate in heat generation. Charts are shown in four columns (protons, neutrons, gamma and pions heating, respectively) and three rows which having different heatmap bar maximum. The first row has the maximum at 0.07 MeV· cm^{-3}· proton^{-1}, the second at 0.01 MeV· cm^{-3}· proton^{-1} and finally the third at 0.001 MeV· cm^{-3}· proton^{-1}. It shows the difference between each particle contributions and primarily it visualises the heating of the Al construction parts.

Appendix E

Chapter 5 sub-data

E.1 Python 3.7 code - MCNPX MESH plotting of single cross-sections

```
# program for plotting mesh from MCNPX output
# author : Josef Svoboda
# aff. : Joint Institute for Nuclear Research // Brno University of Technology;
# email : svoboda@jinr.ru // Josef.Svoboda@vutbr.cz
# Must DO: 1) convert binary mdata (mesh data) into text data, file name "all"
import os
import numpy as np
import pandas as pd
import matplotlib.pyplot as plt
import seaborn as sns
from matplotlib import cm
from matplotlib.colors import ListedColormap, LinearSegmentedColormap
import matplotlib.gridspec as gridspec# do not change!!!!
from matplotlib.ticker import FormatStrFormatter
from matplotlib import rc
cut_xy=None # don't change
cut_xz=None # don't change
cut_yz=None # don't change
rc('font',**{'family':'sans-serif','sans-serif':['Helvetica']})
rc('text', usetex=True)
sns.set(font_scale=1.5, rc={'text.usetex' : True})
# < --- ----- ------ ------- ---------- CHANGE HERE ----------------- <
#change target name (shows in charts)
target_name = "lead"
path = "d:\\MCNP\\Lead20201102_target_mesh\\dis\\" # set the patch here:
# what cross-section (CS) do you want: (if don't need some CS, just comment the line to don't use it)
#cut_xy = [5, 30, 50, 90] # number 1 means xy1, so the first cubes in mesh
cut_xz = [48] # the number 48 means CS right in the middle of target(cube edge=2mm->48*2=96mm, lead target diameter=190mm)
#cut_yz = [2,7, 15, 21]
#-------------------- clearing data set ------------------------!!!!!
# making automatic files from raw all (converted by gridconv) into files 1-5
print("\n-> This data clearing works only for the same size cuts for various particles (the same number of rows and columns)")
talliesnumber=int(input("\nHow many tallies cuts was calculated? : "))
print("\n--------- The program is reading the file..... in progress ----- wait please.....\n\n")
DF_clr = pd.read_fwf(path+"all", header=None, skiprows=(2+4*talliesnumber+1))
for i in range(1, talliesnumber+1):
    globals()['name%s'%i]=DF_clr.iloc[int((i-1)*(len(DF_clr)/5)):int((i-1)*(len(DF_clr)/5)+3),:]
    globals()['content%s'%i]=DF_clr.iloc[int((i-1)*(len(DF_clr)/5)+3):int(i*(len(DF_clr)/5)-(((len(DF_clr)/5)-3)/2)),:]
    globals()['content%s'% i].to_csv(path+str(i),sep=" ", header=None, index=None)
    globals()['content%s'% i]=globals()['content%s' % i].dropna(axis=1)
    print("Length of the file " + str(i) + " is : " + str(len(globals()['content%s' % i])))
# ---------------------- charts preparing and printing ------------------------------------!
data=[1,2,3,4,5] # ------------- change here!!!!!!!!!!!! <-------
data_name=["total", "protons", "neutrons", "gamma", "pions"] # ------------- change here!!!!!!!!!!!! <-------

multi=int(input("\nIf want to print multiple charts based on particle heat deposition, press 1 - if not, press 0 : "))
if multi:
    name = name1 # ------------------------------- if all names the same <-------
    fig = plt.figure(figsize=(7, 10.5))
    gs = gridspec.GridSpec(nrows=4,
                           ncols=1,
                           figure=fig,
                           width_ratios=[0.55],
                           height_ratios=[1, 1, 1, 1],
                           wspace=1.8,
                           hspace=0.2)
    if not os.path.exists(path + "mplot"):
        os.mkdir(path + "mplot") # print("Directory ---- Created")
    # locating name of lines and columns, deleting NaN and convert to list, after make it float
    name_x = name.iloc[[0]].dropna(axis=1).values.tolist()[0] # open DF "name", line 0(1), drop all NaN for
    namex = [float(i) for i in name_x]#axis in line and its values save to list - from this list of lists takes fist list
    name_y = name.iloc[[1]].dropna(axis=1).values.tolist()[0]
```

```
    namey = [float(i) for i in name_y]
    name_z = name.iloc[[2]].dropna(axis=1).values.tolist()[0]
    namez = [float(i) for i in name_z]
    # now it is preparing variable with total number of elements in each axis
    CSx = len(namex) - 1 # number of possible CS (Cross-Sections) in axis x
    CSy = len(namey) - 1 # number of possible CS (Cross-Sections) in axis y
    CSz = len(namez) - 1 # number of possible CS (Cross-Sections) in axis z
    # making average from boundaries items to boundaries-1 (boundaries to mesh cube center)
    namex_real = [] # and round it to 2 decimals, to be used as Index or Cols
    namey_real = []
    namez_real = []
    for x in range(0, len(namex) - 1):
        namex_real.append(float((namex[x] + namex[x + 1]) / 2))
    namex_real = [round(x, 1) for x in namex_real]
    for x in range(0, len(namey) - 1):
        namey_real.append(float((namey[x] + name_y[x + 1]) / 2))
    namey_real = [round(x, 1) for x in namey_real]
    for x in range(0, len(namez) - 1):
        namez_real.append(float((namez[x] + namez[x + 1]) / 2))
    namez_real = [round(x, 1) for x in namez_real]

    full_or_cutted=int(input("If calculated mesh is already cutted, press 1 - if is whole volume, press 0! : "))
    if cut_xz != None:
        # ---------------------------------- cut_xz ------------------------------------
        for i in range(0, len(cut_xz)):
            rows_needy = []
            for z in range(0, CSz):
                rows_needy.append((z * CSy + cut_xz[i]) - 1)
            for a in range (2,6):
                globals()['ax%s' % (a-2)] = fig.add_subplot(gs[a-2, 0])
                if full_or_cutted == 1:
                    xz = globals()['content%s' % (a)].T
                if full_or_cutted == 2:
                    xz = globals()['content%s' % (a)].iloc[rows_needy].T
                xz.index = [namex_real]
                xz.columns = [namez_real]
                xz = xz.rename_axis(index="Axis x - width of " + target_name + " target [cm]",
                                    columns="Axis z - length of " + target_name + " target [cm]")
                g = sns.heatmap(xz.iloc[:, :-10], cmap="nipy_spectral_r", xticklabels=50, yticklabels=16, vmin=0)
                plt.text(143, 13, data_name[a-1]+" heating", fontsize=14, color='gray', backgroundcolor='0.9')
                if a==2:
                    if full_or_cutted == 1:
                        plt.title("Cross-section zx in distance of y = " + str(namey_real[0]) + " mm")
                    if full_or_cutted == 2:
                        plt.title("Cross-section of zx axes in distance of y = " + str(namey_real[cut_xz[i]]) + " mm")
                else:
                    plt.title("")
                if a!= 5:
                    globals()['ax%s' % (a-2)].set_xticklabels(["", "", "", "", ""])
                    g.set_xlabel("")
                else:
                    globals()['ax%s' % (a - 2)].set_xticklabels(["0", "10", "20", "30", "40"])
                if a==4:
                    g.collections[0].colorbar.set_label("Heat deposition density [MeV cm$^{-3}$ proton$^{-1}$]")
                    g.set_ylabel("Axis x - width of " + target_name + " target [cm]")
                if a!=4:
                    g.collections[0].colorbar.set_label("")
                    g.set_ylabel("")
                g.set_xticklabels(g.get_xticklabels(), rotation=0)
                g.set_yticklabels(g.get_yticklabels(), rotation=0)
            plt.rc('text', usetex=True)
            plt.rc('font', family='serif')

        plt.savefig(path + "mplot\\xz" + str(cut_xz[i]) + "_all_plot_automat_multiple.pdf")
        plt.close()
        print("\n...\n...\nAll works fine, xz cross-section file was saved to DIR: path/mplot")
total=int(input("\nIf want to print total heat deposition, press 1 - if not, press 0 : "))
if total:
    name = name1 # ---------------------------------- if all names the same <-------
    fig = plt.figure(figsize=(10, 6))
    gs = gridspec.GridSpec(nrows=2,
                           ncols=1,
                           figure=fig,
                           width_ratios=[1],
                           height_ratios=[1,0.2],
                           wspace=0.2,
                           hspace=0.2)
    if not os.path.exists(path + "mplot"):
        os.mkdir(path + "mplot")
    # locating name of lines and columns, deleting NaN and convert to list, after make it float
    name_x = name.iloc[[0]].dropna(axis=1).values.tolist()[0] # open DF "name", line 0(1), drop all NaN for axis in line
    namex = [float(i) for i in name_x] # and its values save to list - from this list of lists takes fist list
    name_y = name.iloc[[1]].dropna(axis=1).values.tolist()[0]
    namey = [float(i) for i in name_y]
    name_z = name.iloc[[2]].dropna(axis=1).values.tolist()[0]
    namez = [float(i) for i in name_z]
    # now it is preparing variable with total number of elements in each axis
    CSx = len(namex) - 1 # number of possible CS (Cross-Sections) in axis x
    CSy = len(namey) - 1 # number of possible CS (Cross-Sections) in axis y
    CSz = len(namez) - 1 # number of possible CS (Cross-Sections) in axis z
    # making average from boundaries items to boundaries-1 (boundaries to mesh cube center)
    namex_real = [] # and round it to 2 decimals, to be used as Index or Cols
```

```
namey_real = []
namez_real = []
for x in range(0, len(namex) - 1):
    namex_real.append(float((namex[x] + namex[x + 1]) / 2))
namex_real = [round(x, 1) for x in namex_real]
for x in range(0, len(namey) - 1):
    namey_real.append(float((namey[x] + name_y[x + 1]) / 2))
namey_real = [round(x, 1) for x in namey_real]
for x in range(0, len(namez) - 1):
    namez_real.append(float((namez[x] + namez[x + 1]) / 2))
namez_real = [round(x, 1) for x in namez_real]

full_or_cutted=int(input("If calculated mesh is already cutted, press 1 - if is whole volume, press 0! : "))
if cut_xz != None:
    # ---------------------------- cut_xz ----------------------------
    for i in range(0, len(cut_xz)):
        rows_needy = []
        for z in range(0, CSz):
            rows_needy.append((z * CSy + cut_xz[i]) - 1)
        for a in range (1,2):
            globals()['ax%s' % (a-1)] = fig.add_subplot(gs[a-1, 0])
            if full_or_cutted == 1:
                xz = globals()['content%s' % (a)].T
            if full_or_cutted == 2:
                xz = globals()['content%s' % (a)].iloc[rows_needy].T
            xz.index = [namex_real]
            xz.columns = [namez_real]
            xz = xz.rename_axis(index="Axis x - width of the " + target_name + " target [cm]",
                                columns="Axis z - length of the " + target_name + " target [cm]")
            g = sns.heatmap(xz.iloc[:, :-10], cmap="nipy_spectral_r", xticklabels=25, yticklabels=16, vmin=0, vmax=1.5)
            plt.text(150.5, 7, data_name[a-1]+" heating", fontsize=14, color='gray', backgroundcolor='0.9')
            plt.xlim(0,185)
            if a==1:
                if full_or_cutted == 1:
                    plt.title("Cross-section zx in distance of y = " + str(namey_real[0]) + " mm")
                if full_or_cutted == 2:
                    plt.title("Cross-section of zx axes in distance of y = " + str(namey_real[cut_xz[i]]) + " mm")
            else:
                plt.title("")
            if a!= 1:
                globals()['ax%s' % (a-1)].set_xticklabels(["", "", "", "", "", "", "", "", ""])
                g.set_xlabel("")
            else:
                globals()['ax%s' % (a - 1)].set_xticklabels(["0", "5", "10", "15", "20", "25", "30", "35"])
            if a==1:
                g.collections[0].colorbar.set_label("Heat deposition density [MeV cm$^{-3}$ proton$^{-1}$]")
                g.set_ylabel("Axis x - width of " + target_name + " target [cm]")
            if a!=1:
                g.collections[0].colorbar.set_label("")
                g.set_ylabel("")
            g.set_xticklabels(g.get_xticklabels(), rotation=0)
            g.set_yticklabels(g.get_yticklabels(), rotation=0)
        plt.rc('text', usetex=True)
        plt.rc('font', family='serif')
    plt.savefig(path + "mplot\\xz" + str(cut_xz[i]) + "_all_plot_automat_total.pdf")
    plt.close()
    print("\n...\n...\nAll works fine, xz cross-section file was saved to DIR: path/mplot")
```

Python 3.7 code - MCNPX MESH plotting of single cross-sections - output

The outputs from the previous code are two charts shown in Fig. 5.5 for total relative heat deposition mesh and Fig. 5.6 for heat deposition partitioned by each contributing particle. This code is described in YouTube manual video, see https://youtu.be/R6P4zrUihkQ. Printed output from this code is attached in following:

```
D:/MCNP/Lead20201102_target_mesh/dis/MCNP_lead_2mmcube_h_n_p_pion-plus_total_printed_disserattion.py

-> This data clearing works only for the same size cuts for various particles (the same number of rows and columns)

How many tallies cuts was calculated? : 5

--------- The program is reading the file..... in progress ----- wait please.....


Length of the file 1 is : 226
Length of the file 2 is : 226
Length of the file 3 is : 226
Length of the file 4 is : 226
Length of the file 5 is : 226

If want to print multiple charts based on particle heat deposition, press 1 - if not, press 0 : 1
If calculated mesh is already cutted, press 1 - if is whole volume, press 0! : 1

...
...
All works fine, xz cross-section file was saved to DIR: path/mplot

If want to print total heat deposition, press 1 - if not, press 0 : 1
If calculated mesh is already cutted, press 1 - if is whole volume, press 0! : 1

...
...
All works fine, xz cross-section file was saved to DIR: path/mplot

Process finished with exit code 0
```

E.2 Python 3.7 code - 3D heat deposition described by equations

```
# program written by Josef Svoboda, BUT, Czechia; contact: josef.svoboda@vutbr.cz // svoboda@jinr.ru
# Reading data ready to be fitted.
# Creating a several od fit to curves (curve a and curve c) which depended on length z.
# Since having fit, the heat deposition is calculated per 1mm of length for approximation and MCNPX simulation.
# Program integrate these relative heat distribution and print sum -> relative heat deposition in whole target [MeV/proton].
# Finally the heat mesh is plotted for both to compare.
import os, glob, sys, math
import pandas as pd
import numpy as np
import scipy as sp
from scipy.optimize import curve_fit
import matplotlib.pyplot as plt
from matplotlib.colors import ListedColormap
from matplotlib.colors import LogNorm
import matplotlib.colors as colors
import matplotlib.cbook as cbook
import matplotlib.gridspec as gridspec
from matplotlib import rc
import seaborn as sns
rc('font',**{'family':'sans-serif','sans-serif':['Helvetica']}), rc('text', usetex=True) # latex font
pd.set_option('display.max_columns', 16, 'display.width', 250, 'display.max_rows', 20) # printing options
print("\n...\n...\n...\nReading data: path + filtered_making_equations.csv")
#-------------------------------change following 10 rows if needy-------------------------------
path = "d:\\Clouds\\ownCloud\\vut-jinr\\PhD\\dissertation_programs_temp\\"
new_curves=pd.read_csv(path+"no_filtered_making_equations.csv",sep=";", index_col="z_{cm}")
target_name="LEAD"
wanna_plot_equation_fit=1 #if want, tape number1, if not, type 0
wanna_fitplot=1
want_compare=1
wanna_heatmap=1
wanna___relative_heat_deposition_plot=1
a_curve_fit_boundaries_list=[11, 51, 149, 155, 165]
c_curve_fit_boundaries_list=[143, 151, 165]
#-----------------------------------fitting functions-----------------------------------
def func3(x, a, b, c, d):
    return a*x+b*x**2+c*x**3+d
superimpose=0 # if want plot fit to be superimpose in cutting points (variable list - var), type number 1
if wanna_plot_equation_fit:
    fg = plt.figure(figsize=(10,6))
    ax = fg.add_subplot(111)
    ax.plot(new_curves.columns.astype(np.float),new_curves.iloc[0,:], "+", color="r", label="$\mathrm{a_{parameter}}$")
    ax.plot(new_curves.columns.astype(np.float), new_curves.iloc[1, :], "+", color="b", label="$\mathrm{c_{parameter}}$")
```

```
    roots=pd.DataFrame()
    boundary=pd.DataFrame()
    a_data=[]
    c_data=[]
    not_first=1
    var = a_curve_fit_boundaries_list # boundaries of equations (where cuts)
    for i in range(0,len(var)):
        if i == 0:
            short = 1 # drops previous and forwarding of boundaries for making fit
            length_values=np.array(new_curves.columns[0+not_first:var[i]+short+superimpose]).astype(np.float)
            length_values_short=np.array(new_curves.columns[0:var[i]+superimpose]).astype(np.float)
            popt,pcov=curve_fit(func3,length_values,np.array(new_curves.iloc[0, 0+not_first:var[i]+short+superimpose]).astype(np.float))
            ax.plot(length_values_short, func3(length_values_short, *popt), 'g-', label="$\mathrm{fit_{a}}$")
            roots["par_a"+str(i)]=popt
            boundary["par_a"+str(i)]=length_values_short[[0,-1]]
            a_data.extend(func3(length_values_short, *popt).tolist())
        else:
            length_values=np.array(new_curves.columns[var[i-1]-short:var[i]+short+superimpose]).astype(np.float)
            length_values_short = np.array(new_curves.columns[var[i-1]:var[i]+superimpose]).astype(np.float)
            popt,pcov=curve_fit(func3,length_values,np.array(new_curves.iloc[0,var[i-1]-short:var[i]+short+superimpose]).astype(np.float))
            ax.plot(length_values_short, func3(length_values_short, *popt), 'g-')
            roots["par_a"+str(i)]=popt
            boundary["par_a"+str(i)]=length_values_short[[0,-1]]
            a_data.extend(func3(length_values_short, *popt).tolist())
    var = c_curve_fit_boundaries_list # boundaries of equations (where cuts)
    for i in range(0, len(var)):
        if i == 0:
            short = 1 # drops previous and forwarding of boundaries for making fit
            length_values = np.array(new_curves.columns[0:var[i] + short+superimpose]).astype(np.float)
            length_values_short = np.array(new_curves.columns[0:var[i]+superimpose]).astype(np.float)
            popt, pcov = curve_fit(func3, length_values, np.array(new_curves.iloc[1, 0:var[i] + short+superimpose]).astype(np.float))
            ax.plot(length_values_short, func3(length_values_short, *popt), 'y-', label="$\mathrm{fit_{c}}$")
            roots["par_c"+str(i)]=popt
            boundary["par_c"+str(i)]=length_values_short[[0,-1]]
            c_data.extend(func3(length_values_short, *popt).tolist())
        else:
            length_values = np.array(new_curves.columns[var[i - 1] - short:var[i] + short+superimpose]).astype(np.float)
            length_values_short = np.array(new_curves.columns[var[i - 1] :var[i]+superimpose]).astype(np.float)
            popt,pcov=curve_fit(func3,length_values,np.array(new_curves.iloc[1,var[i-1]-short:var[i]+short+superimpose]).astype(np.float))
            ax.plot(length_values_short, func3(length_values_short, *popt), 'y-')
            roots["par_c"+str(i)]=popt
            boundary["par_c"+str(i)]=length_values_short[[0,-1]]
            c_data.extend(func3(length_values_short, *popt).tolist())
    roots.index=["a","b","c","d"]
    print("\n\nParameters of equations = a*x + b*x**2 + c*x**3 + d, are following")
    print(roots)
    print("\n\nBoundaries of each curve fits are following (in [cm], step 0.2cm)")
    boundary.index=["from","to"]
    print(boundary)

    curves_data=pd.DataFrame()
    curves_data["a\_{curve}"]=np.array(a_data)
    curves_data["c\_{curve}"]=np.array(c_data)
    curves_data=curves_data.iloc[:-1,:]
    length=np.linspace(0,32.6, num=164)
    curves_data.index=length

    radius=np.linspace(-9.6, 9.6, num=97)
    p_DF=pd.DataFrame()
    for r in radius:
        p=[]
        for i in range(0,len(length)):
            p.append(curves_data.iloc[i,0]*np.exp(-(r ** 2) / curves_data.iloc[i,1] ** 2))
        for i in range(0,26):
            p.append(0)
        p_DF[str(round(r,1))]=np.array(p)
    length=np.linspace(0,37.6, num=190)
    p_DF.index=np.around(length,1)
    p_DF.to_csv(path+"DF_approximated_by_authors_equation.csv",sep=";")

    if wanna_fitplot:
        plt.rc('text', usetex=True)
        plt.rc('font', family='serif')
        plt.xlabel("\\textit{length z} [cm]",fontsize=14)
        plt.ylabel("\\textit{parameter a, c}",fontsize=14)
        plt.xticks(fontsize=12)
        plt.yticks(fontsize=12)
        plt.legend(loc="best",fontsize=12)
        plt.show()

if want_compare:
    make_csv = 1 # if csv already done, type 0 and it will be read
    if make_csv:
        power_print = pd.read_csv(path +"DF_approximated_by_authors_equation.csv",sep=";")
        list_index = power_print.iloc[:, 0].tolist()
        list_index[0] = 0
        listcol = power_print.columns.tolist()
        power_print = power_print.drop(columns=listcol[0])
        listindex = [round(float(elem), 1) for elem in list_index]
        power_print.index = listindex
        del listcol[0]
        listcol_r = [round(float(elem), 1) for elem in listcol]
```

```
        power_print.columns = listcol_r
        # print(power_print)
        half = 1
        if half:
            power_print.iloc[:, 0:49].to_csv(path + "approximation_half.csv", sep=";")
        else:
            power_print.to_csv(path + "approximation.csv", sep=";")
    content_MeV_cm3_proton = pd.read_csv(path + "approximation_half.csv", sep=";", header=None)
    radius = np.linspace(9.65, .05, num=49)
    content_MeV_cm3_proton = content_MeV_cm3_proton.drop(columns=0, index=0)
    content_MeV_cm3_proton.columns = radius.tolist()
    volume = radius * radius * 3.1415926 * 0.2 # makes cylinder volume from the radius (cm3)
    volume_annulus = volume[0:-1] - volume[1:] # now calculate the rings by subtract previous cylinder
    volume_annulus = np.append(volume_annulus, volume[-1]) # adding the centre cylinder (inner)
    content_MeV_proton = content_MeV_cm3_proton.multiply(volume_annulus, axis=1)
    content_MeV_proton_1mm_cylinder = content_MeV_proton.sum(axis=1)
    content_np = np.array(content_MeV_proton_1mm_cylinder)
    if len(content_MeV_proton_1mm_cylinder)>=220:
        del_list = [50,51,102,103,104,105,106,157,158,159,160,211,212,213,214,215,216,217,218,219,270,271,272,323] # define air gaps
    if len(content_MeV_proton_1mm_cylinder)<=220:
        del_list = [25, 51, 52, 53, 79, 80, 81, 106, 107, 108, 109, 110, 135, 136, 161, 162, 163, 164, 165]
    for i in del_list:
        content_np[i] = 0
    content_np = np.append(content_np, [0, 0, 0, 0, 0, 0, 0, 0])
    content_np = pd.DataFrame(content_np/2) # plot per 2mm length
    content_np.index=np.linspace(0,394,num=198)
    print("\n\nApproximated heat deposition generated in lead "+str(round(content_np.values.sum()*2,2))+" MeV per incident proton")

    heating = pd.read_csv(path + "total_20201105", sep=" ", header=None) # reading file where data xz mesh
    heating = heating.drop(index=17072)
    heating = heating.drop(columns=0)
    heating = heating.iloc[0:int(len(heating))]
    cyl_heating = []
    for i in range(0, 180):
        cyl_heating.append(heating.iloc[i * 97:(i + 1) * 97, :].sum().sum())
    heating_xy = pd.DataFrame(cyl_heating)
    heating_xy.index = heating_xy.index + heating_xy.index
    heating_xy = heating_xy * 8e-3 /2 # divided by 2 because plotting per 1mm length
    target_heat = pd.DataFrame(heating_xy)
    if len(content_MeV_proton_1mm_cylinder)>=220:
        del_list = [50,51,102,103,104,105,106,157,158,159,160,211,212,213,214,215,216,217,218,219,270,271,272,323] #define air gaps
    if len(content_MeV_proton_1mm_cylinder)<=220:
        content_np.sort_index
        del_list = [25,51,52,53,79,80,81,106,107,108,109,110,135,136,161,162,163,164,165,166,167,168,169,170,171,172,173,174,175,176]
    for i in del_list:
        target_heat.iloc[i] = 0 # delete air gaps, reset index and finally delete new column "index"
# in following, the values are multiply by 2, because printer per 1mm (before were divided by 2), but actual cube edge size is 2mm
    print("Simulated MCNPX heat deposition generated in lead "+str(round(target_heat.values.sum()*2,2))+" MeV per incident proton")
    print("\n--> MCNPX simulation total heat generation is "+str(round(target_heat.values.sum()*2*1.602e-13*2.4e15*1e-3,2))+" kJ")
    print("calculated approximated total heat generation is "+str(round(content_np.values.sum()*2*1.602e-13*2.4e15*1e-3,2))+" kJ")
    cylinders_length_heat = pd.concat([content_MeV_proton_1mm_cylinder, target_heat], axis=1)
    cylinders_length_heat.to_csv(path + "heat_per_length.csv", sep=";")

    if wanna_relative_heat_deposition_plot:
        plt.rc('text', usetex=True)
        plt.rc('font', family='serif')
        fg = plt.figure(figsize=(7, 3))
        fg.subplots_adjust(right=0.75)
        ax = fg.add_subplot(111)
        ax.plot(content_np.index, content_np, 'b', linewidth=1, label="Author's sym. approximation")
        ax.plot(target_heat.index, target_heat, 'r', linewidth=1, label="Authort's MCNPX simulation")
        ax.set_ylabel('\\textit{Relative heat deposition}\n[MeV mm$^{-1}$ proton$^{-1}$]')#we already handled the x-label with ax1
        ax.set_xlabel("")
        plt.text(130, -0.4, "\\textit{Target length} [mm]")
        plt.xlim(0, 350)
        ax.set_xticklabels(["0","50","100","","","250","300","350"])
        plt.legend(loc="best")
        plt.show()

if wanna_heatmap:
    fig = plt.figure(figsize=(12, 9))
    gs = gridspec.GridSpec(nrows=1,
                           ncols=3,
                           figure=fig,
                           width_ratios=[1, 0.1, 1],
                           height_ratios=[1],
                           wspace=0.1,
                           hspace=0.1)
    sns.set(font_scale=1.7, rc={'text.usetex': True})
    if not os.path.exists(path + "mplot"):
        os.mkdir(path + "mplot")

    xz=pd.read_csv(path+"nofiltered_1e8.csv",sep=";", header=None)

    ax0= fig.add_subplot(gs[0,0])
    xz=xz.drop(columns=0)
    xz=xz.T.iloc[:-1,:]
    xz.index=np.linspace(0,42.8,num=215)
    xz.columns=np.around(np.linspace(-9.6,9.6,num=97),1)
    xz = xz.rename_axis(index="Axis z - length of the LEAD target [cm]", columns="Axis x - width of the LEAD target [cm]")
    g = sns.heatmap(xz.iloc[:, :], cbar_kws={'format': '%.2f%%', 'ticks': [0, 0.35, 0.7, 1.05, 1.4], 'pad': 0.02, 'shrink': 0.9},
                    cmap="nipy_spectral_r", xticklabels=16, yticklabels=25, vmin=0, vmax=1.4)
```

```
plt.ylim(0, 185)
ax0.set_yticklabels(["0", "5", "10", "15", "20", "25", "30", "35"])
g.collections[0].colorbar.set_label("")
g.set_xlabel("\\textit{Axis x − width of " + target_name + " target} [cm]")
g.set_ylabel("\\textit{Axis z − length of " + target_name + " target} [cm]")
g.set_xticklabels(g.get_xticklabels(), rotation=90)
g.set_yticklabels(g.get_yticklabels(), rotation=0)
plt.text(8, 167, "Author's MCNPX heat\n~~deposition simulation")

power_print=pd.read_csv(path+"DF_approximated_by_authors_equation.csv",sep=";",index_col="Unnamed: 0")
ax1 = fig.add_subplot(gs[0, 2])
plt.text(8, 167,"Author's approximation\nof the heat deposition")
g = sns.heatmap(power_print,cbar_kws={'format': '%.2f%%', 'ticks': [0, 0.35, 0.7, 1.05, 1.4], 'pad':0.02, 'shrink':0.9},
                cmap="nipy_spectral_r", xticklabels=16, yticklabels=25, vmin=0, vmax=1.4)
ax1.set_yticklabels(["0", "5", "10", "15", "20", "25", "30", "35"])
ax1.set_xticklabels(["−9.6", "−6.4", "−3.2", "0", "3.2", "6.4", "9.6"])
plt.ylim(0,185) # invert axis from 0 to 152mm
g.set_xticklabels(g.get_xticklabels(), rotation=90)
g.set_xlabel("\\textit{Axis x − width of " + target_name + " target} [cm]")
g.set_ylabel("")
g.set_yticklabels(g.get_yticklabels(), rotation=0)
g.collections[0].colorbar.set_label("\\textit{Heat deposition density} [MeV cm$^{−3}$ proton$^{−1}$]")
print("\n\n−−−−−−−−− The program is printing the MESH chart..... in progress −−−−− wait please.....\n\n")
plt.rc('text', usetex=True)
plt.rc('font', family='serif')
plt.savefig(path + "mplot\\author_mesh_vs_symetric_approxtimation.pdf")
plt.close()
print("...\n...\nAll works fine, xz cross−section file of total heat deposition was saved to DIR: path/mplot")
```

Output text of the previous code „3D heat deposition by equations“

The output file of the previous Python code (p. E.2) is very crucial. It contents the calculated parameters of each equation for the individual boundaries of these equations. The program takes input data from MCNPX mesh heatmap output (enclosed in appendix F (item 5 for the CARBON target and item 7 for the LEAD target) and based on these data calculates two curves (*curve a* and *curve c*) fit. These equations are parameter functions of the relative heat deposition calculation (related to incident proton particle - units [MeV/proton]). Finally, the heat flux 2D approximation is calculated as described widely in section 5.1.3.

```
D:/Clouds/ownCloud/vut−jinr/PhD/dissertation_programs_temp/fit_to_heatmap_no_gaus_filter_to_DzP_print.py

...
...
...
Reading data: path + filtered_making_equations.csv


Parameters of equations = a*x + b*x**2 + c*x**3 + d, are following
   par_a0      par_a1      par_a2      par_a3          par_a4          par_c0      par_c1          par_c2
a  0.219090   −0.018913   −0.087930   −110.080344     276.293819      0.024925   −160.147586     203.784897
b  −0.10453   −0.007767    0.000851    3.611824      −8.760729       −0.000064   5.506333       −6.104596
c  0.014078    0.000380    0.000013   −0.039480       0.092521        0.000045   −0.063012       0.060292
d  1.318461    1.514514    1.704485    1117.918602    −2902.1011      2.212384    1554.274309    −2243.107934


Boundaries of each curve fits are following (in [cm], step 0.2cm)
       par_a0  par_a1  par_a2  par_a3  par_a4  par_c0  par_c1  par_c2
from      0.0     2.2    10.2    29.8    31.0     0.0    28.6    30.2
to        2.0    10.0    29.6    30.8    32.8    28.4    30.0    32.8


Approximated heat deposition generated in lead 419.99 MeV per incident proton
Simulated MCNPX heat deposition generated in lead 420.33 MeV per incident proton

−−−> MCNPX simulation total heat generation is 161.61 kJ
calculated approximated total heat generation is 161.48 kJ


−−−−−−−−− The program is printing the MESH chart.....  in progress −−−−−− wait please.....


...
...
All works fine, xz cross−section file of total heat deposition was saved to DIR: path/mplot

Process finished with exit code 0
```

E.3 The LEAD target heat deposition density mesh comparison

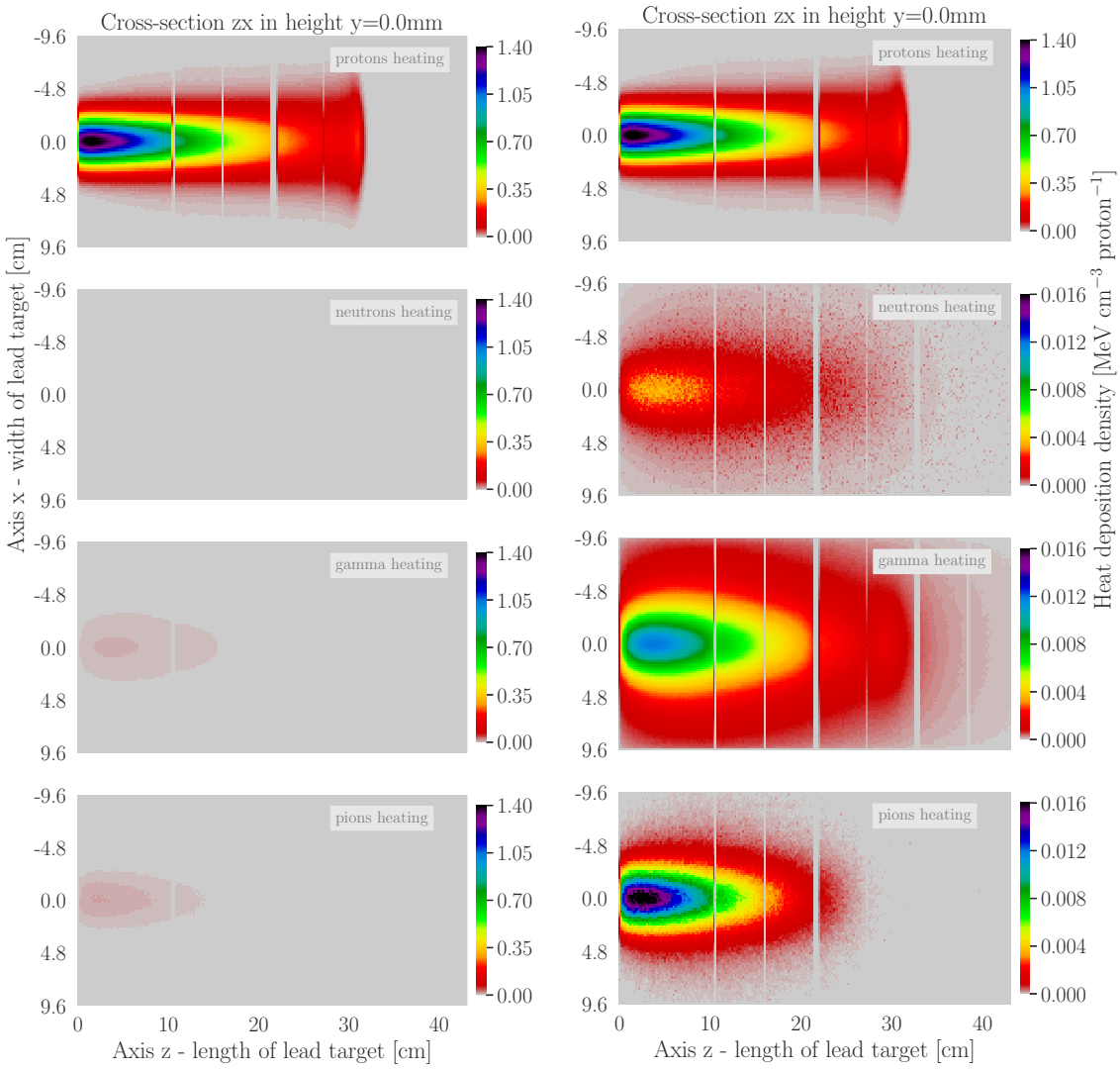

Figure E.1: The LEAD target rel. heat deposition density mesh (zx plane) in the centre of target height (y=0mm). On the left side are shown all charts with the same heatmap bar. On the right side, the proton heating is identical with the left side, but neutron, photon and pion$^+$ heating is having the same heatmap bar with the maximum at 16 keV$\cdot$ cm$^{-3}\cdot$ proton^{-1} (the pion$^+$ maximum. The Python program for plotting this visualisation is described and attached in page 181, data file is enclosed in appendix F (item 7).

E.4 The CARBON target sub-data

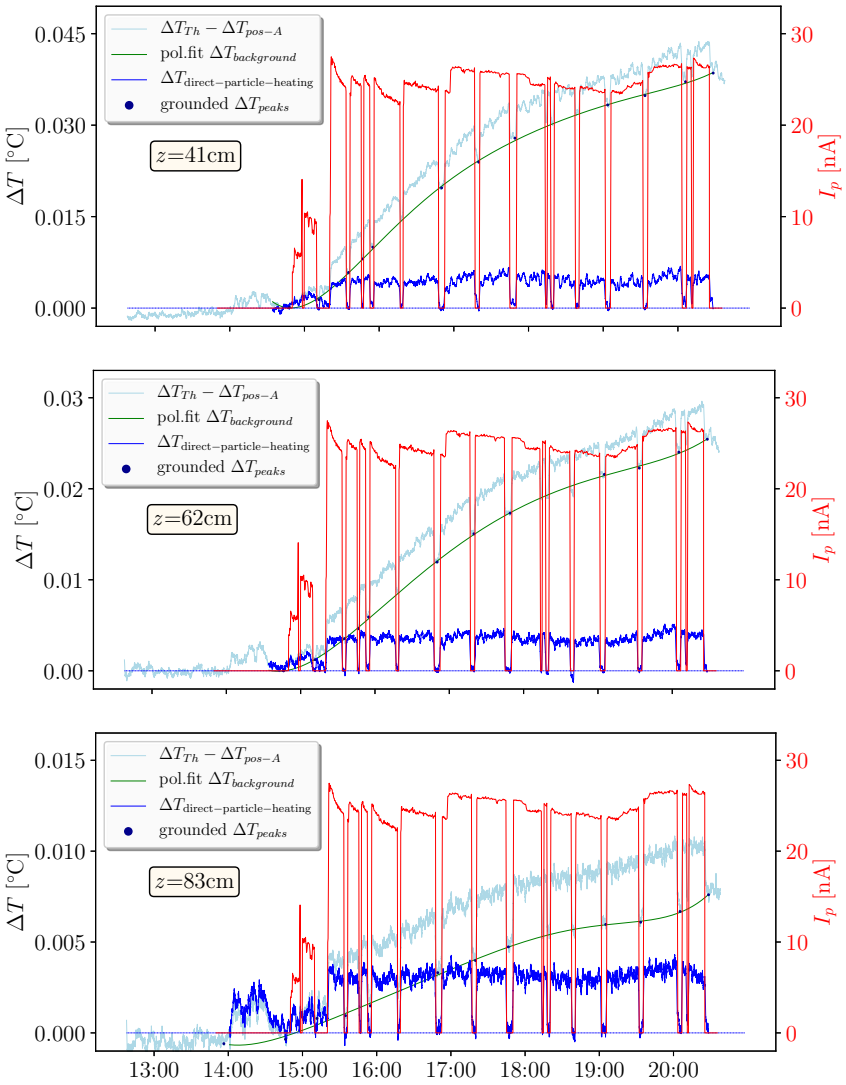

Figure E.2: The thorium sample temperature subtracted from the carbon target temperature (pos.A-pos.B, represented by light blue colour) and its dependency on proton beam occurrence (red colour, axis y2-right). The temperature background of the thorium sample is fitted by polynomial function (green), which is finally subtracted by $\Delta T^{Th-pos.A}_{difference}$ (light blue) - the result of this subtraction is the direct temperature growth caused by direct particles reaction in the Th sample (represented by blue). These charts are just addition to Fig. 5.32. This phenomena and method of calculation is widely described in p. 113.

E.5 Python script - polynomial $T_{background}$ fit, direct ΔT_{direct} storage

```
from scipy import signal
from scipy.signal import savgol_filter
import numpy as np
import pandas as pd
import matplotlib.dates as mdates
import matplotlib.pyplot as plt
import logging
import scipy as sp
from scipy import signal
from scipy.optimize import curve_fit
import datetime
from matplotlib import rc
rc('font', **{'family': 'serif', 'serif': ['Computer Modern'], 'size' : 16})
rc('text', usetex=True)
logging.getLogger('matplotlib.font_manager').disabled = True
# functions definition
def smoothing(x):
    return savgol_filter(x, 17, 1, mode='nearest')
def func6(x, a, b, c, d,e,f,g):
    return a*x+b*x**2+c*x**3+d*x**4+e*x**5+f*x**6 +g
# -------- CHANGE following !!!!! ------------
path = "d:\\Clouds\\owncloud\\vut-jinr\\PhD\\dissertation_programs_temp\\Th_carbon_diff_calc" # setting the path to the files
content_all = pd.read_csv(path + "\\data.csv", sep = ";", parse_dates=["time"], index_col ="time") #loading - dT [K]
beam=pd.read_csv(path + "\\proton_current.csv",sep=";",parse_dates=["Time"],index_col="Time")
TC=content_all.columns.tolist() # reads names of each columns to be more easily to reach
# ----- setting of the script calculation
wanna_show_chart=0 # if zero -> chart not shown, but saved in pdf format into the folder of path
save_dataframe=1
fitfunc=func6 # type an order of polynomial function wanna use
i=4 # starting column location - pos.A z=20 is located in 5th column -> python calculated from zero -> No.4
content_all["time"]=content_all.index #creates column "time" in second with 0=beginning od measured data
df=pd.DataFrame(content_all["time"])
df["time"] = pd.to_timedelta(content_all["time"]) #date format for further calculation
df['tot_seconds_in_day'] = ((df.time - df.time.dt.floor('D')).dt.total_seconds()).round() # calculated total seconds to floor
beginning=df.tot_seconds_in_day[0] # definition of time zero t_0
content_all["time"]=np.int_(df["tot_seconds_in_day"]-beginning) # calculated from t_0, makes integer
beam["time"]=beam.index #creates column "time" in second with 0=beginning od measured data
df=pd.DataFrame(beam["time"])
df['time'] = pd.to_timedelta(beam["time"]) #date format for further calculation
df['tot_seconds_in_day'] = ((df.time - df.time.dt.floor('D')).dt.total_seconds()).round() # calculated total seconds to floor
beam["time"]=np.int_(df["tot_seconds_in_day"]-beginning) # calculated from t_0, makes integer

new_DF=pd.DataFrame(smoothing(np.round(-np.array(content_all[content_all.columns[i]])+np.array(
    content_all[content_all.columns[i+1]]),5))) #calculate difference between carbon and Thorium
new_DF.index=content_all["time"]
# automatic peak location beginning----------------------------------------
#peaks, _ = signal.find_peaks(new_DF.iloc[:,0], width=40, rel_height=0.2, height=-0.025) #automat peak searching
#peaks=np.append(peaks,[500, 28770, 9420,4800,9350,9400]) # these peacks is suitable to add
#peaks=peaks.tolist()
# automatic peak location end----------------------------------------
manual_peak=[4940,7378,9238,10661, 11338, 11828, 15146, 16929, 18685, 23170, 24950, 26814,28236] # used manual due to noise
popt, pcov = curve_fit(fitfunc, manual_peak, -np.array(new_DF.iloc[manual_peak,0]).astype(np.float))
print("Polyfit: a*x+b*x**2+c*x**3+d*x**4+e*x**5+f*x**6 +g\n--->The parameters of fit are:\n", popt)
fig, ax = plt.subplots(figsize=(8.5,4.5))
ax.plot(new_DF.index,-new_DF,color="lightblue",lw=0.3, label="$\Delta T_{pos.A}^{Carbon}-\Delta T_{pos.B}^{Th}$")

indexes_used=np.linspace(5000,28236,num=23237)
ax.plot(indexes_used, fitfunc(indexes_used, *popt), 'g-', label="pol.fit $\Delta T_{background}^{dif.}$",lw=0.4)
indexes_used=np.linspace(7600,28236,num=20637)
ax.plot(indexes_used, -new_DF.iloc[indexes_used,0] - fitfunc(indexes_used,
                                        *popt), 'b-',lw=0.1, label="$\Delta T_{\mathrm{direct-particles-heating}}$")
ax.plot([0,30000],[0,0],"b--",lw=0.2)
ax.plot(manual_peak,-new_DF.iloc[manual_peak,0],".",color="darkblue",ms=2,label="background $\Delta T_{peaks}$")
ax2 = ax.twinx() # define a second axis that shares the same x-axis - for beam current plotting
ax2.set_ylabel('$I_p$ [nA]', color="red") # we already handled the x-label with ax1
ax2.tick_params(axis='y', labelcolor="red")
ax2.plot(beam.iloc[:,1], beam.iloc[:,0], color="red", lw=0.05, label="I_p")
ax.set_ylabel("$\Delta T$ [$^\\circ$C]",color="black")
hours_xtics=[1336,4936,8536,12136,15736,19336,22936,26536]
hours_xticlabels=["13:00","14:00","15:00","16:00","17:00","18:00","19:00","20:00"]
ax.set_xticks(hours_xtics)
ax.set_xticklabels(hours_xticlabels)
plt.text(1340,14,"\\textit{z}=20~cm",color='black',bbox=dict(facecolor='floralwhite', edgecolor='black', boxstyle='round,pad=0.2'))
ax.set_ylim(-0.002,0.033)
ax.set_yticks([0,.01,.02,.03])
ax2.set_ylim(-2,33)
ax2.set_yticks([0,10,20,30])
ax.legend(loc="best", framealpha=0.95, shadow=True, facecolor="white", fontsize=12, markerscale=3,labelspacing=1)
if wanna_show_chart:
    plt.show()
else:
    plt.savefig(path + "\\Th_vs_Carbon_saved_z20.pdf")
    plt.close()
if save_dataframe:
    df=pd.DataFrame(np.round(np.array(indexes_used),0))
    df["data"]=np.array(-new_DF.iloc[indexes_used,0] - fitfunc(indexes_used, *popt))
    df.columns=["time20","data20"]
    df.to_csv(path + "\\Th_vs_Carbon_saved_z20.csv",sep=";")
```

```
print("Finished!")
```

Python script - heating peaks localisation and linear approximation

```
from scipy import stats
from scipy.signal import savgol_filter
import numpy as np
import pandas as pd
import matplotlib.dates as mdates
import matplotlib.pyplot as plt
import logging
from scipy.optimize import curve_fit
from matplotlib import rc
rc('font', **{'family': 'serif', 'serif': ['Computer Modern'], 'size' : 16}) # font definition
rc('text', usetex=True) # using latex text
pd.set_option('display.max_rows', 500) #s etting the number of visualised rows in the output text
logging.getLogger('matplotlib.font_manager').disabled = True # solving potential font error problem
# ———— CHANGE following !!!!! ————————————
path = "d:\\Clouds\\ownCloud\\vut-jinr\\PhD\\dissertation_programs_temp\\Th_carbon\\"
# reading the beam data - first column "Time" in format "14:00:00", second column I_p [nA]
beam=pd.read_csv(path + "proton_current.csv",sep=";",parse_dates=["Time"],index_col="Time")
#loads files per position - already subtracted data (pos.A-pos.B) are column "data(No.)", responding time in "time(No.)"
content83 = pd.read_csv(path + "Th_vs_Carbon_saved_z83.csv", sep = ";")
content62 = pd.read_csv(path + "Th_vs_Carbon_saved_z62.csv", sep = ";")
content41 = pd.read_csv(path + "Th_vs_Carbon_saved_z41.csv", sep = ";")
content20 = pd.read_csv(path + "Th_vs_Carbon_saved_z20.csv", sep = ";")
content_all=pd.concat([content20.iloc[:,[1,2]],content41.iloc[:,[1,2]],content62.iloc[:,[1,2]],content83.iloc[:,[1,2]]],axis=1)
content_all["time"]=content_all.index # creates column "time" in seconds, where 0=beginning of measured data
df=pd.DataFrame(content_all["time"]) # creates new DF by purpose to change the time format
df["time"] = pd.to_timedelta(content_all["time"]) # reads the time in timedelta format
df['tot_seconds_in_day'] = ((df.time - df.time.dt.floor('D')).dt.total_seconds()).round() # calculates tot.s from time (floor)
beginning=df.tot_seconds_in_day[0] # definition of the t_0 - beginning time
beam["time"]=beam.index # creates column "time" in second with 0=beginning od measured data
df=pd.DataFrame(beam["time"]) #the same as previous desription
df["time"] = pd.to_timedelta(beam["time"]) # - || -
df['tot_seconds_in_day'] = ((df.time - df.time.dt.floor('D')).dt.total_seconds()).round() # - || -
beam["time"]=np.int_(df["tot_seconds_in_day"]-beginning) # subtract the seconds calculation beginning and make it integer

content20=content20[content20.time20>7000] # cut data vertically - by time in seconds
newDF=content20[content20.data20>0.00313] # cut data horizontally - by measured dT

plt.plot(newDF["time20"], newDF["data20"], "*",ms=1) # visualise data for controlling
plt.show()

end=[]
beg=[newDF.index[0]]
# following look goes through data ale locate the index where the bew peak begins
# each peak consist of increasing index by 1, so if the step is bigger, it mean the new peak begins
for i in range(1,len(newDF)):
    if newDF.index[i-1]+1!=newDF.index[i]:
        end.append(newDF.index[i-1])
        beg.append(newDF.index[i])
end.append(newDF.index[-1]) # loop found the start of peak, so the end of previous is index-1
del(beg[-1]) # delete last item in the list, because it is not peak (based on visualisation controlling)
print("Ends:", end, "\nBeginnings: ", beg)
print("length of the beginning list = ", len(beg), "\nlength of the end list = ", len(end))
# so now the peak beginnings and ends are known

# the most important is to locate the values of the peak after the growing region - it is performed by following loops
# if dT value in time (t=t_0+5s) < dT value in t_0, it means the edge was found (5s used because of delay and noise)
beg_peak=[] # this list will be fulfill by real peak beginnings
for i in range(0,len(beg)):
    y=beg[i]
    while y<end[i]:
        if newDF.iloc[newDF.index.get_loc(y+5),2] < newDF.iloc[newDF.index.get_loc(y),2]:
            beg_peak.append(newDF.index.get_loc(y+1))
            y=end[i]
        else:
            y+=1
end_peak=[] # this list will be fulfill by real peak ends
for i in range(0,len(beg)):
    y=end[i]
    while y>beg[i]:
        if newDF.iloc[newDF.index.get_loc(y-5),2] < newDF.iloc[newDF.index.get_loc(y),2]:
            end_peak.append(newDF.index.get_loc(y-1))
            y=beg[i]
        else:
            y-=1
print("beg peak: ",beg_peak)
print("end peak: ",end_peak)
beg_time=[] # until now, it works with indexing without real time - in following loops the time is found
for i in beg_peak:
    beg_time.append(newDF.iloc[i,1])
np.round(beg_time,0)
print("real peak maximum beginning:", beg_time)
end_time=[] # the same for the end
for i in end_peak:
    end_time.append(newDF.iloc[i,1])
np.round(end_time,0)
print("real peak maximum end:", end_time)

# between found boundaries the dT data are approximated by linear regression to decrease noise
```

```
linreg_slope=[]
linreg_inter=[]
for i in range(0,len(beg_peak)):
    slope, intercept, r_value, p_value, std_err = stats.linregress(newDF.iloc[beg_peak[i]:end_peak[i],1],
                                                                   newDF.iloc[beg_peak[i]:end_peak[i],2])
    linreg_slope.append(slope)
    linreg_inter.append(intercept)
print("slope: ", linreg_slope, "\nlinreg: ", linreg_inter)

df_save=pd.DataFrame() # all data are load to df and stored to .csv file
df_save["beginning"]=beg_time
df_save["end"]=end_time
df_save["intercept"]=linreg_inter
df_save["slope"]=linreg_slope
df_save.to_csv(path+"z_20_parameters.csv",sep=";")

print(len(end_peak), len(linreg_slope))

def smoothing(x):
    return savgol_filter(x, 11, 1, mode='nearest') # data smoothing for visualisation
fig, ax = plt.subplots(figsize=(8.5,5))
ax.plot(content_all["time83"],smoothing(content_all["data83"]), "-", lw=0.2, color="red")
ax.plot(content_all["time62"],smoothing(content_all["data62"]), "-", lw=0.2, color="green")
ax.plot(content_all["time41"],smoothing(content_all["data41"]), "-", lw=0.2, color="orange")
ax.plot(content_all["time20"],smoothing(content_all["data20"]), "-", lw=0.2, color="blue")
ax.set_xlim(7000,30000)
for i in range(0,len(end_peak)): # prints peak by peak linear regression
    x=np.array([newDF.iloc[beg_peak[i],1],newDF.iloc[end_peak[i],1]])
    ax.plot(x, linreg_inter[i]+linreg_slope[i]*x,"r-")
plt.show()
```

Table E.1: Relative comparison of direct heating of thorium sample, FULL version. The extracted version and description of this measurement is located in and above Tab 5.3

No.	**Median of absolute ΔT growth [mK]**					**Relative ΔT growth [%]**			
	z=20cm	**z=41cm**	**z=62cm**	**z=83cm**	→	**z20**	**z41**	**z62**	**z83**
1	5.57	4.02	3.35	3.07		100%	72%	60%	55%
2	6.01	4.41	3.53	2.96		100%	73%	59%	49%
3	6.58	4.93	3.98	3.39		100%	75%	60%	51%
4	6.05	4.17	3.59	2.97		100%	69%	59%	49%
5	6.52	4.40	3.69	3.16		100%	68%	57%	48%
6	7.05	4.47	3.73	3.29		100%	63%	53%	47%
7	7.43	5.11	3.87	3.24		100%	69%	52%	44%
8	7.09	4.96	3.52	3.15		100%	70%	50%	44%
9	7.96	5.36	3.65	3.22		100%	67%	46%	40%
10	6.34	4.53	3.24	2.92		100%	72%	51%	46%
11	6.33	4.29	3.26	2.92		100%	68%	52%	46%
12	6.08	4.13	3.35	3.09		100%	68%	55%	51%
13	7.29	5.14	4.09	3.51		100%	70%	56%	48%
14	5.90	4.76	4.10	3.48		100%	81%	70%	59%
15	7.00	4.87	3.86	3.16		100%	70%	55%	45%
relative temperature caused by direct heating						**100%**	**70%**	**55%**	**48%**

Table E.2: Direct heating of different materials located in identical particle flux

	Pb				Fe				^{nat}U				Th			
Length [cm]	20	41	62	83	20	41	62	83	20	41	62	83	20	41	62	83
$E^{total}_{deposition}$ [J]	2.35	1.86	1.42	1.13	2.27	1.79	1.38	1.11	5.14	4.09	3.07	2.45	2.90	2.40	1.77	1.39
$E^{proton}_{rel.}$ [%]	94.9	96.3	97.7	99.0	95.4	96.5	97.9	99.1	82.6	84.9	88.5	91.6	88.2	89.4	92.6	94.7
$E^{neutron}_{rel.}$ [%]	0.4	0.3	0.3	0.2	0.5	0.5	0.5	0.3	13.1	12.2	9.8	7.7	7.3	7.5	5.7	4.5
$E^{photon}_{rel.}$ [%]	0.4	0.3	0.3	0.2	0.1	0.1	0.1	0.1	0.3	0.3	0.3	0.2	0.3	0.3	0.3	0.2
$E^{pion^+}_{rel.}$ [%]	4.3	3.0	1.7	0.6	3.9	2.9	1.5	0.5	4.0	2.6	1.5	0.5	4.2	2.8	1.4	0.7

Table E.3: Comparison of MCNPX libraries for CARBON simulation; lib70=ENDF70a; lib24=la150n

	z=20cm				z=41cm				z=62cm				z=83cm			
sample	Pb	Fe	^{nat}U	Th	Pb	Fe	^{nat}U	Th	Pb	Fe	^{nat}U	Th	Pb	Fe	^{nat}U	Th
cell No.	40	140	240	340	41	141	241	341	42	142	242	342	43	143	243	343
mass [g]	1.14	0.79	1.91	1.17	1.14	0.79	1.91	1.17	1.14	0.79	1.91	1.17	1.14	0.79	1.91	1.17
E_{lib24} [J]	2.36	2.27	5.39	2.87	1.86	1.79	4.27	2.39	1.41	1.38	3.17	1.76	1.13	1.11	2.51	1.38
E_{lib70} [J]	2.35	2.27	5.14	2.90	1.86	1.79	4.09	2.40	1.42	1.38	3.07	1.77	1.13	1.11	2.45	1.39
$\delta E^{70=ref}_{lib}$	**0.1%**	**0.0%**	**5.0%**	**0.9%**	**0.1%**	**0.0%**	**4.5%**	**0.4%**	**0.1%**	**0.0%**	**3.2%**	**0.4%**	**0.1%**	**0.0%**	**2.4%**	**0.4%**

CARBON target MCNPX simulation-mesh

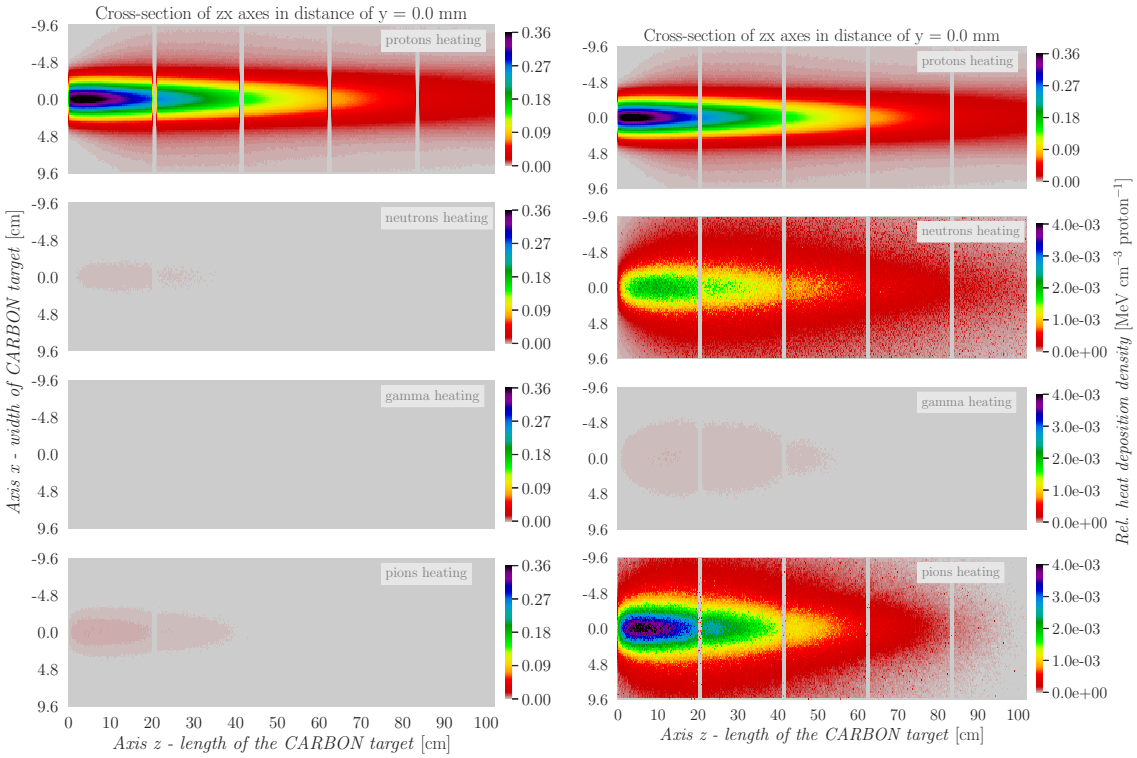

Figure E.3: The CARBON target rel. heat deposition density mesh (zx plane) in the centre of target height (y=0mm). On the left side are shown all charts with the same heatmap bar. On the right side, the proton heating is identical with the left side, but neutron, photon and pion$^+$ heating is having the same heatmap bar with the maximum at 4 keV$\cdot$ cm$^{-3}\cdot$ proton^{-1} (the pion$^+$ maximum. The Python program for plotting this visualisation is described and attached in page 181, data file is enclosed in appendix F (item 5).

Appendix F

Cloud files

The author shares all data as an example of how to perform various tasks. It might be helpful for those dealing with similar topics. The following files are accessible for any student of BUT, after their login to the Google disk by their @vut account. In the case of seeking these files without being a student of the Brno University of Technology, please ask the author for special access to these files by email at Josef.Svoboda@vut.cz. The access will be provided through your email account.
The URL link is not displayed in the printed version, to reach these files, please find the electronics version at: https://www.vutbr.cz/studenti/zav-prace/detail/135700.

F.1 MCNPX simulation files

1. Exp. No.11 - MCNPX output of mesh and n leakage simulation:
   exp11-QUINTA-1e8-cylinders-tallies-output
2. Exp. No.11 - converted MCNPX mesh results:
   exp11-QUINTA-3e8-mesh-gridconv
3. Exp. No.11 - MCNPX output of cylinders tallies simulation:
   exp11-QUINTA-3e8-mesh-output
4. Exp. No.12 - MCNPX output:
   exp12-CARBON-1e8-MCNPX-output
5. Exp. No.12 - converted MCNPX mesh results:
   exp12-CARBON-1e8-mesh-gridconv
6. Exp. No.13 - MCNPX output:
   exp13-LEAD-1e8-MCNPX-output
7. Exp. No.13 - converted MCNPX mesh results:
   exp13-LEAD-1e8-MCNPX-mesh-gridconv

F.2 3D geometries created for the purpose of this thesis

3D models - Invertor/SketchUp:

1. Precise model of the QUINTA target:
   The TA QUINTA - SketchUp
2. Simplified model of the QUINTA target:
   The TA QUINTA - Inventor
3. 3D model of the CARBON target:
   The CARBON target - Inventor
4. 3D model of the LEAD target:
   The LEAD target - Inventor
5. 3D model of the concrete wall:
   The concrete wall in experimental hall - Inventor
6. 3D model of the BURAN sub-critical assembly:
   The BURAN sub-critical assembly - Inventor

3D models - Fluent:

1. Fluent model of the CARBON target:
   Fluent case - 3D - CARBON (137 MB)
2. UDF for the CARBON target:
   Fluent UDF - 3D - CARBON
3. Fluent model of the LEAD target:
   Fluent case - 3D - LEAD (147 MB)
4. UDF for the LEAD target:
   Fluent UDF - 3D - LEAD

In case of using these files for other purposes than studying, please contact the author for permission. Full open access of codes, models, and files is based on the idea of sharing knowledge for boosting student skills and studying rapidity. It is common to share only the results with the calculation examples, which actually does not help much in more advanced problems. Therefore, enjoy and use all data but please, do not misuse!

F.3 List of created YouTube manuals:

1. Python script for volume MCNPX MESH data visualisation (any possible plane):
   https://youtu.be/kUDWkV0juW8
2. The LEAD target 2D geometry creation for ANSYS simulation:
   https://youtu.be/npZvOPxPEkY
3. MCNPX heat mesh tally 2D - calculation and visualisation by Python:
   https://youtu.be/R6P4zrUihkQ
4. Python script for heat deposition approximation by equations:
   https://youtu.be/RRqtm1FfxJU
5. Direct Th heating - data extraction (CARBON target) - Python:
   https://youtu.be/bxQp_vvTLIY
6. Direct temperature peaks location + linear regression (C target) - Python:
   https://youtu.be/9XoYIU1r0Rk
7. Fluent 3D simulation setting - CARBON target:
   https://youtu.be/C85XIkuw4GY
8. Fluent 3D LEAD target - from geometry creation to results:
   https://youtu.be/oOjEZQ1Rqso